Ultrafast Coherent Imaging Spectroscopy of Van-der-Waals Materials

by

Torben Lennart Purz

A dissertation submitted in partial fulfillment
of the requirements for the degree of
Doctor of Philosophy
(Physics)
in The University of Michigan
2023

Doctoral Committee:

Professor Steven T. Cundiff, Chair
Professor Hui Deng
Professor Mackillo Kira
Professor Theodore Norris
Professor Jennifer Ogilvie

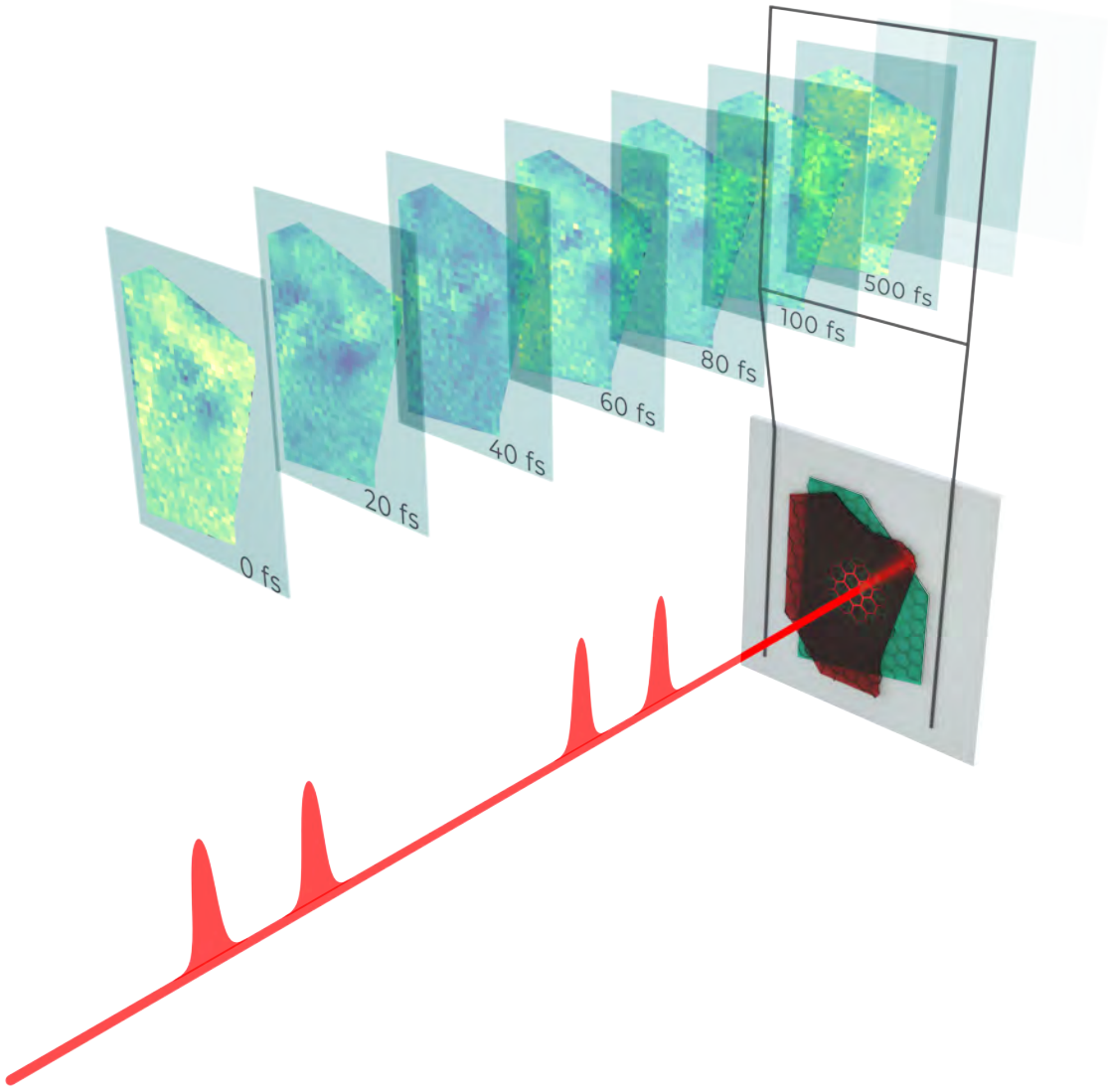
0 fs
20 fs
40 fs
60 fs
80 fs
100 fs
500 fs

Torben Lennart Purz

purz@umich.edu

ORCID iD: 0000-0003-3506-2183

Because maybe

You're gonna be the one that saves me

And after all

You're my van-der-Waals

ACKNOWLEDGEMENTS

It takes a village to raise a child. But it takes even more to do a PhD. The work presented in this thesis is by no means the work of a single individual.

An enormous thank you goes out to my research advisor, Prof. Steven Cundiff, who was always able to provide challenging questions, endless optics and semiconductor trivia knowledge that helped guide my research, and incredible support in getting me to the University of Michigan in the first place. The work in this thesis would also not have been possible without my "second research advisor" and good friend, Dr. Eric Martin. When I first met Eric in 2018, little did I know that he would turn into an inspiring mentor and friend for years to come. His relentless (constructive) criticism, optimism, and out-of-the-box thinking during my PhD shaped me into the researcher and scientist I am today, and I am beyond grateful to him for that.

I would also be remiss not to acknowledge Blake Hipsley's support throughout the past two years. His work on building the SLM pulse-shaper and assistance in the lab has been invaluable and allowed me to focus on other things while knowing the setup would be in good hands. Great thanks also go out to various collaborators who have accompanied me along the way; Kelsey Bates, Adam Alfrey, Pasqual Rivera, and William Holtzmann are only a few to name. Pasqual provided the heterostructure samples that have followed me throughout my PhD, and Will helped provide additional data on them for our publications. Working with Adam has been an exceptional pleasure, as his challenging questions, deep insight, and endless curiosity have guided my scientific endeavors. I have learned a lot about sample fabrication from him.

Kelsey has been an immense resource for discussions, and I greatly benefited from our frequent exchanges on collinear multidimensional coherent spectroscopy and debugging our setups' issues. The same holds true for Albert Liu and Matthew Day, who were especially useful at the beginning of my PhD whenever I needed opinions or guidance. I am thankful for the time and insight provided by Xiaodong Xu at the University of Washington and Hui Deng right here at the University of Michigan. Their material expertise propelled me forward, and I could not have asked for better sample growers. I got additional ideas and impulses from discussions with many other faculty members, including Mackilo Kira, Dmitri Voronine, Jennifer Ogilvie, Parag Deotare, and Ronald Ulbricht. Some ideas might not have always translated into projects presented in this thesis, but their vast knowledge and insight are deeply appreciated and made me a more complete researcher. I also want to thank many of my colleagues, including Cesar Perez, Grace Kerber, and Christoper Ayala, who have been there whenever I needed a late-night coffee/tea break or a middle-of-the-day ice cream break.

Outside the lab, I could not have asked for a better support system. I would not be the person without the love and care of my parents, Andreas Purz and Dorothea Währisch-Purz, and my siblings Anneke Purz and Sören Purz. I am beyond grateful for the support my parents provided me, always encouraging me to be myself and do things my way. You might not have understood why I was doing this work (or why I was doing it at 2 am), but you were always there and had my back when your help was needed. Special thanks also go to my sister for her endless hours of proofreading throughout my scientific career. She has always been a person I have looked up to and whose career pathway inspired me in many ways.

Big thanks also go out to all the Ann Arbor people keeping me out of the lab (at least occasionally). This includes my dear GradTones friends Emma Faulhaber, Jamie Lee, Sasha Kryuchov, and Kai Chan. I have to call out Tori Valvo here for

being a supportive but honest friend at all times; you made me a better person. Also to name are my dear friends Dan McCusker, Tommy Waltman, Susan LaMoireaux, Danielle Santos, and Chami Sangeeth Amarasinghe. Thanks for being a part of my journey in many different ways.

Although we might be 4000 miles apart, the friendship with Jan-Lukas Bosse, Lucia Wesenberg, Noah Ziethen, Tom Straukamp, Robert Kolde, and Ani Papanyan has survived the long distance, and their friendship means the world to me.

TABLE OF CONTENTS

LIST OF FIGURES

Figure

LIST OF APPENDICES

Appendix

ABSTRACT

Transition metal dichalcogenides (TMDs) have received considerable attention in the past decade for their optoelectronic applications in photovoltaics, lasers, and quantum information. In the monolayer limit, these materials exhibit extraordinary properties, including efficient light-matter coupling, ultrafast charge transfer, long-lived interlayer excitons with high binding energies, and many-body excitonic interactions.

In this thesis, we present the development and application of multidimensional coherent imaging spectroscopy (MDCIS), a four-wave mixing (FWM) based nonlinear spectroscopic imaging technique, to TMD monolayers and heterostructures. Based on multidimensional coherent spectroscopy (MDCS), MDCIS allows us to distinguish between homogeneous and inhomogeneous contributions to the material linewidths and distinguish coherent and incoherent coupling mechanisms in TMD heterostructures. The imaging aspect allows us to capture the spatial variation of the aforementioned physical processes across TMDs.

We first discuss our results applying MDCS to an $MoSe_2/WSe_2$ heterostructure, for which we characterize the coherent and incoherent coupling mechanisms present in these materials. We quantify the timescales of rapid electron (91 ± 9 fs) and hole (148 ± 28 fs) transfer between the two materials. Furthermore, we visualize strong coherent coupling between excitons in the $MoSe_2$ and WSe_2 layers by observing oscillations of the coupling peaks in one-quantum MDCS and measuring a mixing energy of 73 meV in zero-Quantum MDCS. We also observe many-body signatures of the interlayer

excitons and, in conjunction with photoluminescence measurements, measure their binding energy to be 254 meV.

To accelerate nonlinear imaging, we develop a lock-in amplifier that uses a box-weighted instead of an exponentially-weighted lowpass filter. The transfer function of the box lock-in has tunable notches in the frequency domain that enable sufficient suppression of adjacent modulations present on the detector. We use Monte-Carlo simulations to quantify the signal-to-noise ratio and suppression of adjacent modulations, demonstrating the superiority of the box lock-in over the conventional exponential lock-in at short pixel-dwell times. We further experimentally demonstrate this advantage by imaging a monolayer of $MoSe_2$ on a distributed Bragg reflector.

Furthermore, we present results using MDCIS to study the potential of $MoSe_2$ monolayers and $MoSe_2/WSe_2$ heterostructures for quantum information applications. We map the distribution of homogeneous and inhomogeneous linewidths across an $MoSe_2$ monolayer, identifying promising areas with low inhomogeneity and long dephasing times that bear the potential for qubits. We also visualize the strain across the $MoSe_2$ monolayer and comment on the detrimental effects strain may have in device applications. Similarly, we map strain across an $MoSe_2/WSe_2$ heterostructure and quantify the spatial homogeneity of coherent coupling (81% of the sample) and charge transfer (91% of the sample). We further map the distribution of interlayer exciton lifetimes. These quantities display a surprising robustness in the presence of strain, strengthening the case for TMD heterostructures as an applications platform for quantum information and photovoltaics.

Lastly, we demonstrate how to further accelerate the nonlinear imaging techniques in this thesis by smart scanning and sampling schemes in the time-domain. We obtain FWM images, dephasing maps, and decay maps within minutes, opening the avenue for moving these techniques out of the lab and into a fabrication/manufacturing setting for advanced materials characterization.

CHAPTER I

Introduction

Aristotle once said, "It is during our darkest moments that we must focus to see the light". Light has indeed been a fascination for thousands of years, with sources crediting the ancient Egyptians and Mesopotamians with the creation of lenses as early as 2000 BC [1]. Since then, optics, the study of light, has made vast progress, finding its way into our everyday lives, e.g., at the supermarket checkout in the form of barcodes, through industrial machining [2], or energy generation with solar cells [3]. The history of light is inherently entrenched with the concepts of emission and absorption. Over 10,000 years ago, humankind realized that when burning oil, one could "generate light" [4], in this case through the emission of blackbody radiation (although humans did not have a deep understanding of the underlying physics). The inverse process, the absorption of light, might have been concealed to many but has dominated the world around us, from human vision [5] to the photosynthesis of plants [6]. The list of applications for both the emission and absorption of light is almost endless.

As harnessing light's absorption and emission properties enters the third decade of the 21st century, a new group of materials with strong absorption and emission properties, potentially revolutionizing many applications, has entered the stage: transition metal dichalcogenides (TMDs). With the goal of identifying the fundamental limits

of the materials for applications, a deep and thorough understanding of this group of materials is necessary. Therefore, the basis of this thesis and the work conducted throughout the PhD is the fundamental desire to understand TMDs and the physical processes fueling their favorable properties.

The investigation of TMDs is a logical continuation of research into semiconductors for both a fundamental understanding and applications. The most ubiquitous semiconductor, silicon, has profoundly impacted electronics and the world around us, ringing in the "Silicon age" [7] in the late 20^{th} century. As electronics rapidly accelerate and new applications such as electric vehicles enter the marketplace, new semiconductor materials with higher switching speeds, higher breakdown voltages/currents, and high-temperature resistance are needed. The past decades have seen vast progress in the fields of III-V semiconductors such as gallium arsenide (GaAs) and gallium nitride (GaN) in both science [8–10] and industry [11] and silicon carbide for electric vehicles [12].

While scientists have studied TMDs for several decades [13–15] and have found applications for bulk MoS_2 in lubrication for motorcycles [16] and skis [17], they recently entered a new era of drastically increased interest due to their transition toward a direct band-gap and strong light-matter coupling when in the monolayer limit [18, 19]. Specifically, researchers have shown near-perfect absorption of 99.6% when coupling a single TMD monolayer with a mirror [20], an impressive number considering the sub-nanometer thickness for a single TMD monolayer [21]. These properties have shifted the interest of almost the entire fundamental optical processes in semiconductors community to this group of materials. Physicists and material scientists alike have been especially interested in the rapid electron and hole transfer (charge transfer) in TMD heterostructures [22–28], coherent coupling in monolayers [29, 30], and interlayer excitons (ILEs) [31–34], as well as Moiré excitons [35–40].

Combined with the efficient light-matter coupling, these physical processes also

spurred interest in the engineering physics community about potential device applications. To this day, applications such as photodiodes [41], lasers [42], photovoltaics [43], and quantum light-emitting diodes [44], to name a few, have been realized. In recent years, strain engineering in TMD monolayers has also gained momentum with the potential for room-temperature entangled-photon sources [45, 46]. Moreover, long-lived ILEs have been proposed as promising candidates for qubits [47, 48].

To understand the underlying physics, as well as push the application potential of these materials forward, numerous material characterization techniques have been employed: white-light optical microscopy to photoluminescence (PL) imaging [49], micro-reflectance and transmission [50], scanning tunneling microscopy [51], angle-resolved photoemission spectroscopy [51], Raman spectroscopy [52–54], atomic force microscopy imaging [55], tip-enhanced spectroscopy [56], ultrafast nanoscopy [57], and four-wave mixing (FWM) imaging [58–61]. However, there often is a trade-off between the amount of information these techniques convey about the sample/material and the experimental complexity/data acquisition time required to collect this information. Moreover, not all information about a material is accessible with a single technique.

In this thesis, we use nonlinear spectroscopy and imaging to characterize TMD samples. Nonlinear imaging and spectroscopy have proven useful for a wide variety of samples, including semiconductor quantum wells (QWs) [62–64], quantum dots (QDs) [65–69], photosynthetic bacteria [70], melanoma [71], cells and tissue [72, 73], label-free DNA imaging [74], molecules [75], gases [76], and even antique oil-paintings [77]. The reason behind the practicality of these techniques, which include, among others, two-photon (2P)- and three-photon absorption, transient absorption spectroscopy (TAS), stimulated Raman Scattering (SRS), and multidimensional coherent spectroscopy (MDCS) lies in the information that these techniques can access. The nonlinearity of these techniques helps with the confinement of the sample-emitted light along the lateral and transverse directions, reducing scattering contributions

and increasing spatial resolution. Moreover, spectrally non-degenerate techniques such as SRS and 2P help with scattering in biological media. Lastly, many of these techniques are more sensitive in their signal strength to sample changes, e.g., FWM is more sensitive to doping, defects, and strain than its linear counterparts [78, 79]. Specifically using ultrafast laser imaging, Huang *et al.* [80] have shown the practicality of two-color transient absorption decay times for defect sensing in graphene, while Jacubczyk *et al.* [60] have shown the potential of FWM strength and dephasing times as an indicator of material quality for TMDs.

With regards to spectral information, MDCS stands out as a valuable technique among many spectroscopy techniques through its ability to correlate absorption and emission energies, enabling access to many-body effects, coupling, and the true homogeneous and inhomogeneous linewidths of a material. Access to these quantities is vital for many applications, such as quantum information, since the spatial and temporal coherence relate to the inhomogeneous and homogeneous linewidths. Furthermore, coupling between resonances, may it be electronic or vibrational, not only reveals the underlying physics that helps us understand photosynthesis [70], deoxyribonucleic acid (DNA) [75], or the nature of the coupling between quantum dots [29] - it also can be harnessed for coherent control of quantum systems [81].

The response cannot be assumed to be spatially homogeneous for many sample systems. While in some instances, an ensemble-averaged response could be preferred, in many cases, information is hidden in the spatial dynamics. As a matter of fact, in the TMD community, many measurements are taken on a single spot or on "magic samples", wherefore the claims derived from these measurements cannot be easily translated to entire samples and larger spatial scales. Hence it is inevitable to combine the spectroscopic richness of MDCS with imaging.

Past implementations have primarily focused on spatially addressed MDCS [58, 70] or small-area MDCS imaging with data acquisition times of hours [60, 61]. While

undoubtedly useful in a scientific setting, these techniques are cumbersome. Moreover, many samples cannot provide the required stability on an hour time scale, often due to sample drifts, sample degradation [82], or photobleaching [70]. Moreover, hour-long wait times are unacceptable if researchers and engineers try to characterize a sample at a manufacturing/fabrication stage. The abovementioned limitations constitute a significant barrier to widespread adoption in in-situ (fabrication) settings.

The goal and mission of this thesis is, therefore, two-fold:

1. Better understand the properties of TMDs by combining temporal, spectral, and spatial information.

2. Develop and accelerate nonlinear imaging techniques that can be used in an in-situ fabrication setting.

The order of chapters in this thesis is chronological with the PhD because many of the technique developments happened in parallel with the learnings from experimental results.

In Chap. II, we will introduce semiconductors and excitons, the quasiparticles at the heart of this thesis. We will then discuss the dynamics of excitons within TMD sample systems, answering the question: "What happens after light impinges on a TMD sample?".

We first introduce nonlinear spectroscopy, specifically MDCS, from a theoretical viewpoint in Chap. III. We motivate this technique by discussing the shortcomings of linear and one-dimensional spectroscopies and highlighting how MDCS can overcome their limitations. Subsequently, we present the experimental implementation of MDCS in Chap. IV. We also discuss how to integrate MDCS with laser-scanning imaging. This chapter contains a majority of the technique development work conducted throughout the PhD, with a discussion on the efficient implementation of collinear MDCS and the build and calibration of the laser-scanning microscope.

Chaps V-VIII subsequently focus on the experimental results and insights derived from them. After Dr. Eric Martin had previously established how homogeneous and inhomogeneous linewidths are affected in TMD monolayers [83], we were initially intrigued to move on from monolayers and study a TMD heterostructure in MDCS. Specifically, reports of charge transfer by Hong *et al.* [22] and many others [23–27] in these heterostructures without the ability to simultaneously resolve the electron and hole transfer made us believe that there is value in studying TMDs with MDCS. Moreover, Hao *et al.* [30] observed coherent coupling between excitons and trions in an $MoSe_2$ monolayer. Similarly, we expected the potential of coherent coupling between intralayer excitons in TMD heterostructures. Chap. V discusses our initial results on studying charge transfer and coherent coupling in an $MoSe_2/WSe_2$ heterostructure. We extract rapid charge transfer times of 91 ± 9 fs for the electron and 149 ± 28 fs for the hole transfer. We further demonstrate the presence of strong coherent coupling between intralayer excitons residing in the $MoSe_2$ and WSe_2 layers. We also simulate the optical response of the system using the optical Bloch equations (OBEs). On a few picosecond time scale, we see signatures of "hot" ILE relaxation into the bound ILE state, while longer time scales of hundreds of picoseconds reveal the ILE lifetime. Through a combination of PL and many-body-sensitive MDCS experiments, we are also extracting the binding energy of the ILEs.

Following this work, we were motivated to combine MDCS with imaging because we noticed significant spatial inhomogeneity while acquiring the data. Faced with the issue of hour-long scans when trying to implement spatially-addressed MDCS, we decided to improve the acquisition speed of nonlinear imaging, especially in multi-pulse experiments. The results of these deliberations, a novel lock-in amplification scheme that enables us to combine MDCS with imaging at reasonable data acquisition times, is discussed in Chap. VI. We present the lock-in design and elucidate how it outperforms conventional lock-ins by efficiently suppressing adjacent modulations in

multi-pulse experiments. The superiority is demonstrated through both simulations and experiments on an $MoSe_2$/distributed Bragg reflector (DBR) sample.

Newly enabled to perform multidimensional coherent imaging spectroscopy (MDCIS), we put this technique to use in Chap. VII to study the strain-induced changes of homogeneous and inhomogeneous linewidths across an $MoSe_2$ monolayer. We visualize significant changes in areas of high tensile strain, especially in the inhomogeneous linewidth. We further visualize strain across an $MoSe_2/WSe_2$ heterostructure through large resonance shifts and show the robustness of coherent coupling, interlayer charge transfer, and ILE lifetimes across the sample despite the presence of considerable and complex strain. Specifically, we find that 81% of the sample shows robust coherent coupling, while 91% shows robust charge transfer.

Having established the usefulness of nonlinear spectroscopic imaging and material properties such as dephasing time for the assessment of sample quality, we were intrigued by the potential of nonlinear imaging for in-situ sample and material characterization. Further accelerating the extraction of relevant sample properties became necessary, encouraging us to apply smart scanning and sampling schemes in the temporal domain. Chap. VIII discusses how to rapidly extract dephasing times, inhomogeneous broadening, and population decay times. We experimentally demonstrate the extraction of FWM intensity, dephasing times, exciton population decay times, and dark exciton state distribution from these rapid measurements that can be performed within minutes.

On the techniques side, the body of work of this thesis has seen a clear transition from sophisticated spectroscopic techniques, to coupling them with imaging, to simplifying the spectroscopy side of things to get spatial information faster. Similarly, the technique development has enabled new insights into exciton dynamics in TMD monolayers and heterostructures that further the development of devices with this group of materials. Chap. IX summarizes the findings and gives a perspective

on what is next for understanding TMDs, their applications, including photovoltaics and quantum information, and accelerating nonlinear imaging techniques.

References

[1] "World's oldest telescope?" In: *BBC News* (July 1999). URL: http://news.bbc.co.uk/1/hi/sci/tech/380186.stm.

[2] Malcolm C. Gower. "Industrial applications of laser micromachining". In: *Opt. Express* 7.2 (July 2000), pp. 56–67. DOI: 10.1364/OE.7.000056.

[3] "Vast Power of the Sun Is Tapped By Battery Using Sand Ingredient; NEW BATTERY TAPS SUN'S VAST POWER". In: *New York Times* (Apr. 1954). URL: https://www.nytimes.com/1954/04/26/archives/vast-power-of-the-sun-is-tapped-by-battery-using-sand-ingredient.html.

[4] Massimo Guarnieri. "An Historical Survey on Light Technologies". In: *IEEE Access* 6 (2018), pp. 25881–25897. DOI: 10.1109/ACCESS.2018.2834432.

[5] ELEK LUDVIGH and E. F. McCARTHY. "ABSORPTION OF VISIBLE LIGHT BY THE REFRACTIVE MEDIA OF THE HUMAN EYE". In: *Archives of Ophthalmology* 20.1 (July 1938), pp. 37–51. ISSN: 0093-0326. DOI: 10.1001/archopht.1938.00850190049005.

[6] Howard Gest. "Bicentenary homage to Dr Jan Ingen-Housz, MD (1730-1799), pioneer of photosynthesis research". In: *Photosynthesis Research* 63.2 (Feb. 2000), pp. 183–190. ISSN: 1573-5079. DOI: 10.1023/A:1006460024843.

[7] P Siffert and E.F Krimmel. *Silicon - Evolution and Future of a Technology*. 1st. Heidelberg: Springer-Verlag Berlin, 2004. DOI: 10.1007/978-3-662-09897-4.

[8] Yan Liang, Chandrasekar Perumal Veeramalai, Guochen Lin, Xiangbin Su, Xiaoming Zhang, Shuai Feng, Yingqiang Xu, and Chuanbo Li. "A review on III-V compound semiconductor short wave infrared avalanche photodiodes". In: *Nanotechnology* 33.22 (Mar. 2022), p. 222003. DOI: 10.1088/1361-6528/ac5442.

[9] Ziyuan Li, Jeffery Allen, Monica Allen, Hark Hoe Tan, Chennupati Jagadish, and Lan Fu. "Review on III-V Semiconductor Single Nanowire-Based Room Temperature Infrared Photodetectors". In: *Materials* 13.6 (2020). ISSN: 1996-1944. DOI: 10.3390/ma13061400.

[10] Julie Tournet, Yonghwan Lee, Siva K. Karuturi, Hark H. Tan, and Chennupati Jagadish. "III–V Semiconductor Materials for Solar Hydrogen Production: Status and Prospects". In: *ACS Energy Letters* 5.2 (2020), pp. 611–622. DOI: 10.1021/acsenergylett.9b02582.

[11] Desire Athow. "How GaN is changing the future of semiconductors". In: *Techradar* (Mar. 2021). URL: https://www.techradar.com/news/how-gan-is-changing-the-future-of-semiconductors.

[12] Hana Askren and Mark Andress. "New Semiconductor Technologies Driving Down Cost Of Electric Vehicle Batteries". In: *Forbes* (Jan. 2020). URL: https://www.forbes.com/sites/mergermarket/2020/01/08/new-semiconductor-technologies-driving-down-cost-of-electric-vehicle-batteries/?sh=57ac00de2f0a.

[13] J.A. Wilson and A.D. Yoffe. "The transition metal dichalcogenides discussion and interpretation of the observed optical, electrical and structural properties". In: *Advances in Physics* 18.73 (1969), pp. 193–335. DOI: 10.1080/00018736900101307.

[14] A. R. Beal, J. C. Knights, and W. Y. Liang. "Transmission spectra of some transition metal dichalcogenides. II. Group VIA: trigonal prismatic coordination". In: *Journal of Physics C: Solid State Physics* 5.24 (Dec. 1972), pp. 3540–3551. DOI: 10.1088/0022-3719/5/24/016.

[15] Manashi Nath and C. N. R. Rao. "$MoSe_2$ and WSe_2 nanotubes and related structures". In: *Chem. Commun.* (21 2001), pp. 2236–2237. DOI: 10.1039/B107296J.

[16] Liqui Moly. *Motorbike MoS_2 Shooter*. 2022. URL: https://www.liqui-moly.com/en/us/motorbike-mos2-shooter-p004197.html#20296.

[17] Lars Karlöf and Leif Torgersen Axell. *On dry lubricants in ski waxes*. 2005. URL: https://web.archive.org/web/20110716174041/http://www.swixsport.com/dav/8dde5f4784.pdf.

[18] Andrea Splendiani, Liang Sun, Yuanbo Zhang, Tianshu Li, Jonghwan Kim, Chi-Yung Chim, Giulia Galli, and Feng Wang. "Emerging Photoluminescence in Monolayer MoS_2". In: *Nano Letters* 10.4 (2010). PMID: 20229981, pp. 1271–1275. DOI: 10.1021/nl903868w.

[19] Gang Wang, Alexey Chernikov, Mikhail M. Glazov, Tony F. Heinz, Xavier Marie, Thierry Amand, and Bernhard Urbaszek. "Colloquium: Excitons in atomically thin transition metal dichalcogenides". In: *Rev. Mod. Phys.* 90 (2 Apr. 2018), p. 021001. DOI: 10.1103/RevModPhys.90.021001.

[20] Jason Horng, Eric W. Martin, Yu-Hsun Chou, Emmanuel Courtade, Tsu-chi Chang, Chu-Yuan Hsu, Michael-Henr Wentzel, Hanna G. Ruth, Tien-chang Lu, Steven T. Cundiff, Feng Wang, and Hui Deng. "Perfect Absorption by an Atomically Thin Crystal". In: *Phys. Rev. Applied* 14 (2 Aug. 2020), p. 024009. DOI: 10.1103/PhysRevApplied.14.024009.

[21] Ying Ying Wang, Ai Zhi Li, Yi Hao Wang, Yao Liang, Jie Jiang, Hai Yan Nan, Zhen Hua Ni, Dong Wang, Bo Zhong, and Guang Wu Wen. "Determination of the thickness of two-dimensional transition-metal dichalcogenide by the Raman intensity of the substrate". In: *Materials Research Express* 3.2 (Jan. 2016), p. 025007. DOI: 10.1088/2053-1591/3/2/025007.

[22] Xiaoping Hong, Jonghwan Kim, Su-Fei Shi, Yu Zhang, Chenhao Jin, Yinghui Sun, Sefaattin Tongay, Junqiao Wu, Yanfeng Zhang, and Feng Wang. "Ultrafast charge transfer in atomically thin MoS_2/WS_2 heterostructures". In: *Nature Nanotechnology* 9.9 (Sept. 2014), pp. 682–686. ISSN: 1748-3395. DOI: 10.1038/nnano.2014.167.

[23] Daichi Kozawa, Alexandra Carvalho, Ivan Verzhbitskiy, Francesco Giustiniano, Yuhei Miyauchi, Shinichiro Mouri, A. H. Castro Neto, Kazunari Matsuda, and Goki Eda. "Evidence for Fast Interlayer Energy Transfer in $MoSe_2/WS_2$ Heterostructures". In: *Nano Letters* 16.7 (2016), pp. 4087–4093. DOI: 10.1021/acs.nanolett.6b00801.

[24] Hailong Chen, Xiewen Wen, Jing Zhang, Tianmin Wu, Yongji Gong, Xiang Zhang, Jiangtan Yuan, Chongyue Yi, Jun Lou, Pulickel M. Ajayan, Wei Zhuang, Guangyu Zhang, and Junrong Zheng. "Ultrafast formation of interlayer hot excitons in atomically thin MoS_2/WS_2 heterostructures". In: *Nat Commun* 7 (2016), p. 12512. DOI: 10.1038/ncomms12512.

[25] Jonas E. Zimmermann, Young Duck Kim, James C. Hone, Ulrich Höfer, and Gerson Mette. "Directional ultrafast charge transfer in a $WSe_2/MoSe_2$ heterostructure selectively probed by time-resolved SHG imaging microscopy". In: *Nanoscale Horiz.* 5 (12 2020), pp. 1603–1609. DOI: 10.1039/D0NH00396D.

[26] S. Ovesen, S. Brem, C. Linderälv, Mikael Kuisma, Tobias Korn, Paul Erhart, Malte Selig, and Ermin Malic. "Interlayer exciton dynamics in van der Waals heterostructures". In: *Commun Phys* 2 (23 2019). DOI: 10.1038/s42005-019-0122-z.

[27] Junyi Liu, Xu Zhang, and Gang Lu. "Excitonic Effect Drives Ultrafast Dynamics in van der Waals Heterostructures". In: *Nano Letters* 20.6 (2020). PMID: 32432887, pp. 4631–4637. DOI: 10.1021/acs.nanolett.0c01519.

[28] Veronica R. Policht, Mattia Russo, Fang Liu, Chiara Trovatello, Margherita Maiuri, Yusong Bai, Xiaoyang Zhu, Stefano Dal Conte, and Giulio Cerullo. "Dissecting Interlayer Hole and Electron Transfer in Transition Metal Dichalcogenide Heterostructures via Two-Dimensional Electronic Spectroscopy". In: *Nano Letters* 21.11 (2021). PMID: 34037406, pp. 4738–4743. DOI: 10.1021/acs.nanolett.1c01098.

[29] B. Kasprzak J.and Patton, V. Savona, and W. Langbein. "Coherent coupling between distant excitons revealed by two-dimensional nonlinear hyperspectral imaging". In: *Nature Photonics* 5.1 (Jan. 2011), pp. 57–63. DOI: 10.1038/nphoton.2010.284.

[30] Kai Hao, Lixiang Xu, Philipp Nagler, Akshay Singh, Kha Tran, Chandriker Kavir Dass, Christian Schüller, Tobias Korn, Xiaoqin Li, and Galan Moody. "Coherent and Incoherent Coupling Dynamics between Neutral and Charged Excitons in Monolayer $MoSe_2$". In: *Nano Letters* 16.8 (2016). PMID: 27428509, pp. 5109–5113. DOI: 10.1021/acs.nanolett.6b02041.

[31] P. Rivera, J.R. Schaibley, A.M. Jones, J.S Ross, S. Wu, G. Aivazian, P. Klement, K. Seyler, G. Clark, N.J. Ghimire, J. Yan, D.G. Mandrus, W. Yao, and X. Xu. "Observation of long-lived interlayer excitons in monolayer $MoSe_2$-WSe_2 heterostructures". In: *Nat Commun* 6 (2015), p. 6242. DOI: 10.1038/ncomms7242.

[32] Junho Choi, Matthias Florian, Alexander Steinhoff, Daniel Erben, Kha Tran, Dong Seob Kim, Liuyang Sun, Jiamin Quan, Robert Claassen, Somak Majumder, Jennifer A. Hollingsworth, Takashi Taniguchi, Kenji Watanabe, Keiji Ueno, Akshay Singh, Galan Moody, Frank Jahnke, and Xiaoqin Li. "Twist Angle-Dependent Interlayer Exciton Lifetimes in van der Waals Heterostructures". In: *Phys. Rev. Lett.* 126 (4 Jan. 2021), p. 047401. DOI: 10.1103/PhysRevLett.126.047401.

[33] Ying Jiang, Shula Chen, Weihao Zheng, Biyuan Zheng, and Anlian Pan. "Interlayer exciton formation, relaxation, and transport in TMD van der Waals heterostructures". In: *Light Sci Appl* 10.72 (2021). DOI: 10.1038/s41377-021-00500-1.

[34] Shengnan Miao, Tianmeng Wang, Xiong Huang, Dongxue Chen, Zhen Lian, Chong Wang, Mark Blei, Takashi Taniguchi, Kenji Watanabe, Sefaattin Tongay, Zenghui Wang, Di Xiao, Yong-Tao Cui, and Su-Fei Shi. "Strong interaction between interlayer excitons and correlated electrons in WSe_2/WS_2 moiré superlattice". In: *Nat Commun* 12 (2021). DOI: 10.1038/s41467-021-23732-6.

[35] Di Huang, Junho Choi, Chih-Kang Shih, and Xiaoqin Li. "Excitons in semiconductor moiré superlattices". In: *Nature Nanotechnology* 17.3 (Mar. 2022), pp. 227–238. ISSN: 1748-3395. DOI: 10.1038/s41565-021-01068-y.

[36] Lei Wang, En-Min Shih, Augusto Ghiotto, Lede Xian, Daniel A. Rhodes, Cheng Tan, Martin Claassen, Dante M. Kennes, Yusong Bai, Bumho Kim, Kenji Watanabe, Takashi Taniguchi, Xiaoyang Zhu, James Hone, Angel Rubio, Abhay N. Pasupathy, and Cory R. Dean. "Correlated electronic phases in twisted bilayer transition metal dichalcogenides". In: *Nature Materials* 19.8 (Aug. 2020), pp. 861–866. ISSN: 1476-4660. DOI: 10.1038/s41563-020-0708-6.

[37] Yanhao Tang, Lizhong Li, Tingxin Li, Yang Xu, Song Liu, Katayun Barmak, Kenji Watanabe, Takashi Taniguchi, Allan H. MacDonald, Jie Shan, and Kin Fai Mak. "Simulation of Hubbard model physics in WSe_2/WS_2 moiré superlattices". In: *Nature* 579.7799 (Mar. 2020), pp. 353–358. ISSN: 1476-4687. DOI: 10.1038/s41586-020-2085-3.

[38] Yang Xu, Song Liu, Daniel A. Rhodes, Kenji Watanabe, Takashi Taniguchi, James Hone, Veit Elser, Kin Fai Mak, and Jie Shan. "Correlated insulating states at fractional fillings of moiré superlattices". In: *Nature* 587.7833 (Nov. 2020), pp. 214–218. ISSN: 1476-4687. DOI: 10.1038/s41586-020-2868-6.

[39] Yuya Shimazaki, Ido Schwartz, Kenji Watanabe, Takashi Taniguchi, Martin Kroner, and Ataç Imamoğlu. "Strongly correlated electrons and hybrid excitons in a moiré heterostructure". In: *Nature* 580.7804 (Apr. 2020), pp. 472–477. ISSN: 1476-4687. DOI: 10.1038/s41586-020-2191-2.

[40] Xiong Huang, Tianmeng Wang, Shengnan Miao, Chong Wang, Zhipeng Li, Zhen Lian, Takashi Taniguchi, Kenji Watanabe, Satoshi Okamoto, Di Xiao, Su-Fei Shi, and Yong-Tao Cui. "Correlated insulating states at fractional fillings of the WS_2/WSe_2 moiré lattice". In: *Nature Physics* 17.6 (June 2021), pp. 715–719. ISSN: 1745-2481. DOI: 10.1038/s41567-021-01171-w.

[41] A. Pospischil, M. Furchi, and T. Mueller. "Solar-energy conversion and light emission in an atomic monolayer p–n diode". In: *Nature Nanotechnology* 9.4 (Apr. 2014), pp. 257–261. DOI: 10.1038/nnano.2014.14.

[42] Yu Ye, Zi Jing Wong, Xiufang Lu, Xingjie Ni, Hanyu Zhu, Xianhui Chen, Yuan Wang, and Xiang Zhang. "Monolayer excitonic laser". In: *Nature Photonics* 9.11 (Nov. 2015), pp. 733–737. ISSN: 1749-4893. DOI: 10.1038/nphoton.2015.197.

[43] Nikolaus Flöry, Achint Jain, Palash Bharadwaj, Markus Parzefall, Takashi Taniguchi, Kenji Watanabe, and Lukas Novotny. "A $WSe_2/MoSe_2$ heterostructure photovoltaic device". In: *Applied Physics Letters* 107.12 (2015), p. 123106. DOI: 10.1063/1.4931621.

[44] Carmen Palacios-Berraquero, Matteo Barbone, Dhiren M. Kara, Xiaolong Chen, Ilya Goykhman, Duhee Yoon, Anna K. Ott, Jan Beitner, Kenji Watanabe, Takashi Taniguchi, Andrea C. Ferrari, and Mete Atatüre. "Atomically thin quantum light-emitting diodes". In: *Nature Communications* 7.12978 (2016). DOI: 10.1038/ncomms12978.

[45] Galan Moody, Chandriker Kavir Dass, Kai Hao, Chang-Hsiao Chen, Lain-Jong Li, Akshay Singh, Kha Tran, Genevieve Clark, Xiaodong Xu, Gunnar Berghäuser, Ermin Malic, Andreas Knorr, and Xiaoqin Li. "Intrinsic homogeneous linewidth and broadening mechanisms of excitons in monolayer transition metal dichalcogenides". In: *Nat Commun* 6 (2015), p. 8315. DOI: 10.1038/ncomms9315.

[46] Darwin F. Cordovilla Leon, Zidong Li, Sung Woon Jang, Che-Hsuan Cheng, and Parag B. Deotare. "Exciton transport in strained monolayer WSe_2". In: *Applied Physics Letters* 113.25 (2018), p. 252101. DOI: 10.1063/1.5063263.

[47] Alberto Ciarrocchi, Dmitrii Unuchek, Ahmet Avsar, Kenji Watanabe, Takashi Taniguchi, and Andras Kis. "Polarization switching and electrical control of interlayer excitons in two-dimensional van der Waals heterostructures". In: *Nature Photonics* 13.2 (Feb. 2019), pp. 131–136. ISSN: 1749-4893. DOI: 10.1038/s41566-018-0325-y.

[48] Mauro Brotons-Gisbert, Hyeonjun Baek, Alejandro Molina-Sánchez, Aidan Campbell, Eleanor Scerri, Daniel White, Kenji Watanabe, Takashi Taniguchi, Cristian Bonato, and Brian D. Gerardot. "Spin-layer locking of interlayer excitons trapped in moiré potentials". In: *Nature Materials* 19.6 (June 2020), pp. 630–636. ISSN: 1476-4660. DOI: 10.1038/s41563-020-0687-7.

[49] Evgeny M. Alexeev, Alessandro Catanzaro, Oleksandr V. Skrypka, Pramoda K. Nayak, Seongjoon Ahn, Sangyeon Pak, Juwon Lee, Jung Inn Sohn, Kostya S. Novoselov, Hyeon Suk Shin, and Alexander I. Tartakovskii. "Imaging of Interlayer Coupling in van der Waals Heterostructures Using a Bright-Field Optical Microscope". In: *Nano Letters* 17.9 (2017). PMID: 28753319, pp. 5342–5349. DOI: 10.1021/acs.nanolett.7b01763.

[50] Riccardo Frisenda, Yue Niu, Patricia Gant, Aday J Molina-Mendoza, Robert Schmidt, Rudolf Bratschitsch, Jinxin Liu, Lei Fu, Dumitru Dumcenco, Andras Kis, David Perez De Lara, and Andres Castellanos-Gomez. "Micro-reflectance and transmittance spectroscopy: a versatile and powerful tool to characterize 2D materials". In: *Journal of Physics D: Applied Physics* 50.7 (Jan. 2017), p. 074002. DOI: 10.1088/1361-6463/aa5256.

[51] Kinga Lasek, Jingfeng Li, Sadhu Kolekar, Paula Mariel Coelho, Lu'an Guo, Min Zhang, Zhiming Wang, and Matthias Batzill. "Synthesis and characterization of 2D transition metal dichalcogenides: Recent progress from a vacuum surface science perspective". In: *Surface Science Reports* 76.2 (2021), p. 100523. ISSN: 0167-5729. DOI: https://doi.org/10.1016/j.surfrep.2021.100523.

[52] R Saito, Y Tatsumi, S Huang, X Ling, and M S Dresselhaus. "Raman spectroscopy of transition metal dichalcogenides". In: *Journal of Physics: Condensed Matter* 28.35 (July 2016), p. 353002. DOI: 10.1088/0953-8984/28/35/353002.

[53] Xin Zhang, Xiao-Fen Qiao, Wei Shi, Jiang-Bin Wu, De-Sheng Jiang, and Ping-Heng Tan. "Phonon and Raman scattering of two-dimensional transition metal dichalcogenides from monolayer, multilayer to bulk material". In: *Chem. Soc. Rev.* 44 (9 2015), pp. 2757–2785. DOI: 10.1039/C4CS00282B.

[54] Maria O'Brien, Niall McEvoy, Damien Hanlon, Toby Hallam, Jonathan N. Coleman, and Georg S. Duesberg. "Mapping of Low-Frequency Raman Modes in CVD-Grown Transition Metal Dichalcogenides: Layer Number, Stacking Orientation and Resonant Effects". In: *Scientific Reports* 6.1 (Jan. 2016), p. 19476. ISSN: 2045-2322. DOI: 10.1038/srep19476.

[55] Hang Zhang, Junxiang Huang, Yongwei Wang, Rui Liu, Xiulan Huai, Jingjing Jiang, and Chantelle Anfuso. "Atomic force microscopy for two-dimensional materials: A tutorial review". In: *Optics Communications* 406 (2018). Optoelectronics and Photonics Based on Two-dimensional Materials, pp. 3–17. ISSN: 0030-4018. DOI: https://doi.org/10.1016/j.optcom.2017.05.015.

[56] Hyeongwoo Lee, Inki Kim, Chulho Park, Mingu Kang, Jinseong Choi, Kwang-Yong Jeong, Jungho Mun, Yeseul Kim, Jeonghoon Park, Markus B. Raschke, Hong-Gyu Park, Mun Seok Jeong, Junsuk Rho, and Kyoung-Duck Park. "Inducing and Probing Localized Excitons in Atomically Thin Semiconductors via Tip-Enhanced Cavity-Spectroscopy". In: *Advanced Functional Materials* 31.33 (2021), p. 2102893. DOI: https://doi.org/10.1002/adfm.202102893.

[57] M. Plankl, P. E. Faria Junior, F. Mooshammer, T. Siday, M. Zizlsperger, F. Sandner, F. Schiegl, S. Maier, M. A. Huber, M. Gmitra, J. Fabian, J. L. Boland, T. L. Cocker, and R. Huber. "Subcycle contact-free nanoscopy of ultrafast interlayer transport in atomically thin heterostructures". In: *Nature Photonics* 15.8 (Aug. 2021), pp. 594–600. ISSN: 1749-4893. DOI: 10.1038/s41566-021-00813-y.

[58] Tomasz Jakubczyk, Valentin Delmonte, Maciej Koperski, Karol Nogajewski, Clement Faugeras, Wolfgang Langbein, Marek Potemski, and Jacek Kasprzak. "Radiatively Limited Dephasing and Exciton Dynamics in $MoSe_2$ Monolayers Revealed with Four-Wave Mixing Microscopy". In: *Nano Letters* 16.9 (2016), pp. 5333–5339. DOI: 10.1021/acs.nanolett.6b01060.

[59] Caroline Boule, Diana Vaclavkova, Miroslav Bartos, Karol Nogajewski, Lukas Zdražil, Takashi Taniguchi, Kenji Watanabe, Marek Potemski, and Jacek Kasprzak. "Coherent dynamics and mapping of excitons in single-layer $MoSe_2$ and WSe_2 at the homogeneous limit". In: *Phys. Rev. Materials* 4 (3 Mar. 2020), p. 034001. DOI: 10.1103/PhysRevMaterials.4.034001.

[60] Tomasz Jakubczyk, Karol Nogajewski, Maciej R Molas, Miroslav Bartos, Wolfgang Langbein, Marek Potemski, and Jacek Kasprzak. "Impact of environment on dynamics of exciton complexes in a WS_2 monolayer". In: *2D Materials* 5.3 (Apr. 2018), p. 031007. DOI: 10.1088/2053-1583/aabc1c.

[61] Tomasz Jakubczyk, Goutham Nayak, Lorenzo Scarpelli, Wei-Lai Liu, Sudipta Dubey, Nedjma Bendiab, Laëtitia Marty, Takashi Taniguchi, Kenji Watanabe, Francesco Masia, Gilles Nogues, Johann Coraux, Wolfgang Langbein, Julien Renard, Vincent Bouchiat, and Jacek Kasprzak. "Coherence and Density Dynamics of Excitons in a Single-Layer MoS_2 Reaching the Homogeneous Limit". In: *ACS Nano* 13.3 (2019). PMID: 30735350, pp. 3500–3511. DOI: 10.1021/acsnano.8b09732.

[62] Alan D. Bristow, Tianhao Zhang, Mark E. Siemens, Steven T. Cundiff, and R. P. Mirin. "Separating Homogeneous and Inhomogeneous Line Widths of Heavy- and Light-Hole Excitons in Weakly Disordered Semiconductor Quantum Wells". In: *The Journal of Physical Chemistry B* 115.18 (2011). PMID: 21384940, pp. 5365–5371. DOI: 10.1021/jp109408s.

[63] Katherine W. Stone, Kenan Gundogdu, Daniel B. Turner, Xiaoqin Li, Steven T. Cundiff, and Keith A. Nelson. "Two-Quantum 2D FT Electronic Spectroscopy of Biexcitons in GaAs Quantum Wells". In: *Science* 324.5931 (2009), pp. 1169–1173. DOI: 10.1126/science.1170274.

[64] Xiaoqin Li, Tianhao Zhang, Camelia N. Borca, and Steven T. Cundiff. "Many-Body Interactions in Semiconductors Probed by Optical Two-Dimensional Fourier Transform Spectroscopy". In: *Phys. Rev. Lett.* 96 (5 Feb. 2006), p. 057406. DOI: 10.1103/PhysRevLett.96.057406.

[65] Albert Liu, Diogo B. Almeida, Luiz G. Bonato, Gabriel Nagamine, Luiz F. Zagonel, Ana F. Nogueira, Lazaro A. Padilha, and S. T. Cundiff. "Multidimensional coherent spectroscopy reveals triplet state coherences in cesium lead-halide perovskite nanocrystals". In: *Science Advances* 7.1 (2021), eabb3594. DOI: 10.1126/sciadv.abb3594.

[66] Albert Liu, Diogo B. Almeida, Wan-Ki Bae, Lazaro A. Padilha, and Steven T. Cundiff. "Simultaneous Existence of Confined and Delocalized Vibrational Modes in Colloidal Quantum Dots". In: *The Journal of Physical Chemistry Letters* 10.20 (2019). PMID: 31556615, pp. 6144–6150. DOI: 10.1021/acs.jpclett.9b02474.

[67] Albert Liu, Luiz G. Bonato, Francesco Sessa, Diogo B. Almeida, Erik Isele, Gabriel Nagamine, Luiz F. Zagonel, Ana F. Nogueira, Lazaro A. Padilha, and Steven T. Cundiff. "Effect of dimensionality on the optical absorption properties of $CsPbI_3$ perovskite nanocrystals". In: *The Journal of Chemical Physics* 151.19 (2019), p. 191103. DOI: 10.1063/1.5124399.

[68] Albert Liu, Gabriel Nagamine, Luiz G. Bonato, Diogo B. Almeida, Luiz F. Zagonel, Ana F. Nogueira, Lazaro A. Padilha, and Steven T. Cundiff. "Toward Engineering Intrinsic Line Widths and Line Broadening in Perovskite Nanoplatelets". In: *ACS Nano* 15.4 (2021). PMID: 33769788, pp. 6499–6506. DOI: 10.1021/acsnano.0c09244.

[69] A. Liu, D. B. Almeida, W. K. Bae, L. A. Padilha, and S. T. Cundiff. "Non-Markovian Exciton-Phonon Interactions in Core-Shell Colloidal Quantum Dots at Femtosecond Timescales". In: *Phys. Rev. Lett.* 123 (5 Aug. 2019), p. 057403. DOI: 10.1103/PhysRevLett.123.057403.

[70] Vivek Tiwari, Yassel Acosta Matutes, Alastair. T. Gardiner, Thomas L.C. Jansen, Richard J. Cogdell, and Jennifer P. Ogilvie. "Spatially-resolved fluorescence-detected two-dimensional electronic spectroscopy probes varying excitonic structure in photosynthetic bacteria". In: *Nat. Comm.* 16 (2018), p. 4219. DOI: 10.1038/s41467-018-06619-x.

[71] Francisco E. Robles, Sanghamitra Deb, Jesse W. Wilson, Christina S. Gainey, M. Angelica Selim, Paul J. Mosca, Douglas S. Tyler, Martin C. Fischer, and Warren S. Warren. "Pump-probe imaging of pigmented cutaneous melanoma primary lesions gives insight into metastatic potential". In: *Biomed. Opt. Express* 6.9 (Sept. 2015), pp. 3631–3645. DOI: 10.1364/BOE.6.003631.

[72] Michael Rubart. "Two-Photon Microscopy of Cells and Tissue". In: *Circulation Research* 95.12 (2004), pp. 1154–1166. DOI: 10.1161/01.RES.0000150593.30324.42.

[73] Richard K.P. Benninger and David W. Piston. "Two-Photon Excitation Microscopy for the Study of Living Cells and Tissues". In: *Current Protocols in Cell Biology* 59.1 (2013), pp. 4.11.1–4.11.24. DOI: https://doi.org/10.1002/0471143030.cb0411s59.

[74] Fa-Ke Lu, Srinjan Basu, Vivien Igras, Mai P. Hoang, Minbiao Ji, Dan Fu, Gary R. Holtom, Victor A. Neel, Christian W. Freudiger, David E. Fisher, and X. Sunney Xie. "Label-free DNA imaging in vivo with stimulated Raman scattering microscopy". In: *Proceedings of the National Academy of Sciences* 112.37 (2015), pp. 11624–11629. ISSN: 0027-8424. DOI: 10.1073/pnas.1515121112.

[75] Ming Yang, Łukasz Szyc, and Thomas Elsaesser. "Decelerated Water Dynamics and Vibrational Couplings of Hydrated DNA Mapped by Two-Dimensional Infrared Spectroscopy". In: *The Journal of Physical Chemistry B* 115.44 (2011). PMID: 21972952, pp. 13093–13100. DOI: 10.1021/jp208166w.

[76] Bachana Lomsadze and Steven T. Cundiff. "Frequency combs enable rapid and high-resolution multidimensional coherent spectroscopy". In: *Science* 357.6358 (2017), pp. 1389–1391. DOI: 10.1126/science.aao1090.

[77] Tana Elizabeth Villafana, William P. Brown, John K. Delaney, Michael Palmer, Warren S. Warren, and Martin C. Fischer. "Femtosecond pump-probe microscopy generates virtual cross-sections in historic artwork". In: *Proceedings of the National Academy of Sciences* 111.5 (2014), pp. 1708–1713. DOI: 10.1073/pnas.1317230111.

[78] Torben L. Purz, Eric W. Martin, William G. Holtzmann, Pasqual Rivera, Adam Alfrey, Kelsey M. Bates, Hui Deng, Xiaodong Xu, and Steven T. Cundiff. "Imaging dynamic exciton interactions and coupling in transition metal dichalcogenides". In: *The Journal of Chemical Physics* 156.21 (2022), p. 214704. DOI: 10.1063/5.0087544.

[79] Torben L. Purz, Blake T. Hipsley, Eric W. Martin, Ronald Ulbricht, and Steven T. Cundiff. "Rapid multiplex ultrafast nonlinear microscopy for material characterization". In: *Opt. Express* 30.25 (Dec. 2022), pp. 45008–45019. DOI: 10.1364/OE.472054.

[80] Kai-Chih Huang, Jeremy McCall, Pu Wang, Chien-Sheng Liao, Gregory Eakins, Ji-Xin Cheng, and Chen Yang. "High-Speed Spectroscopic Transient Absorption Imaging of Defects in Graphene". In: *Nano Letters* 18.2 (2018). PMID: 29342361, pp. 1489–1497. DOI: 10.1021/acs.nanolett.7b05283.

[81] Matthew W. Day, Kelsey M. Bates, Christopher L. Smallwood, Rachel C. Owen, Tim Schröder, Edward Bielejec, Ronald Ulbricht, and Steven T. Cundiff. "Coherent Interactions between Silicon-Vacancy Centers in Diamond". In: *Phys. Rev. Lett.* 128 (20 May 2022), p. 203603. DOI: 10.1103/PhysRevLett.128.203603.

[82] Thomas Quenzel, Daniel Timmer, Moritz Gittinger, Jennifer Zablocki, Fulu Zheng, Manuela Schiek, Arne Lützen, Thomas Frauenheim, Sergei Tretiak, Martin Silies, Jin-Hui Zhong, Antonietta De Sio, and Christoph Lienau. "Plasmon-Enhanced Exciton Delocalization in Squaraine-Type Molecular Aggregates". In: *ACS Nano* 16.3 (2022). PMID: 35188735, pp. 4693–4704. DOI: 10.1021/acsnano.1c11398.

[83] Eric W. Martin, Jason Horng, Hanna G. Ruth, Eunice Paik, Michael-Henr Wentzel, Hui Deng, and Steven T. Cundiff. "Encapsulation Narrows and Preserves the Excitonic Homogeneous Linewidth of Exfoliated Monolayer $MoSe_2$". In: *Phys. Rev. Applied* 14 (2 Aug. 2020), p. 021002. DOI: 10.1103/PhysRevApplied.14.021002.

CHAPTER II

Excitons in Van-der-Waals Materials

2.1 Introduction

Excitons, bound states of an electron and a hole, are at the heart of many optical applications of van-der-Waals (vdW) materials and TMDs in devices. This chapter introduces the theory behind the formation of excitons and how they interact with their environment. Fundamentally, this chapter tries to answer three questions:

1. What is an exciton?

2. How does an exciton form?

3. What happens to an exciton after formation?

We first discuss the Schrödinger equation and Bloch's theorem for an electron in a periodic potential, leading to the concept of the band structure in materials. We will also describe how to interpret band structures with regard to direct vs. indirect band gaps and electron and hole effective masses. Subsequently, we introduce the concept of the exciton, explaining how it forms and alters the optical absorption of semiconductors. In this context, we specifically discuss the binding energy of excitons and how it is affected by electron and hole effective masses and the dielectric environment. The latter is crucial in the following, where we focus on the band

structure evolution from bulk TMDs to monolayer TMDs and the transition from an indirect to a direct band gap. We also discuss other features of the monolayer TMD band structure, such as the strong spin-orbit coupling, a spin-valley coupling that has raised interest in TMDs for valleytronics applications, and the high binding energies of several hundred meVs of excitons in monolayer TMDs. We then introduce how excitons interact with their environment in semiconductors - leading to the observed effects of inhomogeneity, dephasing, and decay. Subsequently, we first discuss the history of semiconductor heterostructures in epitaxially-grown QWs before diving into TMD heterostructures. We specifically highlight the additional pathways for excitons to interact and change: Charge transfer of the electron and holes, leading to the subsequent formation of ILEs, energy transfer, and coherent coupling between intralayer excitons. Lastly, we touch upon Moiré superlattices and their ability to further alter the exciton physics in TMD materials.

2.2 Bulk Semiconductors and Band Structure

Materials are commonly classified into conductors, insulators, and semiconductors, according to their ability to conduct electricity. Conductors (e.g., metals) show a high conductance, and insulators show a very low conductance. However, while intrinsically semiconductors are poor conductors, they are intriguing due to their ability to transition between low and high conductance through techniques such as doping or gating. The physical processes behind this behavior are best understood through the electronic band structure.

The band structure can be derived from the Schrödinger equation for the wave function $\Psi(\mathbf{r})$ single electron in a bulk crystal

$$H\Psi(\mathbf{r}) = \left[-\frac{\hbar}{2m}\nabla^2 + U(\mathbf{r})\right]\Psi(\mathbf{r}) = E\Psi(\mathbf{r})\,. \tag{2.1}$$

with H being the Hamiltonian of the system, m the mass of the electron, and $U(\mathbf{r})$ the periodic potential of the crystal lattice, which fulfills $U(\mathbf{r}+\mathbf{R}) = U(\mathbf{r})$. According to Bloch's theorem, solutions for the wave function can then be expressed as the product of a plane wave envelope function and a periodic Bloch function $u_{n,\mathbf{k}}(\mathbf{r})$ [1],

$$\Psi_{n,\mathbf{k}}(\mathbf{r}) = e^{i\mathbf{k}\cdot\mathbf{r}} u_{n,\mathbf{k}}(\mathbf{r})\,, \tag{2.2}$$

where the plane wave vector in the crystal, $\mathbf{k}$, is proportional to the crystal momentum $\mathbf{p} = \hbar\mathbf{k}$, and the band index, n, accounts for the fact that there are many solutions to the Schrödinger equation for any given $\mathbf{k}$. The energy eigenvalues $E_n(\mathbf{k})$ for the eigenfunctions $\Psi_{n,\mathbf{k}}(\mathbf{r})$ are hence defined as a function of the crystal momentum $\mathbf{k}$ and describe the energies of the electronic states an electron can occupy. The $\mathbf{k}$-dependent energy values are referred to as the band structure.

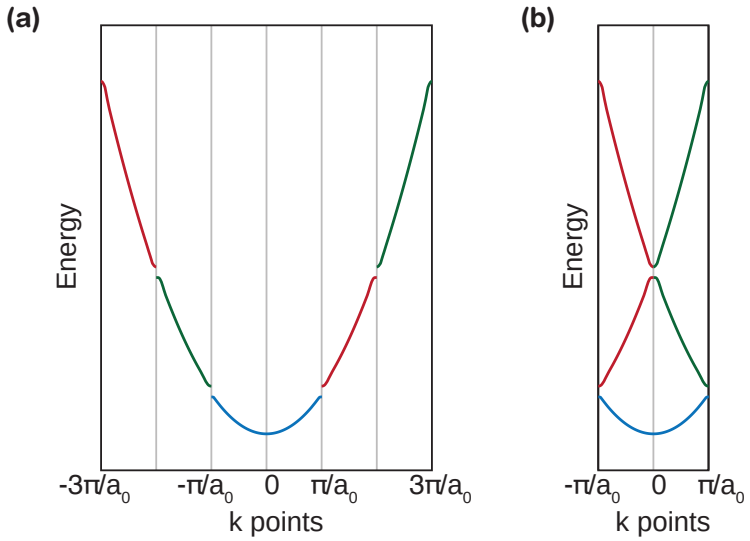

Figure 2.1: Schematic of a simple electronic band structure, showing the energy eigenvalues as a function of k points. Here, a_0 denotes the lattice period. **(a)** Band structure with $|k|$ values larger than π/a_0. **(b)** Band structure with all bands folded into the first Brillouin zone.

Although the $\mathbf{k}$ vector is three-dimensional, plotting this is rather inconvenient. Hence, a common way of plotting band structures involves plotting the energy values

along straight lines connecting high symmetry points in **k**-space, as done in Fig. 2.1. In Fig. 2.1(a), we show the schematic of a single band. It is easy to show from Eq. 2.2 that the energy eigenvalues are periodic with the reciprocal lattice vector **K**. Thus, the band along a single k axis is only defined for the range 0 to π/a_0, with a_0 being the lattice period. The dispersion relation for larger **k** values gets folded back into the Brillouin zone, such that the dispersion relation for $\pi/a_0 < |k| < 2\pi/a_0$ defines the second energy band, $2\pi/a_0 < |k| < 3\pi/a_0$ defines the third, and so on [2]. The back folding is illustrated in Fig. 2.1(b), which shows the same band structure as in Fig. 2.1(a), but with the bands folded back into the range $0 < |k| < \pi/a_0$, often referred to as the (first) Brillouin zone.

With the band structure, the distinction between insulators, semiconductors, and conductors can be understood: The electrons will fill the available states, dictated by the band structure, from the lowest energy up. The highest filled energy level at $T = 0\,\mathrm{K}$ is called the valence band, while the first unfilled level above the valence band is called the conduction band. In insulators, these two bands will be several eVs apart, with the Fermi level in between, while in metals, the Fermi level is mid-band, resulting in one partially filled band. In the latter case, electrons can be easily scattered into unoccupied conduction band states through externally applied electric fields. In insulators, band gaps are too large for electrons to overcome easily, even when applying moderately strong external electric fields (e.g., irradiation with visible light). Some semiconductors have band gaps that fall within the visible to near-infrared spectrum, with GaAs having a band gap of 1.42 eV at room temperature [3] and monolayers of various TMDs in the range of 1.57 eV for $MoSe_2$ to 2.03 eV for WS_2 [4]. Electrons in semiconductors can hence be excited into the conduction band by application of an external light field in the case of direct band gaps.

The band gap in semiconductors can either be direct or indirect, as illustrated in Fig. 2.2 along k points in one dimension. For a direct band gap (Fig. 2.2(a)), the

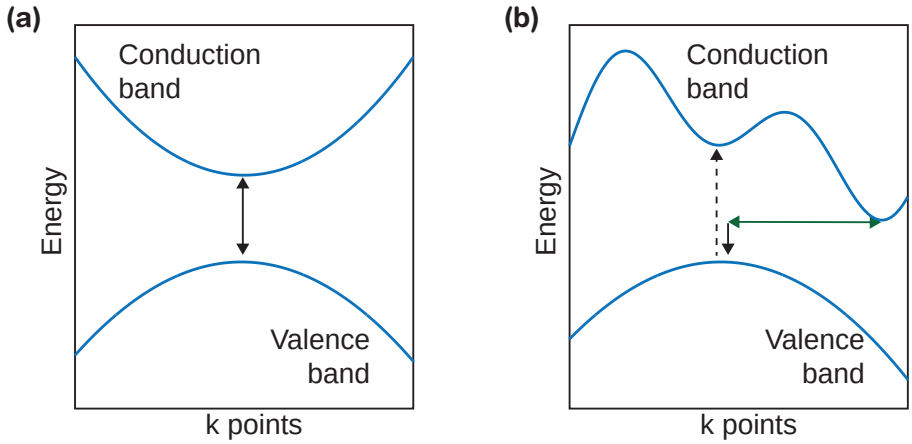

Figure 2.2: Illustration of the difference in band structure for a **(a)** direct and **(b)** indirect band gap. For a direct band gap, a photon (solid black arrow) is sufficient to transfer an electron from the valence to the conduction band and vice versa. For an indirect band gap, additional momentum, e.g., through a phonon (horizontal green arrow), is needed for electron relaxation (dashed black arrow).

minimum of the conduction band and maximum of the valence band have the same crystal momentum $\mathbf{k}$. In this case, a photon can directly excite an electron from the valence to the conduction band, leaving behind a hole in the conduction band. Similarly, an electron can directly emit a photon when relaxing from the conduction back into the valence band and recombining with a hole.

For an indirect band gap, however, the minimum of the conduction band and maximum of the valence band have different $\mathbf{k}$-vectors (Fig. 2.2(b)). While a higher energy photon can excite an electron from the valence to the conduction band (dashed arrow), the same is not true for the emission process: Equilibrium electrons are at the minimum of the conduction band, and because of momentum conservation constraints, momentum needs to be transferred for the electron and hole (situated at the maximum of the valence band) to recombine. The momentum of a photon, $p = h/\lambda$, is small for photons with energies in the range of semiconductor band gaps. In this case, phonons, the quasiparticles for lattice vibrations, need to be emitted or absorbed (green arrow) for an electron to relax through this band gap (solid arrow), significantly lowering the probability of this process.

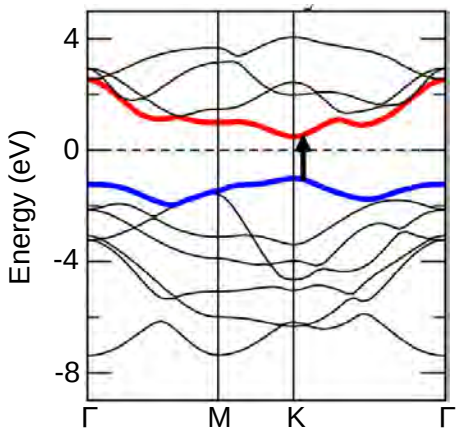

Figure 2.3: Electronic band structure of a monolayer of $MoSe_2$ obtained from first principle calculations in Ref. 5. The top of the valence band is highlighted in blue, and the bottom of the conduction band is highlighted in red. The black arrow highlights the direct band gap around the K-point. Figure adapted from Ref. 5.

In general, semiconductor band structures are complicated and are commonly calculated using first principles, ab-initio density functional theory (DFT) [4–10]. We plot the band structure for a monolayer of $MoSe_2$ obtained from DFT calculations by Kumar *et al.* [5] in Fig. 2.3.

Near high symmetry points, e.g., around the K-point of the Brillouin zone where the smallest direct band gap can be found for TMDs, the band structure can be approximated to be quadratic

$$E(\mathbf{k}) = E_g + \frac{\hbar^2 |\mathbf{k}|^2}{2m_{\text{eff}}}, \tag{2.3}$$

with the band gap at the K-point, E_g, and the effective mass of the electron/hole, m_{eff}. Given the positive curvature of the conduction band and the negative curvature of the valence band, the effective mass for the two bands differs, with the effective mass for the valence band being negative. However, since the mass of a hole is opposite to that of the band electrons, holes still have a positive effective mass.

In the discussion thus far, electrons and holes have been treated as independent particles. However, this is not strictly true in semiconductors, where Coulomb inter-

actions and many-body effects play a significant role and alter the material properties, as discussed in the following section.

2.3 Excitons

When an electron gets excited from the valence band into the conduction band, leaving behind a positively charged hole, the electron and hole can bind together through attraction mediated by their Coulomb interaction [11]. This bound electron-hole state is called an exciton.

Because of the Coulomb force, the wave function of the bound state contains elements of the hydrogenic wave function, describing the binding of the electron and hole while also having components of the Bloch function from the single electron/hole wave functions [2]. The energy of the exciton is [12]

$$E(n, \mathbf{k}) = \frac{\hbar^2}{2M}|\mathbf{k}|^2 + E_g - E_B \,, \tag{2.4}$$

with the exciton center-of-mass wave vector, $\mathbf{k} = \mathbf{k_e} + \mathbf{k_h}$, the electron and hole wave vectors, $\mathbf{k_{e,h}}$, the total mass, $M = m_e + m_h$, the electron and hole effective masses, $m_{e,h}$, the band gap of the semiconductor, E_g, and the binding energy E_B. The binding energy is

$$E_B = \frac{E_R}{n^2} \,, \tag{2.5}$$

with the principle quantum number (band index) of the exciton, n, and the exciton Rydberg constant, E_R. The exciton Rydberg constant is

$$E_R = \frac{\mu e^4}{2\epsilon^2\hbar^2} \,, \tag{2.6}$$

with the exciton reduced mass, $\mu = m_e m_h/(m_e + m_h)$, elementary charge e, and the background dielectric constant ϵ. The center-of-mass momentum of an optically-

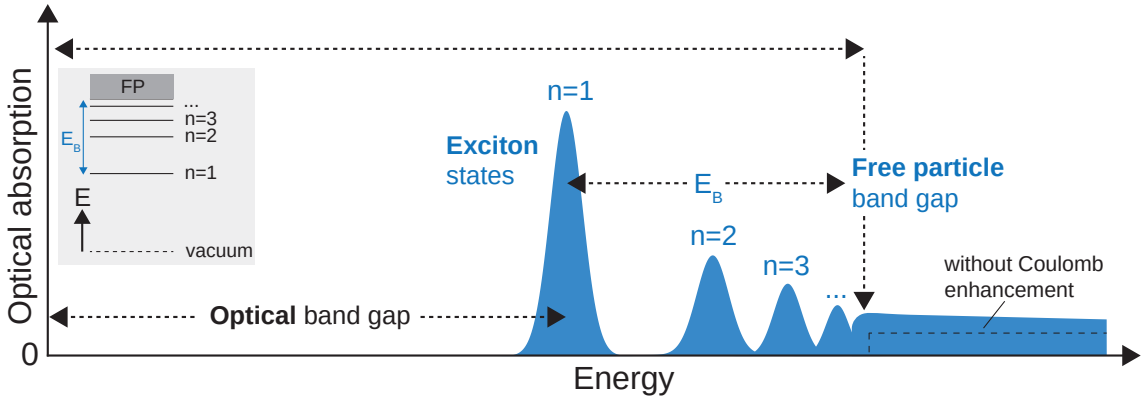

Figure 2.4: Schematic of the optical absorption of a semiconductor showing the absorption due to the exciton states and the absorption above the free particle band gap. The inset shows the energy structure of the semiconductor. Figure adapted from Ref. 14.

created exciton is negligibly small in Eq. 2.4, therefore, the $\frac{\hbar^2}{2M}|\mathbf{k}|^2$ term is often approximated to be zero. Eq. 2.5 is only true for a three-dimensional bulk material. For the TMD monolayers discussed later, no closed expression for the binding energy can be obtained. In this case, the binding energy can be calculated through the Bethe-Salpeter equation, or 2D Wannier models [13].

A schematic of the resulting energy structure, together with the material's absorption, is shown in Fig. 2.4. The free particle band gap (between the vacuum state and the free particle states (FP)) corresponds to the band gap between the conduction and valence band in the aforementioned band structure. However, Eq. 2.4 shows that the $n = 1$ exciton is a binding energy E_B below the free particle band gap, resulting in an energetically lower optical band gap. The higher exciton states can then be found between the $n = 1$ exciton and the free particle band gap, with higher states having decreasing energy spacing until the free particle band gap is reached. Absorption occurs at energies above the free particle band gap, and the Coulomb interaction between electrons and holes increases the continuum absorption ("Coulomb/Sommerfeld enhancement") [2]. However, the absorption of the exciton states below the free particle band gap is significantly stronger.

Although we have thus far described the energetic structure as atom-like, there is an important distinction from this simplified picture: As seen in Fig. 2.4, the exciton states show an energetically broad absorption. As discussed in Sec. 2.5 and Chap. VII, the linewidths associated with exciton transitions can be broadened by the many interaction channels excitons have with their environment. The environment is also crucial for the binding energy, which predominantly depends on the dielectric constant ϵ and the effective masses $m_{e,h}$ for the electron and hole, as further discussed in the following section. As an example, the effective masses for electrons and holes in GaAs yield a reduced exciton mass of around 0.06 m_0 (depending on the measurement) [15], with the free electron mass m_0, while the reduced mass of hydrogen is approximately 1 m_0 [16]. Meanwhile, the dielectric constant ϵ of GaAs is around $13.56\epsilon_0$ [17], while the dielectric constant of Hydrogen is approximately $1\epsilon_0$ [18], with the vacuum permittivity ϵ_0. Hence, despite the similarities in mathematical treatment and because of a lower reduced mass and higher dielectric constant, the binding energy of excitons in semiconductors, including GaAs, is often significantly smaller than the binding energy of hydrogen.

2.4 Bulk vs. Monolayer Transition Metal Dichalcogenides

The discussion of band structures and excitons has been kept general so far and applies to various semiconductor samples. This thesis, however, is dedicated to TMDs, which show particularly interesting band structure and excitonic properties.

As shown in Fig. 2.5, $MoSe_2$ experiences a transition from indirect band gap to direct band gap as its thickness decreases from bulk to the monolayer limit. This transition is caused by the indirect band gap gradually blueshifting due to quantum confinement as the material thickness is decreased. As a result, in the monolayer limit, the valence band maximum and conduction band minimum can both be found at the K-point, transitioning the material from an indirect to a direct band gap.

The direct band gap only arises for a true monolayer and not the bilayer, which still shows an indirect band gap. As shown in Ref. 5, this behavior is reproducible for many TMDs.

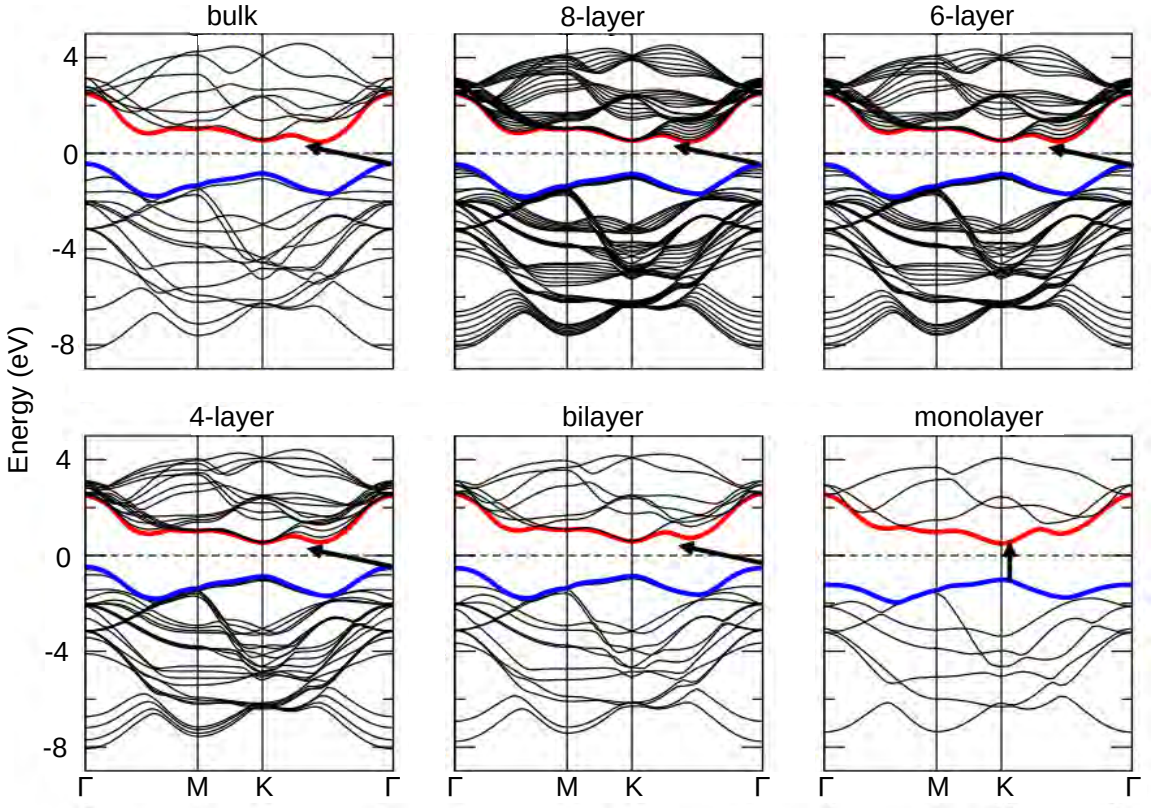

Figure 2.5: Electronic band structure for bulk, 8-layer, 6-layer, 4-layer, bilayer, and monolayer $MoSe_2$, obtained from first principle calculations in [5]. The black arrows show the lowest energy band gap, which transitions from indirect to direct for the monolayer limit. Figure adapted from Ref. 5.

When this transition toward direct band gaps in TMDs was first experimentally discovered by the groups of Feng Wang [19] and Tony Heinz [14] in 2010, it led to a flurry of interest, creating the field of optically active van-der-Waals materials. The field has subsequently been propelled forward by the strong light-matter interaction exhibited by this group of materials: Reduced Coulomb screening in two-dimensional (2D) materials [10, 19, 20] results in transition dipole moments almost two orders of magnitudes higher than for GaAs QWs. This strong light-matter coupling leads to an intriguing potential for optoelectronic device applications using TMDs, with

many device prototypes already being realized, including phototransistors [21], logic circuits [22, 23], and light-producing and harvesting devices [24–27] among others.

Further contributing to the application potential of these materials is the high binding energy of excitons in these materials, determined to be on the order of 500 meV [28–33], far exceeding binding energies in bulk GaAs [34] and GaAs QWs [35] by orders of magnitude and rendering excitons in TMDs stable well beyond room temperature. This significant increase in binding energy can be traced back to Eq. 2.5 and Eq. 2.6: Monolayer TMDs show a reduced background dielectric constant ϵ compared to thicker samples (including QWs) because their surroundings are vacuum (or lower index materials such as hexagonal boron nitride (hBN) for encapsulated samples) instead of bulk material. Hence, the Rydberg energy E_R significantly increases, and so does the exciton binding energy.

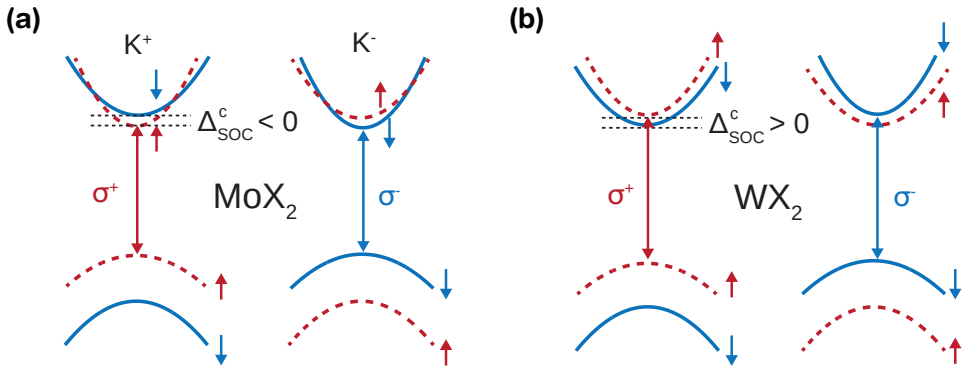

Figure 2.6: Schematic illustration of conduction and valence bands for the K^+ and K^- valley of a MoX_2 **(a)** and WX_2 **(b)** monolayer. Figure adapted from Ref. 14.

Because of symmetry considerations, the direct band gap of monolayer TMDs is located at the K (K^+) and -K (K^-) points of the Brillouin zone. Strong spin-orbit coupling is present at the K^+/K^- points, leading to spin-split bands. Since the two points of the Brillouin zone are connected by time-reversal symmetry, the spin-polarization of the two bands is opposite at the K^+ and K^- points [36]. A schematic of the band structure for a monolayer of MX_2 (M=Mo, W; X=Se, S, Te) at the K^+ and K^- points is shown in Fig. 2.6. The optical transitions are valley-selective,

meaning that σ^+-circularly polarized light can only excite transitions in the K^+ valley, while σ^--circularly polarized light can only excite transitions in the K^- valley. This spin-valley coupling has also raised interest in these materials for valleytronics [37, 38], where valleys (minima in the band structure) are used for quantum information schemes, e.g., by storing information in the exciton valley pseudospin [39].

2.5 Excitons and Their Environment: Inhomogeneity, Dephasing, and Decay

So far, the treatment of excitons and materials has assumed the idealized scenario of infinite crystals with no defects. However, we know that this ideal scenario is not true and that excitons are a product of their environment - the distribution and inhomogeneity of exciton energies across the sample, dephasing and decay times, as well as other relaxation and interaction channels, are both material and sample specific, as we discuss in the following.

2.5.1 Inhomogeneity

Spatial inhomogeneity of exciton energies causes optical linewidths to be broadened and is associated with a lower spatial coherence because the energy shifts destroy the coherence between excitons.

In TMDs, the inhomogeneity of exciton energies can be caused by strain, wrinkling, flake deformations, cracks, changes in doping/trapped charges/impurities/defects, and the free carrier concentration [40–43]. Some of these physical effects alter the band structure of the material itself [43], while some change the dielectric environment of a sample, affecting exciton energies according to Eq. 2.4.

As Martin *et al.* [44] demonstrated, encapsulation of TMD monolayers can significantly lower the inhomogeneity, mainly by passivizing the monolayer from its

environment. However, local strain changes can still lead to residual inhomogeneity [40, 41, 44, 45].

2.5.2 Decay/Dephasing

The strong light-matter coupling for excitons in TMDs can be both a blessing and a curse, depending on the desired application. While strong light-matter coupling allows for efficient excitation of excitons, it also significantly impacts the dephasing time and lifetime of the excited excitons. Decay and dephasing in semiconductors in general is a complex phenomenon whose complete discussion is well beyond the scope of this thesis. As Kira and Koch demonstrate in Ref. 46, effects such as hole burning in exciton distributions due to fast radiative decay through spontaneous emission and slow scattering from dark into bright exciton states, and polarization-to-population transfer related to the concept of coherent and incoherent excitons, play an important role for a complete discussion of decay and dephasing. Additional phenomena, including exciton-exciton scattering that is the leading mechanism for excitation-induced dephasing (EID) in TMDs [47], will not be discussed in detail because the research in this thesis does not focus on these effects.

The population decay time of excitons, T_1, can be expressed as $T_1 = 1/\Gamma$, with the decay rate

$$\Gamma = \frac{1}{T_1} = \Gamma_{\text{rad}} + \Gamma_{\text{non-rad}} \,, \tag{2.7}$$

with Γ_{rad} describing the radiative decay rate, while $\Gamma_{\text{non-rad}}$ describes any additional, non-radiative decay processes. Radiative decay stems from the exciton-light coupling: Optically active excitons, defined as having a wave vector within the light dispersion cone, $|\mathbf{k}| < \frac{E}{\hbar c}$, can decay by (spontaneous) electron-hole recombination and simultaneous emission of a photon, thus contributing to the radiative decay.

Furthermore, non-radiative decay processes can contribute to exciton population decay. In non-radiative processes, no photon is emitted, but other incoherent pro-

cesses, such as exciton-phonon scattering and scattering by defects, change the state of the exciton. A typical example in TMDs is the decay into optically dark exciton states that might be spin-forbidden or momentum-indirect such that no emission of a photon can occur. Optically bright excitons in TMDs scatter into the momentum dark states through exciton-phonon scattering, enabling transitions between different valleys of the band structure [10, 48, 49]. Phonon-mediated and defect-scattering-mediated spin-flip processes have been proposed for bright exciton transitions into spin-dark states [50, 51]. Transitioning out of dark states is usually slow because another scattering process is needed to transfer an exciton back into a bright excited state or the ground state. As another example, spectral diffusion by inelastic scattering of excitons into another excited state is common in many semiconductors [2], which often requires the absorption or emission of a phonon to bridge the momentum mismatch. Lastly, Auger recombination, a process without the involvement of phonons, has been shown to occur in TMDs [52]. In this process, an electron and hole can recombine and transfer their energy to a conduction band electron.

In dephasing processes, the phase of the exciton coherence (i.e., a fixed phase relationship between ground and excited state excitonic wave functions) is destroyed. Hence, it is often also referred to as the coherence time of the exciton system. All processes that affect the population decay time of the excitons also affect the excitons dephasing time $T_2 = 1/\gamma$, with the decay rate

$$\gamma = \frac{1}{T_2} = \Gamma/2 + \gamma^* \,, \tag{2.8}$$

and γ^* denoting the intrinsic (pure) dephasing. Intrinsic dephasing describes processes that decrease the dephasing time of excitons while not affecting the decay of the exciton population. Intrinsic dephasing stems from elastic scattering processes, such as scattering with phonons, or exciton-exciton scattering, that do not change

the lifetime of the exciton coherence [53].

2.6 Excitons in Semiconductor Heterostructures

Although this thesis focuses on TMDs and their corresponding heterostructures, a lot of the physics and observations for these materials have been informed by previous work in other semiconductor nanostructures, such as QWs. What is often referred to as ILEs in TMD heterostructures is well known as indirect excitons in QWs. Almost three decades ago, Butov *et al.* [54] showed that when applying a gate voltage to a coupled GaAs/aluminum arsenide (AlAs) QW, electrons reside in the AlAs QW while holes reside in the GaAs QW. The band structure change with varying gate voltage is illustrated in Fig. 2.7 for a symmetric QW. In the case of zero gate voltage (Fig. 2.7(a)), i.e., no external electric field, the electron and hole ground states split into symmetric (SS) and antisymmetric (AS) combinations, forming coupled well excitons with the electron and hole wave function extending over the entire QW structure [55]. However, when an external electric field is applied (Fig. 2.7(b)), the Coulomb attraction changes, and electrons and holes will be confined in opposite QWs, forming a spatially indirect exciton. Direct excitons with electrons and holes in the same layer can also form in this scenario.

The motivation behind seeking out device applications with these spatially indirect excitons is their increased lifetime because of the reduced electron-hole recombination for spatially separated electrons and holes. High *et al.* have used indirect excitons in QWs to create a cold exciton gas to form a model system for exploring the quantum physics of cold bosons in solids [57]. Using indirect excitons, researchers have further realized excitonic transistors [58] and excitonic integrated circuits [59]. While the prospect of these devices is exciting, indirect excitons in QWs have relatively low binding energies of only a few meVs [60]. The low binding energy renders these devices mostly useless at room temperature because thermal excitation of electrons

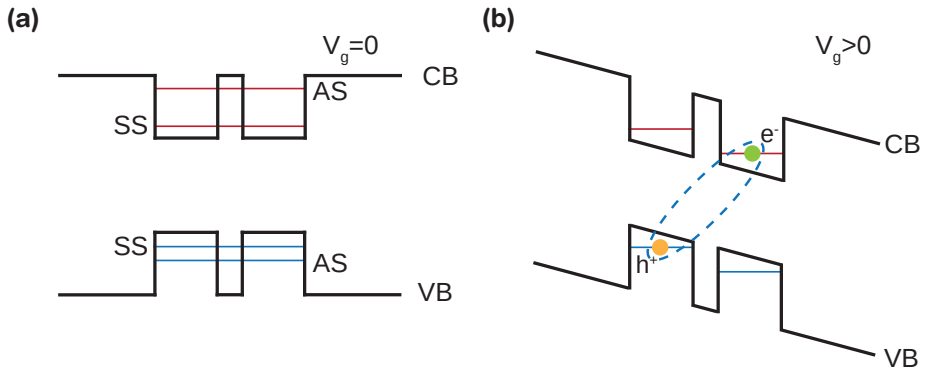

Figure 2.7: **(a)** Coupled QWs without external electric field ($V_g = 0$). AS and SS denotes the asymmetric and symmetric extended states for the electrons and holes, respectively. **(b)** With an external electric field ($V_g > 0$), indirect excitons with electrons and holes residing in opposite QWs form. Figure adapted from Ref. 56.

can easily overcome this binding energy. In contrast, ILEs in TMD heterostructures show large binding energies on the order of hundreds of meV [8, 61], rendering the potential for devices based on these systems much more exciting.

2.7 Transition Metal Dichalcogenide Heterostructures

TMDs have not only received decade-long interest for their efficient light-matter coupling and overall favorable excitonic properties - another reason for the considerable attention that they have received is the strong tunability of their material properties. Vertically stacking different TMD monolayers, as illustrated in Fig. 2.8, allows for a variety of new physics. In TMD heterostructures, coherent coupling between excitons in different monolayers, electron and hole (charge) transfer, and the formation of long-lived interlayer excitons with high binding energies and long valley lifetimes have been observed, as discussed in Chap. I.

Heterostructure samples are usually manufactured by separately manufacturing the monolayers before vertically stacking them by transferring one of the monolayers onto the other, usually via poly(methylmethacrylate) (PMMA) stamps. In the case of hBN encapsulated heterostructures, transferring takes even more steps, with

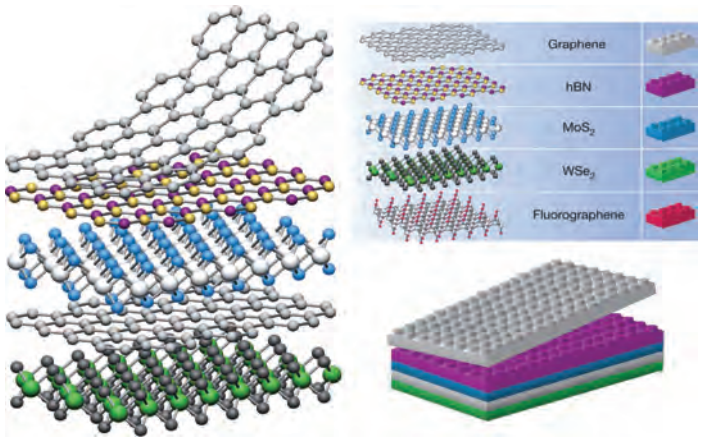

Figure 2.8: 2D heterostructures can be assembled by vertically stacking layers of 2D materials, conceptually similar to Lego. However, TMD heterostructures have more degrees of freedom, including the twist angle between layers of different materials. Figure adapted from Ref. 62.

each layer of the sample (hBN-TMD monolayer - TMD monolayer - hBN) being transferred separately. Over the past decade, numerous techniques to fabricate high-quality monolayer TMDs have been explored. The "standard" techniques are mechanical exfoliation [63–65], liquid exfoliation [66–68], wet chemical growth [69, 70], and chemical vapor deposition (CVD) growth [71–74]. While CVD growth is seen as the most promising method for high-quality, large-area growth of TMDs [75], exfoliation is currently treated as the gold standard for high-quality TMD samples.

2.7.1 Charge Transfer and Interlayer Excitons

One of the earliest interests in TMD heterostructures has been caused by the observation of ultrafast charge transfer, first discovered by Hong *et al.* in 2014 for a MoS_2/WS_2 heterostructure [76]. This charge transfer has been reproduced and further studied in many TMD heterostructures ever since [6, 7, 77–80].

This charge transfer is enabled by the type-II band alignment most TMD heterostructures exhibit. The type-II band alignment of a $MoSe_2/WSe_2$ heterostructure is illustrated in Fig. 2.9. In the type-II band alignment, the maximum of the valence band and the minimum of the conduction band reside in different layers. The electron en-

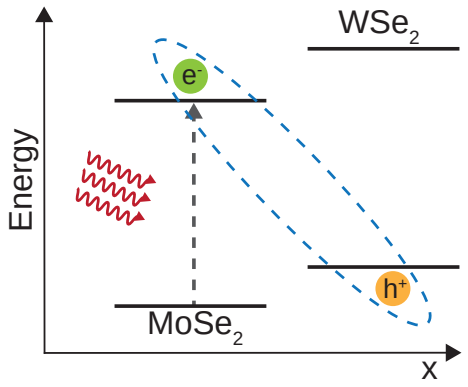

Figure 2.9: Schematic of the type-II band alignment for a $MoSe_2/WSe_2$ heterostructure. Electrons and holes prefer to reside in different materials (layers) due to the band alignment. The electrons and holes in different layers can bind together, forming interlayer excitons (dashed ellipse). Figure adapted from Ref. 76.

ergetically prefers the conduction band minimum, while the hole energetically prefers the valence band maximum. Hence, depending on whether an exciton has been excited in the $MoSe_2$ or WSe_2 layer, the electron or hole transfers into the other layer.

Recently, it has been shown for a MoS_2/WSe_2 heterostructure that the interlayer tunneling process proceeds through intermediate dark exciton levels around the Σ point [81]. Excitons formed at the K-valley tunnel rapidly, on a sub-50 fs timescale to the Σ-valley, forming a dark intralayer-exciton state. Hybridization between the MoS_2 and WSe_2 valence bands is strong around the Σ point, and electron tunneling can efficiently occur. As an additional channel during early times, the authors in Ref. 81 also observe resonant tunneling at the intersection points of the inter- and intralayer dispersion relations, preserving energy and in-plane momentum of the excitons when transitioning from the intralayer into the interlayer state.

After going through the charge transfer process, it has been shown that the electrons and holes residing in different layers can also bind together, forming an ILE [7, 8, 77, 82, 83] that is conceptually very similar to the indirect excitons discussed in Sec. 2.6. The generated ILEs exhibit nanosecond lifetimes [84–86] that are highly tunable by twist-angle [87]. They are therefore seen as potential candidates for qubits [88, 89], especially given their binding energies of hundreds of meVs [8, 9, 61], rendering

them stable far beyond room temperature.

Besides charge transfer and interlayer exciton formation, energy transfer on the scale of a few picoseconds has also been shown to occur in these materials [90].

2.7.2 Coherent Coupling

Excitons cannot only interact incoherently via charge transfer and incoherent exciton-exciton scattering but can also exhibit a Raman-like non-radiative coherent superposition between two excited states. This coherent coupling has been previously observed in semiconductor bulk, quantum wells, and quantum dots [80, 91–98], as well as $MoSe_2$ monolayers [99, 100], and was first demonstrated in a TMD heterostructure by us, as discussed in Ref. 101 and Chap. V.

The nature and origin of coherent coupling can best be understood in the diamond level system displayed in Fig. 2.10. In this model, we take the ground state (E_0), two excited states for the excitons in the respective layers ($E_{\mathrm{A,B}}$), and a two-exciton state (E_{AB}) into account. Here, the dipole moment and energies for the ground state-excited state transitions ($|0\rangle \rightarrow |A\rangle$ and $|0\rangle \rightarrow |B\rangle$, respectively) and excited state-two-exciton state transitions ($|B\rangle \rightarrow |AB\rangle$ and $|A\rangle \rightarrow |AB\rangle$, respectively) are degenerate in the case of no coherent interactions. As Hao *et al.* [100] discussed, this model is equivalent to two independent two-level systems.

However, as first discussed by Bott *et al.* [102], interactions can lift the degeneracy in different ways, depending on the type of interaction. For one, so-called biexcitonic coupling (corresponding to an energy renormalization of the two-exciton state due to static dipole-dipole or exchange interactions) either spectrally shifts the upper level of the diamond (illustrated in Fig. 2.10(a) via the dashed line), or changes its dephasing time, lifting the degeneracy. In contrast, the interaction between excitons can also mix the single exciton states through transition dipole coupling (Förster, radiative). This coupling changes the oscillator strength (illustrated in Fig. 2.10(b) through a

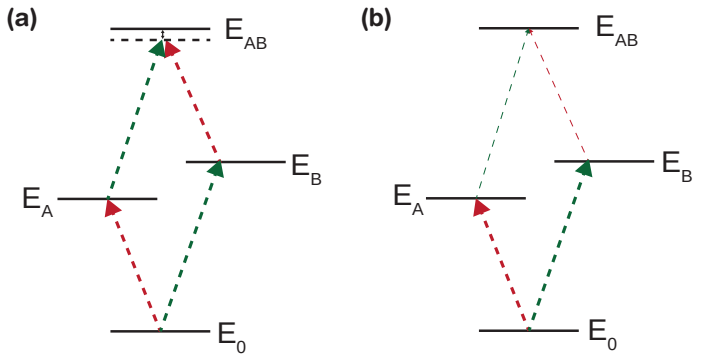

Figure 2.10: Different coherent coupling mechanisms illustrated for a diamond level system: **(a)** displays biexcitonic coupling, corresponding to an energy renormalization of the two-exciton state, **(b)** displays coupling through the mixing of the single exciton state wave functions.

decreased width of the transition arrows), effectively lifting the degeneracy while also affecting the radiative decay rates of the transitions [80].

2.7.3 Moiré Superlattices

Although all TMD samples discussed throughout this thesis do not form moiré patterns to the best of our knowledge, it would be remiss not to discuss moiré patterns and the prospect of excitons in vdW moiré superlattices.

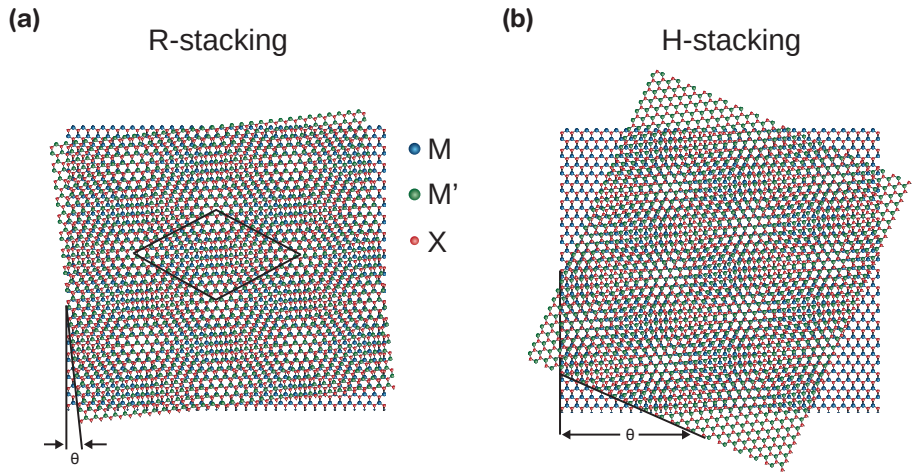

Figure 2.11: **(a)** Moiré pattern formed when two TMD monolayers with small lattice constant mismatch are aligned with a 2°twist-angle (R-stacking). The black diamond shape shows the moiré supercell. **(b)** Moiré pattern formed in H-stacking where the two monolayers are aligned with an angle close to 57°.

Simply put, when stacking two atomically thin vdW layers with different lattice constants or twist angle vertically, areas with near-perfect atomic overlap and areas with poor atomic overlap can be found. The resulting periodic variations in the atomic alignment between the layers are illustrated in Fig. 2.11, where zones of near-perfect overlap show up as white circles (corners of the black diamond). Both the lattice constant mismatch between the two materials and the twist angle between them determines the periodicity of the moiré superlattice. Common periodicities for TMD heterostructures are on the order of 1-100 nm in near-commensurate heterostructures (where both TMD monolayers share the same chalcogen atom) [103–105], with smaller supercell sizes of up to 8 nm for incommensurate heterostructures [106–108]. This spatial variation in atomic alignment gives rise to a spatially dependent energy landscape that is called the moiré potential. It has been shown that these moiré potentials can reach values above 300 meV for the valence band and 150 meV for the conduction band, significantly altering the energy landscape that excitons in these materials experience [109].

The immense interest in these moiré superlattices is caused by the flat bands that emerge in the band structure of these material systems. These flat bands allow for the study of exciting physics, such as correlated insulator states, unconventional superconductivity [110–114], and strongly correlated electronic phases [115–123]. Two common material platforms that have emerged in the past decade for these moiré superlattices are magic-angle twisted bilayer graphene [110–114, 124] and TMD heterostructures [115–120]. TMDs bear several advantages over twisted bilayer graphene: Because of the sizeable band gap of TMDs, excitons are more thermally stable and can be coupled to light. The strong spin-orbit coupling discussed in Sec. 2.4 also provides opportunities for engineering topological bands and optical control of spins/valleys. Moreover, the flat bands arise only at magic angles (e.g., 1.1°) for twisted bilayer graphene but exist over a wide range of twist angles for TMD heterostructures [115,

125, 126].

Moiré excitons in TMD heterostructures can be found either in R-stacking (around 2°) or H-stacking (around 57°). The two different stackings are shown in Fig. 2.11(a) and (b), respectively, and lead to differences in the resulting band structure and band alignment [127]. Moiré excitons in TMD heterostructures were first experimentally observed in 2019 by several groups [128–132]. Tran *et al.* [130] provide experimental evidence of multiple broad linewidth (∼10 meV) ILEs that experience tight lateral confinement due to the moiré potential by observing energy shifts in the ILEs PL emission for different stacking angles. Seyler *et al.* show that ILEs trapped by the moiré potential also show significantly narrowed (100x) linewidths of 100 µeV and strong circular polarization [129] when excited at low power.

The observations of the broad and sharp resonances are not contradictory. Bai *et al.* have shown, in agreement with [129], that the sharp features arise at lower excitation intensities while the broad features arise at higher excitation densities [108, 133]. They attribute the broad resonances to delocalized states and the sharp resonances to zero-dimensional moiré potential traps.

2.8 Conclusions

This chapter introduces the fundamental exciton physics in TMDs that forms the basis of the experimental results discussed in the following chapters. Most of these physics, apart from the moiré potential, have been observed in one way or another in more "traditional" semiconductor systems, such as bulk GaAs, GaAs QW, and QDs. However, the quantitative scale of many of these properties serves as the make-or-break criterion for many applications. What makes TMDs stand out is that they have stronger light-matter coupling than many bulk, QW, and QD systems, as well as a smaller spatial footprint with their atomic thickness and higher binding energy of intralayer excitons and ILEs. The work in the following chapters focuses on

quantifying the exciton properties of interest, such as inhomogeneity, homogeneous broadening, charge transfer times, exciton population decay times, coherent coupling strength, and decay times, both temporally and spatially.

References

[1] Neil W. Ashcroft and N. David Mermin. *Solid State Physics*. 1st ed. Florida: Harcourt, Inc, 1976. ISBN: 0-03-083993-9.

[2] Hartmut Haug and Stephan W Koch. *Quantum Theory of the Optical and Electronic Properties of Semiconductors*. 5th. WORLD SCIENTIFIC, 2009. DOI: 10.1142/7184.

[3] T.E. Schlesinger. "Gallium Arsenide". In: *Encyclopedia of Materials: Science and Technology*. Ed. by K.H. Jürgen Buschow, Robert W. Cahn, Merton C. Flemings, Bernhard Ilschner, Edward J. Kramer, Subhash Mahajan, and Patrick Veyssiére. Oxford: Elsevier, 2001, pp. 3431–3435. ISBN: 978-0-08-043152-9. DOI: https://doi.org/10.1016/B0-08-043152-6/00612-4.

[4] Julia Gusakova, Xingli Wang, Li Lynn Shiau, Anna Krivosheeva, Victor Shaposhnikov, Victor Borisenko, Vasilii Gusakov, and Beng Kang Tay. "Electronic Properties of Bulk and Monolayer TMDs: Theoretical Study Within DFT Framework (GVJ-2e Method)". In: *physica status solidi (a)* 214.12 (2017), p. 1700218. DOI: https://doi.org/10.1002/pssa.201700218.

[5] A. Kumar and P. K. Ahluwalia. "Electronic structure of transition metal dichalcogenides monolayers 1H-MX_2 (M = Mo, W; X = S, Se, Te) from ab-initio theory: new direct band gap semiconductors". In: *The European Physical Journal B* 85.6 (June 2012), p. 186. ISSN: 1434-6036. DOI: 10.1140/epjb/e2012-30070-x.

[6] S. Ovesen, S. Brem, C. Linderälv, Mikael Kuisma, Tobias Korn, Paul Erhart, Malte Selig, and Ermin Malic. "Interlayer exciton dynamics in van der Waals heterostructures". In: *Commun Phys* 2 (23 2019). DOI: 10.1038/s42005-019-0122-z.

[7] Junyi Liu, Xu Zhang, and Gang Lu. "Excitonic Effect Drives Ultrafast Dynamics in van der Waals Heterostructures". In: *Nano Letters* 20.6 (2020). PMID: 32432887, pp. 4631–4637. DOI: 10.1021/acs.nanolett.0c01519.

[8] Roland Gillen and Janina Maultzsch. "Interlayer excitons in $MoSe_2$/WSe_2 heterostructures from first principles". In: *Phys. Rev. B* 97 (16 Apr. 2018), p. 165306. DOI: 10.1103/PhysRevB.97.165306.

[9] Simon Ovesen, Samuel Brem, Christopher Linderaelv, Mikael Kuisma, Tobias Korn, Paul Erhart, Malte Selig, and Ermin Malic. "Interlayer exciton dynamics in van der Waals heterostructures". In: *Communications Physics* 2 (23 2019). DOI: doi.org/10.1038/s42005-019-0122-z.

[10] Malte Selig, Gunnar Berghäuser, Archana Raja, Philipp Nagler, Christian Schüller, Tony F. Heinz, Tobias Korn, Alexey Chernikov, Ermin Malic, and Andreas Knorr. "Excitonic linewidth and coherence lifetime in monolayer transition metal dichalcogenides". In: *Nature Communications* 7.1 (Nov. 2016), p. 13279. ISSN: 2041-1723. DOI: 10.1038/ncomms13279.

[11] Karlheinz Seeger. *Semiconductor Physics: An Introduction*. 2nd ed. Heidelberg: Springer Berlin, 1982. ISBN: 978-3-662-02351-8. DOI: https://doi.org/10.1007/978-3-662-02351-8.

[12] Jagdeep Shah. *Ultrafast Spectroscopy of Semiconductors and Semiconductor Nanostructures*. 2nd. Berlin: Springer-Verlag Berlin, 1999. ISBN: 978-3-662-03770-6. DOI: 10.1007/978-3-662-03770-6.

[13] Mads L Trolle, Thomas G Pedersen, and Valerie Véniard. "Model dielectric function for 2D semiconductors including substrate screening". en. In: *Sci Rep* 7 (Jan. 2017), p. 39844.

[14] Gang Wang, Alexey Chernikov, Mikhail M. Glazov, Tony F. Heinz, Xavier Marie, Thierry Amand, and Bernhard Urbaszek. "Colloquium: Excitons in atomically thin transition metal dichalcogenides". In: *Rev. Mod. Phys.* 90 (2 Apr. 2018), p. 021001. DOI: 10.1103/RevModPhys.90.021001.

[15] Wlodzimierz Nakwaski. "Effective masses of electrons and heavy holes in GaAs, InAs, A1As and their ternary compounds". In: *Physica B: Condensed Matter* 210.1 (1995), pp. 1–25. ISSN: 0921-4526. DOI: https://doi.org/10.1016/0921-4526(94)00921-H.

[16] R. Shankar. "The Hydrogen Atom". In: *Principles of Quantum Mechanics*. New York, NY: Springer US, 1994, pp. 353–371. ISBN: 978-1-4757-0576-8. DOI: 10.1007/978-1-4757-0576-8_13.

[17] D. E. Aspnes, S. M. Kelso, R. A. Logan, and R. Bhat. "Optical properties of $Al_xGa1\text{-}xAs$". In: *Journal of Applied Physics* 60.2 (1986), pp. 754–767. DOI: 10.1063/1.337426.

[18] A. A. Maryott and F Buckley. *Table of Dielectric Constants and Electric Dipole Moments of Substances in the Gaseous State*. 1953.

[19] Andrea Splendiani, Liang Sun, Yuanbo Zhang, Tianshu Li, Jonghwan Kim, Chi-Yung Chim, Giulia Galli, and Feng Wang. "Emerging Photoluminescence in Monolayer MoS_2". In: *Nano Letters* 10.4 (2010). PMID: 20229981, pp. 1271–1275. DOI: 10.1021/nl903868w.

[20] Maurizia Palummo, Marco Bernardi, and Jeffrey C. Grossman. "Exciton Radiative Lifetimes in Two-Dimensional Transition Metal Dichalcogenides". In: *Nano Letters* 15.5 (2015). PMID: 25798735, pp. 2794–2800. DOI: 10.1021/nl503799t.

[21] Oriol Lopez-Sanchez, Dominik Lembke, Metin Kayci, Aleksandra Radenovic, and Andras Kis. "Ultrasensitive photodetectors based on monolayer MoS_2". In: *Nature Nanotechnology* 8.7 (July 2013), pp. 497–501. ISSN: 1748-3395. DOI: 10.1038/nnano.2013.100.

[22] Branimir Radisavljevic, Michael Brian Whitwick, and Andras Kis. "Integrated Circuits and Logic Operations Based on Single-Layer MoS_2". In: *ACS Nano* 5.12 (2011). PMID: 22073905, pp. 9934–9938. DOI: 10.1021/nn203715c.

[23] Han Wang, Lili Yu, Yi-Hsien Lee, Yumeng Shi, Allen Hsu, Matthew L. Chin, Lain-Jong Li, Madan Dubey, Jing Kong, and Tomas Palacios. "Integrated Circuits Based on Bilayer MoS_2 Transistors". In: *Nano Letters* 12.9 (2012). PMID: 22862813, pp. 4674–4680. DOI: 10.1021/nl302015v.

[24] Rui Cheng, Dehui Li, Hailong Zhou, Chen Wang, Anxiang Yin, Shan Jiang, Yuan Liu, Yu Chen, Yu Huang, and Xiangfeng Duan. "Electroluminescence and Photocurrent Generation from Atomically Sharp WSe_2/MoS_2 Heterojunction p-n Diodes". In: *Nano Letters* 14.10 (2014). PMID: 25157588, pp. 5590–5597. DOI: 10.1021/nl502075n.

[25] Oriol Lopez-Sanchez, Esther Alarcon Llado, Volodymyr Koman, Anna Fontcuberta i Morral, Aleksandra Radenovic, and Andras Kis. "Light Generation and Harvesting in a van der Waals Heterostructure". In: *ACS Nano* 8.3 (2014). PMID: 24601517, pp. 3042–3048. DOI: 10.1021/nn500480u.

[26] A. Pospischil, M. Furchi, and T. Mueller. "Solar-energy conversion and light emission in an atomic monolayer p–n diode". In: *Nature Nanotechnology* 9.4 (Apr. 2014), pp. 257–261. DOI: 10.1038/nnano.2014.14.

[27] Jason S. Ross, Philip Klement, Aaron M. Jones, Nirmal J. Ghimire, Jiaqiang Yan, D. G. Mandrus, Takashi Taniguchi, Kenji Watanabe, Kenji Kitamura, Wang Yao, David H. Cobden, and Xiaodong Xu. "Electrically tunable excitonic light-emitting diodes based on monolayer WSe_2 p-n junctions". In: *Nature Nanotechnology* 9.4 (Apr. 2014), pp. 268–272. ISSN: 1748-3395. DOI: 10.1038/nnano.2014.26.

[28] Tawinan Cheiwchanchamnangij and Walter R. L. Lambrecht. "Quasiparticle band structure calculation of monolayer, bilayer, and bulk MoS_2". In: *Phys. Rev. B* 85 (20 May 2012), p. 205302. DOI: 10.1103/PhysRevB.85.205302.

[29] Ashwin Ramasubramaniam. "Large excitonic effects in monolayers of molybdenum and tungsten dichalcogenides". In: *Phys. Rev. B* 86 (11 Sept. 2012), p. 115409. DOI: 10.1103/PhysRevB.86.115409.

[30] Diana Y. Qiu, Felipe H. da Jornada, and Steven G. Louie. "Optical Spectrum of MoS_2: Many-Body Effects and Diversity of Exciton States". In: *Phys. Rev. Lett.* 111 (21 Nov. 2013), p. 216805. DOI: 10.1103/PhysRevLett.111.216805.

[31] Alexey Chernikov, Timothy C. Berkelbach, Heather M. Hill, Albert Rigosi, Yilei Li, Ozgur Burak Aslan, David R. Reichman, Mark S. Hybertsen, and Tony F. Heinz. "Exciton Binding Energy and Nonhydrogenic Rydberg Series in Monolayer WS_2". In: *Phys. Rev. Lett.* 113 (7 Aug. 2014), p. 076802. DOI: 10.1103/PhysRevLett.113.076802.

[32] Keliang He, Nardeep Kumar, Liang Zhao, Zefang Wang, Kin Fai Mak, Hui Zhao, and Jie Shan. "Tightly Bound Excitons in Monolayer WSe_2". In: *Phys. Rev. Lett.* 113 (2 July 2014), p. 026803. DOI: 10.1103/PhysRevLett.113.026803.

[33] G. Wang, X. Marie, I. Gerber, T. Amand, D. Lagarde, L. Bouet, M. Vidal, A. Balocchi, and B. Urbaszek. "Giant Enhancement of the Optical Second-Harmonic Emission of WSe_2 Monolayers by Laser Excitation at Exciton Resonances". In: *Phys. Rev. Lett.* 114 (9 Mar. 2015), p. 097403. DOI: 10.1103/PhysRevLett.114.097403.

[34] S. B. Nam, D. C. Reynolds, C. W. Litton, R. J. Almassy, T. C. Collins, and C. M. Wolfe. "Free-exciton energy spectrum in GaAs". In: *Phys. Rev. B* 13 (2 Jan. 1976), pp. 761–767. DOI: 10.1103/PhysRevB.13.761.

[35] S. Tarucha, H. Okamoto, Y. Iwasa, and N. Miura. "Exciton binding energy in GaAs quantum wells deduced from magneto-optical absorption measurement". In: *Solid State Communications* 52.9 (1984), pp. 815–819. ISSN: 0038-1098. DOI: https://doi.org/10.1016/0038-1098(84)90012-7.

[36] Di Xiao, Gui-Bin Liu, Wanxiang Feng, Xiaodong Xu, and Wang Yao. "Coupled Spin and Valley Physics in Monolayers of MoS_2 and Other Group-VI Dichalcogenides". In: *Phys. Rev. Lett.* 108 (19 May 2012), p. 196802. DOI: 10.1103/PhysRevLett.108.196802.

[37] Jason S. Ross, Pasqual Rivera, John Schaibley, Eric Lee-Wong, Hongyi Yu, Takashi Taniguchi, Kenji Watanabe, Jiaqiang Yan, David Mandrus, David Cobden, Wang Yao, and Xiaodong Xu. "Interlayer Exciton Optoelectronics in a 2D Heterostructure p-n Junction". In: *Nano Letters* 17.2 (2017), pp. 638–643. DOI: 10.1021/acs.nanolett.6b03398.

[38] Pasqual Rivera, Kyle L. Seyler, Hongyi Yu, John R. Schaibley, Jiaqiang Yan, David G. Mandrus, Wang Yao, and Xiaodong Xu. "Valley-polarized exciton dynamics in a 2D semiconductor heterostructure". In: *Science* 351.6274 (2016), pp. 688–691. ISSN: 0036-8075. DOI: 10.1126/science.aac7820.

[39] John R. Schaibley, Hongyi Yu, Genevieve Clark, Pasqual Rivera, Jason S. Ross, Kyle L. Seyler, Wang Yao, and Xiaodong Xu. "Valleytronics in 2D materials". In: *Nature Reviews Materials* 1.11 (Aug. 2016), p. 16055. ISSN: 2058-8437. DOI: 10.1038/natrevmats.2016.55.

[40] Tomasz Jakubczyk, Goutham Nayak, Lorenzo Scarpelli, Wei-Lai Liu, Sudipta Dubey, Nedjma Bendiab, Laëtitia Marty, Takashi Taniguchi, Kenji Watanabe, Francesco Masia, Gilles Nogues, Johann Coraux, Wolfgang Langbein, Julien Renard, Vincent Bouchiat, and Jacek Kasprzak. "Coherence and Density Dynamics of Excitons in a Single-Layer MoS_2 Reaching the Homogeneous Limit". In: *ACS Nano* 13.3 (2019). PMID: 30735350, pp. 3500–3511. DOI: 10.1021/acsnano.8b09732.

[41] Tomasz Jakubczyk, Karol Nogajewski, Maciej R Molas, Miroslav Bartos, Wolfgang Langbein, Marek Potemski, and Jacek Kasprzak. "Impact of environment on dynamics of exciton complexes in a WS_2 monolayer". In: *2D Materials* 5.3 (Apr. 2018), p. 031007. DOI: 10.1088/2053-1583/aabc1c.

[42] Caroline Boule, Diana Vaclavkova, Miroslav Bartos, Karol Nogajewski, Lukas Zdražil, Takashi Taniguchi, Kenji Watanabe, Marek Potemski, and Jacek Kasprzak. "Coherent dynamics and mapping of excitons in single-layer $MoSe_2$ and WSe_2 at the homogeneous limit". In: *Phys. Rev. Materials* 4 (3 Mar. 2020), p. 034001. DOI: 10.1103/PhysRevMaterials.4.034001.

[43] Zahra Khatibi, Maja Feierabend, Malte Selig, Samnuel Brem, Christoper Linderälv, Paul Erhart, and Ermin Malic. "Impact of strain on the excitonic linewidth in transition metal dichalcogenides". In: *2D Materials* 6 (1 2018). DOI: 10.1088/2053-1583/aae953.

[44] Eric W. Martin, Jason Horng, Hanna G. Ruth, Eunice Paik, Michael-Henr Wentzel, Hui Deng, and Steven T. Cundiff. "Encapsulation Narrows and Preserves the Excitonic Homogeneous Linewidth of Exfoliated Monolayer $MoSe_2$". In: *Phys. Rev. Applied* 14 (2 Aug. 2020), p. 021002. DOI: 10.1103/PhysRevApplied.14.021002.

[45] Torben L. Purz, Eric W. Martin, William G. Holtzmann, Pasqual Rivera, Adam Alfrey, Kelsey M. Bates, Hui Deng, Xiaodong Xu, and Steven T. Cundiff. "Imaging dynamic exciton interactions and coupling in transition metal dichalcogenides". In: *The Journal of Chemical Physics* 156.21 (2022), p. 214704. DOI: 10.1063/5.0087544.

[46] Mackillo Kira and Stephan W. Koch. *Semiconductor Quantum Optics*. Cambridge University Press, 2011. DOI: 10.1017/CBO9781139016926.

[47] Florian Katsch, Malte Selig, and Andreas Knorr. "Exciton-Scattering-Induced Dephasing in Two-Dimensional Semiconductors". In: *Phys. Rev. Lett.* 124 (25 June 2020), p. 257402. DOI: 10.1103/PhysRevLett.124.257402.

[48] Galan Moody, Chandriker Kavir Dass, Kai Hao, Chang-Hsiao Chen, Lain-Jong Li, Akshay Singh, Kha Tran, Genevieve Clark, Xiaodong Xu, Gunnar Berghäuser, Ermin Malic, Andreas Knorr, and Xiaoqin Li. "Intrinsic homogeneous linewidth and broadening mechanisms of excitons in monolayer transition metal dichalcogenides". In: *Nat Commun* 6 (2015), p. 8315. DOI: 10.1038/ncomms9315.

[49] Ermin Malic, Malte Selig, Maja Feierabend, Samuel Brem, Dominik Christiansen, Florian Wendler, Andreas Knorr, and Gunnar Berghäuser. "Dark excitons in transition metal dichalcogenides". In: *Phys. Rev. Materials* 2 (1 Jan. 2018), p. 014002. DOI: 10.1103/PhysRevMaterials.2.014002.

[50] Zilong Wang, Alejandro Molina-Sánchez, Patrick Altmann, Davide Sangalli, Domenico De Fazio, Giancarlo Soavi, Ugo Sassi, Federico Bottegoni, Franco Ciccacci, Marco Finazzi, Ludger Wirtz, Andrea C. Ferrari, Andrea Marini, Giulio Cerullo, and Stefano Dal Conte. "Intravalley Spin–Flip Relaxation Dynamics in Single-Layer WS_2". In: *Nano Letters* 18.11 (2018). PMID: 30264571, pp. 6882–6891. DOI: 10.1021/acs.nanolett.8b02774.

[51] Jonghwan Kim, Chenhao Jin, Bin Chen, Hui Cai, Tao Zhao, Puiyee Lee, Salman Kahn, Kenji Watanabe, Takashi Taniguchi, Sefaattin Tongay, Michael F. Crommie, and Feng Wang. "Observation of ultralong valley lifetime in $WSe_2/MoSe_2$ heterostructures". In: *Science Advances* 3.7 (2017), e1700518. DOI: 10.1126/sciadv.1700518.

[52] Paul D. Cunningham, Kathleen M. McCreary, and Berend T. Jonker. "Auger Recombination in Chemical Vapor Deposition-Grown Monolayer WS_2". In: *The Journal of Physical Chemistry Letters* 7.24 (2016). PMID: 27973899, pp. 5242–5246. DOI: 10.1021/acs.jpclett.6b02413.

[53] G. Moody, C. McDonald, A. Feldman, T. Harvey, R. P. Mirin, and K. L. Silverman. "Electronic Enhancement of the Exciton Coherence Time in Charged Quantum Dots". In: *Phys. Rev. Lett.* 116 (3 Jan. 2016), p. 037402. DOI: 10.1103/PhysRevLett.116.037402.

[54] L. V. Butov, A. Zrenner, G. Abstreiter, G. Böhm, and G. Weimann. "Condensation of Indirect Excitons in Coupled AlAs/GaAs Quantum Wells". In: *Phys. Rev. Lett.* 73 (2 July 1994), pp. 304–307. DOI: 10.1103/PhysRevLett.73.304.

[55] T. Suski, G. Staszczak, K. P. Korona, P. Lefebvre, E. Monroy, P. A. Drozdz, G. Muzioł, C. Skierbiszewski, M. Kulczykowski, M. Matuszewski, E. Grzanka, S. Grzanka, K. Pieniak, K. Gibasiewicz, A. Khachapuridze, J. Smalc-Koziorowska, L. Marona, and P. Perlin. "Switching of exciton character in double InGaN/GaN quantum wells". In: *Phys. Rev. B* 98 (16 Oct. 2018), p. 165302. DOI: 10.1103/PhysRevB.98.165302.

[56] T. Suski, G. Staszczak, K. P. Korona, P. Lefebvre, E. Monroy, P. A. Drozdz, G. Muzioł, C. Skierbiszewski, M. Kulczykowski, M. Matuszewski, E. Grzanka, S. Grzanka, K. Pieniak, K. Gibasiewicz, A. Khachapuridze, J. Smalc-Koziorowska, L. Marona, and P. Perlin. "Switching of exciton character in double InGaN/GaN quantum wells". In: *Phys. Rev. B* 98 (16 Oct. 2018), p. 165302. DOI: 10.1103/PhysRevB.98.165302.

[57] A. A. High, J. R. Leonard, A. T. Hammack, M. M. Fogler, L. V. Butov, A. V. Kavokin, K. L. Campman, and A. C. Gossard. "Spontaneous coherence in a cold exciton gas". In: *Nature* 483.7391 (Mar. 2012), pp. 584–588. ISSN: 1476-4687. DOI: 10.1038/nature10903.

[58] A. A. High, A. T. Hammack, L. V. Butov, M. Hanson, and A. C. Gossard. "Exciton optoelectronic transistor". In: *Opt. Lett.* 32.17 (Sept. 2007), pp. 2466–2468. DOI: 10.1364/OL.32.002466.

[59] Alex A. High, Ekaterina E. Novitskaya, Leonid V. Butov, Micah Hanson, and Arthur C. Gossard. "Control of Exciton Fluxes in an Excitonic Integrated Circuit". In: *Science* 321.5886 (2008), pp. 229–231. DOI: 10.1126/science.1157845.

[60] Asghar Asgari, Sara Safa, and Leonidas Mouchliadis. "Theoretical study of indirect excitons' lifetime in coupled AlGaN/GaN quantum wells in the presence of an electrostatic trap". In: *Superlattices and Microstructures* 49.4 (2011), pp. 487–495. ISSN: 0749-6036. DOI: https://doi.org/10.1016/j.spmi.2011.02.001.

[61] Neil R. Wilson, Paul V. Nguyen, Kyle Seyler, Pasqual Rivera, Alexander J. Marsden, Zachary P. L. Laker, Gabriel C. Constantinescu, Viktor Kandyba, Alexei Barinov, Nicholas D. M. Hine, Xiaodong Xu, and David H. Cobden. "Determination of band offsets, hybridization, and exciton binding in 2D semiconductor heterostructures". In: *Science Advances* 3.2 (2017). DOI: 10.1126/sciadv.1601832.

[62] A. K. Geim and I. V. Grigorieva. "Van der Waals heterostructures". In: *Nature* 499.7459 (July 2013), pp. 419–425. ISSN: 1476-4687. DOI: 10.1038/nature12385.

[63] Eric W. Martin, Christopher L. Smallwood, Torben L. Purz, Hanna G. Ruth, and Steven T. Cundiff. "Real-Time Reference for Frequency-Shifted Fourier-Transform Spectrometers Using an Arbitrary-Wavelength CW Reference Laser". In: *2019 Conference on Lasers and Electro-Optics (CLEO)*. 2019, pp. 1–2. DOI: 10.1364/CLEO_SI.2019.SM4F.4.

[64] K. S. Novoselov, D. Jiang, F. Schedin, T. J. Booth, V. V. Khotkevich, S. V. Morozov, and A. K. Geim. "Two-dimensional atomic crystals". In: *Proceedings of the National Academy of Sciences* 102.30 (2005), pp. 10451–10453. DOI: 10.1073/pnas.0502848102.

[65] Changgu Lee, Qunyang Li, William Kalb, Xin-Zhou Liu, Helmuth Berger, Robert W. Carpick, and James Hone. "Frictional Characteristics of Atomically Thin Sheets". In: *Science* 328.5974 (2010), pp. 76–80. DOI: 10.1126/science.1184167.

[66] Dmitri Golberg. "Exfoliating the inorganics". In: *Nature Nanotechnology* 6.4 (Apr. 2011), pp. 200–201. ISSN: 1748-3395. DOI: 10.1038/nnano.2011.57.

[67] Jonathan N. Coleman, Mustafa Lotya, Arlene O'Neill, Shane D. Bergin, Paul J. King, Umar Khan, Karen Young, Alexandre Gaucher, Sukanta De, Ronan J. Smith, Igor V. Shvets, Sunil K. Arora, George Stanton, Hye-Young Kim, Kangho Lee, Gyu Tae Kim, Georg S. Duesberg, Toby Hallam, John J. Boland, Jing Jing Wang, John F. Donegan, Jaime C. Grunlan, Gregory Moriarty, Aleksey Shmeliov, Rebecca J. Nicholls, James M. Perkins, Eleanor M.

Grieveson, Koenraad Theuwissen, David W. McComb, Peter D. Nellist, and Valeria Nicolosi. "Two-Dimensional Nanosheets Produced by Liquid Exfoliation of Layered Materials". In: *Science* 331.6017 (2011), pp. 568–571. DOI: 10.1126/science.1194975.

[68] Goki Eda, Hisato Yamaguchi, Damien Voiry, Takeshi Fujita, Mingwei Chen, and Manish Chhowalla. "Photoluminescence from Chemically Exfoliated MoS_2". In: *Nano Letters* 11.12 (2011). PMID: 22035145, pp. 5111–5116. DOI: 10.1021/nl201874w.

[69] Jung-tak Jang, Sohee Jeong, Jung-wook Seo, Min-Cheol Kim, Eunji Sim, Yuhong Oh, Seunghoon Nam, Byungwoo Park, and Jinwoo Cheon. "Ultrathin Zirconium Disulfide Nanodiscs". In: *Journal of the American Chemical Society* 133.20 (2011). PMID: 21539379, pp. 7636–7639. DOI: 10.1021/ja200400n.

[70] Sohee Jeong, Dongwon Yoo, Jung-tak Jang, Minkyoung Kim, and Jinwoo Cheon. "Well-Defined Colloidal 2-D Layered Transition-Metal Chalcogenide Nanocrystals via Generalized Synthetic Protocols". In: *Journal of the American Chemical Society* 134.44 (2012). PMID: 23106819, pp. 18233–18236. DOI: 10.1021/ja3089845.

[71] Yi-Hsien Lee, Xin-Quan Zhang, Wenjing Zhang, Mu-Tung Chang, Cheng-Te Lin, Kai-Di Chang, Ya-Chu Yu, Jacob Tse-Wei Wang, Chia-Seng Chang, Lain-Jong Li, and Tsung-Wu Lin. "Synthesis of Large-Area MoS_2 Atomic Layers with Chemical Vapor Deposition". In: *Advanced Materials* 24.17 (2012), pp. 2320–2325. DOI: https://doi.org/10.1002/adma.201104798.

[72] Yu-Chuan Lin, Wenjing Zhang, Jing-Kai Huang, Keng-Ku Liu, Yi-Hsien Lee, Chi-Te Liang, Chih-Wei Chu, and Lain-Jong Li. "Wafer-scale MoS_2 thin layers prepared by MoO_3 sulfurization". In: *Nanoscale* 4 (20 2012), pp. 6637–6641. DOI: 10.1039/C2NR31833D.

[73] Desheng Kong, Haotian Wang, Judy J. Cha, Mauro Pasta, Kristie J. Koski, Jie Yao, and Yi Cui. "Synthesis of MoS_2 and $MoSe_2$ Films with Vertically Aligned Layers". In: *Nano Letters* 13.3 (2013). PMID: 23387444, pp. 1341–1347. DOI: 10.1021/nl400258t.

[74] Yongjie Zhan, Zheng Liu, Sina Najmaei, Pulickel M. Ajayan, and Jun Lou. "Large-Area Vapor-Phase Growth and Characterization of MoS_2 Atomic Layers on a SiO_2 Substrate". In: *Small* 8.7 (2012), pp. 966–971. DOI: https://doi.org/10.1002/smll.201102654.

[75] Jiawen You, Md Delowar Hossain, and Zhengtang Luo. "Synthesis of 2D transition metal dichalcogenides by chemical vapor deposition with controlled layer number and morphology". In: *Nano Convergence* 5.1 (Sept. 2018), p. 26. ISSN: 2196-5404. DOI: 10.1186/s40580-018-0158-x.

[76] Xiaoping Hong, Jonghwan Kim, Su-Fei Shi, Yu Zhang, Chenhao Jin, Yinghui Sun, Sefaattin Tongay, Junqiao Wu, Yanfeng Zhang, and Feng Wang. "Ultrafast charge transfer in atomically thin MoS_2/WS_2 heterostructures". In: *Nature Nanotechnology* 9.9 (Sept. 2014), pp. 682–686. ISSN: 1748-3395. DOI: 10.1038/nnano.2014.167.

[77] Hailong Chen, Xiewen Wen, Jing Zhang, Tianmin Wu, Yongji Gong, Xiang Zhang, Jiangtan Yuan, Chongyue Yi, Jun Lou, Pulickel M. Ajayan, Wei Zhuang, Guangyu Zhang, and Junrong Zheng. "Ultrafast formation of interlayer hot excitons in atomically thin MoS_2/WS_2 heterostructures". In: *Nat Commun* 7 (2016), p. 12512. DOI: 10.1038/ncomms12512.

[78] Jonas E. Zimmermann, Young Duck Kim, James C. Hone, Ulrich Höfer, and Gerson Mette. "Directional ultrafast charge transfer in a $WSe_2/MoSe_2$ heterostructure selectively probed by time-resolved SHG imaging microscopy". In: *Nanoscale Horiz.* 5 (12 2020), pp. 1603–1609. DOI: 10.1039/D0NH00396D.

[79] Veronica R. Policht, Mattia Russo, Fang Liu, Chiara Trovatello, Margherita Maiuri, Yusong Bai, Xiaoyang Zhu, Stefano Dal Conte, and Giulio Cerullo. "Dissecting Interlayer Hole and Electron Transfer in Transition Metal Dichalcogenide Heterostructures via Two-Dimensional Electronic Spectroscopy". In: *Nano Letters* 21.11 (2021). PMID: 34037406, pp. 4738–4743. DOI: 10.1021/acs.nanolett.1c01098.

[80] B. Kasprzak J.and Patton, V. Savona, and W. Langbein. "Coherent coupling between distant excitons revealed by two-dimensional nonlinear hyperspectral imaging". In: *Nature Photonics* 5.1 (Jan. 2011), pp. 57–63. DOI: 10.1038/nphoton.2010.284.

[81] David Schmitt, Jan Philipp Bange, Wiebke Bennecke, AbdulAziz AlMutairi, Giuseppe Meneghini, Kenji Watanabe, Takashi Taniguchi, Daniel Steil, D. Russell Luke, R. Thomas Weitz, Sabine Steil, G. S. Matthijs Jansen, Samuel Brem, Ermin Malic, Stephan Hofmann, Marcel Reutzel, and Stefan Mathias. "Formation of moiré interlayer excitons in space and time". In: *Nature* 608.7923 (Aug. 2022), pp. 499–503. ISSN: 1476-4687. DOI: 10.1038/s41586-022-04977-7.

[82] P. Merkl, F. Mooshammer, P. Steinleitner, A. Girnghuber, K.-Q. Lin, P. Nagler, J. Holler, C. Schüller, J. M. Lupton, T. Korn, S. Ovesen, S. Brem, E. Malic, and R. Huber. "Ultrafast transition between exciton phases in van der Waals heterostructures". In: *Nature Materials* 18.7 (July 2019), pp. 691–696. ISSN: 1476-4660. DOI: 10.1038/s41563-019-0337-0.

[83] P. Rivera, J.R. Schaibley, A.M. Jones, J.S Ross, S. Wu, G. Aivazian, P. Klement, K. Seyler, G. Clark, N.J. Ghimire, J. Yan, D.G. Mandrus, W. Yao, and X. Xu. "Observation of long-lived interlayer excitons in monolayer $MoSe_2$-WSe_2 heterostructures". In: *Nat Commun* 6 (2015), p. 6242. DOI: 10.1038/ncomms7242.

[84] Chanyeol Choi, Jiahui Huang, Hung-Chieh Cheng, Hyunseok Kim, Abhinav Kumar Vinod, Sang-Hoon Bae, V. Ongun Özcelik, Roberto Grassi, Jongjae Chae, Shu-Wei Huang, Xiangfeng Duan, Kristen Kaasbjerg, Tony Low, and Chee Wei Wong. "Enhanced interlayer neutral excitons and trions in trilayer van der Waals heterostructures". In: *npj 2D Mater Appl* 2 (2018), p. 30. DOI: 10.1038/s41699-018-0075-1.

[85] M. Baranowski, A. Surrente, L. Klopotowski, J. M. Urban, N. Zhang, D. K. Maude, K. Wiwatowski, S. Mackowski, Y. C. Kung, D. Dumcenco, A. Kis, and P. Plochocka. "Probing the Interlayer Exciton Physics in a $MoS_2/MoSe_2/MoS_2$ van der Waals Heterostructure". In: *Nano Letters* 17.10 (2017). PMID: 28895745, pp. 6360–6365. DOI: 10.1021/acs.nanolett.7b03184.

[86] Bastian Miller, Alexander Steinhoff, Borja Pano, Julian Klein, Frank Jahnke, Alexander Holleitner, and Ursula Wurstbauer. "Long-Lived Direct and Indirect Interlayer Excitons in van der Waals Heterostructures". In: *Nano Letters* 17.9 (2017). PMID: 28742367, pp. 5229–5237. DOI: 10.1021/acs.nanolett.7b01304.

[87] Junho Choi, Matthias Florian, Alexander Steinhoff, Daniel Erben, Kha Tran, Dong Seob Kim, Liuyang Sun, Jiamin Quan, Robert Claassen, Somak Majumder, Jennifer A. Hollingsworth, Takashi Taniguchi, Kenji Watanabe, Keiji Ueno, Akshay Singh, Galan Moody, Frank Jahnke, and Xiaoqin Li. "Twist Angle-Dependent Interlayer Exciton Lifetimes in van der Waals Heterostructures". In: *Phys. Rev. Lett.* 126 (4 Jan. 2021), p. 047401. DOI: 10.1103/PhysRevLett.126.047401.

[88] Alberto Ciarrocchi, Dmitrii Unuchek, Ahmet Avsar, Kenji Watanabe, Takashi Taniguchi, and Andras Kis. "Polarization switching and electrical control of interlayer excitons in two-dimensional van der Waals heterostructures". In: *Nature Photonics* 13.2 (Feb. 2019), pp. 131–136. ISSN: 1749-4893. DOI: 10.1038/s41566-018-0325-y.

[89] Mauro Brotons-Gisbert, Hyeonjun Baek, Alejandro Molina-Sánchez, Aidan Campbell, Eleanor Scerri, Daniel White, Kenji Watanabe, Takashi Taniguchi, Cristian Bonato, and Brian D. Gerardot. "Spin-layer locking of interlayer excitons trapped in moiré potentials". In: *Nature Materials* 19.6 (June 2020), pp. 630–636. ISSN: 1476-4660. DOI: 10.1038/s41563-020-0687-7.

[90] Daichi Kozawa, Alexandra Carvalho, Ivan Verzhbitskiy, Francesco Giustiniano, Yuhei Miyauchi, Shinichiro Mouri, A. H. Castro Neto, Kazunari Matsuda, and Goki Eda. "Evidence for Fast Interlayer Energy Transfer in $MoSe_2/WS_2$ Heterostructures". In: *Nano Letters* 16.7 (2016), pp. 4087–4093. DOI: 10.1021/acs.nanolett.6b00801.

[91] Daniel B. Turner, Patrick Wen, Dylan H. Arias, Keith A. Nelson, Hebin Li, Galan Moody, Mark E. Siemens, and Steven T. Cundiff. "Persistent exciton-type many-body interactions in GaAs quantum wells measured using two-dimensional optical spectroscopy". In: *Phys. Rev. B* 85 (20 May 2012), p. 201303. DOI: 10.1103/PhysRevB.85.201303.

[92] Gaël Nardin, Galan Moody, Rohan Singh, Travis M. Autry, Hebin Li, Francois Morier-Genoud, and Steven T. Cundiff. "Coherent Excitonic Coupling in an Asymmetric Double InGaAs Quantum Well Arises from Many-Body Effects". In: *Phys. Rev. Lett.* 112 (4 Jan. 2014), p. 046402. DOI: 10.1103/PhysRevLett.112.046402.

[93] Jonathan O Tollerud, Christopher R Hall, and Jeffrey A Davis. "Isolating quantum coherence using coherent multi-dimensional spectroscopy with spectrally shaped pulses". In: *Opt. Express* 22.6 (Mar. 2014), pp. 6719–6733. DOI: 10.1364/OE.22.006719.

[94] G. Moody, I. A. Akimov, H. Li, R. Singh, D. R. Yakovlev, G. Karczewski, M. Wiater, T. Wojtowicz, M. Bayer, and S. T. Cundiff. "Coherent Coupling of Excitons and Trions in a Photoexcited CdTeCdMgTe Quantum Well". In: *Phys. Rev. Lett.* 112 (9 Mar. 2014), p. 097401. DOI: 10.1103/PhysRevLett.112.097401.

[95] J. Paul, C. E. Stevens, C. Liu, P. Dey, C. McIntyre, V. Turkowski, J. L. Reno, D. J. Hilton, and D. Karaiskaj. "Strong Quantum Coherence between Fermi Liquid Mahan Excitons". In: *Phys. Rev. Lett.* 116 (15 Apr. 2016), p. 157401. DOI: 10.1103/PhysRevLett.116.157401.

[96] P. Dey, J. Paul, G. Moody, C. E. Stevens, N. Glikin, Z. D. Kovalyuk, Z. R. Kudrynskyi, A. H. Romero, A. Cantarero, D. J. Hilton, and D. Karaiskaj. "Biexciton formation and exciton coherent coupling in layered GaSe". In: *The Journal of Chemical Physics* 142.21 (2015), p. 212422. DOI: 10.1063/1.4917169.

[97] Paola Borri and Wolfgang Langbein. "Four-wave mixing dynamics of excitons in InGaAs self-assembled quantum dots". In: *Journal of Physics: Condensed Matter* 19.29 (June 2007), p. 295201. DOI: 10.1088/0953-8984/19/29/295201.

[98] Elad Harel, Sara M. Rupich, Richard D. Schaller, Dmitri V. Talapin, and Gregory S. Engel. "Measurement of electronic splitting in PbS quantum dots by two-dimensional nonlinear spectroscopy". In: *Phys. Rev. B* 86 (7 Aug. 2012), p. 075412. DOI: 10.1103/PhysRevB.86.075412.

[99] Akshay Singh, Galan Moody, Sanfeng Wu, Yanwen Wu, Nirmal J. Ghimire, Jiaqiang Yan, David G. Mandrus, Xiaodong Xu, and Xiaoqin Li. "Coherent Electronic Coupling in Atomically Thin $MoSe_2$". In: *Phys. Rev. Lett.* 112 (21 May 2014), p. 216804. DOI: 10.1103/PhysRevLett.112.216804.

[100] Kai Hao, Lixiang Xu, Philipp Nagler, Akshay Singh, Kha Tran, Chandriker Kavir Dass, Christian Schüller, Tobias Korn, Xiaoqin Li, and Galan Moody. "Coherent and Incoherent Coupling Dynamics between Neutral and Charged Excitons in Monolayer $MoSe_2$". In: *Nano Letters* 16.8 (2016). PMID: 27428509, pp. 5109–5113. DOI: 10.1021/acs.nanolett.6b02041.

[101] Torben L. Purz, Eric W. Martin, Pasqual Rivera, William G. Holtzmann, Xiaodong Xu, and Steven T. Cundiff. "Coherent exciton-exciton interactions and exciton dynamics in a $MoSe_2/WSe_2$ heterostructure". In: *Phys. Rev. B* 104 (24 Dec. 2021), p. L241302. DOI: 10.1103/PhysRevB.104.L241302.

[102] K. Bott, O. Heller, D. Bennhardt, S. T. Cundiff, P. Thomas, E. J. Mayer, G. O. Smith, R. Eccleston, J. Kuhl, and K. Ploog. "Influence of exciton-exciton interactions on the coherent optical response in GaAs quantum wells". In: *Phys. Rev. B* 48 (23 Dec. 1993), pp. 17418–17426. DOI: 10.1103/PhysRevB.48.17418.

[103] Yi Ding, Yanli Wang, Jun Ni, Lin Shi, Siqi Shi, and Weihua Tang. "First principles study of structural, vibrational and electronic properties of graphene-like MX_2 (M=Mo, Nb, W, Ta; X=S, Se, Te) monolayers". In: *Physica B: Condensed Matter* 406.11 (2011), pp. 2254–2260. ISSN: 0921-4526. DOI: https://doi.org/10.1016/j.physb.2011.03.044.

[104] Jiangang He, Kerstin Hummer, and Cesare Franchini. "Stacking effects on the electronic and optical properties of bilayer transition metal dichalcogenides MoS_2, $MoSe_2$, WS_2, and WSe_2". In: *Phys. Rev. B* 89 (7 Feb. 2014), p. 075409. DOI: 10.1103/PhysRevB.89.075409.

[105] Jun Kang, Sefaattin Tongay, Jian Zhou, Jingbo Li, and Junqiao Wu. "Band offsets and heterostructures of two-dimensional semiconductors". In: *Applied Physics Letters* 102.1 (2013), p. 012111. DOI: 10.1063/1.4774090.

[106] Patrick Zeller and Sebastian Günther. "What are the possible moiré patterns of graphene on hexagonally packed surfaces? Universal solution for hexagonal coincidence lattices, derived by a geometric construction". In: *New Journal of Physics* 16.8 (Aug. 2014), p. 083028. DOI: 10.1088/1367-2630/16/8/083028.

[107] Patrick Zeller, Xinzhou Ma, and Sebastian Günther. "Indexing moiré patterns of metal-supported graphene and related systems: strategies and pitfalls". In: *New Journal of Physics* 19.1 (Jan. 2017), p. 013015. DOI: 10.1088/1367-2630/aa53c8.

[108] Jue Wang, Qianhui Shi, En-Min Shih, Lin Zhou, Wenjing Wu, Yusong Bai, Daniel Rhodes, Katayun Barmak, James Hone, Cory R. Dean, and X.-Y. Zhu. "Diffusivity Reveals Three Distinct Phases of Interlayer Excitons in $MoSe_2/WSe_2$ Heterobilayers". In: *Phys. Rev. Lett.* 126 (10 Mar. 2021), p. 106804. DOI: 10.1103/PhysRevLett.126.106804.

[109] Sara Shabani, Dorri Halbertal, Wenjing Wu, Mingxing Chen, Song Liu, James Hone, Wang Yao, D. N. Basov, Xiaoyang Zhu, and Abhay N. Pasupathy. "Deep moiré potentials in twisted transition metal dichalcogenide bilayers". In: *Nature Physics* 17.6 (June 2021), pp. 720–725. ISSN: 1745-2481. DOI: 10.1038/s41567-021-01174-7.

[110] Yuan Cao, Valla Fatemi, Shiang Fang, Kenji Watanabe, Takashi Taniguchi, Efthimios Kaxiras, and Pablo Jarillo-Herrero. "Unconventional superconductivity in magic-angle graphene superlattices". In: *Nature* 556.7699 (Apr. 2018), pp. 43–50. ISSN: 1476-4687. DOI: 10.1038/nature26160.

[111] Yuan Cao, Valla Fatemi, Ahmet Demir, Shiang Fang, Spencer L. Tomarken, Jason Y. Luo, Javier D. Sanchez-Yamagishi, Kenji Watanabe, Takashi Taniguchi, Efthimios Kaxiras, Ray C. Ashoori, and Pablo Jarillo-Herrero. "Correlated insulator behaviour at half-filling in magic-angle graphene superlattices". In: *Nature* 556.7699 (Apr. 2018), pp. 80–84. ISSN: 1476-4687. DOI: 10.1038/nature26154.

[112] Alexander Kerelsky, Leo J. McGilly, Dante M. Kennes, Lede Xian, Matthew Yankowitz, Shaowen Chen, K. Watanabe, T. Taniguchi, James Hone, Cory Dean, Angel Rubio, and Abhay N. Pasupathy. "Maximized electron interactions at the magic angle in twisted bilayer graphene". In: *Nature* 572.7767 (Aug. 2019), pp. 95–100. ISSN: 1476-4687. DOI: 10.1038/s41586-019-1431-9.

[113] Xiaobo Lu, Petr Stepanov, Wei Yang, Ming Xie, Mohammed Ali Aamir, Ipsita Das, Carles Urgell, Kenji Watanabe, Takashi Taniguchi, Guangyu Zhang, Adrian Bachtold, Allan H. MacDonald, and Dmitri K. Efetov. "Superconductors, orbital magnets and correlated states in magic-angle bilayer graphene". In: *Nature* 574.7780 (Oct. 2019), pp. 653–657. ISSN: 1476-4687. DOI: 10.1038/s41586-019-1695-0.

[114] Youngjoon Choi, Hyunjin Kim, Yang Peng, Alex Thomson, Cyprian Lewandowski, Robert Polski, Yiran Zhang, Harpreet Singh Arora, Kenji Watanabe, Takashi Taniguchi, Jason Alicea, and Stevan Nadj-Perge. "Correlation-driven topological phases in magic-angle twisted bilayer graphene". In: *Nature* 589.7843 (Jan. 2021), pp. 536–541. ISSN: 1476-4687. DOI: 10.1038/s41586-020-03159-7.

[115] Lei Wang, En-Min Shih, Augusto Ghiotto, Lede Xian, Daniel A. Rhodes, Cheng Tan, Martin Claassen, Dante M. Kennes, Yusong Bai, Bumho Kim, Kenji Watanabe, Takashi Taniguchi, Xiaoyang Zhu, James Hone, Angel Rubio, Abhay N. Pasupathy, and Cory R. Dean. "Correlated electronic phases in twisted bilayer transition metal dichalcogenides". In: *Nature Materials* 19.8 (Aug. 2020), pp. 861–866. ISSN: 1476-4660. DOI: 10.1038/s41563-020-0708-6.

[116] Yanhao Tang, Lizhong Li, Tingxin Li, Yang Xu, Song Liu, Katayun Barmak, Kenji Watanabe, Takashi Taniguchi, Allan H. MacDonald, Jie Shan, and Kin Fai Mak. "Simulation of Hubbard model physics in WSe_2/WS_2 moiré superlattices". In: *Nature* 579.7799 (Mar. 2020), pp. 353–358. ISSN: 1476-4687. DOI: 10.1038/s41586-020-2085-3.

[117] Yang Xu, Song Liu, Daniel A. Rhodes, Kenji Watanabe, Takashi Taniguchi, James Hone, Veit Elser, Kin Fai Mak, and Jie Shan. "Correlated insulating states at fractional fillings of moiré superlattices". In: *Nature* 587.7833 (Nov. 2020), pp. 214–218. ISSN: 1476-4687. DOI: 10.1038/s41586-020-2868-6.

[118] Yuya Shimazaki, Ido Schwartz, Kenji Watanabe, Takashi Taniguchi, Martin Kroner, and Ataç Imamoğlu. "Strongly correlated electrons and hybrid excitons in a moiré heterostructure". In: *Nature* 580.7804 (Apr. 2020), pp. 472–477. ISSN: 1476-4687. DOI: 10.1038/s41586-020-2191-2.

[119] Xiong Huang, Tianmeng Wang, Shengnan Miao, Chong Wang, Zhipeng Li, Zhen Lian, Takashi Taniguchi, Kenji Watanabe, Satoshi Okamoto, Di Xiao, Su-Fei Shi, and Yong-Tao Cui. "Correlated insulating states at fractional fillings of the WS_2/WSe_2 moiré lattice". In: *Nature Physics* 17.6 (June 2021), pp. 715–719. ISSN: 1745-2481. DOI: 10.1038/s41567-021-01171-w.

[120] Zhaodong Chu, Emma C. Regan, Xuejian Ma, Danqing Wang, Zifan Xu, M. Iqbal Bakti Utama, Kentaro Yumigeta, Mark Blei, Kenji Watanabe, Takashi Taniguchi, Sefaattin Tongay, Feng Wang, and Keji Lai. "Nanoscale Conductivity Imaging of Correlated Electronic States in WSe_2/WS_2 Moiré Superlattices". In: *Phys. Rev. Lett.* 125 (18 Oct. 2020), p. 186803. DOI: 10.1103/PhysRevLett.125.186803.

[121] Emma C. Regan, Danqing Wang, Chenhao Jin, M. Iqbal Bakti Utama, Beini Gao, Xin Wei, Sihan Zhao, Wenyu Zhao, Zuocheng Zhang, Kentaro Yumigeta, Mark Blei, Johan D. Carlström, Kenji Watanabe, Takashi Taniguchi, Sefaattin Tongay, Michael Crommie, Alex Zettl, and Feng Wang. "Mott and generalized Wigner crystal states in WSe_2/WS_2 moiré superlattices". In: *Nature* 579.7799 (Mar. 2020), pp. 359–363. ISSN: 1476-4687. DOI: 10.1038/s41586-020-2092-4.

[122] You Zhou, Jiho Sung, Elise Brutschea, Ilya Esterlis, Yao Wang, Giovanni Scuri, Ryan J. Gelly, Hoseok Heo, Takashi Taniguchi, Kenji Watanabe, Gergely Zaránd, Mikhail D. Lukin, Philip Kim, Eugene Demler, and Hongkun Park. "Bilayer Wigner crystals in a transition metal dichalcogenide heterostructure". In: *Nature* 595.7865 (July 2021), pp. 48–52. ISSN: 1476-4687. DOI: 10.1038/s41586-021-03560-w.

[123] Tomasz Smoleński, Pavel E. Dolgirev, Clemens Kuhlenkamp, Alexander Popert, Yuya Shimazaki, Patrick Back, Xiaobo Lu, Martin Kroner, Kenji Watanabe, Takashi Taniguchi, Ilya Esterlis, Eugene Demler, and Ataç Imamoğlu. "Signatures of Wigner crystal of electrons in a monolayer semiconductor". In: *Nature* 595.7865 (July 2021), pp. 53–57. ISSN: 1476-4687. DOI: 10.1038/s41586-021-03590-4.

[124] Rafi Bistritzer and Allan H. MacDonald. "Moiré bands in twisted double-layer graphene". In: *Proceedings of the National Academy of Sciences* 108.30 (2011), pp. 12233–12237. DOI: 10.1073/pnas.1108174108.

[125] Mit H. Naik, Sudipta Kundu, Indrajit Maity, and Manish Jain. "Origin and evolution of ultraflat bands in twisted bilayer transition metal dichalcogenides: Realization of triangular quantum dots". In: *Phys. Rev. B* 102 (7 Aug. 2020), p. 075413. DOI: 10.1103/PhysRevB.102.075413.

[126] Xing-Ju Zhao, Yang Yang, Dong-Bo Zhang, and Su-Huai Wei. "Formation of Bloch Flat Bands in Polar Twisted Bilayers without Magic Angles". In: *Phys. Rev. Lett.* 124 (8 Feb. 2020), p. 086401. DOI: 10.1103/PhysRevLett.124.086401.

[127] Long Zhang, Zhe Zhang, Fengcheng Wu, Danqing Wang, Rahul Gogna, Shaocong Hou, Kenji Watanabe, Takashi Taniguchi, Krishnamurthy Kulkarni, Thomas Kuo, Stephen R. Forrest, and Hui Deng. "Twist-angle dependence of moiré excitons in $WS_2/MoSe_2$ heterobilayers". In: *Nature Communications* 11.1 (Nov. 2020), p. 5888. ISSN: 2041-1723. DOI: 10.1038/s41467-020-19466-6.

[128] Evgeny M. Alexeev, David A. Ruiz-Tijerina, Mark Danovich, Matthew J. Hamer, Daniel J. Terry, Pramoda K. Nayak, Seongjoon Ahn, Sangyeon Pak, Juwon Lee, Jung Inn Sohn, Maciej R. Molas, Maciej Koperski, Kenji Watanabe, Takashi Taniguchi, Kostya S. Novoselov, Roman V. Gorbachev, Hyeon Suk Shin, Vladimir I. Fal'ko, and Alexander I. Tartakovskii. "Resonantly hybridized excitons in moiré superlattices in van der Waals heterostructures". In: *Nature* 567.7746 (Mar. 2019), pp. 81–86. ISSN: 1476-4687. DOI: 10.1038/s41586-019-0986-9.

[129] Kyle L. Seyler, Pasqual Rivera, Hongyi Yu, Nathan P. Wilson, Essance L. Ray, David G. Mandrus, Jiaqiang Yan, Wang Yao, and Xiaodong Xu. "Signatures of moiré-trapped valley excitons in $MoSe_2/WSe_2$ heterobilayers". In: *Nature* 567.7746 (Mar. 2019), pp. 66–70. ISSN: 1476-4687. DOI: 10.1038/s41586-019-0957-1.

[130] Kha Tran, Galan Moody, Fengcheng Wu, Xiaobo Lu, Junho Choi, Kyounghwan Kim, Amritesh Rai, Daniel A. Sanchez, Jiamin Quan, Akshay Singh, Jacob Embley, André Zepeda, Marshall Campbell, Travis Autry, Takashi Taniguchi, Kenji Watanabe, Nanshu Lu, Sanjay K. Banerjee, Kevin L. Silverman, Suenne Kim, Emanuel Tutuc, Li Yang, Allan H. MacDonald, and Xiaoqin Li. "Evidence for moiré excitons in van der Waals heterostructures". In: *Nature* 567.7746 (Mar. 2019), pp. 71–75. ISSN: 1476-4687. DOI: 10.1038/s41586-019-0975-z.

[131] Chenhao Jin, Emma C. Regan, Aiming Yan, M. Iqbal Bakti Utama, Danqing Wang, Sihan Zhao, Ying Qin, Sijie Yang, Zhiren Zheng, Shenyang Shi, Kenji Watanabe, Takashi Taniguchi, Sefaattin Tongay, Alex Zettl, and Feng Wang. "Observation of moiré excitons in WSe_2/WS_2 heterostructure superlattices". In: *Nature* 567.7746 (Mar. 2019), pp. 76–80. ISSN: 1476-4687. DOI: 10.1038/s41586-019-0976-y.

[132] Nan Zhang, Alessandro Surrente, Michał Baranowski, Duncan K. Maude, Patricia Gant, Andres Castellanos-Gomez, and Paulina Plochocka. "Moiré Intralayer Excitons in a $MoSe_2/MoS_2$ Heterostructure". In: *Nano Letters* 18.12 (2018). PMID: 30403876, pp. 7651–7657. DOI: 10.1021/acs.nanolett.8b03266.

[133] Yusong Bai, Lin Zhou, Jue Wang, Wenjing Wu, Leo J. McGilly, Dorri Halbertal, Chiu Fan Bowen Lo, Fang Liu, Jenny Ardelean, Pasqual Rivera, Nathan R. Finney, Xu-Chen Yang, D. N. Basov, Wang Yao, Xiaodong Xu, James Hone, Abhay N. Pasupathy, and X.-Y. Zhu. "Excitons in strain-induced one-dimensional moiré potentials at transition metal dichalcogenide heterojunctions". In: *Nature Materials* 19.10 (Oct. 2020), pp. 1068–1073. ISSN: 1476-4660. DOI: 10.1038/s41563-020-0730-8.

CHAPTER III

Theoretical Treatment of Nonlinear Spectroscopy

3.1 Introduction

In Chap. II, we established the exciting physical phenomena that render TMDs an interesting and promising platform for device applications, from photodiodes to lasers and beyond. To explore both the potential and limitations of this group of materials, a thorough understanding of the fundamental physical processes in these materials is necessary. We also introduced the concepts of homogeneous and inhomogeneous linewidths and coherent and incoherent coupling. These are physical phenomena that are hard, if not impossible, to distinguish using common linear and one-dimensional nonlinear techniques (one-dimensional here meaning only resolving one frequency axis, e.g., absorption or emission). MDCS can overcome many of these limitations and thus is ideal for studying TMD monolayers and heterostructures.

We first introduce MDCS in this chapter from a purely theoretical perspective, enabling us to understand the reasoning behind the experimental implementation presented in Chap. IV. We start by introducing linear spectroscopy and the Lorentz oscillator model, a good model to phenomenologically (and roughly quantitatively) understand the concept of absorption. Subsequently, we work up from linear to nonlinear spectroscopy using the density matrix approach. In this context, we introduce the different pulse excitation schemes for zero-quantum, one-quantum, and double-

quantum implementations of MDCS, which allows us to access various physical properties of the TMD samples. The density matrix then leads us to the OBEs employed in Chap. V to simulate the optical response of a $MoSe_2/WSe_2$ heterostructure.

Subsequently, we discuss the different MDCS spectra (rephasing vs. non-rephasing, one-quantum vs. zero-quantum), how to interpret them, and how to extract quantitative information such as homogeneous and inhomogeneous linewidths from them.

3.2 An Introduction to Linear Spectroscopy and Linear Absorption

3.2.1 Linear Spectroscopy

The most fundamental idea behind (linear) spectroscopy is the desire to learn about and understand a material when other experimental techniques are not feasible. One of the first instances of spectroscopy is the determination of the gas content of planets [2]. Still, spectroscopy is also used in applications as varying as the detection of explosives [3, 4], semiconductor characterization [5–7], chemical analysis [8], and pulse oximetry [9], a staple of everyone's doctor's visit nowadays. The idea behind all of these techniques is mostly the same: The spectral characteristics of the sample (i.e.,

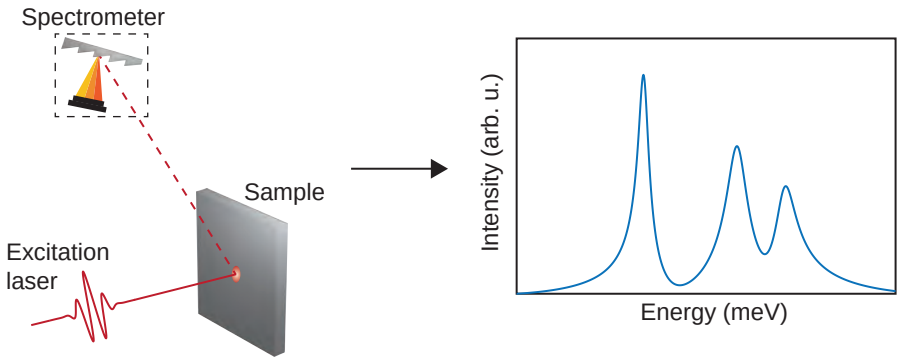

Figure 3.1: Schematic of a linear spectroscopy experiment: An excitation laser impinges on the sample. The sample response is subsequently recorded with a spectrometer. Figure adapted from [1].

the sample response as a function of wavelength/energy) yield absorption/emission energies, linewidths, and more, revealing important information about the sample.

Many linear spectroscopy experiments look similar to Fig. 3.1, where a laser is directed at a sample of interest. The sample absorbs part of the initial laser radiation (and can also emit radiation), and the response of the laser-sample interaction is sent to a spectrometer to spectrally resolve the sample response. In a simplified explanation, a grating-based spectrometer consists of a diffraction grating that disperses different wavelengths at different angles and a camera that records the resulting signal. Because different wavelengths impinge on different pixels, a measured intensity as a function of wavelength can be retrieved, as shown on the right of Fig. 3.1.

Two common modes of operation are either recording the amount of absorbed light by comparing the spectrum with and without the sample (absorption spectroscopy) or looking at the PL the sample emits after initial absorption of the laser light (PL-spectroscopy).

A good first model for understanding light absorption is the Lorentz oscillator model, introduced by Dutch physicist Hendrik Lorentz in the 19th century, which models the response of bound electrons to external optical excitation.

3.2.2 The Lorentz Oscillator Model

When applying an external electric field $\mathbf{E}(t)$ to a material, the electrons of charge e will experience a force

$$\mathbf{F} = -e\mathbf{E}(t)\,. \tag{3.1}$$

The displacement $\mathbf{r}$ for a single electron, caused by the external electric field, then leads to a dipole with a dipole moment

$$\mathbf{p} = -e\mathbf{r}\,. \tag{3.2}$$

The collective dipole moment of all electrons in the material is then

$$\mathbf{p} = \sum_n -e\mathbf{r}_n \,, \tag{3.3}$$

with $\mathbf{r}_n$ being the displacement of the n$^{\text{th}}$ electron. The macroscopic polarization $\mathbf{P}$, defined as the dipole moment per unit volume, can then be obtained as

$$\mathbf{P} = N\mathbf{p} \,, \tag{3.4}$$

with the electron density N.

The electric displacement field $\mathbf{D}$, which can be thought of as the effective electric field in a material, can be obtained as the sum of the external electric field $\mathbf{E}$ and the polarization $\mathbf{P}$ of the electrons, which often opposes the external electric field:

$$\mathbf{D} = \epsilon_0\mathbf{E} + \mathbf{P} \,, \tag{3.5}$$

with the vacuum permittivity ϵ_0.

An expression for the polarization must thus be found to determine the displacement field. The Lorentz oscillator model for the material's polarization describes an electron orbiting a stationary nucleus as a spring-mass-damper system. We consider the driving force $\mathbf{F}_{\text{driving}} = -e\mathbf{E}(t)$ caused by the external electric field, the spring force $\mathbf{F}_{\text{spring}} = m{\omega_0}^2\mathbf{r}$, and a damping force $\mathbf{F}_{\text{damping}} = \frac{m}{\tau}\dot{\mathbf{r}}$. Here, τ is the relaxation/scattering time, ω_0 the resonance frequency of the oscillator, which is given by $\omega_0 = \sqrt{k/m}$ with k being the spring constant and m the effective mass of the electron. As a result, the equation of motion for the electron,

$$\ddot{\mathbf{r}} + \frac{1}{\tau}\dot{\mathbf{r}} + {\omega_0}^2\mathbf{r} = -\frac{e}{m}\mathbf{E}(t) \,, \tag{3.6}$$

is that of a driven, damped, harmonic oscillator [10].

Using a time-harmonic electric field, $\mathbf{E}(\omega,t) = \mathbf{E}_0 e^{-i\omega t}$ and making a time-harmonic ansatz for $\mathbf{r}(\omega,t) = \mathbf{r}_0 e^{-i\omega t}$, we then obtain

$$\mathbf{r}(\omega,t) = \frac{-e/m}{{\omega_0}^2 - \omega^2 - i\omega/\tau}\mathbf{E}(\omega,t)\,, \tag{3.7}$$

for the electron displacement. Using Eq. 3.3 and Eq. 3.4, we obtain

$$\mathbf{P}(\omega,t) = \tilde{\mathbf{P}}(\omega)e^{-i\omega t} = -Ne\mathbf{r}(\omega,t) \tag{3.8}$$

$$= \frac{Ne^2}{m}\left(\left[\frac{{\omega_0}^2 - \omega^2}{(\omega_0^2-\omega^2)^2 + (\omega/\tau)^2}\right] + i\left[\frac{\omega/\tau}{(\omega_0^2-\omega^2)^2 + (\omega/\tau)^2}\right]\right)\mathbf{E_0}e^{-i\omega t}\,, \tag{3.9}$$

for the polarization. Here, we have separated the complex expression for $\mathbf{r}(\omega,t)$ into its real and imaginary parts. The static, time-independent part of the polarization (without the plane wave) is often expressed in terms of the external electric field as

$$\tilde{\mathbf{P}}(\omega) = \epsilon_0\chi(\omega)\mathbf{E_0}\,, \tag{3.10}$$

with the vacuum permittivity ϵ_0, and the susceptibility $\chi(\omega)$ defined as

$$\chi(\omega) = \frac{Ne^2}{\epsilon_0 m}\left(\left[\frac{{\omega_0}^2 - \omega^2}{(\omega_0^2-\omega^2)^2 + (\omega/\tau)^2}\right] + i\left[\frac{\omega/\tau}{(\omega_0^2-\omega^2)^2 + (\omega/\tau)^2}\right]\right)\,. \tag{3.11}$$

The imaginary part of the susceptibility corresponds to absorption, while the real part corresponds to refraction. Thus, the interference of the macroscopic polarization $\mathbf{P}$ and the external electric field leads to features such as absorption dips in linear absorption spectroscopy.

3.3 The Density Matrix Approach

Eventually, the approximations of the Lorentz-oscillator model break down for the solid-state systems treated in this thesis. We must move from our classical, phenomenological approach toward a quantum mechanical description. Again, the final goal is to find an expression for the polarization $\mathbf{P}$. In this section, we use the density matrix, which describes the quantum state of a physical system [11].

The density matrix of a pure quantum state $|\psi\rangle$ is defined as

$$\rho = |\psi\rangle \langle\psi| \ . \tag{3.12}$$

Expanding the wave function ψ in a basis $|n\rangle$, we can write

$$|\psi\rangle = \sum_n c_n |n\rangle \ , \tag{3.13}$$

and similarly

$$\langle\psi| = \sum_m {c_m}^* \langle m| \ . \tag{3.14}$$

The amplitude coefficients c_n need to fulfill $\sum_n |c_n|^2$, i.e., the total probability of being in either of the available states is one. The density matrix can then be described in the Hilbert space spanned by the states $|n\rangle$ as

$$\rho = \sum_{n,m} c_n {c_m}^* |n\rangle \langle m| \ , \tag{3.15}$$

with specific elements of the density matrix

$$\rho_{n,m} = \langle n| \rho |m\rangle = c_n {c_m}^* . \tag{3.16}$$

While every wave function $|\psi\rangle$ can be expressed as a density matrix, the latter is often

more general, and more powerful for describing the optical processes in this thesis. For example, if a physical system has a 50% probability of being either in state $|0\rangle$ or $|1\rangle$ (a realistic scenario for exciton populations after dephasing), the density matrix of the mixed state is

$$\rho = \frac{1}{2}\begin{pmatrix} 1 & 0 \\ 0 & 1 \end{pmatrix}, \tag{3.17}$$

which is distinct from the density matrix for a quantum superposition of the two states, $|\psi\rangle = (|0\rangle + |1\rangle)/\sqrt{2}$, in which case

$$\rho = \frac{1}{2}\begin{pmatrix} 1 & 1 \\ 1 & 1 \end{pmatrix}. \tag{3.18}$$

Before diving more deeply into how to describe the time-dependent evolution of a quantum system in this framework, it is helpful to remind ourselves how this density matrix leads to our eventual goal of determining the polarization $\mathbf{P}$.

In Eq. 3.4 we used the classical value of the dipole moment to calculate the polarization $\mathbf{P}$. Here, instead of having a classical value for the dipole moment, we need to calculate the expectation value of the corresponding operator. The polarization $\mathbf{P}$ can then be calculated as the expectation value of the dipole operator

$$\boldsymbol{\mu} = \begin{pmatrix} 0 & \boldsymbol{\mu}_{01} \\ \boldsymbol{\mu}_{10} & 0 \end{pmatrix}, \tag{3.19}$$

with the transition dipole moment $\boldsymbol{\mu}_{ij} = \langle i|e\mathbf{r}|j\rangle$. In the following, we will omit the vector notation for $\mathbf{r}, \boldsymbol{\mu}$, and $\mathbf{P}$ for simplicity.

Because in quantum mechanics, the expectation value of an operator μ is defined as the trace of the operator applied to the density matrix,

$$\langle\mu\rangle = \langle\psi|\mu|\psi\rangle = \mathrm{Tr}(\mu\rho), \tag{3.20}$$

the polarization can be obtained as

$$P(t) = \mathrm{Tr}(\mu\rho(t))\,. \tag{3.21}$$

Therefore, by calculating the time-dependent density matrix $\rho(t)$, we can obtain a quantum mechanical expression for the polarization.

It follows rather straightforwardly from the Schrödinger equation that the time-evolution of the density matrix is given by the Liouville-von Neumann equation

$$\dot{\rho} = -\frac{i}{\hbar}[H, \rho]\,. \tag{3.22}$$

This description is exact; however, approximations are commonly made when describing the Hamiltonian H. Here we approximate the Hamiltonian as

$$H(t) = H_0 + V(t)\,,$$

with the system Hamiltonian H_0 and a small perturbation $V(t)$ that stems from the interaction of the system with an external light field.

We start with a simple two-level system, with a ground state $|0\rangle$ and an excited state $|1\rangle$. Instead of treating this as an isolated system, we will let the system interact with its environment, assuming it is within the Markovian limit [11, 12] for the system-bath coupling. The Markovian limit describes a system with "no memory" and leads to exponential dephasing of the material's optical response [11]. For the sample systems studied in this work, this is a reasonable approximation, although other frameworks to describe more complicated systems exist [11] and have to be applied to study the dynamics of colloidal QDs [13], for example. In this case, the

system Hamiltonian H_0 can be written as

$$H_0 = \begin{pmatrix} \epsilon_0 & 0 \\ 0 & \epsilon_1 \end{pmatrix} , \tag{3.23}$$

with the energy eigenvalues $\epsilon_{0,1}$ for the ground and excited state, respectively. The light-field-interaction Hamiltonian can then be written as

$$V(t) = \begin{pmatrix} 0 & -\mu E(t) \\ -\mu E(t) & 0 \end{pmatrix} , \tag{3.24}$$

with the transition dipole operator μ and the external electric field $E(t)$. The resulting differential equations for the evolution of the density matrix elements then read

$$\begin{aligned} \dot{\rho} &= \frac{\mathrm{d}}{\mathrm{d}t} \begin{pmatrix} \rho_{00} & \rho_{01} \\ \rho_{10} & \rho_{11} \end{pmatrix} \\ &= -\frac{i}{\hbar} \begin{pmatrix} -\mu E(t)\rho_{10} + \mu E(t)\rho_{01} & \rho_{01}(\epsilon_0 - \epsilon_1) + \mu E(t)(\rho_{00} - \rho_{11}) \\ \rho_{10}(\epsilon_1 - \epsilon_0) + \mu E(t)(\rho_{11} - \rho_{00}) & \mu E(t)\rho_{10} - \mu E(t)\rho_{01} \end{pmatrix} . \end{aligned} \tag{3.25}$$

3.3.1 Liouville Representation and Optical Bloch Equations

It is often more convenient to represent Eq. 3.25 in the Liouville representation

$$\begin{pmatrix} \dot{\rho}_{01} \\ \dot{\rho}_{10} \\ \dot{\rho}_{00} \\ \dot{\rho}_{11} \end{pmatrix} = -\frac{i}{\hbar} \begin{pmatrix} \epsilon_0 - \epsilon_1 & 0 & -\mu E(t) & \mu E(t) \\ 0 & \epsilon_1 - \epsilon_0 & \mu E(t) & -\mu E(t) \\ -\mu E(t) & \mu E(t) & 0 & 0 \\ \mu E(t) & -\mu E(t) & 0 & 0 \end{pmatrix} \cdot \begin{pmatrix} \rho_{01} \\ \rho_{10} \\ \rho_{00} \\ \rho_{11} \end{pmatrix} , \tag{3.26}$$

such that

$$\dot{\rho} = -\frac{i}{\hbar} L\rho \,, \tag{3.27}$$

with the superoperator L. The convenience of this description is that adding additional physics, such as dephasing and decay (relaxation), can be simply done by writing

$$\dot{\rho} = -\frac{i}{\hbar} L\rho - \Gamma\rho \,, \tag{3.28}$$

with another superoperator for the relaxation, Γ. Adding dephasing, the equations of motion for the density matrix read

$$\begin{aligned}
\dot{\rho}_{00} &= -\tfrac{i}{\hbar}(-\mu E(t)\rho_{10} + \mu E^*(t)\rho_{01}) + \Gamma_{11}\rho_{11} \\
\dot{\rho}_{01} &= \rho_{01}(\tfrac{i}{\hbar}(\epsilon_1 - \epsilon_0) + \Gamma_{01}) - i\tfrac{\mu E(t)}{\hbar}(\rho_{00} - \rho_{11}) \\
\dot{\rho}_{10} &= \rho_{10}(-\tfrac{i}{\hbar}(\epsilon_1 - \epsilon_0) + \Gamma_{10}) + i\tfrac{\mu E(t)}{\hbar}(\rho_{00} - \rho_{11}) \\
\dot{\rho}_{11} &= -\tfrac{i}{\hbar}(-\mu E(t)\rho_{10} + \mu E^*(t)\rho_{01}) - \Gamma_{11}\rho_{11}
\end{aligned} \,, \tag{3.29}$$

or more compactly

$$\dot{\rho_{ij}} = -\frac{i}{\hbar}\sum_k (H_{ik}\rho_{kj} - \rho_{ik}H_{kj}) - \Gamma_{ij}\rho_{ij} \,, \tag{3.30}$$

with the relaxation rate $\Gamma_{ij} = (\Gamma_i + \Gamma_j)/2 + {\gamma_{ij}}^{ph}$ containing contributions from the population decay rate $\Gamma_{i,j}$ of state i,j, as well as pure dephasing ${\gamma_{ij}}^{ph}$ $(i \neq j)$ [14]. The model of simple exponential decay for dephasing can be justified by a more rigorous treatment of energy fluctuations and lineshape theory [12]. Eqs. 3.30 are called the OBEs [14], which describe the time evolution of the quantum system when perturbed by an external harmonic electric field.

3.4 Limitations of Linear Spectroscopy

While tremendously useful, there are also severe limitations and ambiguities in linear spectroscopy that hinder a deep and thorough understanding of the underlying material.

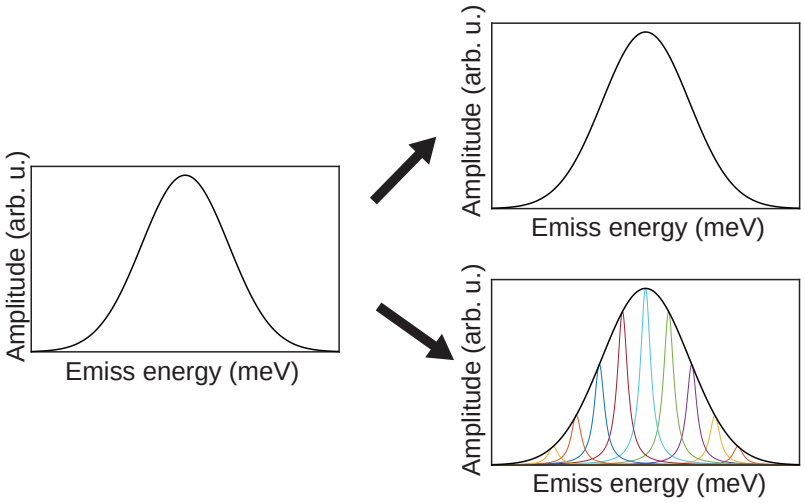

Figure 3.2: Ambiguity in linear/one-dimensional spectroscopy experiments: These experiments will measure the spectrum on the left, which can be either caused by an ensemble of emitters with the same resonance frequency and broad linewidth (right-top panel) or an ensemble of narrow linewidth emitters with varying resonance energies (right-bottom panel).

A classic example of the ambiguity in linear spectroscopy is shown in Fig. 3.2. From the spectrum on the left, which would be obtained in a linear spectroscopy experiment (e.g., absorption or PL), it is not inherently clear if a single, broad linewidth emitter is observed (top-right panel), or if an ensemble of narrow linewidth emitters that are shifted in their resonance energy with respect to each other (bottom-right panel) is observed. The difference in implication for the two scenarios is significant: Commonly, linewidths from PL measurements on TMDs are cited and assumed to be in the homogeneous limit of the upper-right panel of Fig. 3.2 and hence a measure of the homogeneous linewidth [15–18]. However, as illustrated from the bottom-right panel, the individual linewidths of the emitters, corresponding to the homogeneous linewidth, could be much narrower. As shown by Martin *et al.* [19], this is indeed the

case for TMDs. The distinction between homogeneous and inhomogeneous linewidths is important because the physics fundamentally differs: The homogeneous linewidth is a measurement of the true dephasing of the material, while the inhomogeneous linewidth is a measurement of the inhomogeneity of the ensemble. In gases, a common source of inhomogeneous broadening is Doppler broadening, caused by the random movement of the atoms and the associated Doppler shift [20]. In semiconductor nanostructures such as QDs and QWs, the inhomogeneous broadening is caused by an inhomogeneity in size. In TMDs, they are more commonly an indicator of strain and changes in thedielectric environment, as discussed in Ref. 19 and Chap. VII.

Another example of the shortcomings of linear spectroscopy is the inability to measure coupling between resonances. In its simplest way, coupling can be described as the excitation of one resonance at a particular frequency affecting the response of a different resonance at a different frequency. As explained in Chap. II, this coupling can be either coherent or incoherent and can have several physical causes, such as dipole-dipole interactions, wave function overlap, charge transfer, and energy transfer. However, linear spectroscopies have no means to measure this coupling, as shown in Fig. 3.3, because only one frequency axis is resolved. Moreover, no temporal dynamics that could hint towards coupling, e.g., through quantum beats or signal increase due

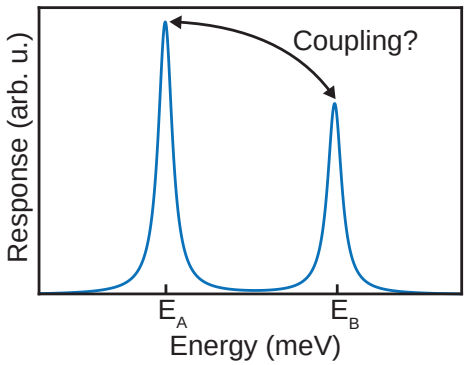

Figure 3.3: Linear spectrum for a system with two species. Resolving a single frequency axis, we cannot obtain any information about potential coupling between the two species. Figure adapted from [1].

to incoherent coupling processes, can be accessed in linear spectroscopy. In this case, the occurrence of two peaks just yields information about the presence of two resonances but not their coupling.

3.5 Nonlinear Spectroscopy in the Density Matrix Treatment

Nonlinear spectroscopies can overcome the limitations of linear spectroscopies with regard to deconvolving the sample response. A nonlinear response of the material can be found in regimes of high-intensity electric fields, such as high-intensity light fields, which will inevitably drive the electron discussed in the Lorentz oscillator model (Sec. 3.2.2) beyond the approximation of a linear restoring force, yielding a breakdown of the simple harmonic oscillator model.

In this case, Eq. 3.10 does not remain true, and P will not only depend linearly on the electric field E but can instead be expanded in powers of E,

$$P = \epsilon_0(\chi^{(1)} \cdot E + \chi^{(2)} \cdot E \cdot E + \chi^{(3)} \cdot E \cdot E \cdot E + \mathcal{O}(E^4)) \,, \tag{3.31}$$

with $\chi^{(n)}$ denoting the n-th order susceptibility of the material. While often omitted, the electric field is a vector; hence $\chi^{(n)}$ is a tensor. Because $\chi^{(n)}$ gets increasingly smaller with increasing n, higher electric field strengths are needed to have noticeable contributions from the higher orders.

How do we connect the perturbative expansion of the polarization with the density matrix approach? Recalling the Liouville-von Neumann Eq. 3.22, we can try to solve this differential equation by integration

$$\rho(t) = -\frac{i}{\hbar} \int_{-\infty}^{t} \mathrm{d}t' \left[H(t'), \rho(t)\right] \,. \tag{3.32}$$

and applying a perturbative expansion similar to Eq. 3.31 to the density matrix

$$\rho(t) = \rho^{(0)}(t) + \rho^{(1)}(t) + \rho^{(2)}(t) + \rho^{(3)}(t) + \mathcal{O}(\rho^{(4)(t)}) \,, \tag{3.33}$$

where $\rho^n(t)$ is the n-th order density matrix.

The system will start in the state $\rho^{(0)}$ and, after one interaction with the light field, will be in the state

$$\rho^{(1)}(t) = -\frac{i}{\hbar} \int_{-\infty}^{t} \mathrm{d}t' [H(t'), \rho^{(0)}(t)] \,. \tag{3.34}$$

By induction, it is then straightforward to show that the n-th order density matrix can be found as

$$\rho^{(n)}(t) = -\frac{i}{\hbar} \int_{-\infty}^{t} \mathrm{d}t' [H(t'), \rho^{(n-1)}(t)] \,. \tag{3.35}$$

When working in the interaction picture and rotating wave approximation [12], it can be shown that this can be expressed more conveniently as [21]

$$\rho_{ij}{}^{(n)}(t) = -\frac{i}{\hbar} \int_{-\infty}^{t} \mathrm{d}t' [V(t'), \rho^{(n-1)}(t')]_{ij} e^{-\Omega_{ij}(t-t')} \mathrm{d}t' \,, \tag{3.36}$$

with the complex resonance frequency

$$\Omega_{ij} = \omega_{ij} - i\gamma_{ij} \quad \text{with} \quad \omega_{ij} = \frac{E_i - E_j}{\hbar} \,. \tag{3.37}$$

Hence, each interaction with the electric field contained in the perturbation $V(t)$ increases the order of the density matrix by one. The so-called rotating-wave approximation employed to obtain Eq. 3.36 can be understood from the fact that the electric field of a single laser pulse can be written as $E(t) = 2A(t) \cdot \cos(\omega_0 t) = A(t) \cdot (e^{-i\omega_0 t} + e^{i\omega_0 t})$. Inserting this electric field into Eq. 3.36 yields a term rapidly

oscillating with t' and a term slowly oscillating with t' for the respective exponential functions. The rapidly oscillating term will average out upon integration, so only the slowly oscillating survives.

Since the work in this thesis employs third-order nonlinear spectroscopy, we will focus on the third-order nonlinear polarization in the following, which is given by

$$P^{(3)}(t) = \mathrm{Tr}(\mu\rho^{(3)}(t))\,, \tag{3.38}$$

according to Eq. 3.21. The motivation behind employing third-order nonlinear techniques is the information that can be gained by correlating absorption and emission energies of an underlying system or by observing the coupling between excited states, as further discussed in Sec. 3.6. Because each interaction of the light field with the material can only increment or decrement one side of the density matrix (e.g., $|0\rangle\langle 0| \rightarrow |0\rangle\langle 1|$ or $|0\rangle\langle 0| \rightarrow |1\rangle\langle 0|$), correlating the absorption polarization field with the emission polarization field inherently requires at least three interactions, i.e., a third-order nonlinear technique. Similarly, coupling between two excited states requires at least two interactions, and because these coherences are commonly non-radiative, a third interaction is needed to probe the system.

Separating the contributions from electric fields and material properties in Eq. 3.38 and using Eq. 3.36, we can write

$$P^{(3)}(t) = \int_0^\infty \mathrm{d}t_3 \int_0^\infty \mathrm{d}t_2 \int_0^\infty \mathrm{d}t_1 E(t-t_3)E(t-t_3-t_2)E(t-t_3-t_2-t_1)R(t_3,t_2,t_1)\,, \tag{3.39}$$

with R being the response function of the material [12]. Because the response function R is triple-convolved with the three electric field interactions, comparison with Eq. 3.31 shows that $\mathcal{F}\left(R(t_1,t_2,t_3)\right) = \epsilon_0\chi^{(3)}(\omega_1,\omega_2,\omega_3)$.

According to Eq. 3.39, the most general third-order time domain FWM experiment

consists of three laser pulses with variable inter-pulse delays τ, T, and t (which differs from the generic time t used earlier), as illustrated in Fig. 3.4.

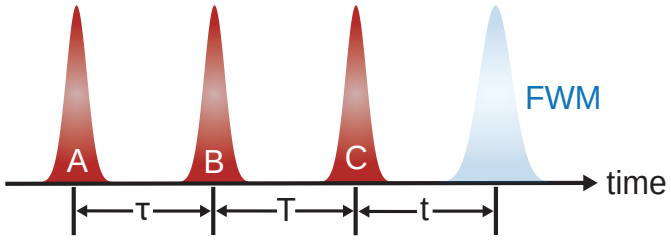

Figure 3.4: Schematic of the three laser pulses with variable time delays to generate a FWM signal in the time domain. In the case of strong inhomogeneity, the FWM is emitted after $t = \tau$, as shown here.

In general, the electric field at the generic time (not time delay) $\tilde{t}$ can be written as

$$\begin{aligned} E(\tilde{t}) &= 2E_1(\tilde{t}) \cdot \cos(\omega_0 \tilde{t}) + 2E_2(\tilde{t}) \cdot \cos(\omega_0 \tilde{t}) + 2E_3(\tilde{t}) \cdot \cos(\omega_0 \tilde{t}) \\ &= E_1(\tilde{t}) \cdot (e^{-i\omega_0 \tilde{t}} + e^{i\omega_0 \tilde{t}}) + E_2(\tilde{t}) \cdot (e^{-i\omega_0 \tilde{t}} + e^{i\omega_0 \tilde{t}}) \\ &\quad + E_3(\tilde{t}) \cdot (e^{-i\omega_0 \tilde{t}} + e^{i\omega_0 \tilde{t}}) \,, \end{aligned} \tag{3.40}$$

with the pulse envelopes $E_{1,2,3}(\tilde{t})$ and carrier frequency ω_0. Eq. 3.39 can be solved analytically in some instances [21]. However, the most general solution can be obtained by numerically solving the OBEs (Eq. 3.30). To get a general understanding of the spectral response for a given sample system, it is often assumed that the excitation pulses are short compared with any time scale of the sample system, in which case we can assume δ-pulses for the electric fields E, such that Eq. 3.40 simplifies to

$$E(\tilde{t}) = E_A \delta(\tilde{t}) + E_B \delta(\tilde{t} - \tau) + E_C \delta(\tilde{t} - \tau - T) \,. \tag{3.41}$$

In this approximation, called the semi-impulsive limit, we obtain for Eq. 3.39

$$P^{(3)}(t) = R(t, T, \tau) \,, \tag{3.42}$$

with the time delays τ, T, and t from Fig. 3.4. Hence, by employing three short pulses in the temporal domain, we get complete access to the third-order optical response of the sample. The third-order response of the sample, even in the case of δ-pulses, and assuming proper time-ordering of these pulses consists of many terms. Here we focus on a single term to understand the intuition behind the sample response and how each light-matter interaction alters the state of the density matrix.

We assume a simple two-level system with $\omega_{01} = \frac{E_1 - E_0}{\hbar}$ and assume the initial density matrix to be in the ground state

$$\rho_0 = |0\rangle \langle 0| = \begin{pmatrix} 1 & 0 \\ 0 & 0 \end{pmatrix} . \tag{3.43}$$

Using Eq. 3.36 with the perturbation from Eq. 3.24 and the initial state from Eq. 3.43, we then obtain the density matrix after the first interaction

$$\rho^{(1)}(\tau_1) = \begin{pmatrix} 0 & e^{i\omega_{01}(\tau_1 - t_0)}\mu_{01} \\ 0 & 0 \end{pmatrix} , \tag{3.44}$$

with the absolute time τ_1 (see Fig. 3.5). After the first interaction with a laser pulse, the ground state population (an on-diagonal element) is converted into a coherence (an off-diagonal matrix element). It is important to note that only a fraction of the ground state population gets converted into a coherence, and most of the system remains in the ground state. However, the signal isolation techniques presented in Sec. 4.2.2 ensure that only the contributions that interacted exactly once with each pulse are filtered out.

Similarly, the second and third interactions yield the density matrices

$$\rho^{(2)}(\tau_2) = \begin{pmatrix} 0 & 0 \\ 0 & \mu_{01} e^{i\omega_{01}(\tau_2-\tau_1)} \mu_{01} \end{pmatrix}$$
$$\rho^{(3)}(\tau_3) = \begin{pmatrix} 0 & 0 \\ \mu_{01} e^{i\omega_{01}(\tau_3-t_0)} \mu_{01} e^{i\omega_{01}(\tau_2-\tau_1)} \mu_{01} & 0 \end{pmatrix}, \tag{3.45}$$

with the absolute times τ_1, τ_2, and τ_3, shown in Fig. 3.5. The second interaction thus converts the coherence of $\rho^{(1)}$ into an excited state population. Subsequently, the third interaction converts this excited state population back into a coherence.

Lastly, the fourth interaction ($\mu_I(t)$) is the coherence relaxing into a ground state population by emitting a light field:

$$\mu_I(t)\rho^{(3)}(\tau_3) = \begin{pmatrix} \mu_{01} e^{i\omega_{01}(t-\tau_3)} \mu_{01} e^{i\omega_{01}(\tau_2-\tau_1)} \mu_{01}\mu_{01} & 0 \\ 0 & 0 \end{pmatrix}. \tag{3.46}$$

The polarization, according to Eq. 3.38, can then be obtained as

$$P^{(3)}(t) = \mu_{01}^4 e^{i\omega_{01}(\tau_2-\tau_1)} e^{-\frac{\tau_2-\tau_1}{T_2}} e^{-\frac{\tau_3-\tau_2}{T_1}} e^{i\omega_{01}(t-\tau_3)} e^{-\frac{t-\tau_3}{T_1}}, \tag{3.47}$$

where we have phenomenologically included dephasing with the dephasing time $T_2 = 1/\gamma_{10} = 1/\gamma_{01}$ and population decay, with the decay time $T_1 = 1/\gamma_{11}$, as defined in Sec. 3.3.1.

An easier way to visualize these interactions is shown in Fig. 3.5. This diagram, called a double-sided Feynman diagram, shows the evolution of the system's density matrix from the ground state to a coherence, to an excited state population, and back to a coherence. The color coding shows the corresponding terms from Eq. 3.47. Each pulse interaction is represented by an arrow, with a (rightward) leftward pointing arrow for a (non-)conjugate interaction.

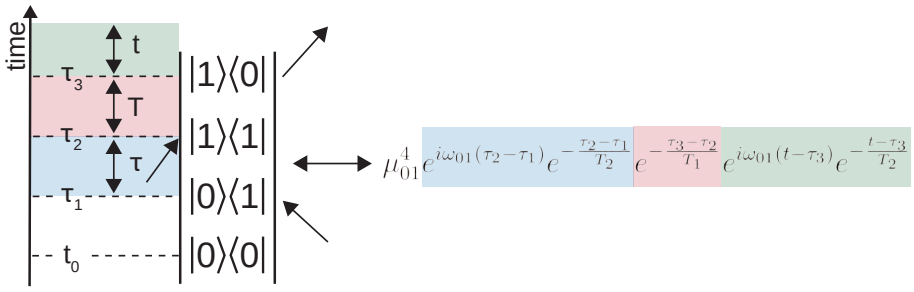

Figure 3.5: Example of a double-sided Feynman diagram for a simple two-level system (left). The expression on the right is the material's optical response function and is related to the Feynman diagram by color coding. Dephasing and population decay have been phenomenologically introduced. Figure adapted from [22].

3.5.1 Modalities of Multidimensional Coherent Spectroscopy

The single quantum pathway highlighted in Fig. 3.5 is not the only third-order pathway that can be obtained with three pulses. E.g., the second interaction could convert the system into a ground state population instead of an excited state population. Moreover, third-order nonlinear pathways can include several interactions with the same pulse, etc. Filtering out the contributions of interest requires some sort of signal isolation - e.g., through wave vector selection, which can be best understood by the following consideration: As an extension of Eq. 3.40, the electrical field of each pulse can be written as

$$E(t) = E_0(t)(e^{i\omega_0 t - i\mathbf{kr}} + e^{-i\omega_0 t + i\mathbf{kr}})\,. \tag{3.48}$$

The two exponentials are complex conjugates of each other. To obtain a spectrally degenerate FWM signal, one of the three excitations needs to be "conjugate", i.e., involve the second exponential, while the other two interactions involve the first exponential. The signal will be emitted at a wave vector $\mathbf{k}$ that is a combination of the three wave vectors $\mathbf{k}_{1,2,3}$ of the excitation pulses, e.g., $\mathbf{k} = -\mathbf{k_1} + \mathbf{k_2} + \mathbf{k_3}$. The requirement of one conjugate interaction then leads to the four pulse schemes highlighted in Fig. 3.6. The desired signal can then be obtained in a specific spatial direction given

by **k**. As discussed in Sec. 4.2.2, there are other schemes to filter out the signal that do not rely on different wave vectors.

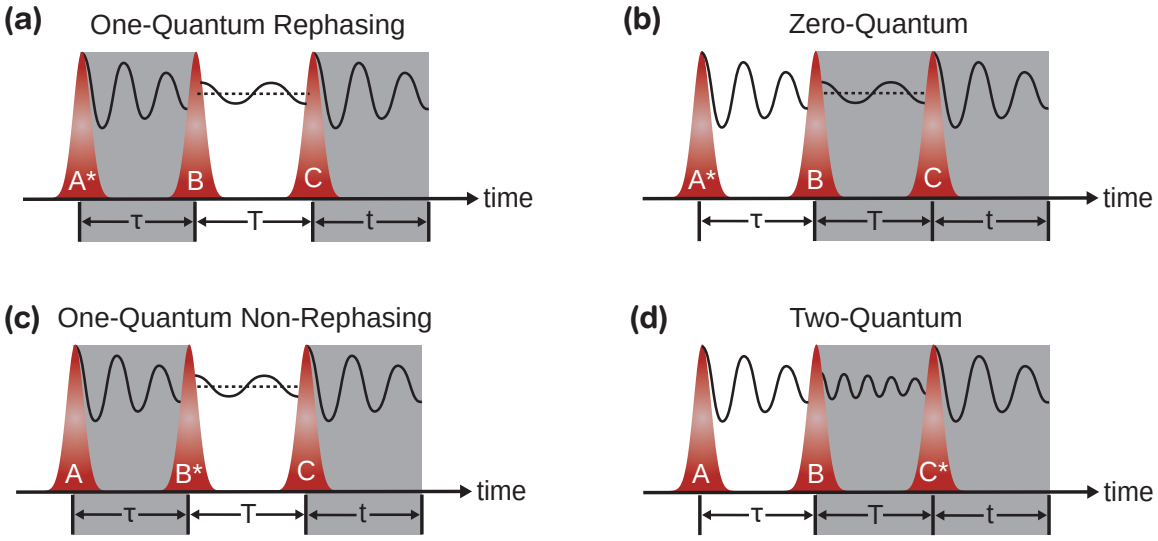

Figure 3.6: Pulse time-ordering sequences for different MDCS modalities. In the rephasing one-quantum and rephasing zero-quantum modality, the first pulse interaction is conjugate, but different time delays are scanned. For the non-rephasing one quantum modality, the second interaction is conjugate. For the two-quantum modality, the third interaction is conjugate. The different modalities give access to different dynamics and physical processes within the sample. Figure adapted from Ref. 14.

For a rephasing one-quantum rephasing scan, shown in Fig. 3.6(a), the first interaction is conjugate (signaled by a * on the pulse name), while the first (τ) and third (t) time delays are scanned. Upon Fourier transform, scanning the τ-delay gives access to the absorption energy as elucidated in Sec. 3.6 while scanning the t-delay gives access to the emission energy. For a rephasing zero-quantum scan (Fig. 3.6(b)), the pulse ordering is the same, but the second (T) and third (t) time delays are scanned. In this case, mixing between excited states that can occur during T can be energy-resolved. For a non-rephasing one-quantum scan (Fig. 3.6(c)), the second interaction is conjugate while the first (τ) and third (t) time delays are scanned. Lastly, for a two-quantum scan (Fig. 3.6(d)), the third interaction is conjugate, and the second (T) and third (t) time delays are scanned. This scheme resolves the energy of the two-quantum coherence that the system is in during T.

As further discussed in the following section, each scan modality gives a different insight into the sample system by accessing different quantum pathways. The rephasing one-quantum scheme is often the "default" scheme, as it provides access to a myriad of information, including the homogeneous and inhomogeneous linewidths, as well as coupling between resonances. The non-rephasing one-quantum scan is sometimes used to help separate and quantify overlapping quantum pathways between rephasing and non-rephasing scans. A zero-quantum scan is helpful for studying Raman-like non-radiative coherent coupling contributions that oscillate during the second time delay. Lastly, the two-quantum scheme gives insights into many-body effects, including EID [23] and excitation-induced shift (EIS) [24].

3.6 Multidimensional Coherent Spectra

3.6.1 One-quantum Spectra

While our scheme of MDCS is implemented in the temporal domain, the acquired complex time domain signal can be translated into spectra via Fourier transform. In the following, we will discuss the two types of MDCS spectra presented in this thesis, namely one-quantum and zero-quantum spectra, and highlight their capabilities and how to interpret them.

Fig. 3.7 illustrates how (one-quantum rephasing) MDCS overcomes the shortcomings of linear spectroscopies discussed in Sec. 3.4 by resolving and correlating absorption and emission energies. In the case of an ensemble of emitters with a two-level system energetic structure and identical resonance energies (Fig. 3.7(a)), the MDCS spectrum shows a singular peak at an absorption and emission energy E_1. In this scenario, the information obtained from a linear emission spectrum is the same as from the MDCS spectrum. It is important to note here that the absorption energy in the MDCS spectra has a negative sign because of the opposite evolution of the

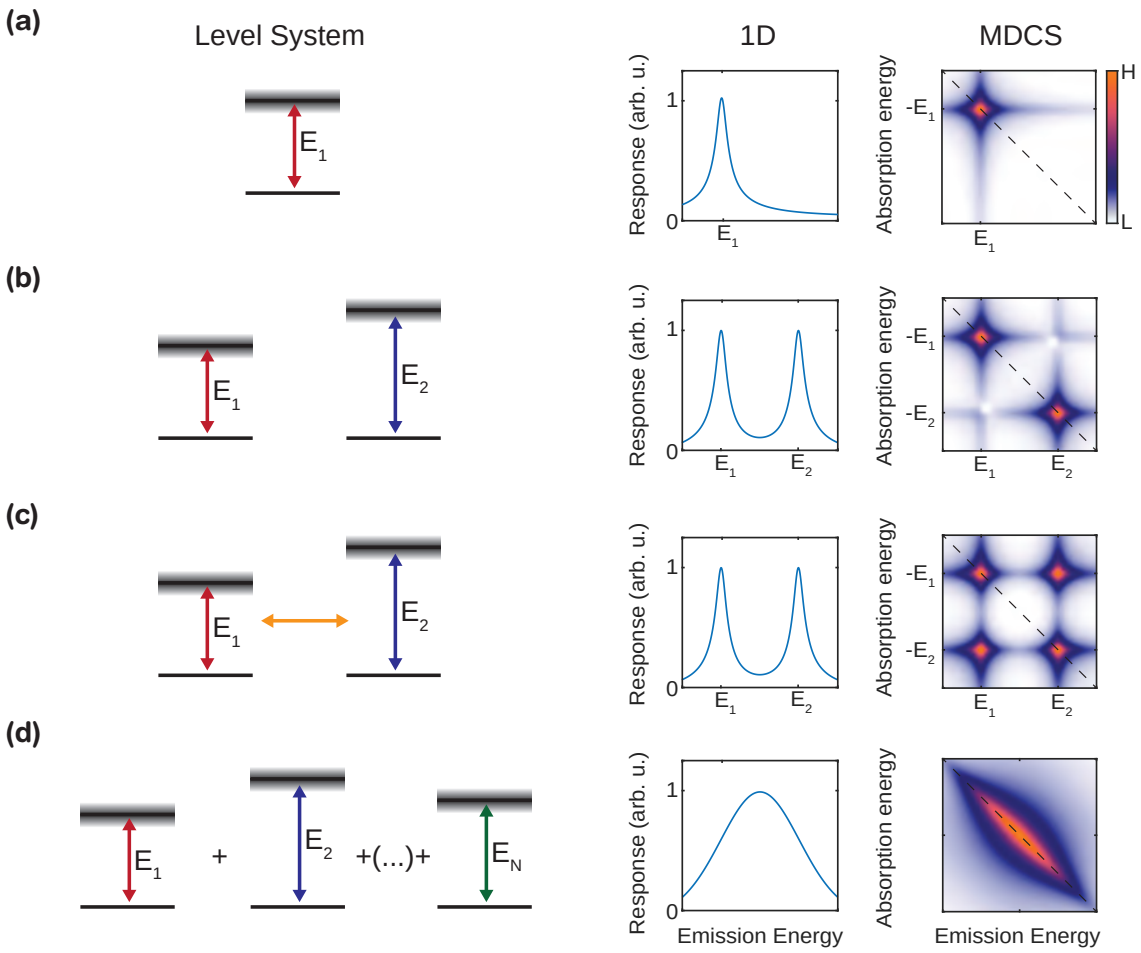

Figure 3.7: Level systems and corresponding one-dimensional (1D) and MDCS spectra. **(a)** A single two-level system with a non-zero homogeneous linewidth. **(b)** Two uncoupled two-level systems. **(c)** Two coupled two-level systems. **(d)** N uncoupled two-level systems with varying resonance energies. Figure adapted from Ref. 1.

signal in time along τ than t, as evident from Eq. 3.46. In Fig. 3.7(b), the spectra of a set of two uncoupled emitters with a two-level energy system are plotted. Because the two emitters absorb and emit at the same energy, respectively, they line up along the diagonal (dashed line), where |Absorption energy| = Emission energy. In this scenario, the information obtained from a linear emission spectrum appears to be the same as from the MDCS spectrum. However, 1D spectroscopy cannot distinguish between the case of two uncoupled two-level systems in Fig. 3.7(b) and the case of two coupled two-level systems in Fig. 3.7(c). The 1D spectrum in Fig. 3.7(c) is iden-

tical to the uncoupled scenario in Fig. 3.7(b). However, the MDCS spectrum clearly shows two coupling peaks off the diagonal. These coupling peaks are identified by absorption at one resonance energy (e.g., $-E_1$) and emission at the energy of the other resonance (e.g., E_2). A linear measurement obscures this crucial piece of information. Moreover, even a nonlinear but one-dimensional measurement cannot retrieve the information about coupling: Projecting onto the emission energy axis, which corresponds to a nonlinear, but "one-dimensional" measurement, still only shows two peaks. Another dimension, e.g., absorption energy or a scan of the T delay, which can reveal signatures of coupling, is thus necessary.

Lastly, Fig. 3.7(d) shows the linear and MDCS spectrum for an ensemble of uncoupled two-level system emitters with varying resonance energies. Because the emitters absorb and emit at the same energy, they line up along the diagonal. Hence, the linewidth along the diagonal will reflect the inhomogeneous distribution of resonance energies and is indicative of the inhomogeneous broadening (though mathematically speaking, this is not strictly true, as discussed in Sec. 3.7). Meanwhile, the narrower linewidth of the single emitters, found across the diagonal, is unaffected and extracting the linewidth across the diagonal thus enables measurement of the homogeneous linewidth of the single emitters. In this case, the linear spectrum only shows a broader linewidth, which is not indicative that this linewidth broadening is associated with broader homogeneous linewidths of the single emitters or an increased inhomogeneity of the sample system.

3.6.2 Zero-Quantum Spectra

The level scheme shown in Fig. 3.7(c) can show the existence of coupling between two resonances but does not yield complete information about the nature of the coupling. The easiest way to distinguish between coherent and incoherent coupling is to vary the T-delay between the second and third pulse. Hence, the zero-quantum

scheme from Fig. 3.6(b) is uniquely suited to study the nature of coupling. The (simplified) level system for two coherently coupled resonances is shown in Fig. 3.8(b). In this simplified picture of Fig. 2.10, it is assumed that the uppermost level is significantly energetically detuned because of the coupling, such that it does not noticeably contribute to the MDCS spectrum in the selected spectral range.

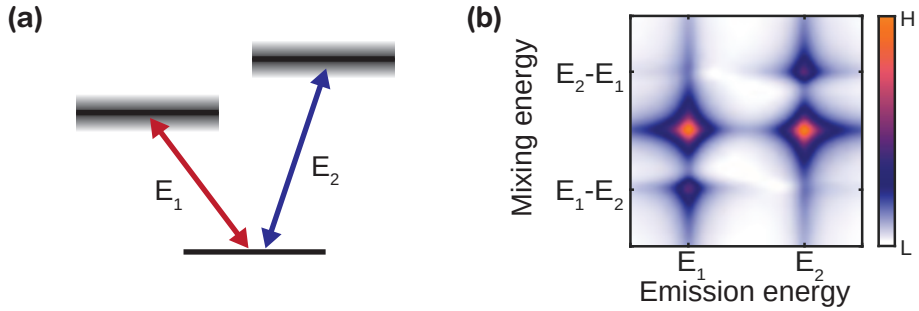

Figure 3.8: **(a)** V-Level system, which represents two coupled two-level systems. **(b)** Zero-quantum spectrum of a coherently coupled two-level system, showing the coherent coupling contribution at positive and negative mixing energies.

For the corresponding zero-Quantum spectrum in Fig. 3.8(b), the T-delay between the second and third pulse is scanned instead of the τ delay between the first and second pulse. The zero-quantum spectrum is thus similar, but not identical, to spectrally-resolved pump-probe spectroscopy with an additional Fourier transform along the pump-probe delay T, which yields the mixing energy axis. The term "mixing" energy stems from the useful application of zero-quantum MDCS spectra for systems that are in a non-radiative, Raman-like coherence during T. The crucial difference between pump-probe (or transient absorption) spectroscopy and zero-quantum spectroscopy is the fact that zero-quantum spectroscopy is phase-resolved. The implications can be understood from Fig. 3.8(b), which shows two strong peaks at the two emission energies $E_{1,2}$, and zero mixing energy - these are all "population" contributions from both on- and off-diagonal peaks that either stay constant, decay, or increase in amplitude during T. The oscillating mixing contributions from coherent coupling, however, show up at positive and negative mixing energies, respectively, with the lower energy

emission displaying a negative mixing energy. The reason for the sign shift between the E_1 emitting and the E_2 emitting mixing lies in the sign evolution during T, which can be understood by writing out the Feynman diagrams for a V-Level system [25]. In spectrally resolved TAS, the sign of the oscillations cannot be resolved. The sign of the oscillation can be important for understanding the system dynamics, though, with Liu et al. [13] showing that the deviations from the "expected" two peaks at positive and negative mixing energies can be an indication of non-Markovian exciton-phonon interactions. While this thesis focuses on the coherent coupling that leads to the occurrence of mixing peaks in zero-quantum spectra, other effects that lead to an oscillation along T, such as LO-phonon coupling [13] and Terahertz inter-triplet coherences in Cesium lead-halide perovskite nanocrystals [26] can also be discerned with zero-quantum spectroscopy.

3.7 Fitting Multidimensional Coherent Spectra

To extract the homogeneous and inhomogeneous linewidths from one-quantum MDCS spectra, we need to fit the lineshape to models that consider both the homogeneous and inhomogeneous contributions to the lineshape. A rule of thumb says that the linewidth across the diagonal of an MDCS spectrum gives the inhomogeneous linewidth, while the linewidth in the cross-diagonal direction can be associated with homogeneous broadening. However, Siemens *et al.* [27] show that this is not strictly the case, and the two linewidths are coupled along the diagonal and cross-diagonal directions of the spectrum. They assume δ-function pulses in the semi-impulsive limit in their derivation, which is reasonable given that finite pulse (i.e., limited bandwidth) effects on linewidths are either negligible or can be considered by normalizing with the laser spectrum, as shown in Ref. 21. The FWM signal in the time-domain for an ensemble of uncoupled emitters with varying resonance energy, assuming δ-function pulses, a Gaussian inhomogeneous distribution, and the Markovian approximation

can then be written as

$$R(t,\tau) = R_0 e^{-\gamma(t+\tau)+i\omega_0(t-\tau)+\sigma^2(t-\tau)^2/2}\Theta(t)\Theta(\tau)\,, \tag{3.49}$$

with the homogeneous linewidth γ, the inhomogeneous linewidth σ, and the two Heaviside functions (Θ) that ensure causality, such that the signal only arises after the pulses have arrived, i.e., for positive times [27]. Eq. 3.49 looks very similar to Eq. 3.47, with the distinction of the inhomogeneous broadening included in Eq. 3.49. The reasoning behind the Gaussian form of the inhomogeneous broadening is that the inhomogeneous distribution of resonance energies is modeled by convolving the time domain signal with a Gaussian distribution G for the resonance energy,

$$R(t,T,\tau) \rightarrow \int \mathrm{d}\omega_{01} G\left(\omega_{01} - {\omega_{01}}^{(0)}\right) R(t,T,\tau)\,, \tag{3.50}$$

with the center resonance frequency ${\omega_{01}}^{(0)}$ [12].

An exemplary two-dimensional time-domain signal for a homogeneous linewidth of $\gamma = 1\,\mathrm{meV}$ and an inhomogeneous linewidth of $\sigma = 3.75\,\mathrm{meV}$ is plotted in Fig. 3.9(a).

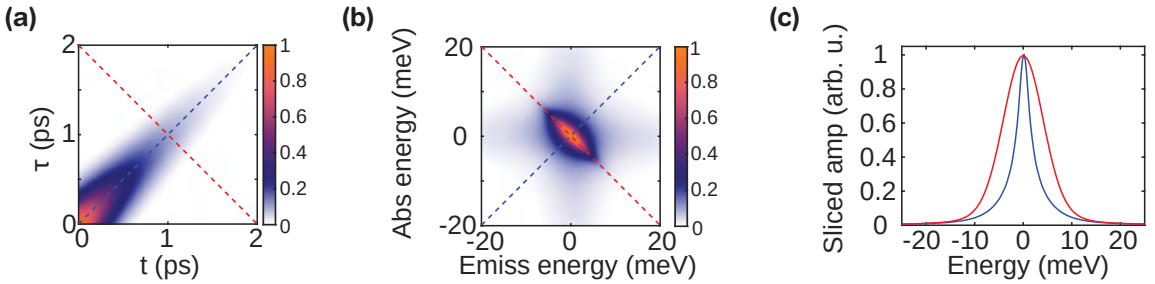

Figure 3.9: **(a)** Time trace for an MDCS measurement, showing the characteristic photon echo. **(b)** MDCS spectrum obtained by Fourier transform of the time-trace in (a). **(c)** Slices in the frequency domain along the diagonal (red) and cross-diagonal (blue) drawn in (b).

A more convenient and intuitive coordinate system in the two-dimensional time-domain can be obtained by introducing a new, rotated coordinate system with the photon echo direction $t' = t + \tau$ (blue dashed line in Fig. 3.9(a)) and the anti-echo di-

rection $\tau' = t - \tau$ (red dashed line in Fig. 3.9(a)). Rewriting Eq. 3.49 in this coordinate system, we obtain

$$R(t', \tau') = R_0 e^{-(\sqrt{2}\gamma t' + i\sqrt{2}\omega_0 \tau' + \sigma^2 \tau'^2)} \Theta(t' - \tau') \Theta(t' + \tau') \,, \tag{3.51}$$

where the signal consists of a homogeneous decay along the photon-echo direction and a Gaussian multiplied by an oscillation along the anti-echo direction:

As discussed in Ref. 28, this form allows us to obtain the homogeneous and inhomogeneous linewidths in the temporal domain by taking slices along the photon-echo direction (t')

$$R(t', \tau' = 0) = e^{-\sqrt{2}\gamma t'} \Theta^2(t') \,, \tag{3.52}$$

and across the photon-echo direction (τ')

$$R(t' = t_0, \tau') = e^{-\sqrt{2}\gamma t_0' + i\sqrt{2}\omega_0 \tau' + \sigma^2 \tau'^2} \Theta(t_0' - \tau') \Theta(t_0' + \tau') \,, \tag{3.53}$$

Alternatively, one can fit in the frequency domain by Fourier transforming the complex time signal from Eq. 3.51 and Fig. 3.9(a), obtaining the MDCS spectrum plotted in Fig. 3.9(b). In this case, the projection along the diagonal (red dashed line in Fig. 3.9(b)) can be expressed as

$$R_{\mathrm{Proj},\omega_0}(\omega_{\tau'}) = \frac{2\pi}{\gamma} \mathrm{Voigt}(\gamma, \sigma, \omega_{\tau'}) \,, \tag{3.54}$$

where we use the Voigt profile, which is defined as the convolution of a Gaussian with a Lorentzian and can be obtained through the real part of the Faddeeva function:

$$\mathrm{Voigt}(\gamma, \sigma, \omega_{\tau'}) = \frac{1}{\sigma\sqrt{2\pi}} \mathrm{Re}\left[\mathrm{erfz}\left(\frac{\omega_{\tau'} - \omega_0 + i\gamma}{\sqrt{2}\sigma} \right) \right] \,, \tag{3.55}$$

with the complex complementary error function erfz. The projection across the diag-

onal (blue dashed line in Fig. 3.9(b)) can be expressed as

$$R_{\mathrm{Proj},\omega_0}(\omega_{t'}) = \frac{e^{\frac{(\gamma - i\omega_{t'})^2}{2\sigma^2}} \mathrm{Erfc}\left(\frac{\gamma - i\omega_{t'}}{\sqrt{2}\sigma}\right)}{\sigma(\gamma - i\omega_{t'})}\,, \tag{3.56}$$

with the complementary error function erfc. Eqs. 3.54 and 3.56 are valid for arbitrary inhomogeneity and yield robust quantitative retrieval of γ and σ in most cases.

An even more general solution

$$\begin{aligned} R_{SI}(\omega_t, \omega_\tau) = \frac{1}{2\sigma(2\gamma - i(\omega_t + \omega_\tau))} \Bigg(& e^{\frac{(\gamma - i(\omega_t - \omega_0))^2}{2\sigma^2}} \mathrm{Erfc}\left[\frac{\gamma - i(\omega_t - \omega_0)}{\sqrt{2}\sigma}\right] \\ & + e^{\frac{(\gamma - i(\omega_\tau + \omega_0))^2}{2\sigma^2}} \mathrm{Erfc}\left[\frac{\gamma - i(\omega_t + \omega_0)}{\sqrt{2}\sigma}\right] \Bigg)\,, \end{aligned} \tag{3.57}$$

that considers the entire MDCS spectrum has been derived by Bell *et al.* [29]. Dr. Eric Martin has employed this scheme in his thesis [30] to further derive a fit function with an inhomogeneous dephasing rate across the inhomogeneous distribution to account for spectral diffusion. Moreover, Namuduri *et al.* [31] have employed this scheme to train a neural network to fit linewidths with arbitrary inhomogeneity.

In this thesis, we employ linewidth fits together with imaging. Because the underlying sample systems, monolayer $MoSe_2$ and WSe_2, and a $MoSe_2/WSe_2$ heterostructure are well-described within the constraints and limitations of the model in Ref. 27 and Eqs. 3.54 and 3.56, we employ the slice-fitting procedure here. Furthermore, this leaves us with reasonable data evaluation times since we combine linewidth fitting with imaging and have to perform thousands of linewidth fits across the sample.

3.8 Conclusions

In this chapter, we have introduced the techniques employed to obtain the experimental results in this thesis from a theoretical perspective. We first introduced linear spectroscopy and absorption from a Lorentz oscillator model approach. We then intro-

duced how to combine the density matrix approach and spectroscopy before pointing out the limitations and shortcomings of linear spectroscopy. The limitations and shortcomings led to the discussion of nonlinear spectroscopy, specifically third-order nonlinear spectroscopy and MDCS in the density matrix framework. Furthermore, we introduced different MDCS modalities and a guide on how to interpret the spectra, including how to extract linewidths.

To acquire MDCS spectra, however, we are still missing a crucial piece: The experimental implementation. In the next chapter, we are thus going to explore how to acquire MDCS spectra with our Coherent Imaging Nonlinear Multifunctional Spectrometer (CINeMaS) setup and further introduce laser-scanning imaging to combine the spectroscopic might of MDCS with microscopy.

References

[1] Matthew W. Day. "Characterizing the Nonlinear Optical Response of Silicon Vacancy Centers in Diamond and Showcasing the Next Generation of Optical Frequency Combs". PhD thesis. University of Michigan, Ann Arbor, 2021.

[2] Hearnshaw John B. *The Analysis of Starlight: Two Centuries of Astronomical Spectroscopy*. 2nd ed. Cambridge University Press, 2014. ISBN: 9781107031746.

[3] Frank. Pristera, Michael. Halik, Alexander. Castelli, and Walter. Fredericks. "Analysis of Explosives Using Infrared Spectroscopy". In: *Analytical Chemistry* 32.4 (1960), pp. 495–508. DOI: 10.1021/ac60160a013.

[4] Wei Zhang, Yue Tang, Anran Shi, Lirong Bao, Yun Shen, Ruiqi Shen, and Yinghua Ye. "Recent Developments in Spectroscopic Techniques for the Detection of Explosives". In: *Materials* 11.8 (2018). ISSN: 1996-1944. DOI: 10.3390/ma11081364.

[5] Kai-Chih Huang, Jeremy McCall, Pu Wang, Chien-Sheng Liao, Gregory Eakins, Ji-Xin Cheng, and Chen Yang. "High-Speed Spectroscopic Transient Absorption Imaging of Defects in Graphene". In: *Nano Letters* 18.2 (2018). PMID: 29342361, pp. 1489–1497. DOI: 10.1021/acs.nanolett.7b05283.

[6] Tomasz Jakubczyk, Karol Nogajewski, Maciej R Molas, Miroslav Bartos, Wolfgang Langbein, Marek Potemski, and Jacek Kasprzak. "Impact of environment on dynamics of exciton complexes in a WS_2 monolayer". In: *2D Materials* 5.3 (Apr. 2018), p. 031007. DOI: 10.1088/2053-1583/aabc1c.

[7] Torben L. Purz, Blake T. Hipsley, Eric W. Martin, Ronald Ulbricht, and Steven T. Cundiff. "Rapid multiplex ultrafast nonlinear microscopy for material characterization". In: *Opt. Express* 30.25 (Dec. 2022), pp. 45008–45019. DOI: 10.1364/OE.472054.

[8] Ralph E. Sturgeon. "Spectrochemical analysis : James D. Ingle, Jr. and Stanley R. Crouch. Prentice Hall, Englewood Cliffs, New Jersey, 1988, xv+590 pp., $52.00, ISBN 0-13-826876-2." In: *Spectrochimica Acta Part A: Molecular and Biomolecular Spectroscopy* 44 (1988), pp. 1229–1230.

[9] Meir Nitzan, Ayal Romem, and Robert Koppel. "Pulse oximetry: fundamentals and technology update". In: *Med Devices (Auckl)* 7 (July 2014), pp. 231–239.

[10] A F J Levi. "The Lorentz oscillator model". In: *Essential Classical Mechanics for Device Physics*. 2053-2571. Morgan & Claypool Publishers, 2016, 5-1 to 5–21. ISBN: 978-1-6817-4413-1. DOI: 10.1088/978-1-6817-4413-1ch5.

[11] Shaul Mukamel. *Principles of nonlinear optical spectroscopy*. English. Oxford series in optical and imaging sciences. New York: Oxford University Press, 1995. ISBN: 0195092783.

[12] Peter Hamm and Martin Zanni. *Concepts and Methods of 2D Infrared Spectroscopy*. Cambridge University Press, 2011. DOI: 10.1017/CBO9780511675935.

[13] A. Liu, D. B. Almeida, W. K. Bae, L. A. Padilha, and S. T. Cundiff. "Non-Markovian Exciton-Phonon Interactions in Core-Shell Colloidal Quantum Dots at Femtosecond Timescales". In: *Phys. Rev. Lett.* 123 (5 Aug. 2019), p. 057403. DOI: 10.1103/PhysRevLett.123.057403.

[14] Galan Moody and Steven T. Cundiff. "Advances in multi-dimensional coherent spectroscopy of semiconductor nanostructures". In: *Advances in Physics: X* 2.3 (2017). PMID: 28894306, pp. 641–674. DOI: 10.1080/23746149.2017.1346482.

[15] F. Cadiz, E. Courtade, C. Robert, G. Wang, Y. Shen, H. Cai, T. Taniguchi, K. Watanabe, H. Carrere, D. Lagarde, M. Manca, T. Amand, P. Renucci, S. Tongay, X. Marie, and B. Urbaszek. "Excitonic Linewidth Approaching the Homogeneous Limit in MoS_2-Based van der Waals Heterostructures". In: *Phys. Rev. X* 7 (2 May 2017), p. 021026. DOI: 10.1103/PhysRevX.7.021026.

[16] Obafunso A Ajayi, Jenny V Ardelean, Gabriella D Shepard, Jue Wang, Abhinandan Antony, Takeshi Taniguchi, Kenji Watanabe, Tony F Heinz, Stefan Strauf, X-Y Zhu, and James C Hone. "Approaching the intrinsic photoluminescence linewidth in transition metal dichalcogenide monolayers". In: *2D Materials* 4.3 (July 2017), p. 031011. DOI: 10.1088/2053-1583/aa6aa1.

[17] Jakob Wierzbowski, Julian Klein, Florian Sigger, Christian Straubinger, Malte Kremser, Takashi Taniguchi, Kenji Watanabe, Ursula Wurstbauer, Alexander W. Holleitner, Michael Kaniber, Kai Müller, and Jonathan J. Finley. "Direct exciton emission from atomically thin transition metal dichalcogenide heterostructures near the lifetime limit". In: *Scientific Reports* 7.1 (Sept. 2017), p. 12383. ISSN: 2045-2322. DOI: 10.1038/s41598-017-09739-4.

[18] Garima Gupta and Kausik Majumdar. "Fundamental exciton linewidth broadening in monolayer transition metal dichalcogenides". In: *Phys. Rev. B* 99 (8 Feb. 2019), p. 085412. DOI: 10.1103/PhysRevB.99.085412.

[19] Eric W. Martin, Jason Horng, Hanna G. Ruth, Eunice Paik, Michael-Henr Wentzel, Hui Deng, and Steven T. Cundiff. "Encapsulation Narrows and Preserves the Excitonic Homogeneous Linewidth of Exfoliated Monolayer $MoSe_2$". In: *Phys. Rev. Applied* 14 (2 Aug. 2020), p. 021002. DOI: 10.1103/PhysRevApplied.14.021002.

[20] Luigi Lugiato, Franco Prati, and Massimo Brambilla. "Inhomogeneous broadening". In: *Nonlinear Optical Systems*. Cambridge University Press, 2015, pp. 170–176. DOI: 10.1017/CBO9781107477254.017.

[21] Christopher L. Smallwood, Travis M. Autry, and Steven T. Cundiff. "Analytical solutions to the finite-pulse Bloch model for multidimensional coherent spectroscopy". In: *J. Opt. Soc. Am. B* 34.2 (Feb. 2017), pp. 419–429. DOI: 10.1364/JOSAB.34.000419.

[22] Albert Liu. "Electronic and Vibrational Properties of Colloidal Nanocrystals". PhD thesis. University of Michigan, Ann Arbor, 2019.

[23] Mackillo Kira and Stephan W. Koch. *Semiconductor Quantum Optics*. Cambridge University Press, 2011. DOI: 10.1017/CBO9781139016926.

[24] Justin M. Shacklette and Steven T. Cundiff. "Role of excitation-induced shift in the coherent optical response of semiconductors". In: *Phys. Rev. B* 66 (4 July 2002), p. 045309. DOI: 10.1103/PhysRevB.66.045309.

[25] Christopher L. Smallwood and Steven T. Cundiff. "Multidimensional Coherent Spectroscopy of Semiconductors". In: *Laser & Photonics Reviews* 12.12 (2018), p. 1800171. DOI: https://doi.org/10.1002/lpor.201800171.

[26] Albert Liu, Diogo B. Almeida, Luiz G. Bonato, Gabriel Nagamine, Luiz F. Zagonel, Ana F. Nogueira, Lazaro A. Padilha, and S. T. Cundiff. "Multidimensional coherent spectroscopy reveals triplet state coherences in cesium lead-halide perovskite nanocrystals". In: *Science Advances* 7.1 (2021), eabb3594. DOI: 10.1126/sciadv.abb3594.

[27] Mark E. Siemens, Galan Moody, Hebin Li, Alan D. Bristow, and Steven T. Cundiff. "Resonance lineshapes in two-dimensional Fourier transform spectroscopy". In: *Opt. Express* 18.17 (Aug. 2010), pp. 17699–17708. DOI: 10.1364/OE.18.017699.

[28] Geoffrey M. Diederich, Travis M. Autry, and Mark E. Siemens. "Diagonal slice four-wave mixing: natural separation of coherent broadening mechanisms". In: *Opt. Lett.* 43.24 (Dec. 2018), pp. 6061–6064. DOI: 10.1364/OL.43.006061.

[29] Joshua D. Bell, Rebecca Conrad, and Mark E. Siemens. "Analytical calculation of two-dimensional spectra". In: *Opt. Lett.* 40.7 (Apr. 2015), pp. 1157–1160. DOI: 10.1364/OL.40.001157.

[30] Eric W. Martin. “Coherent Spectroscopy at the Diffraction Limit”. PhD thesis. University of Michigan, Ann Arbor, 2018.

[31] Srikanth Namuduri, Michael Titze, Shekhar Bhansali, and Hebin Li. “Machine learning enabled lineshape analysis in optical two-dimensional coherent spectroscopy”. In: *J. Opt. Soc. Am. B* 37.6 (June 2020), pp. 1587–1591. DOI: 10.1364/JOSAB.385195.

CHAPTER IV

Experimental implementation of coherent nonlinear imaging spectroscopy

4.1 Introduction

After the theoretical discussion of nonlinear spectroscopy in Chap. III, we present the experimental implementation of MDCS in the CINeMaS setup in this chapter. MDCS becomes even more powerful when combined with imaging because it allows us to visualize the spatial variations of the spectroscopic and temporal quantities extracted with MDCS. Hence, we work towards introducing an imaging version of MDCS, referred to as MDCIS, as a "universal microscopy" technique in this chapter.

First, we focus on the spectroscopy aspect of the CINeMaS setup. We introduce passive phase stabilization and Fourier transform spectroscopy, a common way of implementing collinear MDCS [1, 2]. We also discuss experimental improvements specific to the CINeMaS setup, including the Michelson interferometer design, arbitrary reference, continuous scanning, and phase correction modalities, some of which were developed by Dr. Eric Martin and Dr. Chris Smallwood.

In the second part of this chapter, we present the integration of the spectroscopy setup with laser-scanning imaging. We introduce the design of the imaging apparatus of the CINeMaS setup, discuss its calibration, and discuss how to implement rapid

MDCIS with this setup. The focus on rapid MDCIS is motivated by setup stability limitations and the desire to achieve reasonable data acquisition times.

4.2 Experimental Implementation of Collinear Multidimensional Coherent Spectroscopy

We introduced the three-pulse scheme used to obtain FWM and the concept of phase-matching in Sec. 3.5. Historically, a box geometry with the three pulses A, B, and C impinging at different angles (different wave vectors $\mathbf{k_A}, \mathbf{k_B}$, and $\mathbf{k_C}$) has often been used [3]. In this geometry, illustrated in Fig. 4.1(a), the FWM signal is emitted in the signal direction $\mathbf{k_S} = -\mathbf{k_A} + \mathbf{k_B} + \mathbf{k_C}$. The different MDCS modalities discussed in Fig. 3.6 can then be achieved by changing the time ordering of the pulses. Fig. 4.1(a) assumes the time-ordering for a rephasing scan. The signal is subsequently heterodyne-detected with pulse D that propagates in the signal direction. In addition, extensive phase-cycling schemes have been developed and applied to reduce scattering contributions [4].

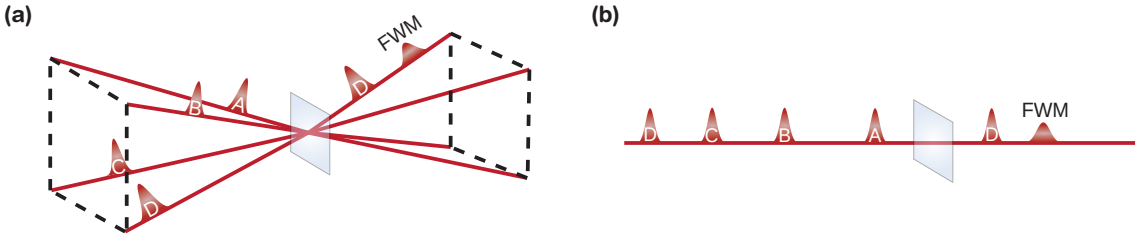

Figure 4.1: Pulse geometries for MDCS experiments. **(a)** Box geometry employing wave vector selection. **(b)** Collinear geometry employing frequency-tagging. Figure adapted from [5].

However, there are experimental limitations when employing this scheme, mainly the large spot sizes, which are fundamentally limited to 20-30 µm. For many state-of-the-art TMD samples, this is equal to or greater than the size of the samples [6–11]. Instead, to allow for diffraction-limited spot sizes on the order of 1 µm diameter or smaller, a collinear MDCS scheme, as illustrated in Fig. 4.1(b), is required. In

collinear MDCS, all pulses are spatially overlapped and propagate in the same direction. The collinear scheme allows MDCS to be combined with standard microscopy and diffraction-limited resolution.

4.2.1 Phase-Matching Scheme Using Acousto-Optic Modulators

[12]

Tekavec et al. [1] developed a scheme for collinear MDCS in 2007. Instead of using wave vector selection, a continuous phase-cycling scheme is implemented to filter the FWM signal by subsequent lock-in detection. More specifically, the four pulses are each tagged with a specific frequency by an acousto-optic modulator (AOM) in the tens of MHz range. This scheme is a continuation of the efforts by Hall *et al.* [12], who demonstrated heterodyne detection to separate the pump and probe signals in ultrafast (femtosecond) experiments, and Borri *et al.* [13], who scanned the time delay between the local oscillator and probe to time-resolve the FWM signal. In the scheme from Ref. 1, the individual electric fields of each pulse can then be written as

$$E_i = E_0(t)(e^{i\omega_0 t - i\Omega_i t} + e^{-i\omega_0 t + i\Omega_i t}), \tag{4.1}$$

with the AOM frequency, Ω_i, for i =A, B, C, D, and the carrier frequency, ω_0, of the laser field. In our experiment, pulses A, B, and C generate the FWM, while pulse D is used for heterodyne detection. In the fluorescence-detected approach to MDCS of Ref. 1, the fourth pulse also interacts with the sample. Because Ω_i in Eq. 4.1 is six orders of magnitude below ω_0, the frequency tag results in a pulse-to-pulse carrie- envelope phase shift. The phase-matching condition introduced earlier for wave vectors then easily translates to AOM frequencies, based on which beams provide the conjugated interaction with the sample. In the collinear scheme illustrated in Fig. 4.1(b), time ordering is explicitly assumed, and different MDCS modalities can

be obtained by varying the AOM frequencies for the different pulses. The rephasing FWM signal is then modulated at the frequency $\Omega_{S_I} = -\Omega_A + \Omega_B + \Omega_C - \Omega_D$, and the non-rephasing FWM signal is modulated at $\Omega_{S_{II}} = \Omega_A - \Omega_B + \Omega_C - \Omega_D$.

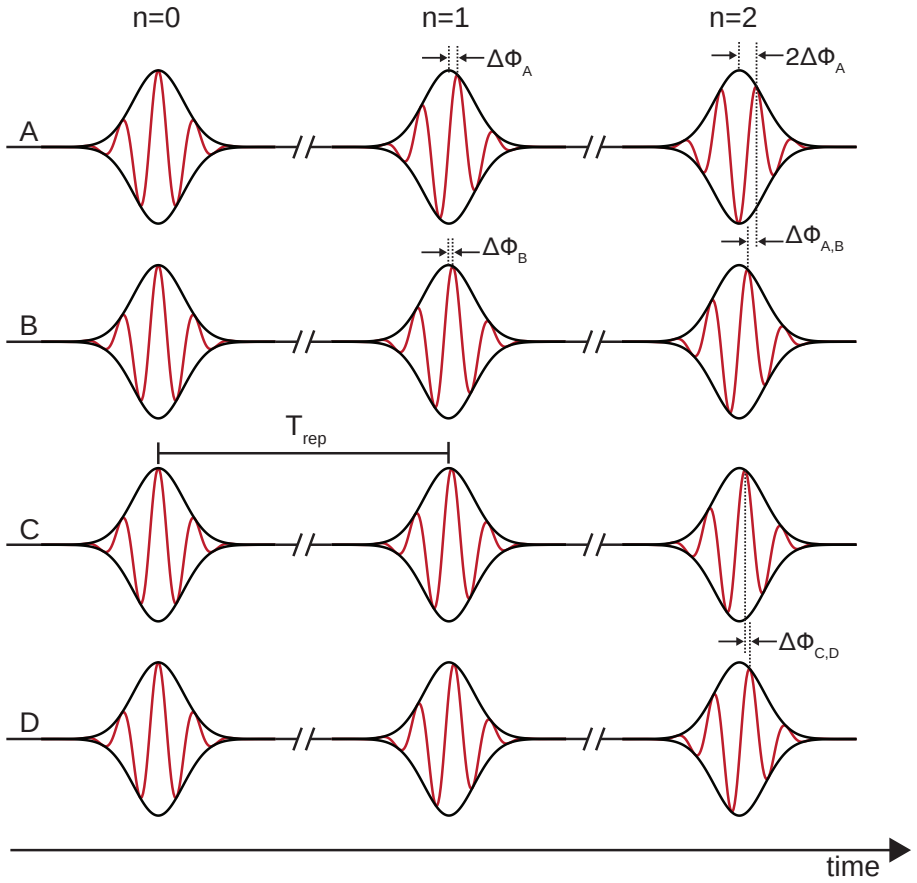

Figure 4.2: Illustration of the AOM phase-modulation as a continuous phase-cycling scheme. The four beams (A, B, C, D) are shown for $\tau = T = t = 0$ here. The distinct radio frequency shift for each beam leads to a shift of the carrier-envelope phase between beams that evolves with time. Figure adapted from Ref. 14.

In Fig. 4.2, we illustrate how this phase-matching procedure corresponds to a continuous phase-cycling scheme. As shown in Ref. 14, the pulse-to-pulse carrier-envelope shift for beam i can be expressed as

$$\Delta\phi_i = (\Omega_i + 2\pi f_{\mathrm{CE}})T_{\mathrm{rep}}\,, \tag{4.2}$$

with the carrier-envelope offset frequency f_{CE} and the repetition period $T_{\mathrm{rep}} = 1/f_{\mathrm{rep}}$

with repetition rate f_{rep}. The phase difference between A/B and C/D for the n-th pulse then is

$$\Delta\phi_{A,B} = \Omega_{A,B}(nT_{\mathrm{rep}}) \qquad \Delta\phi_{C,D} = \Omega_{C,D}(nT_{\mathrm{rep}})\,. \tag{4.3}$$

The phase evolution of the rephasing (S_I) and non-rephasing (S_{II}) FWM signals then reads

$$\phi_{S_I} = \Delta\phi_{C,D} - \Delta\phi_{A,B} \qquad \phi_{S_{II}} = \Delta\phi_{C,D} + \Delta\phi_{A,B}\,. \tag{4.4}$$

This phase-cycling of all four beams imparted onto the signal leads to oscillations of the rephasing and non-rephasing FWM signals at the frequencies $\Omega_{S_{I,II}}$ introduced earlier. The signal can subsequently be filtered out with a lock-in amplifier by setting the detection frequency to $\Omega_{S_{I,II}}$.

While this phase-cycling scheme allows for retrieval of the FWM signal in the temporal domain, spectroscopy relies on the fact that a Fourier transform of the time-domain signal can be easily achieved. In the following, we explain how phase stabilization is required for accurate retrieval of a spectrum in Fourier transform spectroscopy.

4.2.2 Passive Phase Stabilization for Fourier-Transform Spectroscopy

The Fourier transform requires knowledge of the complex electric signal field in the temporal domain, including amplitude and phase, to reconstruct the spectral amplitude and phase. Given the wavelength range of 720-880 nm that our CINeMaS setup operates in, acceptable $\lambda/20$ fluctuations [15] are on the order of sub-40 nm. However, as discussed in Fig. 4.3 below, temperature fluctuations and air currents lead to phase instabilities that can be larger than 40 nm. Therefore, to obtain a meaningful phase in the temporal domain that allows for the realization of Fourier-transform spectroscopy, a phase stabilization scheme is required.

Active phase stability of $\lambda/100$ has been previously demonstrated with loop filters

and piezoelectric-controlled mirrors [16]. While feasible, active phase stabilization significantly increases both the complexity of the setup and the data acquisition time. As described by Nardin *et al.* [14], one can use a continuous wave (CW) reference laser to retrieve the phase fluctuations between the interferometer arms at all times, thus passively phase-stabilizing the setup when using this phase in the lock-in detection of the nonlinear signal. To clarify, when co-propagating the reference laser with the signal, the phase evolution of the reference and signal reads

$$\phi_{\mathrm{sig}} = \phi_{\mathrm{sig},0} + \frac{2\pi}{\lambda_{\mathrm{sig}}}(x_t + \delta_{\mathrm{fluc}}) + f_{\mathrm{mod}} t\,, \tag{4.5}$$

$$\phi_{\mathrm{ref}} = \phi_{\mathrm{ref},0} + \frac{2\pi}{\lambda_{\mathrm{ref}}}(x_t + \delta_{\mathrm{fluc}}) + f_{\mathrm{mod}} t\,, \tag{4.6}$$

with the intended change of path length (through the movement of a delay stage) x_t, the path length difference due to unwanted fluctuations in the interferometer (influenced by temperature changes, table vibrations, and air currents) δ_{fluc}, and the relative frequency modulation of the two arms f_{mod}, given by the difference of the two AOM frequencies (e.g., Ω_{AB} from Sec. 4.2.1 for the A and B pulse). Additionally, λ_{ref} is the reference wavelength, and λ_{sig} is the signal wavelength. When using the reference laser interference as the reference input in the subsequent lock-in detection, the phase error on the resulting phase is suppressed by $|\lambda_{\mathrm{sig}}/\lambda_{\mathrm{ref}} - 1|$. Even for a relatively broad bandwidth of 50 nm, this results in a factor of 15 for the suppression of phase fluctuations for the edges of the spectrum. As evidenced in Fig. 4.3, short-term length fluctuations are on the order of 100 nm, yielding sub-10 nm fluctuations in the passive phase stabilization scheme. Moreover, measurement of the reference phase during the experiment allows for phase correction of slow, larger path length fluctuations in the postprocessing, as elucidated in Sec. 4.2.5.

Fig. 4.3 also shows that these unwanted phase fluctuations can be significant. For this measurement, the entire setup was enclosed, significantly reducing the influence of

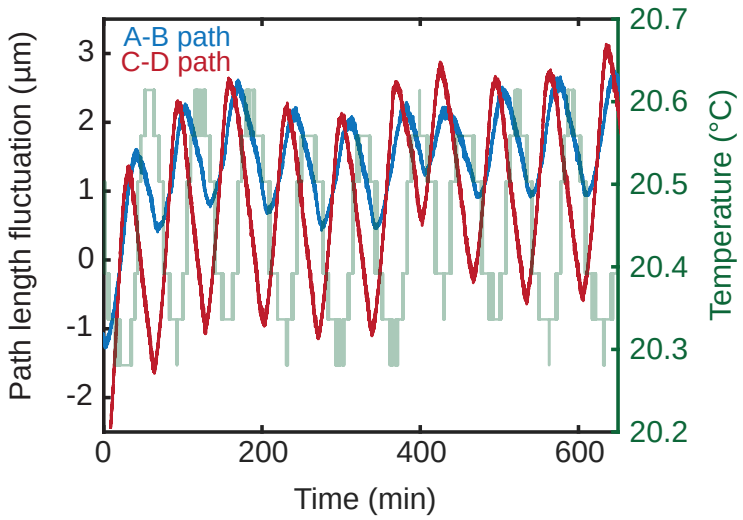

Figure 4.3: Phase stability of the CINeMaS setup in the presence of laboratory temperature fluctuations. The fluctuations of the lab temperature by less than 0.5 °C alter the path length A-B and C-D interferometers by several µm.

air currents. Nonetheless, noticeable oscillations of the relative length of beam paths, in-phase with the temperature fluctuations, can be observed. For example, the C-D path changes by as much as 3 µm, corresponding to 10 fs, over 40 minutes.

Another advantage of passive phase stabilization using a reference laser is that the evolution of x_t (the change in path length) during a scan, which corresponds to a time delay, leads to a phase evolution at the energy difference between the reference laser and signal. Upon subsequent Fourier transform, the signal energies are measured with respect to the reference laser energy. Therefore, this method also allows for significant undersampling when the reference laser is reasonably close in energy to the signal.

4.2.3 Arbitrary Reference

A major obstacle of past collinear MDCS implementations is the need to change the diode of the external-cavity diode reference laser every time a sample is changed. The change is required because of the reference laser's constraints to be energetically below the signal but close in energy such that the phase fluctuations are effectively canceled out. Martin, Smallwood, and Cundiff [17, 18] invented a method for an arbi-

trary reference, where a constant CW laser is used as a co-propagating reference laser, but its effective wavelength can be continuously and easily tuned by postprocessing in a field-programmable gate array (FPGA).

The concept behind the scheme is as follows:

1. The measured interference between two reference beams, e.g., A and B, can be obtained from $I = |E_A + E_B|^2$. Noting that a bandpass filter around the AOM difference frequency $\Omega_{AB} = \Omega_A - \Omega_B$ is applied and $E_{A,B} \propto \sin(\Omega_{A,B}t + \phi_B - \phi_A)$, the only term after the interference filter is $I \propto \sin(\Omega_{A,B}t + \phi_{A,B})$ with $\phi_{A,B} = \phi_B - \phi_A$.

2. Once the signal is digitized, we can apply a Hilbert transform to obtain a 90° phase-shifted signal. From the original and phase-shifted signal, we note that $\frac{\sin(\theta)}{\sin(\theta+90°)} = \tan(\theta)$, such that applying the arctan to the division of the two signals yields the term $\Omega_{A,B}t + \phi_{A,B}$.

3. The term $\Omega_{A,B}t$ can be removed from the previous expression by subtraction for all time points t because $\Omega_{A,B}$ is known. While this leaves us with the desired term $\phi_{A,B}$, there is an ambiguity because the phase only ranges from 0 to 2π (corresponding to a path difference of λ_{ref}). As such, a minimum of four data points per full modulation (from 0 to 2π or 2π to 0) is needed to resolve said ambiguity.

4. Every time the phase crosses 0 or 2π, we can track it, effectively unwrapping the phase from the 0-2π domain. The resulting, unwrapped phase can then be multiplied by the ratio of the actual reference wavelength (here: 1064 nm) and the desired reference wavelength to create the arbitrary wavelength reference phase.

5. This phase can then generate a phase-locked reference input for a lock-in amplifier. It can also be used in postprocessing, as explained in Sec. 4.2.5.

4.2.4 Continuous Scanning

Another limitation to the widespread adoption of MDCS, apart from its experimental complexity, is the long acquisition time necessary to acquire two-dimensional spectral (or, in our case, temporal) data. Historically, an MDCS measurement, e.g., of a one-quantum rephasing pathway, that does not involve a grating spectrometer proceeds as follows: The τ- and t-stages are initially moved to their respective time zeros. Time zero between two pulses is defined as the point of perfect overlap where both pulses arrive at the same time. Subsequently, the t-stage is equidistantly stepped until the signal has decayed. It is then moved back to the t stage time zero, while the τ-stage is translated by a single step. This procedure is repeated until the signal has also decayed along τ. For each of the N^2 sample points (N being the number of steps along either temporal dimension), the stages need to move, settle from their movement, then wait for several time constants of the lock-in amplifier for the signal to stabilize and record the values from the lock-in amplifier. This scheme yields long acquisition times ranging from several minutes to tens of minutes, depending on the sample parameters. When needing to change beam powers, step the T-stage, or alter another experimental parameter, this can very quickly lead to hour-long measurements that exceed the time range during which our cryostat is stable.

An efficient way of speeding up these measurements is to accelerate the acquisition of one of the two time axes by scanning it continuously. The continuous acquisition procedure was mainly developed by Dr. Eric Martin during his PhD and subsequent work at MONSTR Sense Technologies, LLC, while we provided occasional input and testing. While he described a rudimentary continuous scanning procedure in his thesis [19], several crucial improvements have been made since his departure.

An important consideration already described in Dr. Eric Martin's thesis was the correlation of adjacent data points when continuously moving a delay stage. While discussed in further detail in Chap. VI, the exponentially-weighted low-pass filter

employed in a lock-in has a settling time associated with it during which the measured signal stabilizes. A two-pole lock-in (6-dB/octave slope) has a settling time of 4.75 time constants TC for a 95% stabilization of the signal, corresponding to a 95% decay of the exponential weight of the low-pass filter. Hence, the effective step size in the temporal domain should be $4.75TC$. Given the bandwidth BW of the laser spectrum and speed of light c, the stage velocity is

$$v_s = \frac{c}{4BW \cdot 4.75TC} \,. \tag{4.7}$$

The factor of 4 results from the double-passing of the stage, which results in a time delay of four times the stage step size. Because of the undersampling requirement mentioned in Sec. 4.2.2, a reference close to the desired signal reduces the required bandwidth. In the case of 100 meV bandwidth and a lock-in time constant of 3 ms, this leads to a stage velocity of 0.22 mm/s.

The improvements made to the continuous scanning method during the PhD are detailed in the following. An issue with continuous scanning is that the stage cannot be expected to have a reliable, constantly changing position over time. This issue is illustrated in Fig. 4.4(a), where we plot the assumed stage position vs. the measured stage position. Although the deviations seem small, they can have noticeable effects, especially on broadband spectra. In the magnified insets of Fig. 4.4(a), the difference between the assumed and actual stage position is more than 25 fs. This difference constitutes a phase shift of π for a signal 83 meV away from the reference energy (and hence even larger phase shifts for signals further away). In Fig. 4.4(b), we plot an excerpt of an MDCS spectrum on a $MoSe_2/WSe_2$ heterostructure. The $MoSe_2$ peak is offset from the diagonal by a few meV. While there are actual physical processes in the sample that can lead to this behavior, applying a phase correction by considering the measured, not the assumed, stage position shifts the peak back onto the diagonal, as

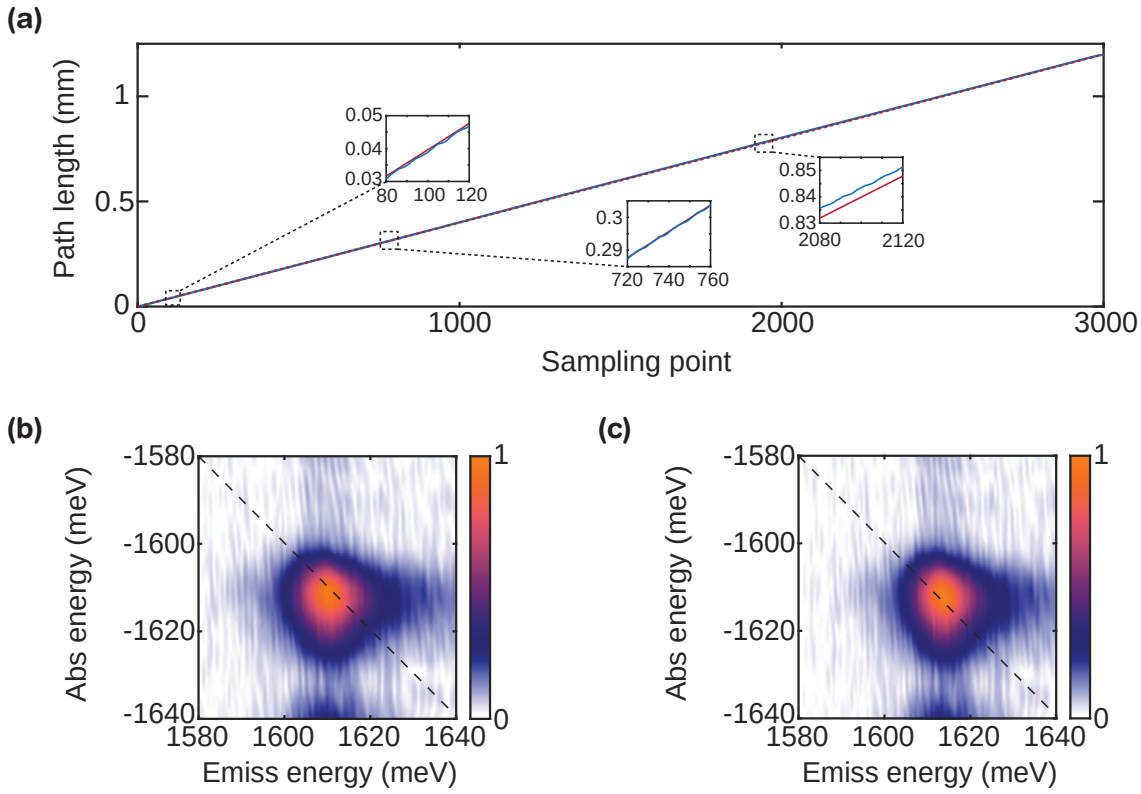

Figure 4.4: **(a)** Measured stage position and expected stage position as a function of sampling points as the stage moves, highlighting the inconsistent continuous stage movement. **(b)** MDCS spectrum obtained assuming a constant stage velocity, showing a shift of the FWM peak off the diagonal along the emission energy. **(c)** MDCS spectrum phase-corrected for the stage position deviation, showing the FWM peak on the diagonal.

evident from Fig. 4.4(c), identifying the off-diagonal shift as a measurement artifact. The shift only occurs along the emission energy (corresponding to the t delay in the time domain).

While postprocessing is reasonable to correct this issue, given the powerful passive phase stabilization technique, this issue can be overcome in situ: By tracking the reference phase, we have means to monitor variations in path length at all times, allowing us to trigger the measurement on specific stage positions while the stage is moving, thus guaranteeing equidistant sample points along the continuous scan axis.

4.2.5 Phase Correction Scheme for Multidimensional Spectra

Another advantage of the continuous scanning is the ability to account for time zero shifts that can be caused by phase fluctuation and stage backlash. Starting the scan of the t-delay stage at negative delays, such that we scan both negative and positive t-delays, we can determine any relative dispersion between the probe beam C and local oscillator D. We can also use the negative delay-scanning to determine time zero, which can differ from the previously set time zero due to the abovementioned factors. The relative dispersion and time zero offset between C and D will then similarly apply to the FWM-signal and D. The time zero and chirp correction scheme can be summarized as:

1. Fourier transform C-D interference and FWM-D interference signals.
2. Extract spectral phase of C-D interference, ϕ_{CD}.
3. Subtract the C-D spectral phase from the FWM-D spectral phase: $\phi_{\mathrm{FWM-corr}} = \phi_{\mathrm{FWM}} - \phi_{\mathrm{CD}}$.
4. Inverse Fourier transform FWM-D signal.
5. Set all values for $t < 0$ to zero.

By the abovementioned scheme, we can correct for any residual relative spectral chirp and ensure that the time zero is consistent across all measurements. While not currently implemented, this scheme can similarly be applied along τ.

From the discussion of Fig. 4.3 above, it is evident that there is an issue with passive phase stabilization: While phase-fluctuations can be tracked and mitigated using setup enclosures and improved temperature stability environments, they will still alter the measured sample points along the slow (non-continuous) scan axis. In some instances, using the phase measurement as a feedback mechanism is feasible, but this will significantly extend the scan duration. Furthermore, for small stage steps as

required for rapid sample dynamics present in most TMD samples, the stage accuracy limit of the Newport M-UTM100CC1DD/MFA-PPD stages employed in our setup approaches 20% of the step size. In this case, a robust phase-correction algorithm needs to be used. From Eq. 3.43, the FWM signal contains a phase factor $e^{i\omega t}$ along the τ and t axis, respectively. The unwanted phase change due to a fluctuation in stage position can then be considered by multiplying the measured FWM signal in the time-domain with

$$\phi_{\text{correct}} = e^{-i\omega_t(t_{real}-t_{ideal})}e^{-i\omega_\tau(\tau_{real}-\tau_{ideal})}\,, \tag{4.8}$$

where t_{ideal} and τ_{ideal} are the assumed sampling points along t and τ while t_{real} and τ_{real} are the temporal delays inferred from the measured stage positions. This phase-correction requires N^2 Fourier transforms, one for each combination of $\omega_{t,\tau}$, with N being the number of zero-padded sampling points along either temporal axes. This phase correction does not account for effects that alter dephasing or inhomogeneous broadening. However, assuming that most phase changes correspond to path length changes that are much smaller than dephasing or decay times, the influence on the extracted times is negligible. In the case of continuous scanning for the t axis, only the phase correction along τ needs to be employed for MDCS scans. The phase correction along both axes is vital for the MDCIS spectra introduced in Sec. 4.5.

4.2.6 The Transfer Function for Lock-In Amplifiers

Another factor that we have to consider for continuous scanning with rapidly moving stages is the transfer function of the lock-in amplifier. The low-pass filter employed in the lock-in amplifier will impart a spectrally varying attenuation onto the signal because of the continuous stage movement. The time-domain signal is convolved with the impulse response function of the low-pass filter. Since a convolution

in the time domain is the same as a multiplication in the frequency domain, the resulting Fourier transformed signal needs to be divided by the transfer function (the Fourier transform of the impulse response function) of the low-pass filter to accurately reflect the signal amplitudes.

The transfer function of an exponentially-weighted moving average filter can be obtained by considering the impulse response in the temporal domain and applying a Fourier transform. The difference equation for this filter in the time domain reads

$$y[n] = \alpha x[n] + (1-\alpha)y[n-1]\,, \tag{4.9}$$

with $y[n]$ being the current output, $x[n]$ being the current input, and $y[n-1]$ being the previous output. Additionally, α is an expression for the weight of the filter that can be related to the time constant via $TC = \Delta_T(1-\alpha)/(\alpha)$, with Δ_T being the digital lock-in sampling period. By recursively substituting the previous inputs into the difference equation, we obtain

$$y[n] = \alpha \sum_{k=0}^{n} (1-\alpha)^k x[n-k]\,. \tag{4.10}$$

The impulse response is obtained as the output in the time domain when a δ-function is applied to the input. Plugging into Eq. 4.10, we obtain

$$y_{\text{impulse}}[n] = \alpha(1-\alpha)^n\,. \tag{4.11}$$

Fourier transform of this expression then yields the transfer function

$$H(f) = \frac{\alpha}{1-(1-\alpha)e^{-i2\pi f}}\,. \tag{4.12}$$

4.3 Experimental Setup

The experimental setup based on the concepts of collinear MDCS introduced in this chapter is shown in Fig. 4.5. Changes made to the setup throughout the PhD are elucidated in later sections and chapters. Our setup employs a Coherent Vitara titanium-sapphire (Ti:Sapph) oscillator laser with an adjustable bandwidth between 30-125 nm (full-width at half maximum (FWHM)) and a tuning range between 755-860 nm at minimum bandwidth. The laser has an output above 525 mW for all spectrum settings and a repetition rate of 80 MHz.

The broad bandwidth of the laser requires efficient pulse compression, especially because several elements of the setup, including a Faraday rotator and the AOMs, impart large dispersion onto the laser pulses. We initially employed a Grism compressor for the results in Chap. V and moved to a spatial light modulator (SLM)-based pulse compressor for later chapters. Details about the pulse compression setup can be found in App. A.

After initial dispersion pre-compensation, we send the laser through a half-wave plate (HWP) and polarizing beamsplitter (Thorlabs PBS102, PBS) for power adjustment. We subsequently send the laser through a combination of a polarizer, Faraday rotator, half-wave plate, and polarizer to prevent reflected beams from coupling back into the laser, leading to FWM in the laser crystal and laser instabilities. This combination is commonly known as a Faraday isolator (ISOL). Using a beam splitter, the laser emerging from the Faraday isolator setup is combined with a 1064 nm CW laser (CrystaLaser). The CW laser is co-propagating the Ti:Sapph laser and serves to generate the reference discussed in Sec. 4.2.2.

The two lasers are subsequently split into four beams (A, B, C, D) using four cube beamsplitters (Thorlabs BS011). The advantage of beamsplitter cubes in the Michelson configuration is that it eliminates relative chirp between the respective beams. Since other optical elements, such as AOMs, already require chirp pre-compensation,

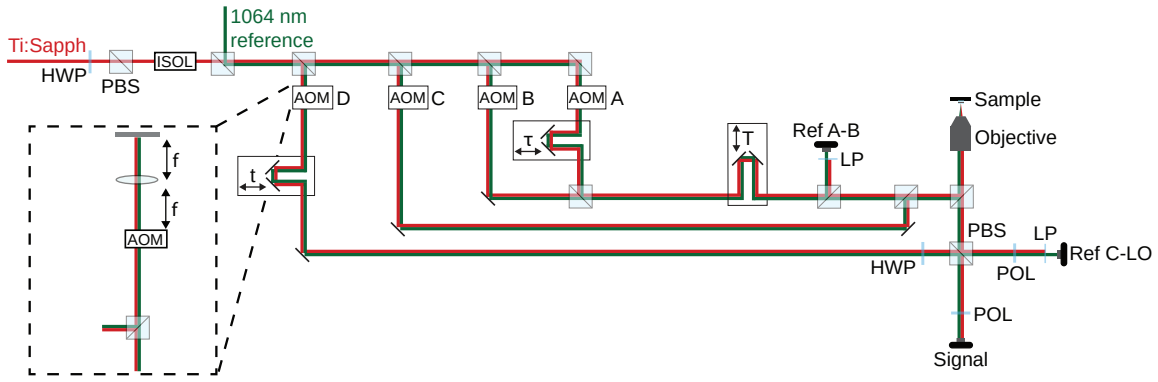

Figure 4.5: Schematic of the MDCS setup employed for the measurements in Chap. V with the local oscillator beam (D) routed around the sample. A half-wave plate (HWP) and polarizing beam splitter (PBS) are used for power adjustment. Long pass filters (LP) are used in front of the reference (Ref) detectors to isolate the reference laser and block the pulsed laser. A combination of polarized beam splitters and polarizers (POL) is used to recombine C and D.

compensating for the additional chirp from the beamsplitters is straightforward. The four beams then double-pass AOMs, as illustrated in the dashed box in Fig. 4.5: The beams transmit through the AOM and are reflected after passing through a lens (f=10 cm) that is a focal length away from the AOM and a mirror. The double passing eliminates spatial chirp that is acquired from the dispersive lead-molybdate in the AOMs, as further elucidated in Sec. 4.3.1.

The A beam impinges on a retroreflector (Newport UBBR1-1I) mounted onto a 25 mm travel delay stage (Newport UTM100CC1DD) [τ-stage], as does the D beam [t-stage]. In contrast to the schematic in Fig. 4.5, which is simplified to emphasize clarity, the A and B beams are subsequently recombined on the same beam splitter they were split off. The combined A-B beams impinge on a retroreflector on a 100 mm travel delay stage (Newport MFA-PPD). After this stage, a low-group-delay dispersion (GDD) ultrafast beamsplitter (Thorlabs UFBS5050) splits off half of the A-B beam and sends it onto a reference detector with a long pass filter (Thorlabs FEL1050, LP) installed in front of it. The A-B beam is recombined with the C beam before being sent onto the sample with a microscope objective (Nikon ELWD 20x,

NA=0.4). The beams reflected from the sample and the FWM signal pass through a polarizing beam splitter and get combined with beam D, which acts as a local oscillator for heterodyne detection. The reason for employing a polarizing beam splitter is the power of beam D, which is significantly larger than that of A/B/C and the FWM because it is not reflected off the sample. With the polarizer in front of the signal and reference detector, the transmission of A/B/C/FWM, which have horizontal polarization, and D, which has vertical polarization, can be tuned such that the detector is not saturated while the detected interference signal is maximized. The signal detector output is subsequently sent into the signal input of a lock-in amplifier (MONSTR Sense Technologies, LLC). The employed FPGA-based lock-in amplifier also has two inputs for the AB and CD references and employs the arbitrary reference scheme introduced in Sec. 4.2.3.

4.3.1 Michelson Interferometry for Broadband Spectroscopy

Although the spectroscopy part of the CINeMaS setup shows strong similarities with the MDCS setup presented by Dr. Eric Martin in his thesis [19], there are important improvements that have been made to the experiment since. The most significant change is upgrading the setup to a Coherent Vitara Ti:Sapph laser with >100 nm bandwidth, requiring treatment of both spatial and temporal chirp.

Spatial chirp is caused by a wavelength-dependent diffraction angle of the AOMs, which is given by Bragg's law

$$\sin(\theta_m) = \frac{m}{2\Lambda}\frac{\lambda}{n} = \frac{m\lambda\Omega_{\mathrm{mod}}}{2v_s}\,. \tag{4.13}$$

Here, θ_m denotes the diffraction angle of the m-th order, Λ is the wavelength of sound in the AOM medium, λ is the wavelength of the laser, n is the refractive index of the AOM, Ω_{mod} is the modulation frequency of the AOM, and v_s is the speed

of sound. While the wavelength-dependent diffraction angle strictly only leads to angular dispersion, subsequent propagation and transmission through the glass in optical elements along the beam path yields spatial chirp.

The solution to spatial chirp, which we borrow from the atomic physics community, is to double-pass the AOM [20].

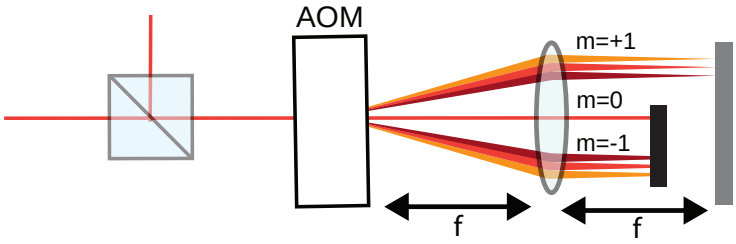

Figure 4.6: Double-pass design for the AOM, eliminating spatial chirp.

The double-pass configuration is shown in Fig. 4.6. The beam is transmitted through the AOM to apply the frequency tag discussed in Sec. 4.2.2. The different diffraction orders ($m = 0, m = \pm 1$) can be seen for the beam exiting the AOM. Higher diffraction orders exist but rapidly decrease in intensity with increasing order. The AOM is slightly tilted to operate at Bragg condition such that $\theta_i = \theta_{m=1} = \theta_B$ for the incoming angle θ_i and Bragg angle θ_B. Subsequently, the $m = 0$ and $m = -1$ orders are blocked. By placing a lens a focal length f away from the AOM and a planar mirror a focal length f away from the lens, the diffracted beam can be reflected through the AOM along the same path, canceling the angular dispersion while doubling the frequency of the modulation inscribed onto the beam. The specific lens-mirror combination is commonly called a cat's eye retroreflector.

4.4 Laser-Scanning Imaging

The collinearity of our MDCS scheme allows not only for combination with a microscope objective, yielding a diffraction-limited spot on the sample, but also enables the MDCS setup to be used as a nonlinear microscope.

While spatially addressed spectroscopy has been realized in the past [6, 21], the common denominator of rapid nonlinear laser-based microscopes [22–24] is their laser-scanning based imaging approach. In laser-scanning imaging applications, the laser beam is scanned across the static sample instead of having a widefield implementation (typical for white-light microscopy) or scanning the sample across a fixed laser beam. The laser scanning is achieved with rapid scanning mirrors, usually galvanometric (galvo) mirrors or resonant scanners, that are imaged onto the back of the microscope objective with a $4f$-imaging setup using a scan and tube lens (see Fig. 4.7).

4.4.1 Designing and Building the Michigan CINeMaS

In Fig. 4.7(a), we illustrate the galvo-based imaging setup we constructed during the PhD, with a realistic rendering of the setup displayed in Fig. 4.7(b).

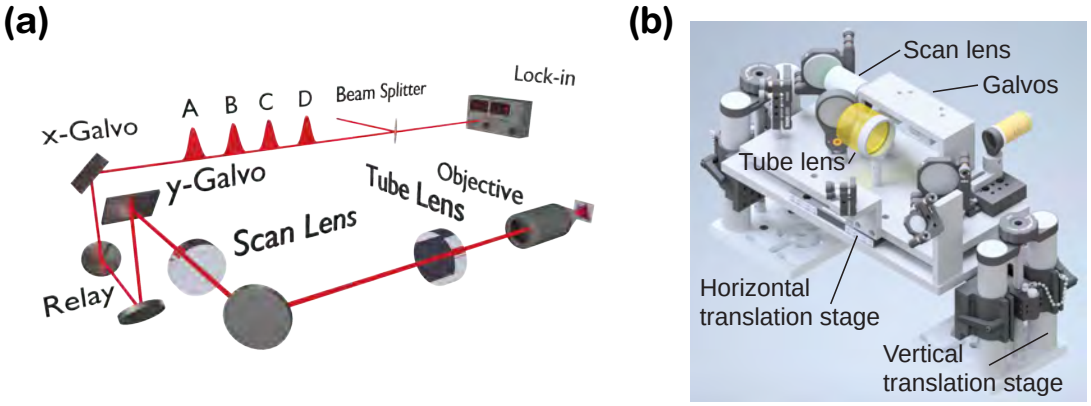

Figure 4.7: **(a)** Schematic of the laser-scanning imaging setup. The x-galvo is relayed onto the y-galvo with a pair of off-axis parabolic mirrors. The galvos are then relayed onto the objective with a pair of scan and tube lens. **(b)** Rendering of the laser-scanning imaging setup on the CINeMaS setup.

The incoming beam impinges on a galvo mirror rotating around its x-axis (Thorlabs GVS001). Commonly, the galvo mirror rotating around its y-axis is placed close to the x-galvo so that both are roughly but not perfectly imaged onto the back of the objective [25]. However, in our setup, we first image the x-galvo onto the y-galvo using two f=2-inch off-axis Parabolic mirrors (Thorlabs MPD129-P01). The first

parabolic mirror is a distance f away from the x-galvo. A distance $2f$ away from the first is the second parabolic mirror, which is also a distance f away from the y-galvo mirror. These mirrors are subsequently imaged onto the microscope objective using a scan lens (Thorlabs SL50-CLS2) and tube lens (Thorlabs TTL200MP). While, in a simplified way, these can be thought of as simple lenses in a $4f$ setup, the scan and tube lenses are specifically designed to reduce chromatic and spherical aberrations. Moreover, they act as a 1:4 telescope due to their different effective focal lengths, increasing the beam size such that it fills the back of the microscope objective to obtain the minimum spot size at the sample plane. The scan lens is placed a focal length f_{scan} away from the y-galvo mirror, and the tube lens is placed a distance $f_{\text{scan}} + f_{\text{tube}}$ away from the scan lens, with the tube lens focal length f_{tube}. The microscope objective is then placed a distance f_{tube} away from the tube lens.

Because we work with a cryostat that does not allow for sample movement, we mount the imaging setup onto a horizontal translation stage (Thorlabs TBB0606) and a vertical translation stage (Thorlabs VAP4), as shown in Fig. 4.7(b). The two mirrors steering the incoming beam are mounted to different base plates, such that changing the imaging setup's vertical and horizontal position does not affect the beam's position on any of the imaging optics.

4.4.2 Galvanometer Calibration Procedure

The electronics, including firmware and software, of the CINeMaS setup were entirely designed during an internship at MONSTR Sense Technologies. The galvo mirrors are controlled via a digital-to-analog converter (DAC) output of an FPGA. Because of noise and simplicity considerations, we trigger the data acquisition not on the measured position but on the FPGA-internal galvo driving position (the digital signal that is sent to the DAC that drives the galvos). To trigger at the correct position, the delay between the driving signal and galvo movement is characterized,

as shown in Fig. 4.8. For one, it can be seen that the galvo movement scales almost perfectly linearly with the driving signal, such that triggering on the driving signal instead of the galvo position is possible. Moreover, the delay between the driving signal and the galvo movement is constant and must only be calibrated once. The delay does vary for the up- vs. down-movement. However, this can be easily considered in post-processing, allowing us to acquire data during both the ascending and descending movement of the fast galvo, as explained in the following.

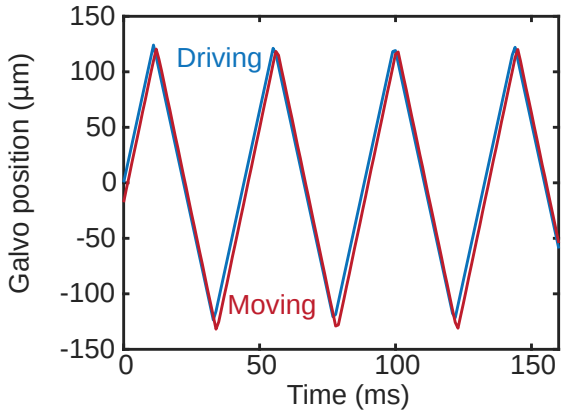

Figure 4.8: Galvo position as a function of time for the driving signal (blue) and the recorded (moving) position (red).

Irregularities in the data acquisition can stem from three sources: Backlash of the galvos, a delay between the galvo driving and galvo motion, and delay effects associated with lock-in detection (because the fast galvo moves across one pixel during the pixel dwell time, instead of remaining static). The first effect can be considered by driving the galvos beyond the field-of-view (FOV) and triggering the data acquisition within a subset of that FOV, such that the galvo can restore constant velocity by the time data acquisition starts. This also ensures that the galvo movement covers the entire FOV. The latter two effects lead to a shift between adjacent rows because they are acquired during opposing motions of the fast galvo. However, every other line in the image will be consistent with itself. Therefore, a constant pixel shift between even and odd rows can correct this issue in post-processing. We use the measured

driving and moving position of the galvo for rough calibration while we fine-tune the delay considered for data triggering in the software on the actual image by minimizing jagged edges between adjacent imaging rows. This allows additional delays associated with the electronics to be accounted for.

4.4.3 Determining Spatial Resolution

Fig 4.9 shows the spatial calibration procedure for the CINeMaS microscope.

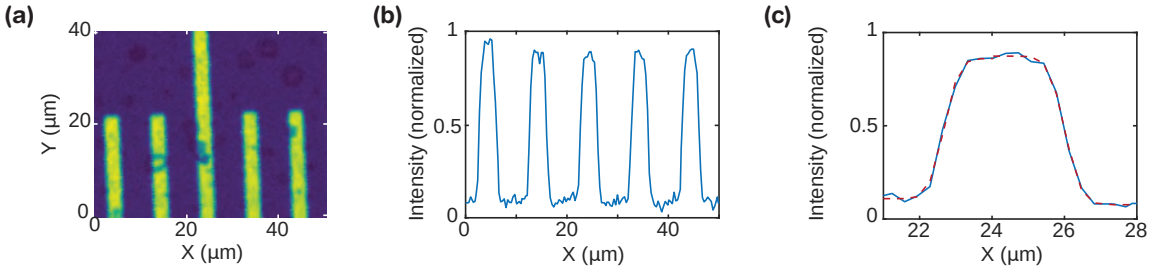

Figure 4.9: **(a)** Linear reflection image of the calibration slide. **(b)** Slice of the image in (a) taken along $y = 6\,\mu\text{m}$. **(c)** Zoomed in section of the image slice. Fits to the edge rise behavior are shown as a dashed line and used to determine the spatial resolution of the setup.

We use a conventional calibration slide which consists of a glass microscope slide with a metal-printed ruler pattern with a line spacing of 10 µm. In Fig. 4.9(a), we plot a linear reflection image taken with the CINeMaS setup on the calibration slide. A slice along the x direction for a fixed y position is plotted in Fig. 4.9(b). From this slice, we can determine the spatial resolution as follows:

We assume a Gaussian spatial profile

$$A(x) = e^{-x^2/\sigma^2}\,, \tag{4.14}$$

for the laser beam, with beam radius σ. The rise of the signal at the edges of the

metal ruler markings,

$$s(x) = \int_0^x A(z)\mathrm{d}z = \frac{1}{2}\sqrt{\pi}\mathrm{erf}\left(\frac{x}{\sigma}\right) . \tag{4.15}$$

then follows an error function.

Thus, by fitting the rise and fall of the signal with an error function and extracting σ from the fit parameters, we can extract the FWHM of the Gaussian beam

$$\mathrm{FWHM} = \sqrt{2\ln 2}\sigma \approx 1.18\sigma\,, \tag{4.16}$$

which is commonly employed as the "spatial resolution".

An exemplary fit of the signal to the error function is shown in Fig. 4.9(c). Here, we add an amplitude and constant background parameter to the fit function because the reflection of the microscope slide outside the metal ruler area is non-zero, and the amplitudes of reflection are arbitrary here. The fit shows excellent agreement with the experimental data. We extract the FWHM for each fall and rise of the signal displayed in Fig. 4.9(b) and average to obtain a spatial resolution of 870 nm in this case. Given the 633 nm wavelength of the Helium-Neon (HeNe) laser used here and an objective with a numerical aperture NA=0.4, the diffraction limit is 790 nm, very close to our obtained resolution.

Another test for the spatial performance of the custom-built imaging setup is the obtainable FOV. The current limit for the FOV is the incidence angles a given objective accepts and the driving voltage resolution the FPGA can provide to the galvos. FOV and spatial resolution are always at a trade-off: The field of view for an objective with a given effective focal length f_{obj} is [26]

$$\mathrm{FOV} = 2f_{\mathrm{obj}}\tan(\alpha)\,, \tag{4.17}$$

with incident angle α. At the same time, the diffraction limit for a given objective is defined as

$$d = \frac{\lambda f_{\text{obj}}}{nD}\,, \tag{4.18}$$

with the refractive index n of the objective and beam diameter D at the back of the objective (assuming the treatment of an objective as a simple lens). Therefore, choosing a larger focal length objective increases the FOV while simultaneously increasing the spot size and thus decreasing the spatial resolution. Furthermore, specific to our setup, the galvos have a different amplification setting, in which case larger angles can be achieved, increasing the FOV according to Eq. 4.17. However, this goes at the expense of the galvo step size, given the limited resolution of the DAC driving the galvos.

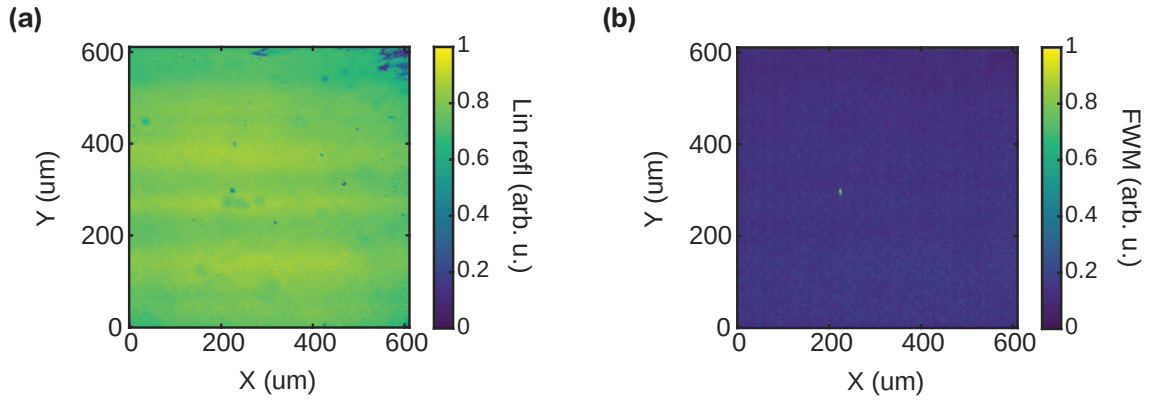

Figure 4.10: **(a)** Linear reflection image of an undoped GaAs wafer, highlighting the large FOV. **(b)** Corresponding FWM image.

The currently employed NA = 0.4, 20x objective is a good compromise between a reasonably large FOV of 600 µm x 600 µm and sub-µm diffraction-limited spot size. In Fig. 4.10, we show a linear and FWM image obtained with the CINeMaS setup on an undoped GaAs wafer. Fig. 4.10 (a) shows the linear reflection image, while Fig. 4.10(b) shows the FWM image. From the linear reflection image, it is clear that the entire FOV shows a homogeneous strength of reflection (apart from local changes due to defects and other contamination of the wafer), and no vignetting is visible.

Furthermore, the bright spot at a defect in the FWM image in Fig. 4.10(b) proves that the beam intensities achieved with this objective are sufficient to obtain a noticeable FWM signal on the sample.

4.5 Multidimensional Coherent Imaging Spectroscopy

We have discussed the benefits of MDCS in the preceding chapters. MDCS is a great tool to access various information about a sample. Combining it with nonlinear imaging allows the study of inhomogeneity and spatial dynamics of various samples with this "universal microscope".

During the PhD, we developed a rapid imaging version of MDCS that we coined MDCIS. Using a novel scheme for lock-in detection (see Chap. VI), we developed a new acquisition scheme for spatially addressed MDCS spectra. Instead of acquiring a full MDCS spectrum at specific sample points, we acquire an image for each fixed temporal delay stage position while stepping the stages, obtaining a full two-dimensional time trace. Upon Fourier transform, we obtain an MDCS spectrum at every image pixel. The data acquisition scheme is illustrated in Fig. 4.11.

The fundamental MDCS excitation schemes remain the same in this technique, with three pulses (A, B, C) generating the FWM signal and a fourth pulse (D) used for heterodyne detection. The fourth pulse is also sent onto the sample, which requires additional considerations, as further discussed in Sec. 4.5.2. Instead of using the continuous scanning of one stage (introduced in Sec. 4.2.4), we step the stages of interest while acquiring full images. We still designate the t-stage as the fast stage, as illustrated in the data acquisition scheme in Fig. 4.11. Each red dot signifies the capture of an entire image. After each image, the t-stage (horizontal direction) is moved. Once the full scan range of the t-stage has been sampled, the τ-stage position is incremented, and the t-stage moves again over its full scan range. This procedure is repeated until the τ-stage scan range is also sampled. The resulting two-

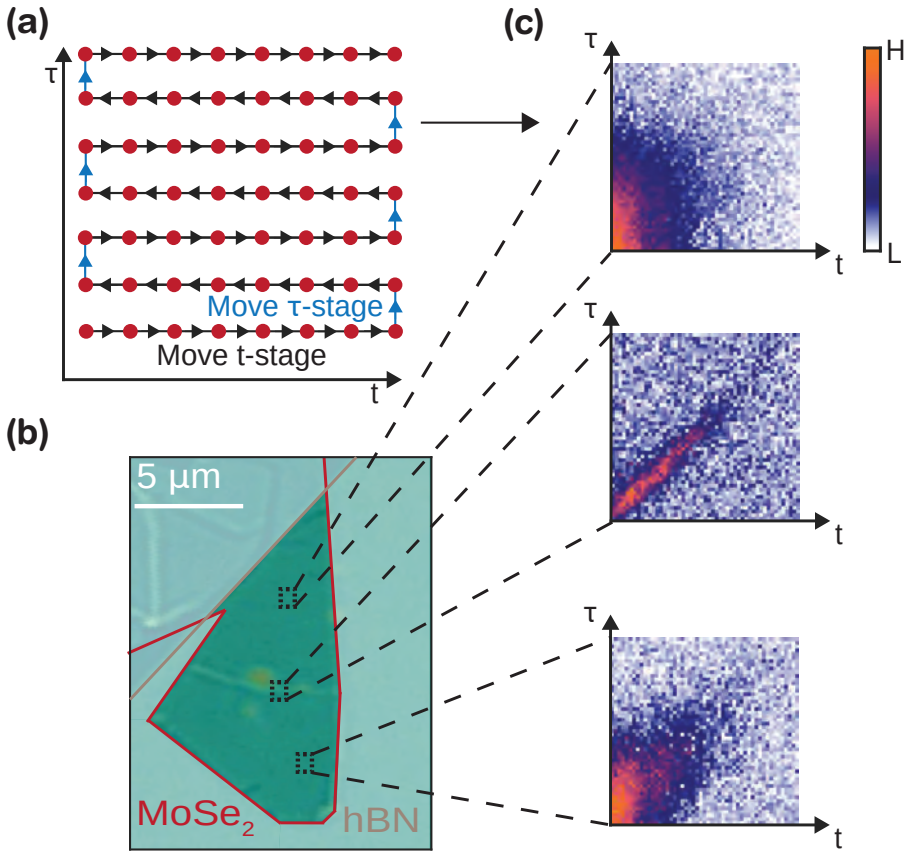

Figure 4.11: **(a)** Illustration of the MDCIS data acquisition scheme. Each circle, corresponding to a fixed τ, T, and t position, represents the acquisition of an image. Between images, the τ and t delay stages are stepped. **(b)** hBN-encapsulated monolayer of $MoSe_2$. **(c)** Two-dimensional data sets in the time domain for different sample positions, acquired with the MDCIS technique.

dimensional time traces for different spots on the hBN-encapsulated $MoSe_2$ monolayer in Fig. 4.11(b) are plotted in Fig 4.11(c). By obtaining complete temporal information along τ and t for every single image pixel, a simple Fourier transform yields full MDCS spectra at every image pixel. Given the short time constants realizable with the novel box lock-in (Chap. VI), images can be acquired in less than a second, allowing for sub-30-minute MDCIS scans of the desired sample.

4.5.1 Experimental Setup Changes

Apart from attaching an imaging apparatus to the spectroscopic part of the CINeMaS setup, a few additional experimental changes have to be realized to combine the setup in Fig. 4.5 with imaging. Obtaining a reference signal from C-D interference when routing D around the sample poses a significant challenge when adding the imaging setup because additional losses to the power of D and hyper-sensitive alignment render the setup non-robust. Instead, we decided to send D to the sample, enabling us to split off the C-D reference before the imaging setup. As such, we have constructed the C-D interferometer in the same way as the A-B interferometer, with the pulses being recombined on the same beam splitter that they are split up. This change also means no additional beam splitters have to be used after the imaging setup, and the signal can be sent from the imaging setup straight into the signal detector. Because all four beams now have the same power, no adjustment of the beam powers using polarizing beam splitters and polarizers in front of the detector is necessary.

Sending the D beam to the sample requires careful treatment of a few post-processing corrections, as explained in the following.

4.5.2 Local Oscillator Corrections

For MDCIS, it is more convenient for the fourth pulse (D) to be recombined with the three excitation beams before the sample and impinge on it. The recombination before the sample leads to two additional factors that need to be considered in the post-processing of the measurement: For one, the absorption of D by the sample is imparted onto the detected FWM signal since $R_{detect}(\omega) \propto E_{FWM}(\omega) \cdot E_D(\omega)$ with $R_{detect}(\omega)$ being the Fourier transform of the amplitude detected with the lock-in amplifier. The D absorption can easily be accounted for by measuring the linear interference between C and D, which is inherently measured and recorded by the

CINeMaS setup. For this measurement, the digital lock-in amplifier digitally copies the signal input and detects at both the FWM beating frequency and C-D beating frequency, hence acquiring both the FWM and linear interference signal. Since $R_{CD}(\omega) \propto E_C(\omega) \cdot E_D(\omega)$, dividing the detected FWM by the square root of the C-D interference (all in the frequency domain) gives the accurate FWM spectrum. This normalization procedure assumes that the spectrum of C and D are the same, which is reasonable given that the sample excitation changes the reflectivity by less than 1% [27].

Moreover, the contributions where D interacts before C need to be carefully filtered out since real FWM (e.g., non-rephasing contributions) will leak into the desired rephasing FWM signal when the interaction ordering between C and D is altered. These contributions can be minimized when using short and nearly transform-limited 30 fs pulses, as is the case for the CINeMaS setup. However, great care needs to be taken to minimize relative chirp between C and D, which can easily occur on the order of 100-200 fs^2 given the strongly dispersive nature of the lead-molybdate AOMs. We minimize relative chirp by routinely checking relative chirp between all four beams after realignment and inserting thin fused silica windows in the respective beam paths.

4.6 Summary

After the theoretical introduction of the technique in the previous chapter, we talked about the experimental implementation of collinear MDCS and the specifics of the CINeMaS setup, including the laser-scanning microscope that allows us to perform MDCIS. Not all the spectroscopic techniques and features and none of the imaging ones presented in this chapter were available at the beginning of the PhD. In fact, many features, such as continuous scanning, phase correction, and the laser scanning imaging setup, have been developed as a response to experimental challenges

in studying the nonlinear response of TMDs. Time was also spent on optimizing pulse compression for the setup, which is presented in Appendix A.

Fully equipped with these sophisticated spectroscopic and imaging techniques, the PhD work was able to shed light onto the underlying physics of TMD monolayers and heterostructures, as discussed in the ensuing chapters.

References

[1] Patrick F. Tekavec, Geoffrey A. Lott, and Andrew H. Marcus. "Fluorescence-detected two-dimensional electronic coherence spectroscopy by acousto-optic phase modulation". In: *The Journal of Chemical Physics* 127.21 (2007), p. 214307. DOI: 10.1063/1.2800560.

[2] Eric W. Martin, Jason Horng, Hanna G. Ruth, Eunice Paik, Michael-Henr Wentzel, Hui Deng, and Steven T. Cundiff. "Encapsulation Narrows and Preserves the Excitonic Homogeneous Linewidth of Exfoliated Monolayer $MoSe_2$". In: *Phys. Rev. Applied* 14 (2 Aug. 2020), p. 021002. DOI: 10.1103/PhysRevApplied.14.021002.

[3] S.T. Cundiff and S. Mukamel. "Optical multidimensional coherent spectroscopy". In: *Phys. Today* 44.66 (2013). DOI: 10.1063/PT.3.2047.

[4] Peifang Tian, Dorine Keusters, Yoshifumi Suzaki, and Warren S. Warren. "Femtosecond Phase-Coherent Two-Dimensional Spectroscopy". In: *Science* 300.5625 (2003), pp. 1553–1555. ISSN: 0036-8075. DOI: 10.1126/science.1083433.

[5] Galan Moody and Steven T. Cundiff. "Advances in multi-dimensional coherent spectroscopy of semiconductor nanostructures". In: *Advances in Physics: X* 2.3 (2017). PMID: 28894306, pp. 641–674. DOI: 10.1080/23746149.2017.1346482.

[6] Tomasz Jakubczyk, Valentin Delmonte, Maciej Koperski, Karol Nogajewski, Clement Faugeras, Wolfgang Langbein, Marek Potemski, and Jacek Kasprzak. "Radiatively Limited Dephasing and Exciton Dynamics in $MoSe_2$ Monolayers Revealed with Four-Wave Mixing Microscopy". In: *Nano Letters* 16.9 (2016), pp. 5333–5339. DOI: 10.1021/acs.nanolett.6b01060.

[7] Caroline Boule, Diana Vaclavkova, Miroslav Bartos, Karol Nogajewski, Lukas Zdražil, Takashi Taniguchi, Kenji Watanabe, Marek Potemski, and Jacek Kasprzak. "Coherent dynamics and mapping of excitons in single-layer $MoSe_2$ and WSe_2 at the homogeneous limit". In: *Phys. Rev. Materials* 4 (3 Mar. 2020), p. 034001. DOI: 10.1103/PhysRevMaterials.4.034001.

[8] Tomasz Jakubczyk, Karol Nogajewski, Maciej R Molas, Miroslav Bartos, Wolfgang Langbein, Marek Potemski, and Jacek Kasprzak. "Impact of environment on dynamics of exciton complexes in a WS_2 monolayer". In: *2D Materials* 5.3 (Apr. 2018), p. 031007. DOI: 10.1088/2053-1583/aabc1c.

[9] Tomasz Jakubczyk, Goutham Nayak, Lorenzo Scarpelli, Wei-Lai Liu, Sudipta Dubey, Nedjma Bendiab, Laëtitia Marty, Takashi Taniguchi, Kenji Watanabe, Francesco Masia, Gilles Nogues, Johann Coraux, Wolfgang Langbein, Julien Renard, Vincent Bouchiat, and Jacek Kasprzak. "Coherence and Density Dynamics of Excitons in a Single-Layer MoS_2 Reaching the Homogeneous Limit". In: *ACS Nano* 13.3 (2019). PMID: 30735350, pp. 3500–3511. DOI: 10.1021/acsnano.8b09732.

[10] Torben L. Purz, Eric W. Martin, Pasqual Rivera, William G. Holtzmann, Xiaodong Xu, and Steven T. Cundiff. "Coherent exciton-exciton interactions and exciton dynamics in a $MoSe_2/WSe_2$ heterostructure". In: *Phys. Rev. B* 104 (24 Dec. 2021), p. L241302. DOI: 10.1103/PhysRevB.104.L241302.

[11] Torben L. Purz, Steven T. Cundiff, and Eric W. Martin. "Lock-in detector for accelerated nonlinear imaging". In: *Opt. Lett.* 46.19 (Oct. 2021), pp. 4813–4816. DOI: 10.1364/OL.432353.

[12] K. L. Hall, G. Lenz, E. P. Ippen, and G. Raybon. "Heterodyne pump-probe technique for time-domain studies of optical nonlinearities in waveguides". In: *Opt. Lett.* 17.12 (June 1992), pp. 874–876. DOI: 10.1364/OL.17.000874.

[13] P. Borri, W. Langbein, S. Schneider, U. Woggon, R. L. Sellin, D. Ouyang, and D. Bimberg. "Ultralong Dephasing Time in InGaAs Quantum Dots". In: *Phys. Rev. Lett.* 87 (15 Sept. 2001), p. 157401. DOI: 10.1103/PhysRevLett.87.157401.

[14] Gaël Nardin, Travis M. Autry, Kevin L. Silverman, and S. T. Cundiff. "Multidimensional coherent photocurrent spectroscopy of a semiconductor nanostructure". In: *Opt. Express* 21.23 (Nov. 2013), pp. 28617–28627. DOI: 10.1364/OE.21.028617.

[15] Albert Liu. "Electronic and Vibrational Properties of Colloidal Nanocrystals". PhD thesis. University of Michigan, Ann Arbor, 2019.

[16] Franklin D. Fuller and Jennifer P. Ogilvie. "Experimental Implementations of Two-Dimensional Fourier Transform Electronic Spectroscopy". In: *Annual Review of Physical Chemistry* 66.1 (2015). PMID: 25664841, pp. 667–690. DOI: 10.1146/annurev-physchem-040513-103623.

[17] Eric W. Martin, Christopher L. Smallwood, Torben L. Purz, Hanna G. Ruth, and Steven T. Cundiff. "Real-Time Reference for Frequency-Shifted Fourier-Transform Spectrometers Using an Arbitrary-Wavelength CW Reference Laser". In: *2019 Conference on Lasers and Electro-Optics (CLEO)*. 2019, pp. 1–2. DOI: 10.1364/CLEO_SI.2019.SM4F.4.

[18] Steven T Cundiff, Chris Smallwood, and Eric Martin. *PATH FLUCTUATION MONITORING FOR FREQUENCY MODULATED INTERFEROMETER*. Nov. 2019.

[19] Eric W. Martin. "Coherent Spectroscopy at the Diffraction Limit". PhD thesis. University of Michigan, Ann Arbor, 2018.

[20] E. A. Donley, T. P. Heavner, F. Levi, M. O. Tataw, and S. R. Jefferts. "Double-pass acousto-optic modulator system". In: *Review of Scientific Instruments* 76.6 (2005), p. 063112. DOI: 10.1063/1.1930095.

[21] Vivek Tiwari, Yassel Acosta Matutes, Alastair. T. Gardiner, Thomas L.C. Jansen, Richard J. Cogdell, and Jennifer P. Ogilvie. "Spatially-resolved fluorescence-detected two-dimensional electronic spectroscopy probes varying excitonic structure in photosynthetic bacteria". In: *Nat. Comm.* 16 (2018), p. 4219. DOI: 10.1038/s41467-018-06619-x.

[22] Francisco E. Robles, Sanghamitra Deb, Jesse W. Wilson, Christina S. Gainey, M. Angelica Selim, Paul J. Mosca, Douglas S. Tyler, Martin C. Fischer, and Warren S. Warren. "Pump-probe imaging of pigmented cutaneous melanoma primary lesions gives insight into metastatic potential". In: *Biomed. Opt. Express* 6.9 (Sept. 2015), pp. 3631–3645. DOI: 10.1364/BOE.6.003631.

[23] Michael Rubart. "Two-Photon Microscopy of Cells and Tissue". In: *Circulation Research* 95.12 (2004), pp. 1154–1166. DOI: 10.1161/01.RES.0000150593.30324.42.

[24] Fa-Ke Lu, Srinjan Basu, Vivien Igras, Mai P. Hoang, Minbiao Ji, Dan Fu, Gary R. Holtom, Victor A. Neel, Christian W. Freudiger, David E. Fisher, and X. Sunney Xie. "Label-free DNA imaging in vivo with stimulated Raman scattering microscopy". In: *Proceedings of the National Academy of Sciences* 112.37 (2015), pp. 11624–11629. ISSN: 0027-8424. DOI: 10.1073/pnas.1515121112.

[25] Zeiss. *ZEISS LSM 980 with Airyscan 2*. 2022. URL: https://www.zeiss.com/microscopy/us/products/confocal-microscopes/lsm-980.html.

[26] John E. Greivenkamp. *Field Guide to Geometrical Optics*. SPIE, 2004. ISBN: 9780819478160. DOI: 10.1117/3.547461.

[27] Xiaoping Hong, Jonghwan Kim, Su-Fei Shi, Yu Zhang, Chenhao Jin, Yinghui Sun, Sefaattin Tongay, Junqiao Wu, Yanfeng Zhang, and Feng Wang. "Ultrafast charge transfer in atomically thin MoS_2/WS_2 heterostructures". In: *Nature Nanotechnology* 9.9 (Sept. 2014), pp. 682–686. ISSN: 1748-3395. DOI: 10.1038/nnano.2014.167.

CHAPTER V

Exciton-Exciton Interactions and Rapid Charge Transfer in a $MoSe_2/WSe_2$ Heterostructure

Reproduced in part with permission from:

Torben L. Purz, Eric W. Martin, Pasqual Rivera, William G. Holtzmann, Xiaodong Xu, and Steven T. Cundiff. "Exciton-exciton interactions and rapid charge transfer in a $MoSe_2/WSe_2$ heterostructure". *Phys. Rev. B* **104**, 24 (2021).

5.1 Introduction

In chapter II, we established the exciting physical phenomena that render TMDs an interesting and promising platform for device applications ranging from solar cells to lasers. To explore both the potential and limitations of this group of materials, a thorough understanding of the fundamental physical processes in these materials is needed. We have specifically introduced the concept of coherent and incoherent coupling, the latter of which is usually present in the form of charge transfer in these materials.

Coherent coupling between excitons is a manifestation of many-body effects, which are at the heart of electromagnetically induced transparency [1, 2], lasing without inversion [3–5], and excitonic quantum degenerate gases [6]. Furthermore, understand-

ing the interactions between excitons is essential for efficient optoelectronic device design, such as photovoltaics [7] and photodiodes [8].

The coherent coupling between these quasiparticles also opens a new avenue for quantum information and quantum electronics applications, with the electronic states of TMDs being easily accessible both optically and electronically. Quantum coherent control of exciton qubits in QDs has been demonstrated previously [9–11]. Moreover, ILEs in TMD heterostructures [12], QDs on TMD monolayers [13], and defects in TMD monolayers [14] have been proposed as novel candidates for qubits in TMDs.

Coherent coupling has already been observed in numerous conventional semiconductors [15–18] and recently in $MoSe_2$ monolayers [19, 20]. While for TMD heterostructures, incoherent processes, including ultrafast charge transfer [21–27], the associated ILE formation [23, 26, 28–30], and energy transfer [22] have been extensively studied in the past, coherent coupling has been elusive in these samples due to the rapidness of the incoherent effects. In this chapter and the accompanying paper [31], we reveal the existence of coherent coupling between intralayer excitons in the $MoSe_2$ and WSe_2 monolayers of a $MoSe_2/WSe_2$ heterostructure.

Furthermore, the high binding energy of ILEs in TMD heterostructures has raised interest in these excitons and their associated dynamics for excitonic integrated circuits and qubits [12, 28, 32]. However, not all heterostructure ILE binding energies have been determined experimentally but have only been theoretically predicted [30, 33]. Moreover, previous studies using linear or one-dimensional techniques [21–26] have only been able to isolate charge transfer in an isolated manner and were unable to resolve any coherent coupling in these materials due to experimental limitations. While this work was in the publishing process, Policht *et al.* showed rapid electron and hole transfer in a similar heterostructure using MDCS [27].

This chapter presents results applying MDCS to a $MoSe_2/WSe_2$ heterostructure. We first show results comparing PL and MDCS on the sample. Using MDCS, we then

extract linewidths for the $MoSe_2$ and WSe_2 resonances, showing significantly broadened linewidths compared to the monolayer case. Subsequently, we demonstrate the existence of coherent coupling and rapid electron and hole transfer in the heterostructure sample. We further extract the charge transfer times. Moreover, we simulate the optical response of the system using the OBEs from Chap. III. We also show intermediate and long-term temporal dynamics (500 fs-600 ps) for this heterostructure, hinting at the time scale of ILE formation and ILE lifetimes. Additionally, we see signatures of the ILE through many-body effects, which allows us to determine the ILE binding energy in the $MoSe_2/WSe_2$ heterostructure. Lastly, we show data on a second $MoSe_2/WSe_2$ heterostructure that shows the same coherent coupling, charge transfer, and ILE dynamics, corroborating the assertion that the observed behavior is "universal" and does not depend on a "magic" sample.

5.2 Photoluminescence and Multidimensional Coherent Spectroscopy

A white-light microscopy image of the sample studied in this chapter is provided in Fig. 5.1(a). The sample consists of mechanically exfoliated $MoSe_2$ and WSe_2 monolayers stacked on top of each other with a near-zero twist angle. The heterostructure is encapsulated in hBN and contains thin graphite layers on top and bottom. The sample was assembled using a dry-transfer technique with a stamp made of a polydimethylsiloxane cylinder with a thin film of poly(bisphenol A carbonate) on top.
A PL spectrum for this heterostructure taken at 5 K is shown in Fig. 5.1 (b). This measurement was performed by our collaborator William G. Holtzmann in the group of Xiaodong Xu at the University of Washington. In this experiment, a HeNe laser (632.8 nm, 100 µW) is used for excitation and focused to a 940 nm spot diameter on the sample. A 90/10 beam splitter transmits the collected PL, which is subsequently

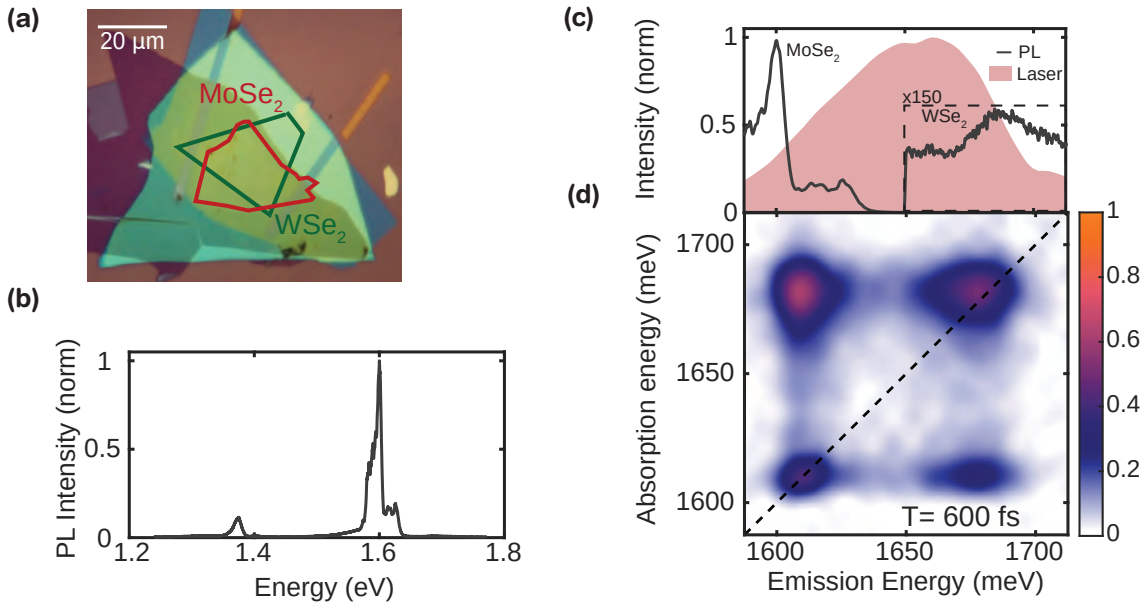

Figure 5.1: **(a)** Microscope image of the heterostructure sample. **(b)** Full energy range PL spectrum of the $MoSe_2/WSe_2$ heterostructure with right-circular polarized excitation and left-circular polarized detection. **(c)** PL spectrum (gray curve) of the sample and the laser excitation spectrum (red shade). **(d)** Characteristic low-temperature, low-power MDCS spectrum of the $MoSe_2/WSe_2$ heterostructure at a pump-probe delay $T = 600$ fs.

passed through a long pass filter and polarization optics. PL measurements presented in this chapter use right-handed circular excitation and left-handed circular detection. The PL is detected using a spectrometer (Princeton Instruments Acton 500 mm) and a liquid-nitrogen-cooled silicon-based charge-coupled device (CCD) array. The grating employed in the spectrometer has 600 grooves per mm. The PL in Fig. 5.1(b) clearly shows the emission of the $MoSe_2$ resonance (around 1.6 eV) and the ILE emission (around 1.38 eV). The center energy of the ILE emission varies across the sample, as further discussed in Chap. VII. The WSe_2 resonance can only be seen in Fig. 5.1(c), where the PL emission of the WSe_2 is magnified. Despite bright PL in monolayer TMDs [34], the PL in TMD heterostructures is significantly suppressed due to the rapid charge transfer in the heterostructure samples [29]. Fig. 5.1(c) also shows the excitation spectrum of the laser employed for the results in this chapter.

In Fig. 5.1(d), we show an MDCS spectrum acquired for $T = 600$ fs at a fluence

of 13 μJ/cm^2 per beam. Because the resonances in these heterostructure samples are very broad, even at the cryogenic temperatures (5 K) and low powers used for the measurements in this work, we add up two different measurements to obtain Fig. 5.1(d): A one-quantum rephasing measurement in which the first pump interaction is conjugate, and a one-quantum non-rephasing measurement in which the second pump interaction is conjugate (see Sec. 3.5.1). The resulting absorptive spectra [35] are spectrally narrower than the rephasing one-quantum spectra and allow us to discern the dynamics within this heterostructure further. In contrast to the rephasing spectra discussed in Sec. 3.6, the absorption energy in Fig. 5.1(d) is per convention positive.

The MDCS spectrum in Fig. 5.1 (d) shows four peaks. The two peaks on the diagonal (dashed line) correspond to the two resonances of the $MoSe_2$ and WSe_2 monolayers. Meanwhile, the two cross (or coupling) peaks with different absorption and emission energies indicate the presence of coupling between the two resonances. The spectral shift between features in PL and MDCS can be traced back to a combination of Stokes shift, spatial inhomogeneity, and limited bandwidth of the laser. From the roughly round shape of the on-diagonal peaks, we can deduce that the linewidths in this heterostructure sample are limited by the homogeneous linewidth. To confirm this conclusion, we fit cross-diagonal and on-diagonal slices of only the rephasing spectra according to the procedure outlined in Sec. 3.7.

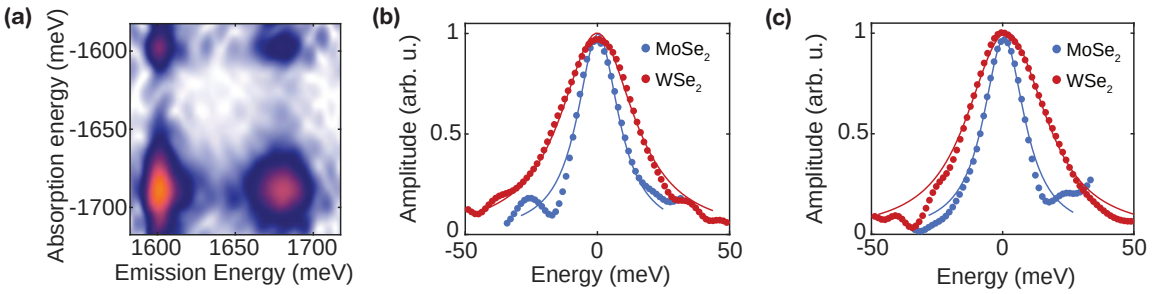

Figure 5.2: **(a)** Rephasing spectrum for the $MoSe_2/WSe_2$ heterostructure **(b)** Cross-diagonal slices for the $MoSe_2$ and WSe_2 peak (circles) with corresponding fits (solid line). **(c)** On-diagonal slices for the $MoSe_2$ and WSe_2 peak (circles) with corresponding fits (solid line).

Fig. 5.2(a) shows the rephasing spectrum for the heterostructure, which shows significantly broadened peaks compared to the absorptive spectra in Fig. 5.1(d). The linewidth of the peaks is further amplified due to the normalization of the rephasing spectrum by the laser spectrum, which enhances the wings of the spectrum. Since it is not essential to the time-dynamic effects observed in this chapter and increases noise, we only normalize the rephasing spectrum here with this procedure to extract quantitatively more accurate linewidths.

The cross-diagonal slices for the two resonances are plotted in Fig. 5.2 (b), and the on-diagonal slices are plotted in Fig. 5.2 (c). As outlined in Sec. 3.7, we fit the slices simultaneously for each resonance. The fits are indicated by the solid lines in Fig. 5.2 (b,c). We extract the homogeneous linewidths γ_{MoSe_2}=9.3 meV, γ_{WSe_2}=14.9 meV, and inhomogeneous linewidths σ_{MoSe_2}=1.4 meV, σ_{WSe_2}=5.7 meV. The fits are not well constrained at the peaks' edges because the spectrum's normalization procedure enhances noise features. Therefore, we weigh the fit with the amplitude to de-emphasize those data points. However, the fits still give a good estimate of the homogeneous and inhomogeneous linewidths within a factor of 1-2 and show a clear increase of the homogeneous linewidth compared to the literature, which has seen intrinsic (zero-temperature, zero-power) homogeneous linewidths of 0.26 meV for monolayer $MoSe_2$ [36] and 1.6 meV for monolayer WSe_2 [37]. The latter measurement was performed on a CVD-grown sample in a non-collinear geometry, substantially increasing the spot size at the sample. We cannot extract an intrinsic linewidth due to experimental limitations. However, the power- and temperature-dependent data the authors provide in their respective publications indicate that our intrinsic linewidth should, at best, be 2-3 times smaller than the values above, still showing a significant increase for the linewidths in the heterostructure compared to the monolayers. It is reasonable to assume that this increase is due to additional population decay channels, such as charge transfer, in the heterostructure.

5.3 Distinguishing Coupling via Time-Resolved Multidimensional Coherent Spectroscopy

Discerning any coupling between the excitons from the dominant charge transfer contribution is important. The temporal evolution of the off-diagonal coupling peaks in the MDCS spectrum is key to isolating the coupling. There are two likely sources for the occurrence of these peaks:

1. After excitation by a laser, electrons and holes bind together to form excitons in the $MoSe_2$ and WSe_2, respectively, as shown in Fig. 5.3 (a). These excitons can coherently interact (coherent coupling), as discussed in Sec. 2.7.2. This coupling manifests itself through an oscillating amplitude along T whose frequency matches the energy difference between the resonances, as illustrated in Fig. 5.3(b). Decay of the oscillations stems from dephasing processes. In an ideal chirp-free case, both coupling peaks oscillate in phase.

2. Incoherent coupling channels, such as energy or charge transfer, can also lead to the appearance of coupling peaks. As discussed in Sec. 2.7.1, charge transfer via electron and hole transfer, as illustrated in Fig. 5.3(a), with subsequent formation of the ILE, is common in these TMD heterostructures. For this coupling, separate level systems do not need to share a common ground state in contrast to the coherent coupling, as illustrated in Fig. 5.3(b). Here, the coupling manifests itself via a rise of the peak amplitude having a time scale characteristic of the transfer for these processes.

To better resolve the dynamics of the heterostructure and determine the coupling mechanisms, we take several MDCS spectra with varying T delay. We show exemplary spectra taken at $T = 25\,\text{fs}$, $50\,\text{fs}$, and 75 fs in Fig. 5.3 (c). The most notable changes between these spectra are a visible decay for the two on-diagonal peaks and varying

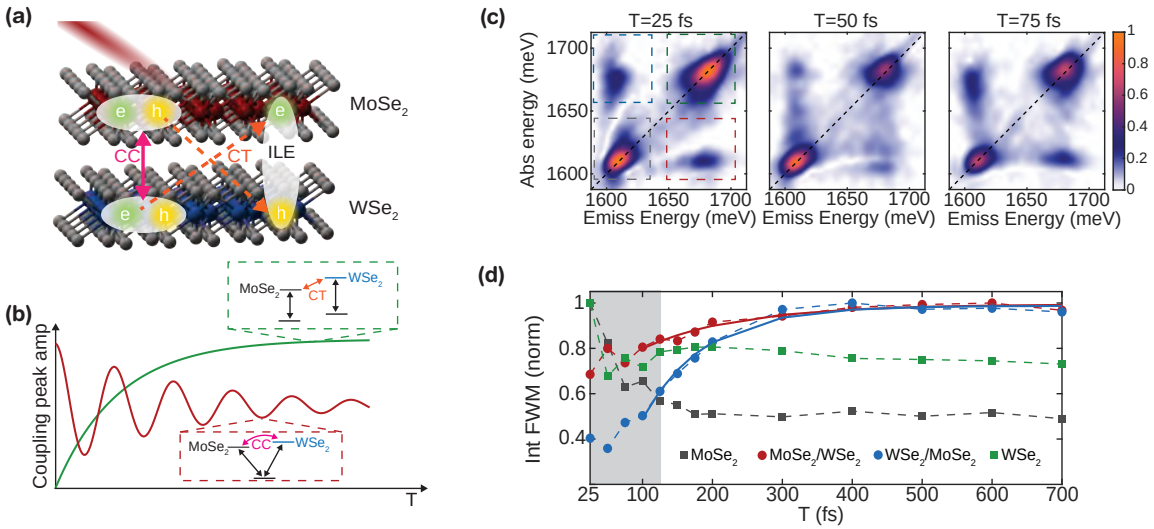

Figure 5.3: **(a)** Illustration of coherently coupled $MoSe_2$ and WSe_2 excitons and the dephasing of coherent coupling (CC) via incoherent charge transfer (CT), yielding ILEs in the heterostructure. **(b)** Characteristic coupling peak amplitude dynamics and associated level-systems for incoherent vs. coherent coupling. **(c)** Characteristic low-temperature, low-power multidimensional coherent spectra of the $MoSe_2/WSe_2$ heterostructure at time-delays T=25 fs, T=50 fs, and T=75 fs. All spectra are plotted on the same color scale, shown for the spectrum taken at $T = 600$ fs in Fig. 5.1 (d). **(d)** Integrated FWM of the four peaks in the MDCS spectrum. Integration areas are marked by the dashed boxes in (c). Also shown are exponential fits to the rising behavior of the two coupling peaks from 100 fs on (solid lines).

amplitude for the coupling peaks. Overall, the coupling peak amplitude increases over time (compare Fig. 5.1 (d)). To better visualize these dynamics, we spectrally integrate over each of the four peaks (integration area indicated by the dashed rectangles in Fig. 5.3 (c)) and plot the resulting integrated amplitudes in Fig. 5.3 (d). The decay of the on-diagonal peaks (squares)and the rise of the coupling peaks (circles) are visible. Moreover, the amplitude of the two cross-peaks shows features suggestive of oscillations, a strong indication of coherent coupling. The coherent coupling also explains the significant non-zero amplitude of the two peaks at early times.

The decay for both on-diagonal peaks occurs rapidly and noticeably faster than the rise of the coupling peaks. This decay can be explained by the multitude of processes, including charge transfer, rapid decay into dark or localized states, as reported for both materials in the literature [37, 38], and population decay into the

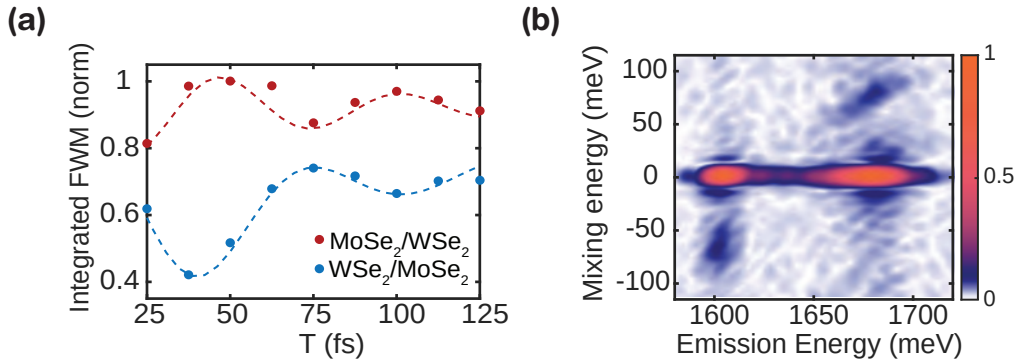

Figure 5.4: **(a)** High temporal resolution measurement of the two-coupling peaks from Fig. 5.3(b). Curves have been offset to increase readability. The $MoSe_2/WSe_2$ curve was recorded with positive intentional GDD, and the $WSe_2/MoSe_2$ curve was recorded with negative intentional GDD. **(b)** Zero-quantum spectrum, similar to Fourier-transforming with respect to the delay of a spectrally-resolved pump-probe experiment. Here, we added measurements taken with positive and negative intentional GDD. Complete data sets can be found in Sec. 5.4.

ground state, all of which affect the on-diagonal peaks. However, the rise of the coupling peaks occurs only due to processes that incoherently couple the two materials together, such as energy and charge transfer. Based on the extensive literature on these heterostructures [21, 22, 24, 39] and the similar time scale of the rise for the two coupling peaks, we deduce charge transfer to be the dominant incoherent coupling mechanism in this sample.

We fit an inverse exponential for $T \geq 100$ fs to the rise of the coupling peaks (solid lines), which yields an estimated rise time $\tau_{M\to W} < 149 \pm 28$ fs for the $MoSe_2/WSe_2$ peak and $\tau_{W\to M} < 91 \pm 9$ fs for the $WSe_2/MoSe_2$ peak, limited by the temporal resolution of 92 fs in our experiment (see Appendix A). These values are in good agreement with the charge transfer times in the literature for similar samples [21, 24, 27, 39, 40], which are in the range of 30 fs-600 fs.

5.3.1 Coherent Coupling

A separate data set with smaller T steps (range indicated by the gray area in Fig. 5.3 (d)), shown in Fig. 5.4 (a), resolves early time dynamics better. Both coupling

peaks show clear oscillations with a frequency around $\hbar\omega = 74\,\mathrm{meV}$, corresponding to the energy difference between the $MoSe_2$ and WSe_2 excitons. These oscillations are emphasized by plotting a decaying cosine with an exponential rise (dashed lines) as a guide to the eye. Since we see signatures of both coherent coupling and incoherent charge transfer, the resulting plots in Fig. 5.3(d) and Fig. 5.4(a) are the sum of a decaying oscillation and an exponential rise, as expected from Fig. 5.4(b).

A more quantitative measure of these oscillations can be obtained by taking a zero-quantum MDCS spectrum, introduced in Sec. 3.6.2. Because we use phase-resolved heterodyne detection, we can resolve the sign of the oscillation, which is different for the two coupling features in the zero-quantum spectrum shown in Fig. 5.4(b). The two features at zero mixing energy and $MoSe_2$ or WSe_2 emission energy correspond to the non-oscillating contributions of both on-diagonal and coupling peaks. Two features around a mixing energy of -74 meV and +71 meV can be seen for the $MoSe_2$ and WSe_2 emissions, respectively. Within the sample inhomogeneity, this matches the energy spacing between the $MoSe_2$ and WSe_2-A excitons. This agreement supports the assertion that excitons in the two materials are indeed coherently coupled and oscillate during T with a frequency determined by the energy difference of the two resonances. The broadness of the features stems from the fact that both coupling contributions decay rapidly along T. The low energy (10-20 meV) signatures are due to truncation effects. The nature of the coherent coupling is not immediately evident and needs further investigation. Common interactions that lead to coherent coupling are biexcitonic in nature, such as static dipole-dipole or exchange interactions, or due to mixing of the single exciton states, such as transition dipole (Förster) coupling [41, 42]. They can, for example, be distinguished by careful analysis of the real part of the MDCS spectrum, as demonstrated in [42]. Future experiments using double-quantum coherent spectroscopy can also provide insight into the nature of the coherent coupling [15, 16]. In the current stage, the rapid dephasing of coherent

coupling due to the rapid dephasing of the excitons, which is caused by the rapid charge transfer, limits applications of coherent coupling in these samples, and further work is required to transform this into viable applications. In Fig. 5.4 (a) and (b), we combine measurements with intentional small negative and positive GDD on the three excitation pulses, which enhances the coherent oscillations that are otherwise obscured by residual third-order dispersion. In the following section, we discuss the chirp dependence of coherent coupling and how applying intentional GDD can enhance the coherent coupling oscillation.

5.4 Chirp Dependence of Coherent Coupling

The time resolution for incoherent and coherent dynamics is essentially different. In this section, we discuss the chirp dependence of both coherent and incoherent dynamics. While the chirped pulse duration limits the incoherent dynamics, the measurement of the coherent processes, in theory, is not affected by chirp and is given by the transform-limited pulse. However, as demonstrated here, there are intricacies regarding dephasing that render efficient dispersion control necessary for the observation of coherent coupling.

Fig. 5.5 shows the coherent coupling measurements with negative intentional and positive intentional GDD that are the components of Fig. 5.4 (a). We apply this chirp by adjusting the grism distance in the Grism compressor discussed in Appendix A. While this slightly affects the third-order dispersion, too, the effect is negligible here. The integrated FWM curves are normalized to their respective maximum and offset. The offset between the curves in Fig. 5.5 is chosen arbitrarily to enhance visibility. We also plot a decaying oscillation together with an exponential rise as a guide-to-the-eye. The time-zero for the exponential rise is adjusted for some of the guide-to-the-eye curves presented here because the chirp shifts the time-zero for transfer dynamics along T.

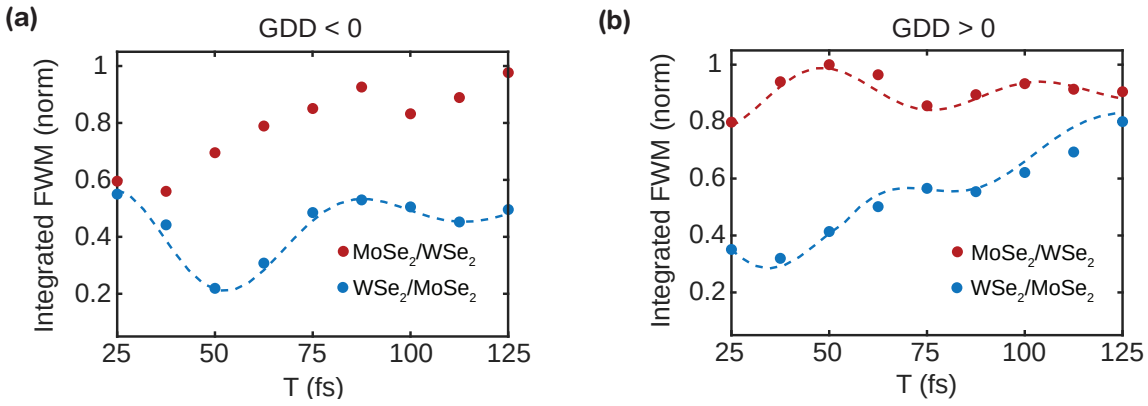

Figure 5.5: Chirp dependence of the two coupling peak amplitudes in one-quantum spectra for **(a)** negative GDD and **(b)** positive GDD. The $MoSe_2/WSe_2$ curve in (a) has no guide-to-the-eye because it lacks a visible decaying oscillation.

In Fig. 5.5 (a), we detuned the GDD to be negative. As a result, the oscillation on the $WSe_2/MoSe_2$ coupling peak can be resolved, while the $MoSe_2/WSe2_2$ coupling peak only shows a weak oscillatory feature. Because of the chirp, the rise of the coupling peak has occurred at negative T delays here and thus does not show up for the $WSe_2/MoSe_2$ coupling peak, while the peak rise is the dominant contribution for the $MoSe_2/WSe_2$ peak. In Fig. 5.5 (b), we detune the GDD to be positive. Here, the $MoSe_2/WSe_2$ peak has a visible oscillation with no significant exponential rise, as explained above. Even the $WSe_2/MoSe_2$ shows a residual oscillation, although the rising behavior obstructs it, and the oscillation is not as pronounced as in Fig. 5.5 (a).

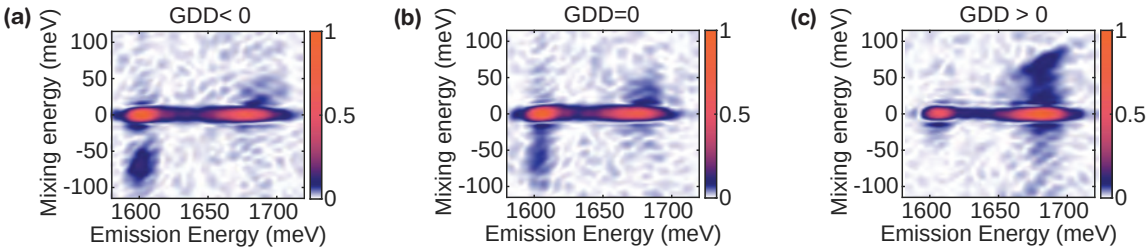

Figure 5.6: Zero-quantum spectra **(a)** in the presence of additional negative GDD, **(b)** with no intentional GDD but residual third-order dispersion (TOD), and **(c)** with additional positive GDD. The coherent coupling between $MoSe_2$ and $WSe2_2$ can be clearly resolved for negative and positive intentional GDD.

We similarly adjust the chirp for the zero-quantum measurements. The spectra

provided in Fig. 5.4 are a combination of Fig. 5.6 (a), which shows the zero-quantum spectrum for negative GDD, and Fig. 5.6 (c), which shows the zero quantum spectrum for positive GDD. We also show a zero intentional GDD (and thus limited by the third-order dispersion (TOD)) spectrum in Fig. 5.6 (b). Similarly to Fig. 5.5, we can resolve the coherent coupling from WSe_2 to $MoSe_2$ with intentional negative GDD in Fig. 5.6 (a) and the coherent coupling from $MoSe_2$ to WSe_2 with intentional positive GDD in Fig. 5.6 (c). For the positive GDD case, we have removed values below T=25 fs for Fig. 5.4, eliminating some spurious contributions at intermediate mixing energies. However, we did not remove the values here to simplify the comparison with the simulations below. Even in the zero intentional GDD case, we can retain features reminiscent of the two coupling peaks. The broad features extending toward negative mixing energies for the $MoSe_2$ emission and towards positive mixing energies for the WSe_2 emission are reminiscent of coherent coupling. They show up at lower mixing energies because only the edges of the broad resonances closer together in energy (and thus timing) contribute to these zero-quantum spectra.

5.4.1 Temporal Resolution in the Context of Coherent Coupling

The temporal resolution of 100 fs referred to earlier refers to the temporal resolution of the charge transfer and does not immediately translate into the temporal resolution for the coherent oscillations. The reason for the difference is the different nature of coherent and incoherent dynamics and how they are affected by chirp and overall pulse duration. As discussed by Tekavec *et al.* [43], absorption frequencies exceeding 400 THz, corresponding to sub-3 fs oscillation in the temporal domain, can be readily resolved by scanning the τ delay stage between the two pump pulses whose pulse duration exceeds 200 fs in their experiment. The reason is that, despite the dispersion, as the τ stage is scanned, the phase of the FWM signal evolves rapidly with the period determined by the resonance energy. This consideration is similarly

true for a linear pulsed Fourier transform experiment, as can be easily shown from

$$P^{(1)}(t) \propto ie^{-i\omega_0 t} \int_0^\infty \mathrm{d}t'_1 E(t-t_1)e^{-t_1/T_2}, \tag{5.1}$$

for arbitrary chirp [44]. In this case, the temporal amplitude and phase, corresponding to a chirped pulse, only contribute as a constant.

Incoherent dynamics along T are limited in their resolution by chirped pulses. However, the evolution of coherences along T, as is the case for the coherent coupling described in this chapter, can be resolved with chirped pulses, as long as their bandwidth covers the oscillation period in the temporal domain. Therefore, the temporal resolution for the coherent coupling is the transform-limited pulse duration. However, there are conditions under which chirped pulses, partially or entirely, obscure the coherent oscillations. Therefore, we use the intentional chirp in our experiments to properly resolve the coherent oscillations. The chirp dependence of coherent oscillations can be best understood from the following simplified density matrix description: For the example of one coupling peak, a coherent oscillation can be thought of as the following evolution of the matrix elements of the density operator ρ: $|0\rangle\langle M| \rightarrow |W\rangle\langle M| \rightarrow |W\rangle\langle 0|$, where the respective states occur after interaction with pulse A, B, and C respectively. Here, the $|M\rangle$ and $|W\rangle$ states are the $MoSe_2$ and WSe_2 exciton states, respectively.

In order to observe coherent oscillations, two critical conditions have to be fulfilled:

1. When the third pulse arrives to convert the $\langle M|$ state into $\langle 0|$, the $|0\rangle\langle M|$ coherence cannot have fully dephased yet.

2. Similarly, the $|W\rangle\langle 0|$ coherence that mixes with the $|0\rangle\langle M|$ coherence during T cannot have fully dephased by the time the third pulse arrives.

To meet these conditions, the dispersion thus needs to be optimized. In the

ideal case of no dispersion, this is trivial. However, with the dominant higher-order dispersion in our experiment, the intentional GDD is necessary to sufficiently fulfill these conditions and observe a coherent oscillation indicative of the coupling of the two exciton states.

This explanation for the temporal resolution and chirp dependence of coherent coupling significantly simplifies the complex dynamics of the system, especially in the presence of dispersion. In the following, we present a full model of the sample system using the OBEs.

5.5 Simulation of Multidimensional Coherent Spectra in the Presence of Arbitrary Laser Pulses

To fully support the conclusions of this simplified explanation, we simulate different level systems using the optical Bloch equations (Eq. 3.30) introduced in Chap. III. For the most general solution to Eq. 3.30, we incorporate our pulse's spectral amplitude and phase and negative, positive, and no intentional chirp, as applied in the experiment, into the system Hamiltonian H. Other parameters used for dephasing and resonance energies can be found in table 5.1.

γ_{0M}	γ_{0W}	γ_{MW}	γ_{MM}, γ_{WW}
12.5 ps^{-1}	20 ps^{-1}	6.67 ps^{-1}	20 ps^{-1}
E_M	E_W	μ_{0M},μ_{0W}	E_0
1610 meV	1680 meV	50 Debye	2,000 kV/m

Table 5.1: Parameters used in the simulation of the OBEs. For simplicity, we assumed equal transition dipole moments for $MoSe_2$ and WSe_2.

Since the OBEs make no approximation about the order of the interaction, the resulting solutions would contain all contributions to the polarization from 0th to (technically) infinitely high orders, although lower orders dominate the resulting polarization. In order to filter out the FWM contributions detected in our experiment,

we implemented a discrete phase-cycling scheme in the simulation. We subsequently emulate the lock-in amplifier in our setup that filters out the heterodyne-detected sample response. It is important to filter out the response *a posteriori* since saturation effects, which result from lower- and higher-order signal contributions, can still affect the third-order nonlinear response.

5.5.1 One-Quantum Spectra

We first simulate the rephasing one-quantum spectra with varying T with the measured pulses and intentionally added GDD of -1500 fs^2, 0 fs^2, and +1500 fs^2. We do not incorporate charge transfer into the simulation except for a rapid population decay for $MoSe_2$ and WSe_2. The results of this simulation are shown in Fig. 5.7. We only simulate the rephasing spectrum instead of adding non-rephasing and rephasing as in Fig. 5.3 for the sake of simplicity.

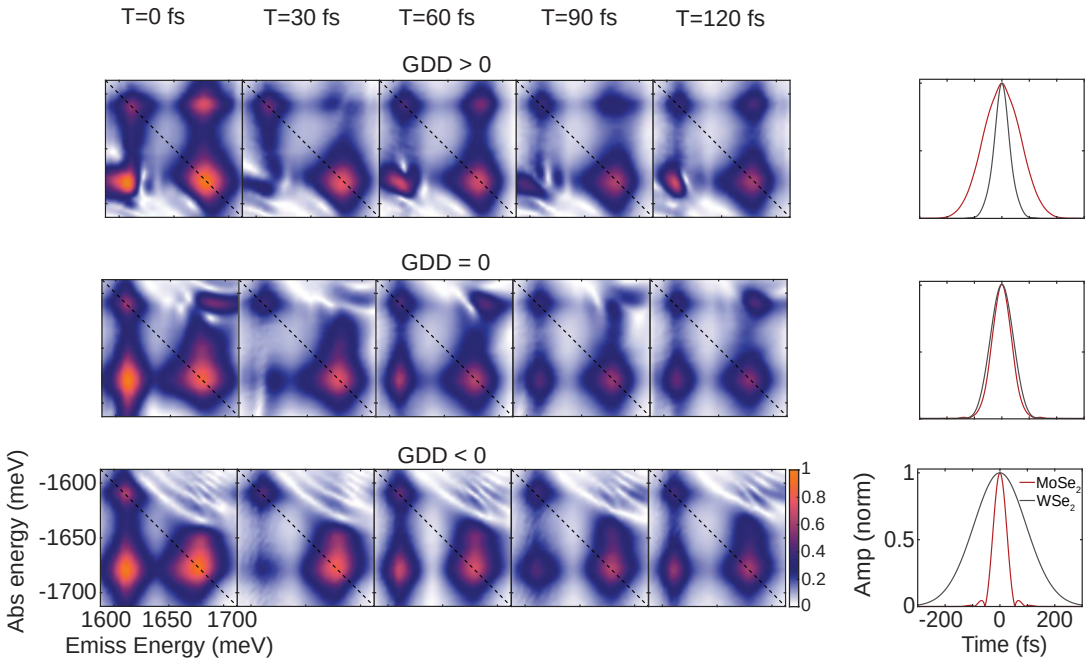

Figure 5.7: Simulated MDCS rephasing one-quantum spectra for varying T delays with the parameters detailed in table 5.1 and additional GDD of -1500 fs^2 (GDD<0), 0 fs^2 (GDD=0), and +1500 fs^2 (GDD>0). The resulting interaction windows for the two resonances are shown on the right.

As can be seen from the middle panel of Fig. 5.7, when no intentional GDD is added, the upper right coupling peak looks distorted for early times, an indicator of dispersion effects. However, a small oscillation of this peak's amplitude can still be seen. Nonetheless, the dominant oscillation is on the bottom left coupling peak, whose profile is much less distorted. When adding negative GDD to the pulse in the simulation, the lower left coupling peak is even less distorted (compare T=30 fs), while the upper right coupling peak is essentially non-existent due to the aforementioned limitations related to dephasing for this peak. In contrast, when adding additional positive GDD, the bottom left coupling peak gets distorted, while the upper right coupling peak now shows significantly less distortion and an apparent amplitude oscillation. The resulting interaction windows for the two resonances, as defined in [45], are shown on the right of the respective simulations. The intentional GDD narrows one of the interaction windows while significantly lengthening the other. Thus, the simulations indicate that despite a nominal temporal resolution well above the oscillation frequency, an amplitude oscillation can be observed for the coupling peaks.

5.5.2 Zero-Quantum Spectra

We employed the same OBE solver to show that zero-quantum spectra of a V-level system vs. two uncoupled two-level systems, even in the presence of chirp, can be distinguished, further strengthening the evidence of the observation of coherent coupling.

We simulate two independent two-level systems and a V-Level system in which the two excited states are coupled via a common ground state. The simulation allows us to see if we can distinguish between coherent coupling in a V-Level system and chirp-related contributions to two independent two-level systems in the zero-Quantum spectra in the presence of complex chirp.

We exemplarily plot the results of the simulations in Fig. 5.8 for additional GDD

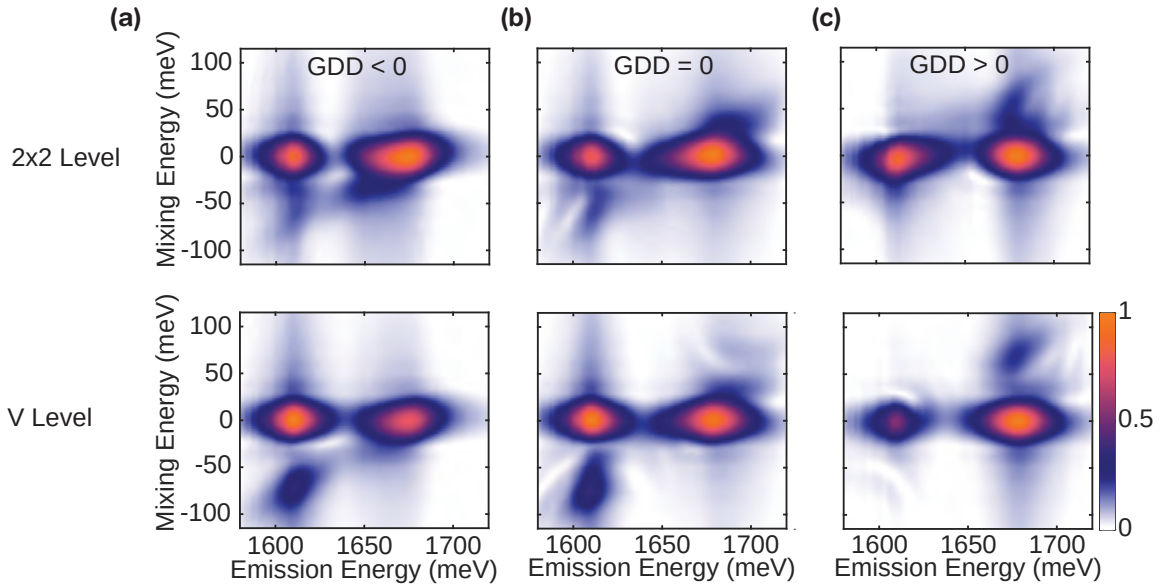

Figure 5.8: OBE simulations of zero-quantum spectra for two independent two-level systems and a V-Level system in the presence of higher-order residual chirp and intentional GDD of -1500 fs^2 **(a)**, 0 fs^2 **(b)**, and 1500 fs^2 **(c)**.

= -1500 fs^2 (a), GDD = 0 fs^2 (b), and GDD = 1500 fs^2 (c). Note the different color axes from the experimental results.

It is evident from these figures that a V-Level and two independent two-level systems can be distinguished, despite the influence of chirp. While both systems show somewhat of a contribution around the correct mixing energy around -74 meV in Fig. 5.8(a), for the two two-level systems, it is only a weak tail with a maximum at much lower mixing energies and emission energies between the two resonances. However, there is an emphasized peak around -74 meV for the V-Level system, in much better agreement with the experimental results. Moreover, for zero additional GDD, there is a distinct peak at the correct mixing energy for the V-Level system that does not occur for the two two-level systems. Our data shows a peak around -60 meV in this case (see Fig. 5.6(b)). For positive GDD, the mixing peak is more pronounced for a V-Level system, while the independent two-level systems again only show a peak stretching out from zero mixing energy. All observations considered, it is evident that our data does not match a simple two-level system but instead

resembles the behavior of a V-Level system. The data and simulations for the V-Level system agree well enough and are distinguished enough from two two-level systems that we are confident that we are indeed resolving coherent coupling in the heterostructure. Moreover, we have shown oscillations of the coupling peaks in the one-quantum spectra, which do not occur for two independent two-level systems. We did not fine-tune the simulation parameters to get maximum agreement between the simulation and data because there are too many unconstrained variables. Instead, the simulation illustrates that despite complex chirp, a V-Level and two independent two-level systems can be clearly distinguished in a zero-quantum spectrum.

5.6 Intermediate Dynamics and Interlayer Exciton Binding Energy

We furthermore acquired MDCS spectra with varying T delay over an intermediate (500 fs-5 ps) to long-term (150 ps-600 ps) time range, whose integrated peak amplitudes are shown in Fig. 5.9. The plot starts at 500 fs, after the initial coupling peak rise and on-diagonal peak decay. The displayed data consists of three datasets taken separately due to sample drift considerations. The three measurement ranges are 0.5-10.5 ps, 10.5-50.5 ps, and 50.5-600.5 ps. Measurements are repeated several times and discarded if sample drift has been observed between datasets. The separate time-range measurements are combined by overlapping points between them (10.5 ps and 50.5 ps) and are normalized to the integrated peak amplitudes at T=500 fs from the early-time measurement (not displayed, but part of the data set in Fig. 5.3(c)).

Fig. 5.9 clearly shows two separate decays, one on a scale of a few picoseconds and another on a scale of hundreds of picoseconds. In the literature, commonly, bi-exponential decays are fitted for the two time scales. However, bi-exponential fits are not a suitable model in our case because of the superposition of different dynamics we

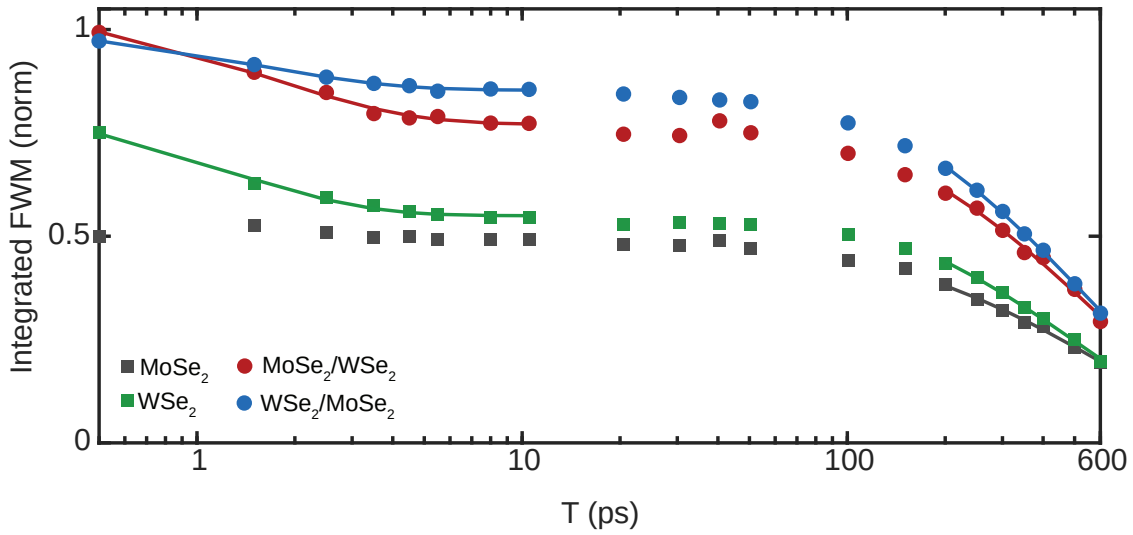

Figure 5.9: Integrated FWM of the four peaks in the MDCS spectrum for intermediate and long times (500 fs-600 ps).

can resolve in MDCS. Since the time scales of the early (fast) and late (slow) decay differ by over two orders of magnitude, it is reasonable to separate the fits into two independent exponentials and disregard the intermediate temporal dynamics from 5-100 ps. The fits show good agreement with the data, justifying the model of fitting two separate exponentials.

Within the first 5 ps, three of the four peaks (except the $MoSe_2$ peak) display an amplitude decay, followed by another decay of all four peaks for $T \geq 100$ ps. This behavior is consistent with the literature, which reports bi-exponential time scales in these samples' intermediate and long-term dynamics [23, 24, 26]. In contrast to previous experiments, which look at the coupling dynamics in an isolated setting, the MDCS approach reveals distinctly different decay constants for the four peaks. The difference in decay constants hints at a superposition of dynamics that cannot be obtained in the selective experiments in the literature. On the intermediate time scale, the $MoSe_2/WSe_2$ peak (τ=1.22±0.12 ps), as well as the WSe_2 peak (τ=1.51±0.12 ps) decay quicker and with a larger amplitude than the $WSe_2/MoSe_2$ peak (τ=1.69±0.16 ps) and $MoSe_2$ peak (no fit). Here, τ denotes the decay constant

from a simple exponential decay. Competition between several dynamical processes can explain this surprising behavior.

The difference in decay between the $MoSe_2$ and WSe_2 during the first 5 ps warrants further study. However, the likely explanation is energy transfer from WSe_2 into the $MoSe_2$ that contributes on these intermediate time scales [22]. We attribute the initial decay of the coupling peaks to the phonon-assisted relaxation of momentum-space "hot" ILEs [28] into a tightly bound ILE state. Either the difference in many-body effects of the hot vs. tightly bound ILE or the fact that the hot ILEs are more prone to electron-hole recombination than their tightly bound counterparts can explain an initial decay of the coupling peaks. Both processes would indirectly affect the intralayer excitons and, thus, the coupling peak strength. In the case of altered many-body effects, the changed interactions between ILEs and intralayer excitons that lead to the occurrence of the coupling peak in the first place would affect the coupling peak amplitude. In the case of electron-hole recombination, the initial recombination of electrons and holes would fill the ground state, reducing the peak amplitude. After the formation of tightly bound ILE states, this relaxation into the ground state occurs on a much longer time scale.

After initial relaxation of the "hot" ILEs, the FWM amplitudes stagnate during intermediate times (10-100 ps). The long-term decay of hundreds of picoseconds does not noticeably contribute during these time scales. The long-term decay, which is fitted separately due to competing dynamics at early times, shows a roughly uniform time scale for all four peaks: The $MoSe_2$ on-diagonal peak ($\tau = 607 \pm 22$ ps), WSe_2 on-diagonal peak ($\tau = 520 \pm 13$ ps), $MoSe_2/WSe_2$ coupling peak ($\tau = 580 \pm 28$ ps), and $WSe_2/MoSe_2$ coupling peak ($\tau = 540 \pm 8$ ps) all show decay times in the range of 500-600 ps within the uncertainty of the measurement and noise. We attribute this decay to the ILE population decay. The literature has reported ILE lifetimes from hundreds of picoseconds to hundreds of nanoseconds, depending on the twist

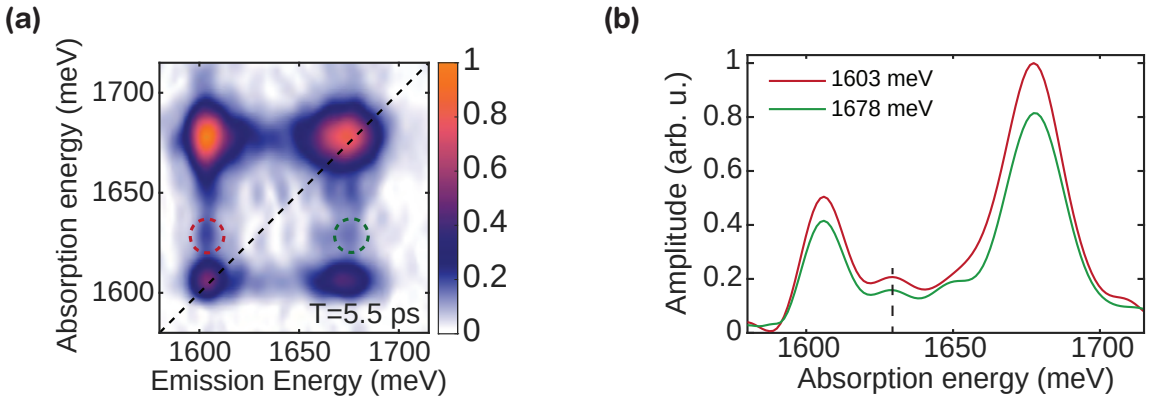

Figure 5.10: **(a)** Characteristic low-temperature, low-power multidimensional coherent spectrum of the $MoSe_2/WSe_2$ heterostructure at a pump-probe time-delay of T=5.5 ps. **(b)** Slices of fixed emission energy taken along the absorption energy axis. The dashed line indicates the absorption energy for the ILE feature.

angle and other sample parameters [29, 46–49], with [46] reporting a decay time of 1.3 ns for a 1° twist angle, increasing by more than an order of magnitude for a 3.5° twist angle. Given the near zero-twist angle of the sample studied in this report and common sample-to-sample variations, our values are in good agreement with these findings.

After the relaxation of the hot ILEs, another signature of the ILE is obtained in the MDCS spectra. An MDCS spectrum with a T delay of 5.5 ps is shown in Fig. 5.10 (a). The features that show absorption at continuum energies around 1629 meV and emission at the $MoSe_2$ and WSe_2-A exciton resonances (dashed circles) have no visible corresponding on-diagonal peaks and no emission at comparable energies. Therefore, these spectral features cannot be due to another material resonance. Instead, we believe these features occur due to the continuum absorption generating free interlayer electron/hole pairs, which subsequently affect the emission of the $MoSe_2$ and WSe_2 excitons via many-body effects. The weak absorption by the free interlayer electron-hole pairs is compensated by their very strong Coulomb interaction with the excitons. Similar effects have been observed in GaAs QWs [41, 50]. Two slices, taken at fixed emission energies of 1603 meV and 1678 meV along the absorption energy

axis are displayed in Fig. 5.10 (b). We determine the ILE absorption feature to be at 1629 meV from the slices. From our PL measurement in Fig. 5.1(b), the ILE emission is known to be at 1.375 eV. From the difference between these energies, we deduce the binding energy of the ILEs in this sample to be around 254 meV. This value is in excellent agreement with a recently performed first principle calculation [30], which estimates the binding energy to be around 250 meV, and above other theoretically predicted values [33]. This binding energy is consistent with previously measured binding energies in these samples at 110 K using micro-angle-resolved photoemission spectroscopy (ARPES) and PL [51] and two times larger than measured binding energies in a WSe_2/WS_2 heterostructure [28].

As alluded to previously, many measurements of TMDs are taken on single spots or magic samples. To render the observations and conclusions in this chapter meaningful, we are thus interested in the reproducibility of the sample dynamics. In the following section, we present MDCS data on a second $MoSe_2/WSe_2$ heterostructure.

5.7 Data on Second $MoSe_2/WSe_2$ Heterostructure

Figure 5.11: Microscope image of the second $MoSe_2/WSe_2$ heterostructure sample. This heterostructure sample contains a 3 nm graphite lead on top and a 5 nm graphite lead at the bottom.

We have obtained data on a second, similar $MoSe_2/WSe_2$ heterostructure sample that shows that all the dynamics - the peak rise due to charge transfer, the coherent

coupling between the two materials, and any intermediate and long-term dynamics - are highly reproducible and not sample-specific. A microscopy image of the heterostructure sample is shown in Fig. 5.11. The $MoSe_2$ layer is placed on top of the WSe_2 layer. The sample is encapsulated in hBN and contains a 5 nm graphite lead at the bottom and a 3 nm graphite lead at the top.

In Fig. 5.12(a), we show the MDCS spectrum with rephasing and non-rephasing contributions added. Despite adding the two contributions, the four peaks are overall less separated than for the heterostructure presented in Fig. 5.1. The increased overlap between peaks is partially due to the resonance energy of the $MoSe_2$ being roughly 15 meV higher in this material and partially because the $MoSe_2$ peak is significantly broader. While the absolute time scales differ, it is evident from Fig. 5.12(b) that the dynamics agree with the other heterostructure qualitatively: We see a rapid decay of the on-diagonal peaks, accompanied by a rapid rise for the two coupling peaks. The broader linewidths correlate with faster charge transfer (67 fs from WSe_2 to $MoSe_2$ and 85 fs from $MoSe_2$ to WSe_2), supporting the statement in Sec. 5.2 that the new dephasing channels are significantly influenced by population decay due to charge transfer.

We also again see a signature of coherent coupling at early times, with non-zero amplitudes for the coupling peaks and residual oscillations, which can be supported by the zero-quantum spectrum in Fig. 5.12 (c). This zero-quantum spectrum was taken at zero additional GDD, and the center of the zero-quantum peaks is thus slightly lower than the 55 meV energy difference between the resonances in the two materials. The intermediate and long-term dynamics in Fig. 5.12(d) also show a behavior very similar to the one observed for the heterostructure discussed in Fig. 5.9. At intermediate times, the WSe_2 peak and the $MoSe_2/WSe_2$ see a significant decay while the $WSe_2/MoSe_2$ peak barely decays and the $MoSe_2$ peak rises. Again, the peaks decay at longer time scales (891 ± 36 ps, 861 ± 55 ps, 634 ± 35 ps, 615 ± 30 ps

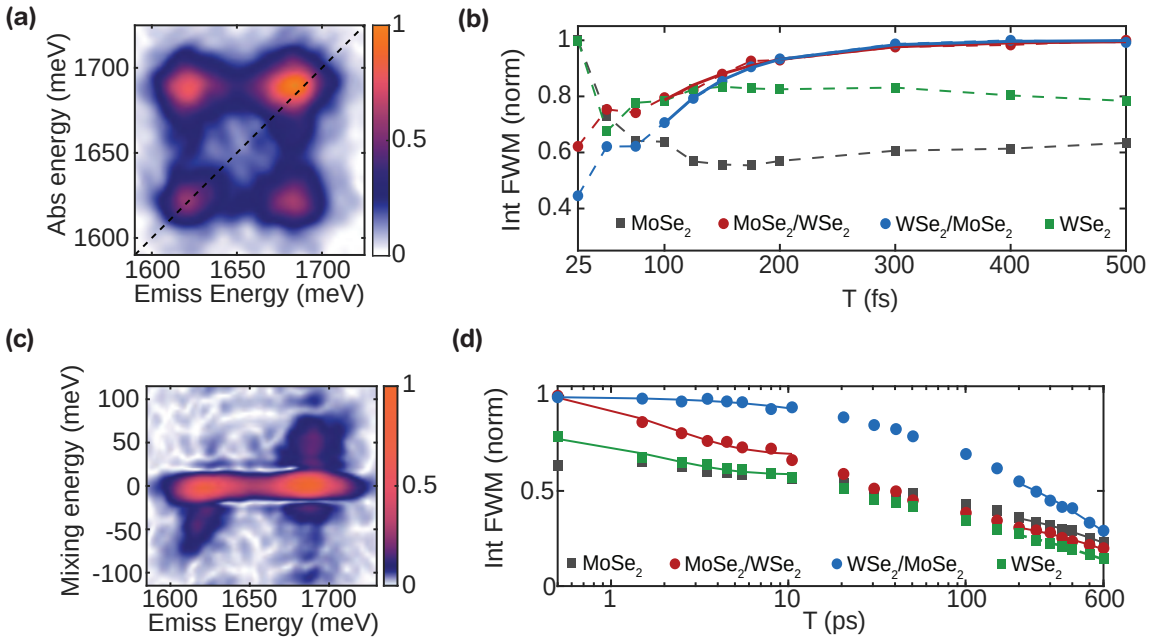

Figure 5.12: **(a)** One-quantum MDCS spectrum at $T = 600\,\text{fs}$ taken on a similar $MoSe_2/WSe_2$ heterostructure. **(b)** Early peak dynamics for the sample, showing exponential fits to the rise of the coupling peaks (solid lines) **(c)** Zero-quantum MDCS spectrum for no intentional GDD **(d)** Intermediate/long-term peak dynamics with exponential fits (solid lines).

from left to right, top to bottom), which we attribute to the ILE relaxation.

5.8 Conclusions and Outlook

In this chapter, we use MDCS to study the coherent exciton-exciton interactions and exciton dynamics in a $MoSe_2/WSe_2$ heterostructure. We show that the linewidths of the $MoSe_2$ and WSe_2 resonances in the heterostructure are in the homogeneous limit, dominated by exciton population decay caused by charge transfer. We use MDCS to disentangle the contributions of coherent and incoherent coupling to the FWM signal through a T-dependence of the MDCS spectra. We quantify the electron transfer from WSe_2 to $MoSe_2$ happening on a characteristic time $\tau_{W\to M} < 91\pm9\,\text{fs}$ and the hole transfer from $MoSe_2$ to WSe_2 to happen with a characteristic time $\tau_{M\to W} < 149\pm28\,\text{fs}$.

We further observe strong signatures of coherent coupling between the excitons

in the $MoSe_2$ and WSe_2 layer in both one-quantum and zero-quantum MDCS. We model the system with different level systems and numerically solve the OBEs for the residually-chirped input pulses to demonstrate that despite residual chirp, the experiment is sensitive toward coherent coupling. The observations are a logical evolution and continuation of the observation of coherent coupling between excitons and trions in TMD monolayers [20]. While further work, e.g., using the absolute phase to analyze the real part of the signal similar to Ref. 42, is necessary to determine the nature of the coherent coupling, the existence of it opens the avenue for quantum coherent control, an essential aspect of quantum computing. Moreover, we measure complex intermediate and long-term temporal dynamics of the MDCS spectrum peaks, containing dynamics of the phonon-assisted relaxation of momentum-space "hot" ILEs into a tightly bound ILE state, and the radiative decay of ILEs. Lastly, we observe a many-body signature of the ILEs in the MDCS spectrum and determine the binding energies of these ILEs to be 254 meV from a combination of MDCS and PL measurements.

These results manifest a significant step towards a better understanding of TMDs - characterizing both electron and hole transfer in a non-isolated setting has only been realized in our work and the work by Policht *et al.* [27], which was published simultaneously. Moreover, coherent coupling had not been observed in TMD heterostructure before, mainly because the MDCS experiments studying TMDs [20, 42] did not have sufficient bandwidth. As illustrated in this chapter, increasing the bandwidth comes with experimental challenges that we were able to overcome. Lastly, few reports of the ILE binding energy for TMD heterostructures have been published [28, 51], and a majority of studies have been theoretical [30, 33]. Our measurements further corroborate the expectations of high binding energies for the ILEs, which renders them promising candidates for room-temperature device applications.

While unraveling interesting physical phenomena, the work in this chapter also

served as proof of principle for our experimental setup. When I joined this project, the broadband Ti:Sapph had just been installed, and double passing had just been set up. As a result, there were numerous experimental challenges that had to be met in order for these experiments to work, including implementing pulse-chirp compensation and integration of continuous scanning and the MONSTR Sense Technologies electronics and software. Early during the experiments, we noticed inconsistencies in the spectra and overall FWM strength across the sample. These observations motivated us to go further and dream bigger: Spatially-addressed MDCS had been previously realized [38, 52–54]; however, long acquisition times associated with MDCS spectra and slow imaging had been significant barriers to widespread adoption. More specifically, in our experiment, sample stability could not be guaranteed on the time scale of hours. We thus wanted to incorporate rapid laser-scanning imaging with our spectroscopy experiments - which required the invention of a custom lock-in amplifier, detailed in the next chapter.

References

[1] K.-J. Boller, A. Imamo ğlu, and S. E. Harris. "Observation of electromagnetically induced transparency". In: *Phys. Rev. Lett.* 66 (20 May 1991), pp. 2593–2596. DOI: 10.1103/PhysRevLett.66.2593.

[2] J. E. Field, K. H. Hahn, and S. E. Harris. "Observation of electromagnetically induced transparency in collisionally broadened lead vapor". In: *Phys. Rev. Lett.* 67 (22 Nov. 1991), pp. 3062–3065. DOI: 10.1103/PhysRevLett.67.3062.

[3] S. E. Harris. "Lasers without inversion: Interference of lifetime-broadened resonances". In: *Phys. Rev. Lett.* 62 (9 Feb. 1989), pp. 1033–1036. DOI: 10.1103/PhysRevLett.62.1033.

[4] Marlan O. Scully, Shi-Yao Zhu, and Athanasios Gavrielides. "Degenerate quantum-beat laser: Lasing without inversion and inversion without lasing". In: *Phys. Rev. Lett.* 62 (24 June 1989), pp. 2813–2816. DOI: 10.1103/PhysRevLett.62.2813.

[5] A. S. Zibrov, M. D. Lukin, D. E. Nikonov, L. Hollberg, M. O. Scully, V. L. Velichansky, and H. G. Robinson. "Experimental Demonstration of Laser Oscillation without Population Inversion via Quantum Interference in Rb". In: *Phys. Rev. Lett.* 75 (8 Aug. 1995), pp. 1499–1502. DOI: 10.1103/PhysRevLett.75.1499.

[6] Monique Combescot, Roland Combescot, and François Dubin. "Bose-Einstein condensation and indirect excitons: a review". In: *Reports on Progress in Physics* 80.6 (Mar. 2017), p. 066501. DOI: 10.1088/1361-6633/aa50e3.

[7] Nikolaus Flöry, Achint Jain, Palash Bharadwaj, Markus Parzefall, Takashi Taniguchi, Kenji Watanabe, and Lukas Novotny. "A $WSe_2/MoSe_2$ heterostructure photovoltaic device". In: *Applied Physics Letters* 107.12 (2015), p. 123106. DOI: 10.1063/1.4931621.

[8] Ji Eun Kim, Won Tae Kang, Van Tu Vu, Young Rae Kim, Yong Seon Shin, Ilmin Lee, Ui Yeon Won, Boo Heung Lee, Kunnyun Kim, Thanh Luan Phan, Young Hee Lee, and Woo Jong Yu. "Ideal PN photodiode using doping controlled WSe_2-$MoSe_2$ lateral heterostructure". In: *J. Mater. Chem. C* 9 (10 2021), pp. 3504–3512. DOI: 10.1039/D0TC05625A.

[9] David Press, Thaddeus D. Ladd, Bingyang Zhang, and Yoshihisa Yamamoto. "Complete quantum control of a single quantum dot spin using ultrafast optical pulses". In: *Nature* 456.7219 (Nov. 2008), pp. 218–221. ISSN: 1476-4687. DOI: 10.1038/nature07530.

[10] J. Berezovsky, M. H. Mikkelsen, N. G. Stoltz, L. A. Coldren, and D. D. Awschalom. "Picosecond Coherent Optical Manipulation of a Single Electron Spin in a Quantum Dot". In: *Science* 320.5874 (2008), pp. 349–352. ISSN: 0036-8075. DOI: 10.1126/science.1154798.

[11] M. Koch, J. Feldmann, G. von Plessen, E. O. Göbel, P. Thomas, and K. Köhler. "Quantum beats versus polarization interference: An experimental distinction". In: *Phys. Rev. Lett.* 69 (25 Dec. 1992), pp. 3631–3634. DOI: 10.1103/PhysRevLett.69.3631.

[12] Shengnan Miao, Tianmeng Wang, Xiong Huang, Dongxue Chen, Zhen Lian, Chong Wang, Mark Blei, Takashi Taniguchi, Kenji Watanabe, Sefaattin Tongay, Zenghui Wang, Di Xiao, Yong-Tao Cui, and Su-Fei Shi. "Strong interaction between interlayer excitons and correlated electrons in WSe_2/WS_2 moiré superlattice". In: *Nat Commun* 12 (2021). DOI: 10.1038/s41467-021-23732-6.

[13] J. Pawłowski, M. Bieniek, and T. Wozniak. "Valley Two-Qubit System in a MoS_2-Monolayer Gated Double Quantum dot". In: *Phys. Rev. Applied* 15 (5 May 2021), p. 054025. DOI: 10.1103/PhysRevApplied.15.054025.

[14] Pedro Miguel M.C. de Melo, Pedro Miguel, Zeila Zanolli, and Matthieu J. Verstraete. "Optical Signatures of Defect Centers in Transition Metal Dichalcogenide Monolayers". In: *Advanced Quantum Technologies* 4.3 (2021), p. 2000118. DOI: https://doi.org/10.1002/qute.202000118.

[15] Gaël Nardin, Galan Moody, Rohan Singh, Travis M. Autry, Hebin Li, Francois Morier-Genoud, and Steven T. Cundiff. "Coherent Excitonic Coupling in an Asymmetric Double InGaAs Quantum Well Arises from Many-Body Effects". In: *Phys. Rev. Lett.* 112 (4 Jan. 2014), p. 046402. DOI: 10.1103/PhysRevLett.112.046402.

[16] G. Moody, I. A. Akimov, H. Li, R. Singh, D. R. Yakovlev, G. Karczewski, M. Wiater, T. Wojtowicz, M. Bayer, and S. T. Cundiff. "Coherent Coupling of Excitons and Trions in a Photoexcited CdTeCdMgTe Quantum Well". In: *Phys. Rev. Lett.* 112 (9 Mar. 2014), p. 097401. DOI: 10.1103/PhysRevLett.112.097401.

[17] Elad Harel, Sara M. Rupich, Richard D. Schaller, Dmitri V. Talapin, and Gregory S. Engel. "Measurement of electronic splitting in PbS quantum dots by two-dimensional nonlinear spectroscopy". In: *Phys. Rev. B* 86 (7 Aug. 2012), p. 075412. DOI: 10.1103/PhysRevB.86.075412.

[18] Paola Borri and Wolfgang Langbein. "Four-wave mixing dynamics of excitons in InGaAs self-assembled quantum dots". In: *Journal of Physics: Condensed Matter* 19.29 (June 2007), p. 295201. DOI: 10.1088/0953-8984/19/29/295201.

[19] Akshay Singh, Galan Moody, Sanfeng Wu, Yanwen Wu, Nirmal J. Ghimire, Jiaqiang Yan, David G. Mandrus, Xiaodong Xu, and Xiaoqin Li. "Coherent Electronic Coupling in Atomically Thin $MoSe_2$". In: *Phys. Rev. Lett.* 112 (21 May 2014), p. 216804. DOI: 10.1103/PhysRevLett.112.216804.

[20] Kai Hao, Lixiang Xu, Philipp Nagler, Akshay Singh, Kha Tran, Chandriker Kavir Dass, Christian Schüller, Tobias Korn, Xiaoqin Li, and Galan Moody. "Coherent and Incoherent Coupling Dynamics between Neutral and Charged Excitons in Monolayer $MoSe_2$". In: *Nano Letters* 16.8 (2016). PMID: 27428509, pp. 5109–5113. DOI: 10.1021/acs.nanolett.6b02041.

[21] Xiaoping Hong, Jonghwan Kim, Su-Fei Shi, Yu Zhang, Chenhao Jin, Yinghui Sun, Sefaattin Tongay, Junqiao Wu, Yanfeng Zhang, and Feng Wang. "Ultrafast charge transfer in atomically thin MoS_2/WS_2 heterostructures". In: *Nature Nanotechnology* 9.9 (Sept. 2014), pp. 682–686. ISSN: 1748-3395. DOI: 10.1038/nnano.2014.167.

[22] Daichi Kozawa, Alexandra Carvalho, Ivan Verzhbitskiy, Francesco Giustiniano, Yuhei Miyauchi, Shinichiro Mouri, A. H. Castro Neto, Kazunari Matsuda, and Goki Eda. "Evidence for Fast Interlayer Energy Transfer in $MoSe_2/WS_2$ Heterostructures". In: *Nano Letters* 16.7 (2016), pp. 4087–4093. DOI: 10.1021/acs.nanolett.6b00801.

[23] Hailong Chen, Xiewen Wen, Jing Zhang, Tianmin Wu, Yongji Gong, Xiang Zhang, Jiangtan Yuan, Chongyue Yi, Jun Lou, Pulickel M. Ajayan, Wei Zhuang, Guangyu Zhang, and Junrong Zheng. "Ultrafast formation of interlayer hot excitons in atomically thin MoS_2/WS_2 heterostructures". In: *Nat Commun* 7 (2016), p. 12512. DOI: 10.1038/ncomms12512.

[24] Jonas E. Zimmermann, Young Duck Kim, James C. Hone, Ulrich Höfer, and Gerson Mette. "Directional ultrafast charge transfer in a $WSe_2/MoSe_2$ heterostructure selectively probed by time-resolved SHG imaging microscopy". In: *Nanoscale Horiz.* 5 (12 2020), pp. 1603–1609. DOI: 10.1039/D0NH00396D.

[25] S. Ovesen, S. Brem, C. Linderälv, Mikael Kuisma, Tobias Korn, Paul Erhart, Malte Selig, and Ermin Malic. "Interlayer exciton dynamics in van der Waals heterostructures". In: *Commun Phys* 2 (23 2019). DOI: 10.1038/s42005-019-0122-z.

[26] Junyi Liu, Xu Zhang, and Gang Lu. "Excitonic Effect Drives Ultrafast Dynamics in van der Waals Heterostructures". In: *Nano Letters* 20.6 (2020). PMID: 32432887, pp. 4631–4637. DOI: 10.1021/acs.nanolett.0c01519.

[27] Veronica R. Policht, Mattia Russo, Fang Liu, Chiara Trovatello, Margherita Maiuri, Yusong Bai, Xiaoyang Zhu, Stefano Dal Conte, and Giulio Cerullo. "Dissecting Interlayer Hole and Electron Transfer in Transition Metal Dichalcogenide Heterostructures via Two-Dimensional Electronic Spectroscopy". In: *Nano Letters* 21.11 (2021). PMID: 34037406, pp. 4738–4743. DOI: 10.1021/acs.nanolett.1c01098.

[28] P. Merkl, F. Mooshammer, P. Steinleitner, A. Girnghuber, K.-Q. Lin, P. Nagler, J. Holler, C. Schüller, J. M. Lupton, T. Korn, S. Ovesen, S. Brem, E. Malic, and R. Huber. "Ultrafast transition between exciton phases in van der Waals heterostructures". In: *Nature Materials* 18.7 (July 2019), pp. 691–696. ISSN: 1476-4660. DOI: 10.1038/s41563-019-0337-0.

[29] P. Rivera, J.R. Schaibley, A.M. Jones, J.S Ross, S. Wu, G. Aivazian, P. Klement, K. Seyler, G. Clark, N.J. Ghimire, J. Yan, D.G. Mandrus, W. Yao, and X. Xu. "Observation of long-lived interlayer excitons in monolayer $MoSe_2$-WSe_2 heterostructures". In: *Nat Commun* 6 (2015), p. 6242. DOI: 10.1038/ncomms7242.

[30] Roland Gillen and Janina Maultzsch. "Interlayer excitons in $MoSe_2/WSe_2$ heterostructures from first principles". In: *Phys. Rev. B* 97 (16 Apr. 2018), p. 165306. DOI: 10.1103/PhysRevB.97.165306.

[31] Torben L. Purz, Eric W. Martin, Pasqual Rivera, William G. Holtzmann, Xiaodong Xu, and Steven T. Cundiff. "Coherent exciton-exciton interactions and exciton dynamics in a $MoSe_2/WSe_2$ heterostructure". In: *Phys. Rev. B* 104 (24 Dec. 2021), p. L241302. DOI: 10.1103/PhysRevB.104.L241302.

[32] Ying Jiang, Shula Chen, Weihao Zheng, Biyuan Zheng, and Anlian Pan. "Interlayer exciton formation, relaxation, and transport in TMD van der Waals heterostructures". In: *Light Sci Appl* 10.72 (2021). DOI: 10.1038/s41377-021-00500-1.

[33] Simon Ovesen, Samuel Brem, Christopher Linderaelv, Mikael Kuisma, Tobias Korn, Paul Erhart, Malte Selig, and Ermin Malic. "Interlayer exciton dynamics in van der Waals heterostructures". In: *Communications Physics* 2 (23 2019). DOI: doi.org/10.1038/s42005-019-0122-z.

[34] Andrea Splendiani, Liang Sun, Yuanbo Zhang, Tianshu Li, Jonghwan Kim, Chi-Yung Chim, Giulia Galli, and Feng Wang. "Emerging Photoluminescence in Monolayer MoS_2". In: *Nano Letters* 10.4 (2010). PMID: 20229981, pp. 1271–1275. DOI: 10.1021/nl903868w.

[35] Christopher L. Smallwood and Steven T. Cundiff. "Multidimensional Coherent Spectroscopy of Semiconductors". In: *Laser & Photonics Reviews* 12.12 (2018), p. 1800171. DOI: https://doi.org/10.1002/lpor.201800171.

[36] Eric W. Martin, Jason Horng, Hanna G. Ruth, Eunice Paik, Michael-Henr Wentzel, Hui Deng, and Steven T. Cundiff. "Encapsulation Narrows and Preserves the Excitonic Homogeneous Linewidth of Exfoliated Monolayer $MoSe_2$". In: *Phys. Rev. Applied* 14 (2 Aug. 2020), p. 021002. DOI: 10.1103/PhysRevApplied.14.021002.

[37] Galan Moody, Chandriker Kavir Dass, Kai Hao, Chang-Hsiao Chen, Lain-Jong Li, Akshay Singh, Kha Tran, Genevieve Clark, Xiaodong Xu, Gunnar Berghäuser, Ermin Malic, Andreas Knorr, and Xiaoqin Li. "Intrinsic homogeneous linewidth and broadening mechanisms of excitons in monolayer transition metal dichalcogenides". In: *Nat Commun* 6 (2015), p. 8315. DOI: 10.1038/ncomms9315.

[38] Tomasz Jakubczyk, Valentin Delmonte, Maciej Koperski, Karol Nogajewski, Clement Faugeras, Wolfgang Langbein, Marek Potemski, and Jacek Kasprzak. "Radiatively Limited Dephasing and Exciton Dynamics in $MoSe_2$ Monolayers Revealed with Four-Wave Mixing Microscopy". In: *Nano Letters* 16.9 (2016), pp. 5333–5339. DOI: 10.1021/acs.nanolett.6b01060.

[39] Bo Peng, Guannan Yu, Xinfeng Liu, Bo Liu, Xiao Liang, Lei Bi, Longjiang Deng, Tze Chien Sum, and Kian Ping Loh. "Ultrafast charge transfer in MoS_2/WS_2 p-n Heterojunction". In: *2D Materials* 3.2 (May 2016), p. 025020. DOI: 10.1088/2053-1583/3/2/025020.

[40] Haiming Zhu, Jue Wang, Zizhou Gong, Young Duck Kim, James Hone, and X.-Y. Zhu. "Interfacial Charge Transfer Circumventing Momentum Mismatch at Two-Dimensional van der Waals Heterojunctions". In: *Nano Letters* 17.6 (2017). PMID: 28481550, pp. 3591–3598. DOI: 10.1021/acs.nanolett.7b00748.

[41] Tianhao Zhang, Irina Kuznetsova, Torsten Meier, Xiaoqin Li, Richard P. Mirin, Peter Thomas, and Steven T. Cundiff. "Polarization-dependent optical 2D Fourier transform spectroscopy of semiconductors". In: *Proceedings of the National Academy of Sciences* 104.36 (2007), pp. 14227–14232. ISSN: 0027-8424. DOI: 10.1073/pnas.0701273104.

[42] B. Kasprzak J.and Patton, V. Savona, and W. Langbein. "Coherent coupling between distant excitons revealed by two-dimensional nonlinear hyperspectral imaging". In: *Nature Photonics* 5.1 (Jan. 2011), pp. 57–63. DOI: 10.1038/nphoton.2010.284.

[43] Patrick F. Tekavec, Jeffrey A. Myers, Kristin L. M. Lewis, Franklin D. Fuller, and Jennifer P. Ogilvie. "Effects of chirp on two-dimensional Fourier transform electronic spectra". In: *Opt. Express* 18.11 (May 2010), pp. 11015–11024. DOI: 10.1364/OE.18.011015.

[44] Peter Hamm and Martin Zanni. *Concepts and Methods of 2D Infrared Spectroscopy*. Cambridge University Press, 2011. DOI: 10.1017/CBO9780511675935.

[45] D. Polli, D. Brida, S. Mukamel, G. Lanzani, and G. Cerullo. "Effective temporal resolution in pump-probe spectroscopy with strongly chirped pulses". In: *Phys. Rev. A* 82 (5 Nov. 2010), p. 053809. DOI: 10.1103/PhysRevA.82.053809.

[46] Junho Choi, Matthias Florian, Alexander Steinhoff, Daniel Erben, Kha Tran, Dong Seob Kim, Liuyang Sun, Jiamin Quan, Robert Claassen, Somak Majumder, Jennifer A. Hollingsworth, Takashi Taniguchi, Kenji Watanabe, Keiji Ueno, Akshay Singh, Galan Moody, Frank Jahnke, and Xiaoqin Li. "Twist Angle-Dependent Interlayer Exciton Lifetimes in van der Waals Heterostructures". In: *Phys. Rev. Lett.* 126 (4 Jan. 2021), p. 047401. DOI: 10.1103/PhysRevLett.126.047401.

[47] Chanyeol Choi, Jiahui Huang, Hung-Chieh Cheng, Hyunseok Kim, Abhinav Kumar Vinod, Sang-Hoon Bae, V. Ongun Özcelik, Roberto Grassi, Jongjae Chae, Shu-Wei Huang, Xiangfeng Duan, Kristen Kaasbjerg, Tony Low, and Chee Wei Wong. "Enhanced interlayer neutral excitons and trions in trilayer van der Waals heterostructures". In: *npj 2D Mater Appl* 2 (2018), p. 30. DOI: 10.1038/s41699-018-0075-1.

[48] M. Baranowski, A. Surrente, L. Klopotowski, J. M. Urban, N. Zhang, D. K. Maude, K. Wiwatowski, S. Mackowski, Y. C. Kung, D. Dumcenco, A. Kis, and P. Plochocka. "Probing the Interlayer Exciton Physics in a $MoS_2/MoSe_2/MoS_2$ van der Waals Heterostructure". In: *Nano Letters* 17.10 (2017). PMID: 28895745, pp. 6360–6365. DOI: 10.1021/acs.nanolett.7b03184.

[49] Bastian Miller, Alexander Steinhoff, Borja Pano, Julian Klein, Frank Jahnke, Alexander Holleitner, and Ursula Wurstbauer. "Long-Lived Direct and Indirect Interlayer Excitons in van der Waals Heterostructures". In: *Nano Letters* 17.9 (2017). PMID: 28742367, pp. 5229–5237. DOI: 10.1021/acs.nanolett.7b01304.

[50] Camelia N. Borca, Tianhao Zhang, Xiaoqin Li, and Steven T. Cundiff. "Optical two-dimensional Fourier transform spectroscopy of semiconductors". In: *Chemical Physics Letters* 416.4 (2005), pp. 311–315. ISSN: 0009-2614. DOI: https://doi.org/10.1016/j.cplett.2005.09.090.

[51] Neil R. Wilson, Paul V. Nguyen, Kyle Seyler, Pasqual Rivera, Alexander J. Marsden, Zachary P. L. Laker, Gabriel C. Constantinescu, Viktor Kandyba, Alexei Barinov, Nicholas D. M. Hine, Xiaodong Xu, and David H. Cobden. "Determination of band offsets, hybridization, and exciton binding in 2D semiconductor heterostructures". In: *Science Advances* 3.2 (2017). DOI: 10.1126/sciadv.1601832.

[52] Tomasz Jakubczyk, Karol Nogajewski, Maciej R Molas, Miroslav Bartos, Wolfgang Langbein, Marek Potemski, and Jacek Kasprzak. "Impact of environment on dynamics of exciton complexes in a WS_2 monolayer". In: *2D Materials* 5.3 (Apr. 2018), p. 031007. DOI: 10.1088/2053-1583/aabc1c.

[53] Tomasz Jakubczyk, Goutham Nayak, Lorenzo Scarpelli, Wei-Lai Liu, Sudipta Dubey, Nedjma Bendiab, Laëtitia Marty, Takashi Taniguchi, Kenji Watanabe, Francesco Masia, Gilles Nogues, Johann Coraux, Wolfgang Langbein, Julien Renard, Vincent Bouchiat, and Jacek Kasprzak. "Coherence and Density Dynamics of Excitons in a Single-Layer MoS_2 Reaching the Homogeneous Limit". In: *ACS Nano* 13.3 (2019). PMID: 30735350, pp. 3500–3511. DOI: 10.1021/acsnano.8b09732.

[54] Vivek Tiwari, Yassel Acosta Matutes, Alastair. T. Gardiner, Thomas L.C. Jansen, Richard J. Cogdell, and Jennifer P. Ogilvie. "Spatially-resolved fluorescence-detected two-dimensional electronic spectroscopy probes varying excitonic structure in photosynthetic bacteria". In: *Nat. Comm.* 16 (2018), p. 4219. DOI: 10.1038/s41467-018-06619-x.

CHAPTER VI

Lock-in Detector for Accelerated Nonlinear Imaging

Reproduced in part with permission from:

Torben L. Purz, Steven T. Cundiff, and Eric W. Martin. "Lock-in detector for accelerated nonlinear imaging". *Optics Letters* **46**, 4813-4816 (2021).

6.1 Introduction

Every physics undergraduate student at a reputable research institution encounters a lock-in amplifier at some point throughout their study. The rationale behind introducing aspiring young physicists to this technology is that the lock-in amplifier has enabled numerous scientific achievements over its almost 90-year-long career due to its characterizing quality: filtering out a weak signal against a large background [1–3]. Contemporary digital lock-in amplifiers have dynamic reserves of up to 120 dB, enabling the extraction of signals a factor of one million lower in amplitude than the "noise" at a specific frequency (and a factor of a trillion in intensity) [4]. "Noise" can both refer to a generic broadband noise floor or a well-defined interfering tone that is not the signal of interest. In the following, those are referred to as extraneous modulations. Additional bandpass filters preceding the lock-in amplifier can

further increase the dynamic reserve. Nowadays, lock-in amplifiers are used in fields of research spanning everything from the Nobel prize-awarded measurement of the fractional quantum Hall effect [5] and direct imaging of the bond characteristics between atoms in a molecule [6] to characterizing solid-state samples [7, 8] and photosynthetic bacteria [9].

Simultaneously, researchers at universities [9, 10], national labs [11], and hospitals [12] rely heavily on nonlinear spectroscopy and imaging methods from 2P imaging to SRS imaging. SRS imaging has proven useful for identifying biological tissue by its molecular composition [13, 14], in-vivo imaging of numerous systems, including mouse and human epidermis [15], and DNA [16]. Optically degenerate ultrafast four-wave mixing (DUF-FWM) has proven itself more broadly useful in both imaging [10, 17, 18] and spatially-addressed spectroscopy [9, 10, 19–21] with applications from identifying defects and inhomogeneity in semiconductor nanostructures [10] to distinguishing bacterial colonies [9]. We distinguish DUF-FWM from other nonlinear imaging microscopies because the broadband excitation pulses and signal are spectrally overlapped. While nonlinear imaging microscopies such as 2P microscopy offer a resolution enhancement of up to 1.4 (when compared to linear techniques) and an enhanced transverse resolution, DUF-FWM techniques have several other additional advantages. For one, DUF-FWM is naturally sensitive to defects and interfaces due to its scaling with material oscillator strength [22], which is not true for all third-order nonlinear spectroscopies. Moreover, using ultrafast pulses as excitations, we can obtain time-resolved information about dephasing, electronic decays, and other rapid processes, including electron/hole and energy transfer [8, 23, 24]. Specifically using ultrafast lasers, Huang *et al.* [25] have shown the practicality of two-color transient absorption decay times for defect sensing in graphene, while Jacubczyk *et al.* [17] have shown the potential of dephasing times as an indicator of material quality for TMDs.

In non-degenerate nonlinear microscopies, including 2P microscopy, near-degenerate four-wave mixing microscopy [26, 27], and SRS [13–16], the signal can be easily isolated using dichroic mirrors and color filters. However, the isolation of a weak signal that is spectrally degenerate with the excitation beams poses a challenge in DUF-FWM microscopies. Commonly, the aforementioned lock-in detection is used to filter out the signal. Even so, lock-in detection itself can impede rapid nonlinear imaging because of the long pixel dwell times required to fulfill the constraints of signal-to-noise ratio (SNR) and avoid correlation between adjacent pixels.

Gottschall *et al.* [28] have demonstrated rapid nonlinear imaging with a 1 µs pixel dwell time for SRS by designing a custom laser system. However, their system is currently using almost 10 full modulation cycles within the pixel dwell time, and this implementation could be further accelerated by reducing the number of modulation cycles. Moreover, their implementation of SRS uses a single modulation, while several DUF-FWM imaging techniques [9, 10, 21] use multiple modulations, increasing the necessary pixel dwell time to suppress adjacent modulations efficiently. Fimpel *et al.* [29] have used boxcar averaging to obtain superior SNR to conventional lock-in detection in their pump-probe imaging. Nonetheless, deriving benefit from boxcar averaging requires a detector bandwidth that exceeds the laser repetition frequency, a drawback for some imaging applications due to noise and acquisition speed considerations.

In this chapter, we present an approach for signal filtering using a simple moving-average filter instead of an exponentially-weighted-moving-average filter for the low-pass filter in the lock-in amplifier. We coin the term box lock-in for the technique and demonstrate increased SNR through efficient suppression of extraneous modulations with this lock-in, making it a prime choice for imaging applications.

We first introduce the principles of lock-in detection, followed by a discussion of impulse response and transfer functions for the conventional lock-in and box lock-in.

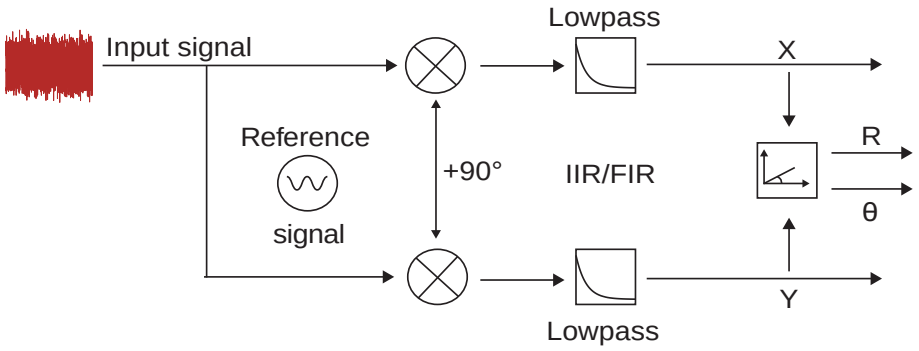

Figure 6.1: **(a)** The scheme for lock-in detection. The low-pass filter can either be realized as an infinite impulse response (IIR) filter (conventional exponentially-weighted moving average) or as a finite impulse response (FIR) filter such as a simple moving average.

Thereafter, we show simulations of the two lock-ins, establishing the superior performance of the box lock-in for suppression of extraneous modulations (and therefore imaging speed), before showing an experimental demonstration of the two lock-ins, which corroborates the findings from our simulations.

6.2 Principles of Lock-In Detection

The lock-in detection scheme, as first introduced in the 1930s and 1940s [1–3], is illustrated in Fig. 6.1 (a). Lock-in amplifiers extract a signal with a known frequency modulation from a noisy environment. The frequency modulation of the signal is usually achieved using choppers [30], electro-optic modulators [31], or AOMs [32]. A noisy input, which consists of the desired signal and several extraneous modulations at different frequencies, is mixed with a reference and a 90° phase-shifted replica. The mixing down-shifts the signal to direct current (DC), and the resulting output is sent through a bandwidth-adjustable low-pass filter [33, 34]. The mixing with two references, one of them phase-shifted, is often referred to as a dual-phase demodulation circuit [35].

In this chapter, we show that a tailored finite impulse response (FIR) filter allows for the suppression of extraneous modulations more efficiently than a conventional

lock-in amplifiers' infinite impulse response (IIR) filter. The reason to shift the signal to DC by multiplying it with a reference signal (and a 90° phase-shifted reference signal) is two-fold: While a simple bandpass filter could still filter out the signal at the tagged signal frequency, phase noise that is common to both the reference and signal (and caused, e.g., by vibrations and temperature shifts) is canceled in this scheme. Furthermore, this phase-sensitive scheme allows for the Fourier-transform spectroscopy implementation discussed in Sec. 4.2.2, which requires passive phase stabilization with a reference laser.

The signal down-mixing to DC can be best understood in the time domain: We assume a cosinusoidal signal

$$V_S(t) = R \cdot \cos(\omega_S t + \Theta) = \frac{R}{2} e^{+i(\omega_S t + \Theta)} + \frac{R}{2} e^{-i(\omega_S t + \Theta)}\,, \tag{6.1}$$

in the temporal domain with the amplitude of the signal R, the phase of the signal Θ, and the frequency of the oscillation ω_S, which in our case depends on the frequency tag of the detected signal.

The reference and phase-shifted reference can be expressed as

$$V_R(t) = \cos(\omega_R t) = \frac{1}{2}(e^{i\omega_R t} + e^{-i\omega_R t}) \tag{6.2}$$

$$V_R^{90°}(t) = \cos(\omega_R t + 90°) = -\sin(\omega_R t) = \frac{1}{2i}(e^{-i\omega_R t} - e^{i\omega_R t})\,, \tag{6.3}$$

with ω_R being the reference frequency.

The multiplications of the signal with the unshifted and phase-shifted reference then yield:

$$V_S \cdot V_R = \frac{R}{4}(e^{i(\omega_S-\omega_R)t+i\Theta} + e^{i(\omega_S+\omega_R)t+i\Theta} + e^{-i(\omega_S-\omega_R)t-i\Theta} + e^{-i(\omega_S+\omega_R)t-i\Theta}) \tag{6.4}$$

$$V_S \cdot V_R^{90°} = \frac{R}{4i}(e^{i(\omega_S-\omega_R)t+i\Theta} - e^{i(\omega_S+\omega_R)t+i\Theta} - e^{-i(\omega_S-\omega_R)t-i\Theta} + e^{-i(\omega_S+\omega_R)t-i\Theta})\,. \tag{6.5}$$

The subsequent low-pass filter, corresponding to a time average, then removes all fast-rotating terms with $\omega_R + \omega_S$ because the reference frequency ω_R is set close (or equal) to the signal frequency ω_S. In this case, the down-mixed signal becomes

$$X = V_S \cdot V_R = \frac{R}{4}(e^{i(\omega_S-\omega_R)t+i\Theta} + e^{-i(\omega_S-\omega_R)t-i\Theta}) = \frac{R}{2}\cos((\omega_S - \omega_R)t + \Theta) \tag{6.6}$$

$$Y = V_S \cdot V_R^{90^\circ} = \frac{R}{4i}(e^{i(\omega_S-\omega_R)t+i\Theta} - e^{-i(\omega_S-\omega_R)t-i\Theta}) = \frac{R}{2}\sin((\omega_S - \omega_R)t + \Theta)\,. \tag{6.7}$$

These two signals are referred to as the real part of the signal, X, and the imaginary part of the signal, Y. Setting $\omega_R = \omega_S$, we then obtain the familiar result

$$X = R\cos(\Theta)\,, \tag{6.8}$$

$$Y = R\sin(\Theta)\,. \tag{6.9}$$

Lock-in amplifiers in their earliest stages only had one stage of phase-sensitive detection (i.e., the signal was not multiplied with a 90°phase-shifted reference, and one would only retrieve X [36]). One advantage of this approach is that any phase noise will equally (randomly) increase or decrease X, such that there is no systematic noise background or noise floor. Another advantage of tracking the phase of the detected signal instead of just its amplitude is the information contained in the phase. As discussed in Chaps. III and IV, the phase information allows us to perform Fourier transform spectroscopy. Furthermore, other phase evolutions, such as the ones discussed by Boule *et al.* [37], can also yield crucial insights into the underlying physics of sample systems.

6.3 Impulse Response and Transfer Function

The conventional (exponential) lock-in uses an IIR filter for its low-pass filter, the digital implementation of which can be described as

$$y_{\text{exp}}[k] = y_{\text{exp}}[k-1] + \alpha(x_{\text{exp}}[k] - y_{\text{exp}}[k-1])\,, \tag{6.10}$$

with $y_{\text{exp}}[k]$ being the k^{th} filter output, $x_{\text{exp}}[k]$ being the k^{th} filter input for the exponential lock-in, and α the degree of weighting decrease. The weighting decrease α has a value between zero and one, with larger α discarding older observations faster, and is related to the time-constant of a conventional lock-in as $\tau = \Delta_T(1-\alpha)/\alpha$, where Δ_T denotes the sampling period. It is also common to use multi-pole filters to achieve a faster high-frequency roll-off at the expense of longer settling times [35], in which case the lock-in is referred to as a j^{th}-pole lock-in, with j being the pole order. The filter's impulse response for the exponential lock-in in the time domain is shown in Fig. 6.2(a). A significant change in the filter input x will immediately affect the output y and affect it for a considerable amount of time. In imaging applications, a rapid change from low to high signal and vice versa can be real, in which case blurring occurs if the wait time between adjacent data points is too short.

The low-pass filter for the box lock-in is an FIR filter,

$$y_{\text{box}}[k] = y_{\text{box}}[k-1] + x_{\text{box}}[k] - x_{\text{box}}[k-N]\,, \tag{6.11}$$

where N denotes an integer number related to the time constant of the filter by $\tau = N\Delta_T$, and y_{box} and x_{box} are the respective filter outputs and inputs for the box lock-in. This low-pass is a simple moving average of length N, where all values older than N are discarded. The box lock-ins filters impulse response in the time domain is shown in Fig. 6.2(a). This method of filtering makes the lock-in less susceptible

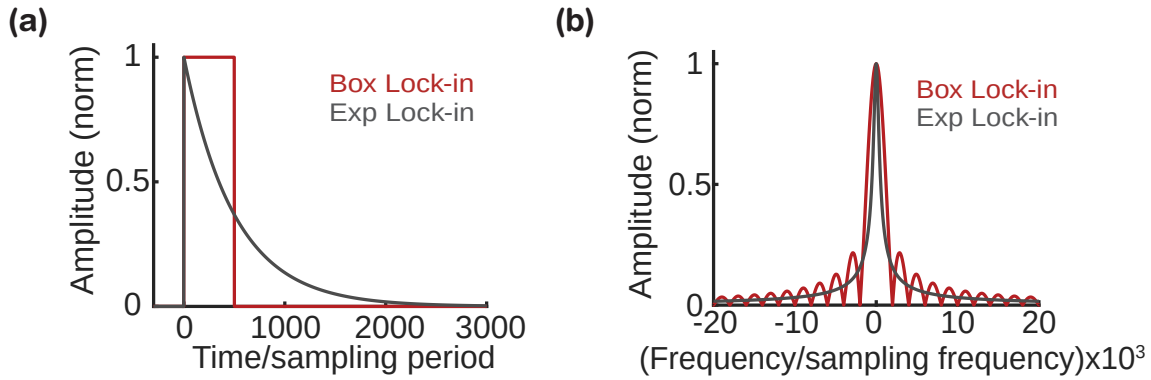

Figure 6.2: **(a)** Impulse response function of the exponential (gray) and box (red) lock-in. **(b)** Transfer function of the exponential (gray) and box (red) lock-in.

to strong correlation of adjacent pixels, and thus blurring, for rapid acquisition in imaging applications.

In the following, the term wait time refers to the 100% settle time for the box lock-in and the 95% settle time of the exponential lock-in, corresponding to the necessary pixel dwell time. Using the wait time allows for a better comparison of the two lock-ins.

For a frequency domain description of the filters, the transfer function can be obtained by performing a Z-transform. The frequency response for the IIR filter then reads

$$H_{\mathrm{exp}}(\omega) = \frac{\alpha}{1-(1-\alpha)\exp[-i\omega]}, \tag{6.12}$$

with $\omega = 2\pi f/f_s$, and the frequency f with respect to the reference (detection) frequency, normalized by the sampling frequency f_s. For the FIR filter, the transfer function is expressed as

$$H_{\mathrm{box}}(\omega) = \frac{N}{f_s} \times \mathrm{sinc}\left(\frac{\omega N}{2}\right) \exp[-i\omega N/2]. \tag{6.13}$$

The resulting amplitudes of the transfer functions for the two low-pass filters are shown in Fig. 6.2(b). For a similar nominal time constant, the central lobe for the box lock-in transfer function is wider than for the exponential lock-in in Fig. 6.2(b),

but this changes when we compare transfer functions of the same wait time and the exponential low-pass filter broadens. A narrower transfer function is generally considered advantageous since it suppresses modulations outside the signal frequency more efficiently.

While the transfer function of the exponential lock-in shows a smooth decay towards higher and lower frequencies, the notches in the transfer function of the box lock-in can be harnessed to improve data acquisition in experiments with multiple modulations by efficiently attenuating spurious modulations. For example, in a differential absorption/reflection experiment, modulated pump and probe beams have modulation frequencies f_1 and f_2. The nonlinear interaction between the two beams leads to signals at four modulations: f_1, f_2, $f_2 - f_1$, and $f_1 + f_2$. When detecting at one of the modulation frequencies, the other undesired modulations can be placed in one of the minima of the sinc function, yielding effective suppression. The condition for suppressing extraneous modulations is that all modulations must have an integer number of cycles within the averaging box. Fulfillment of this condition leads to undesired modulations coinciding with a minimum in the sinc function as follows: Using Eq. 6.13, we obtain

$$f_0 = (n/N) \times f_s \,, \tag{6.14}$$

for zero-crossings with n being an integer. The condition for the frequency f to have an integer number of cycles can be written as

$$f = \frac{m}{\tau} \,, \tag{6.15}$$

with the time constant τ of the box lock-in. Using $\tau = N/f_s$, this can be rewritten as

$$f = \frac{m}{N} f_s \,. \tag{6.16}$$

If the two modulations $f_{1,2}$ from above fulfill this condition, then $f_1 \pm f_2 = ((m_1 \pm$

$m_2)/N) \times f_s$. However, $m_1 \pm m_2$ will still be an integer, and $f_1 \pm f_2$ will fulfill Eq. 6.14 and be at a zero crossing. Detecting at either f_1, f_2, or $f_1 \pm f_2$ thus shifts the respective other modulation frequencies onto a zero crossing.

In more sophisticated four-pulse experiments [32, 38, 39], the four beams (A, B, C, D) are frequency-shifted so that each beam pair's interference is modulated at lock-in detectable frequencies. Here, a total of nine different modulations (six linear interference modulations such as $\Omega_B - \Omega_A$, and three third-order-nonlinear modulation signals such as $-\Omega_A + \Omega_B + \Omega_C - \Omega_D$, see Sec. 3.5.1) can be observed. If $f_1 = \Omega_B - \Omega_A$, $f_2 = \Omega_C - \Omega_B$, and $f_3 = \Omega_D - \Omega_C$ fulfill the condition from Eq. 6.16, all other modulations will. Since it is necessary to sample at least one full modulation of each signal while requiring modulations to have a distinct number of cycles within the averaging box, the nonlinear modulation frequency of interest (e.g., the FWM modulation) for M pulse pairs can be given as

$$f_{\mathrm{FWM}} = \frac{f_{max}}{K}\,, \tag{6.17}$$

with

$$K = 4q + a\,, \tag{6.18}$$

with the quotient, q, and variable, a, given by

$$q = \mathrm{mod}(M-2, 4)\,, \tag{6.19}$$

$$a = \left\{ \begin{array}{ll} 1, & \text{for } r = 0 \\ 2, & \text{for } r = 1 \\ 4, & \text{for } r = 2 \\ 5, & \text{for } r = 3 \end{array} \right\}\,, \tag{6.20}$$

with the remainder of the modulo division r. The laser repetition rate f_{rep} dictates

the maximum sampling frequency, and the highest possible modulation frequency (Nyquist) is thus $f_{rep}/2$. Relating the two equations, one retrieves

$$\tau = \frac{1}{f_{\mathrm{FWM}}} = \frac{2K}{f_{rep}}\,, \tag{6.21}$$

as the lower limit on the time constant.

6.4 Simulation of Exponential and Box Lock-In

Implementing various lock-in schemes into a digital lock-in amplifier is relatively straightforward. In order to implement Eq. 6.10, at each sampling point, the measured input (voltage) is multiplied with the generated (or externally provided) reference and a 90° phase-shifted reference, as explained in Sec. 6.2. Subsequently, the difference between this number and the lock-in value from the previous iteration is bit-shifted, with the number of shifted bits determined by the time-constant. For example, a time-constant corresponding to 256 sampling points would lead to a bit shift of 8 since $2^8 = 256$. This bit shift corresponds to $\alpha = 2^{-8}$ in Eq. 6.10. Adding the bit-shifted number to the lock-in value from the previous iteration then yields the new lock-in value. This procedure is implemented separately for the reference and phase-shifted reference and yields the values for X and Y of the lock-in amplifier. Multi-pole digital lock-in amplifiers are implemented by further bit shifting: To implement a two-pole exponential lock-in, we again use Eq. 6.10, but use the updated value $y[k]$ for the 1-pole lock-in instead of the input $x[k]$. Higher-order lock-ins can then be obtained iteratively using the filter output $y[k]$ of the one-lower-pole lock-in amplifier instead of $x[k]$. To digitally implement the box lock-in is straightforward from Eq. 6.11 and requires no further discussion.

In Fig. 6.3, we present the results of simulations comparing the conventional exponential lock-in with a box lock-in. The input of the lock-in amplifier is shown in

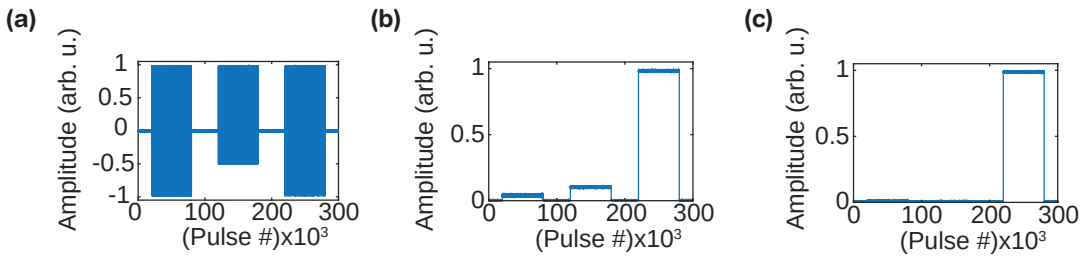

Figure 6.3: **(a)** Simulated signal consisting of three beat notes at $f_1 = \frac{1}{2}f_s$, $f_2 = \frac{1}{3}f_s$, and $f_3 = \frac{1}{6}f_s$, each of which is sequentially turned on for 60×10^3 pulses. **(b)** Signal detected with a 4-pole exponential lock-in having a time constant of 15.5 pulses. **(c)** Signal detected with a box lock-in having a time constant of 12 pulses.

Fig. 6.3(a). It consists of three different modulations at $f_1 = \frac{1}{2}f_s$,$f_2 = \frac{1}{3}f_s$, and $f_3 = \frac{1}{6}f_s$ that are consecutively turned on at different times. These sampling frequencies are a realistic model of a nonlinear experiment in which linear modulations exist at the two higher frequencies ($f_{1,2}$) while the nonlinear signal is modulated at a lower frequency (f_3). We detect the input at the nonlinear signal frequency f_3 for a four-pole exponential lock-in in Fig. 6.3(b) and the box lock-in in Fig. 6.3(c). Here, we employ a wait time of 15.5 pulses for the exponential lock-in and 12 pulses for the box lock-in. In this case, we assume the data acquisition rate to be synced with the laser's repetition rate, which is necessary when approaching the few-pulse limit for lock-in detection. To put real-life numbers to this theoretical example, for a laser with a repetition rate of 120 MHz, the FWM signal at f_3 is modulated at a frequency of 20 MHZ and 12 pulses correspond to a wait time of 100 ns. Fig. 6.3(b) shows a well-detected signal with tolerable noise. However, the signal also displays a significant breakthrough of the signals modulated at f_1 and f_2. In contrast to the exponential lock-in, the box lock-in, whose response is shown in Fig. 6.3(c), shows very efficient suppression of all undesired modulations while maintaining a comparable SNR to the exponential lock-in for the signal modulation. In real-life applications, the insufficient suppression of spurious modulations will lead to a significantly reduced SNR for the exponential lock-in. An additional effect that favors the box lock-in is few cycle effects that become important when the time constants approach the modulation pe-

riods of the signals. In this limit, only a few oscillation cycles are captured by the exponential lock-in, and the detected signal is strongly affected by which part of the few cycles is captured. In contrast, because the averaging box has the same length as the modulation periods, this issue does not occur for the box lock-in, and a single cycle can be sufficient to filter the desired signal.

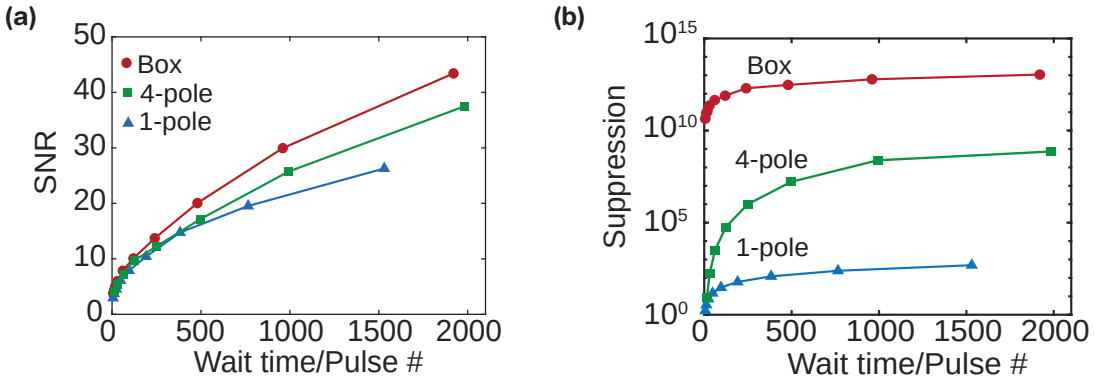

Figure 6.4: **(a)** SNR of the detected signal at f_3 for an input SNR of 1. **(b)** Suppression of the f_2 modulation when detecting at f_3 as a function of wait time for the 1-pole exponential lock-in, 4-pole exponential lock-in, and box lock-in.

In the following, we emulate a 1-pole, and 4-pole exponential lock-in, as well as a box lock-in, detecting at the frequency f_3 for varying wait times. At first, we study how the SNR of the signal evolves as a function of wait time for the three lock-ins. Here, we set the SNR of the simulated signal to 1. As evidenced by Fig. 6.4(a), the SNR of all three lock-ins increases by about an order of magnitude when the wait time increases from 10 sampling periods to 2000 sampling periods. The decreasing slopes of the SNR curves can be understood by the fact that doubling the averaging time increases the SNR by a factor of $\sqrt{2}$. Most notably, the SNR between the three lock-ins does not vary significantly, with the box lock-in having a slight edge over the exponential lock-in. Therefore, the primary influence on SNR at short wait times is insufficient suppression of adjacent modulations. As a measure of suppression, we use the ratio of the amplitude of the signal (f_3) over the breakthrough amplitude of the linear modulation at f_1. The resulting behavior of the suppression for different wait

times is shown in Fig. 6.4(b).

Firstly, a large difference between the 1-pole and higher-order filter 4-pole lock-in detection can be observed here. The main strength of the higher-order filters lies in having a sharper high-frequency roll-off, and as such, they more efficiently suppress the spurious modulations by about six orders of magnitude. However, neither lock-in comes remotely close to the box lock-in, which achieves suppression factors that exceed the exponential lock-ins by ten orders of magnitude for short wait times. The advantage of the box lock-in is especially evident for these short wait times and quickly decreases as the wait times increase. Nonetheless, the box lock-in shows superior suppression, still by three orders of magnitude for wait times exceeding 1000 pulses. This behavior can be traced back to the transfer functions in Fig. 6.2(b): the narrower the exponential lock-in transfer function (i.e., for longer time constants), the more efficiently it can suppress extraneous modulations. In contrast, the box lock-in shows perfect suppression, independent of the time constant (this is not strictly true once noise is added). The slight difference in suppression between early and late times for the box lock-in can be assigned to numerical artifacts.

The results of Fig. 6.4 can vary depending on the data correlation requirements. For example, requiring 99% settling instead of 95% settling for the exponential lock-in would shift the curves for the exponential lock-ins in Fig. 6.4 towards higher wait times by a factor of 1.3-1.4, further increasing the advantage of the box lock-in over the exponential lock-in.

6.5 Experimental Demonstration on $MoSe_2$/Distributed Bragg Reflector Sample

The advantages of the box lock-in over the conventional exponential one can also be seen directly in laser-scanning-based imaging applications. For the data shown in

the following, we use the laser-scanning imaging setup introduced in Sec. 4.4.1 with the spectroscopy setup detailed in Sec. 4.3. We set the Ti:Sapph laser to a center wavelength of 785 nm and a bandwidth of 30 nm (FWHM). Furthermore, we measure the amplitude of the FWM signal with all pulses overlapped in time, $\tau = T = t = 0$. We use the AOM frequencies Ω_A=78.74 MHz, Ω_B=78.7 MHz, Ω_C=79.755 MHz, and Ω_D=79.7 MHz to put the FWM signal frequency $(-\Omega_A + \Omega_B + \Omega_C - \Omega_D)$ at 30 kHz, $\Omega_A - \Omega_B$ at 80 kHz, and $\Omega_C - \Omega_D$ at 110 kHz. The sampling rate of the digital lock-in is 5 MSamp/s.

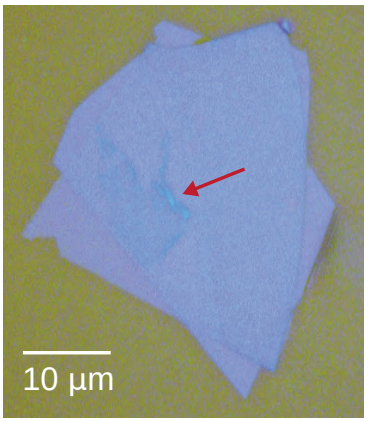

Figure 6.5: Microscope image of the $MoSe_2$/DBR sample. The $MoSe_2$ flake can be seen as a lighter blue shape at the left of the sample (indicated by the red arrow).

The sample used in this chapter for the proof of principle is a monolayer of $MoSe_2$ encapsulated in hBN, placed on a DBR. A microscope image of the sample is shown in Fig. 6.5. The DBR gives this sample a near-perfect absorption at cryogenic temperatures [40] and a strong absorption even at room temperature. The sample is extensively described in Ref. 40.

We record three different data sets, using *(I)* an exponential lock-in with a time constant of 25 µs (wait time: 105 µs), *(II)* an exponential lock-in with a time constant of 100 µs (wait time: 100 µs), and *(III)* a box lock-in with a 100 µs time constant. The wait time in the first dataset corresponds to 91.5% settling time to allow for comparable wait times with the box lock-in. We average five images for the data

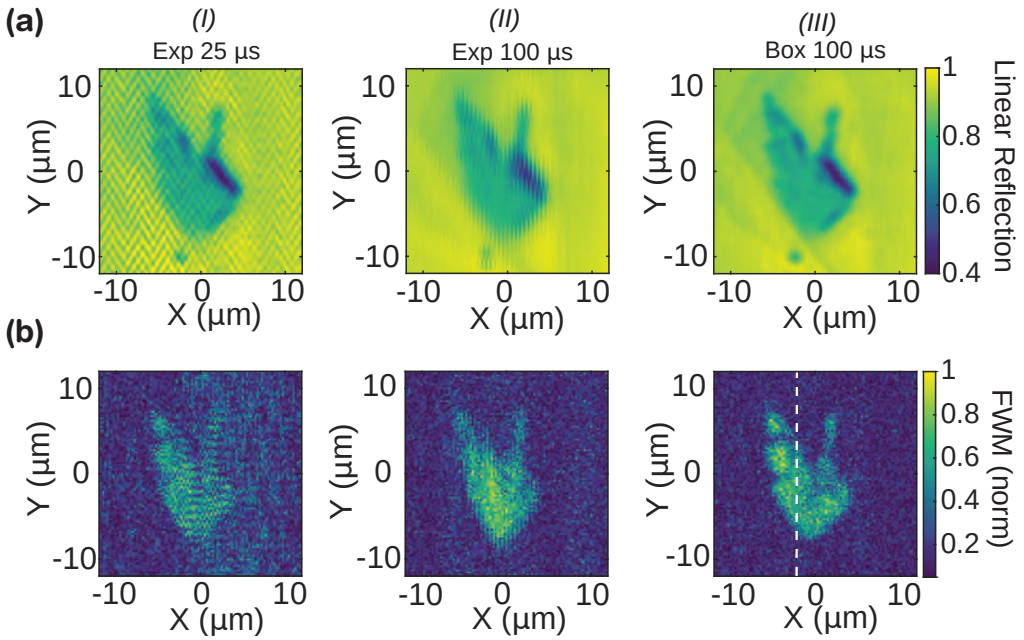

Figure 6.6: **(a)** Schematic layout of the experimental setup, consisting of a multi-pulse spectroscopy and subsequent laser scanning imaging setup. **(b)** Linear absorption for the monolayer $MoSe_2$ sample on a distributed Bragg reflector for three different lock-in settings: *(I)* Exponential lock-in with 25 µs time-constant (105 µs wait time), *(II)* Exponential lock-in with 100 µs time-constant (100 µs wait time) *(III)* Box lock-in with 100 µs time-constant (100 µs wait time). **(c)** FWM images on the sample corresponding to the linear images described for (b). All images consist of five averages.

provided here, though faster measurements with comparable SNR may be achieved with a higher power laser. Here, we used pulse energies of 0.5 pJ/pulse (2 pJ total), well below energies used for medical imaging [41], and damage thresholds for semiconductor samples [8]. Fig. 6.6(a) shows the corresponding linear absorption images obtained by taking the linear interference between C and D. Fig. 6.6(b) shows the matching FWM images for the three data sets. Both in linear and FWM images, the box lock-in shows an improved SNR over the exponential lock-in. Only for a nominal time constant of 100 µs for the exponential lock-in (corresponding to a 486 µs wait time) does the SNR become comparable to the 100 µs wait time box lock-in. The main reason for the difference in SNR here is that extraneous modulations are not efficiently filtered out by the exponential lock-in at short wait times. A signature of the

breakthrough of extraneous modulations can be seen in column *I* of Fig. 6.6(a). The spurious modulation leads to the signal's slow beating, which ultimately creates a zig-zag pattern when imaged. In the corresponding FWM image, an overall large noise floor, as well as random pixel-to-pixel fluctuations, can be observed. This noise can again be attributed to spurious modulations breaking through. Moreover, the short dwell time measurement using the exponential lock-in (column *II* of Fig. 6.6) shows a strong correlation between adjacent pixels along the fast scan axis compared to its long dwell time counterpart and the box lock-in. The correlation can be best seen from the line-to-line variation of the image, which occurs for the insufficient wait time because adjacent vertical lines are taken with opposing motions of the galvo. Finally, images acquired using the box lock-in are presented in column *III* of Fig. 6.6(b,c), showing efficient suppression of extraneous modulations and increased SNR. These images also show no blurring at the edges of the sample.

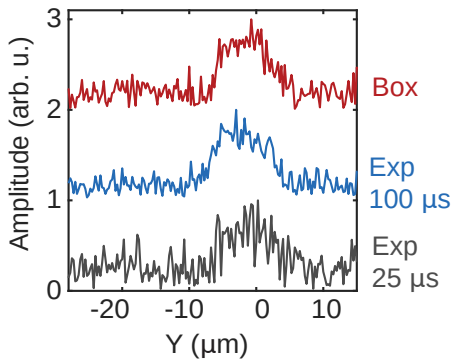

Figure 6.7: Slice along the y-axis for the three FWM images (slice indicated by white dashed line in Fig. 6.6(b)). The graphs are normalized and offset.

In Fig. 6.7, we present slices of the FWM image along the y-axis (fast scan axis) for the three data sets at the fixed x position indicated by the white dashed line in Fig. 6.6(c). We quantify the SNR by calculating the standard deviation in a region of constant signal in the central area of the slice and normalize it by the average signal strength. This procedure yields an SNR of 3.1 for the 25 µs exponential lock-in, an SNR of 6.3 for the 100 µs exponential lock-in, and an SNR of 7.2 for the 100 µs box

lock-in. Most strikingly, the 100 µs box lock-in even outperforms the 100 µs (required wait time: 486 µs) exponential lock-in, yielding an improvement of more than a factor of 4.8 in data acquisition speed.

6.6 Conclusions and Outlook

In conclusion, we have introduced in this chapter a method for enhancing the scan speed for imaging in collinear multi-pulse nonlinear experiments by implementing a box lock-in. We first introduce the principles of lock-in detection as well as impulse response and transfer function, which are crucial to understanding the box lock-in's advantages: In the temporal domain, the box lock-in allows for less correlation between adjacent pixels than the exponential lock-in. In the frequency domain, the notches of the box lock-in's sinc transfer function can be harnessed to achieve efficient suppression of extraneous modulations, resulting in the box lock-in's SNR being improved compared to the exponential lock-in. We first demonstrate the superiority in suppression and SNR for the box lock-in with a simulation before experimentally validating the results on a $MoSe_2$/DBR sample. The strong suppression of extraneous modulations enables an order of magnitude enhancement in scan speed for nonlinear imaging as the wait time approaches fundamental limits.

Future technological improvements will mainly focus on pushing the modulation frequencies towards their fundamental limit, which will further the need for the box lock-in because of the short time constants, as discussed in Fig. 6.4(b). In the example above, modulating the linear signals at $\frac{1}{2}$ and $\frac{1}{3}$ of the laser repetition rate would yield a FWM signal modulated at $\frac{1}{6}^{\text{th}}$ of the laser repetition rate, yielding detection frequencies of up to 20 MHz for the FWM and 60 MHz for the linear signals. The high modulation frequencies require higher sampling rates from the analog-to-digital converter (ADC) in the detection electronics and syncing up the detection electronics and AOMs with the laser repetition rate.

Together with these future technological improvements, box lock-in detection in laser scanning microscopy opens the avenue for improved semiconductor inspection, medical imaging, and other applications in substance-sensitive imaging in both science and industry.

For our CINeMaS setup, the implementation of this box lock-in enables us to combine MDCS with imaging at reasonable data acquisition times. In the following chapter, we use this newly gained capability to image linewidths, strain, and exciton coupling strengths across TMD monolayers and heterostructures.

References

[1] C R Cosens. "A balance-detector for alternating-current bridges". In: *Proceedings of the Physical Society* 46.6 (Nov. 1934), pp. 818–823. DOI: 10.1088/0959-5309/46/6/310.

[2] Walter C. Michels. "A Double Tube Vacuum Tube Voltmeter". In: *Review of Scientific Instruments* 9.1 (1938), pp. 10–12. DOI: 10.1063/1.1752338.

[3] Walter C. Michels and Norma L. Curtis. "A Pentode Lock-In Amplifier of High Frequency Selectivity". In: *Review of Scientific Instruments* 12.9 (1941), pp. 444–447. DOI: 10.1063/1.1769919.

[4] Zurich Instruments. *Zurich Instruments HF2LI - Data sheet*. 2016. URL: http://www.zhinst.com/products/hf2li.

[5] D. C. Tsui, H. L. Stormer, and A. C. Gossard. "Two-Dimensional Magnetotransport in the Extreme Quantum Limit". In: *Phys. Rev. Lett.* 48 (22 May 1982), pp. 1559–1562. DOI: 10.1103/PhysRevLett.48.1559.

[6] Leo Gross, Fabian Mohn, Nikolaj Moll, Bruno Schuler, Alejandro Criado, Enrique Guitián, Diego Peña, André Gourdon, and Gerhard Meyer. "Bond-Order Discrimination by Atomic Force Microscopy". In: *Science* 337.6100 (2012), pp. 1326–1329. DOI: 10.1126/science.1225621.

[7] Kelsey M. Bates, Matthew W. Day, Christopher L. Smallwood, Rachel C. Owen, Tim Schröder, Edward Bielejec, Ronald Ulbricht, and Steven T. Cundiff. "Using silicon-vacancy centers in diamond to probe the full strain tensor". In: *Journal of Applied Physics* 130.2 (2021), p. 024301. DOI: 10.1063/5.0052613.

[8] Eric W. Martin, Jason Horng, Hanna G. Ruth, Eunice Paik, Michael-Henr Wentzel, Hui Deng, and Steven T. Cundiff. "Encapsulation Narrows and Preserves the Excitonic Homogeneous Linewidth of Exfoliated Monolayer $MoSe_2$". In: *Phys. Rev. Applied* 14 (2 Aug. 2020), p. 021002. DOI: 10.1103/PhysRevApplied.14.021002.

[9] Vivek Tiwari, Yassel Acosta Matutes, Alastair. T. Gardiner, Thomas L.C. Jansen, Richard J. Cogdell, and Jennifer P. Ogilvie. "Spatially-resolved fluorescence-detected two-dimensional electronic spectroscopy probes varying excitonic structure in photosynthetic bacteria". In: *Nat. Comm.* 16 (2018), p. 4219. DOI: 10.1038/s41467-018-06619-x.

[10] Tomasz Jakubczyk, Valentin Delmonte, Maciej Koperski, Karol Nogajewski, Clement Faugeras, Wolfgang Langbein, Marek Potemski, and Jacek Kasprzak. "Radiatively Limited Dephasing and Exciton Dynamics in $MoSe_2$ Monolayers Revealed with Four-Wave Mixing Microscopy". In: *Nano Letters* 16.9 (2016), pp. 5333–5339. DOI: 10.1021/acs.nanolett.6b01060.

[11] J. K. Wahlstrand, G. M. Wernsing, J. Paul, and A. D. Bristow. "Automated polarization-dependent multidimensional coherent spectroscopy phased using transient absorption". In: *Opt. Express* 27.22 (Oct. 2019), pp. 31790–31799. DOI: 10.1364/OE.27.031790.

[12] Daniel G. Eichberg, Ashish H. Shah, Long Di, Alexa M. Semonche, George Jimsheleishvili, Evan M. Luther, Christopher A. Sarkiss, Allan D. Levi, Sakir H. Gultekin, Ricardo J. Komotar, and Michael E. Ivan. "Stimulated Raman histology for rapid and accurate intraoperative diagnosis of CNS tumors: prospective blinded study". In: *Journal of Neurosurgery JNS* 134.1 (2021), pp. 137–143. DOI: 10.3171/2019.9.JNS192075.

[13] Christian W. Freudiger, Wei Min, Brian G. Saar, Sijia Lu, Gary R. Holtom, Chengwei He, Jason C. Tsai, Jing X. Kang, and X. Sunney Xie. "Label-Free Biomedical Imaging with High Sensitivity by Stimulated Raman Scattering Microscopy". In: *Science* 322.5909 (2008), pp. 1857–1861. ISSN: 0036-8075. DOI: 10.1126/science.1165758.

[14] Minbiao Ji, Daniel A. Orringer, Christian W. Freudiger, Shakti Ramkissoon, Xiaohui Liu, Darryl Lau, Alexandra J. Golby, Isaiah Norton, Marika Hayashi, Nathalie Y. R. Agar, Geoffrey S. Young, Cathie Spino, Sandro Santagata, Sandra Camelo-Piragua, Keith L. Ligon, Oren Sagher, and X. Sunney Xie. "Rapid, Label-Free Detection of Brain Tumors with Stimulated Raman Scattering Microscopy". In: *Science Translational Medicine* 5.201 (2013). ISSN: 1946-6234. DOI: 10.1126/scitranslmed.3005954.

[15] Brian G. Saar, Christian W. Freudiger, Jay Reichman, C. Michael Stanley, Gary R. Holtom, and X. Sunney Xie. "Video-Rate Molecular Imaging in Vivo with Stimulated Raman Scattering". In: *Science* 330.6009 (2010), pp. 1368–1370. ISSN: 0036-8075. DOI: 10.1126/science.1197236.

[16] Fa-Ke Lu, Srinjan Basu, Vivien Igras, Mai P. Hoang, Minbiao Ji, Dan Fu, Gary R. Holtom, Victor A. Neel, Christian W. Freudiger, David E. Fisher, and X. Sunney Xie. "Label-free DNA imaging in vivo with stimulated Raman scattering microscopy". In: *Proceedings of the National Academy of Sciences* 112.37 (2015), pp. 11624–11629. ISSN: 0027-8424. DOI: 10.1073/pnas.1515121112.

[17] Tomasz Jakubczyk, Karol Nogajewski, Maciej R Molas, Miroslav Bartos, Wolfgang Langbein, Marek Potemski, and Jacek Kasprzak. "Impact of environment on dynamics of exciton complexes in a WS_2 monolayer". In: *2D Materials* 5.3 (Apr. 2018), p. 031007. DOI: 10.1088/2053-1583/aabc1c.

[18] Tomasz Jakubczyk, Goutham Nayak, Lorenzo Scarpelli, Wei-Lai Liu, Sudipta Dubey, Nedjma Bendiab, Laëtitia Marty, Takashi Taniguchi, Kenji Watanabe, Francesco Masia, Gilles Nogues, Johann Coraux, Wolfgang Langbein, Julien Renard, Vincent Bouchiat, and Jacek Kasprzak. "Coherence and Density Dynamics of Excitons in a Single-Layer MoS_2 Reaching the Homogeneous Limit". In: *ACS Nano* 13.3 (2019). PMID: 30735350, pp. 3500–3511. DOI: 10.1021/acsnano.8b09732.

[19] Thomas P. Dougherty, Gary P. Wiederrecht, and Keith A. Nelson. "Impulsive stimulated Raman scattering experiments in the polariton regime". In: *J. Opt. Soc. Am. B* 9.12 (Dec. 1992), pp. 2179–2189. DOI: 10.1364/JOSAB.9.002179.

[20] Yifan Zhu and Ji-Xin Cheng. "Transient absorption microscopy: Technological innovations and applications in materials science and life science". In: *The Journal of Chemical Physics* 152.2 (2020), p. 020901. DOI: 10.1063/1.5129123.

[21] B. Kasprzak J.and Patton, V. Savona, and W. Langbein. "Coherent coupling between distant excitons revealed by two-dimensional nonlinear hyperspectral imaging". In: *Nature Photonics* 5.1 (Jan. 2011), pp. 57–63. DOI: 10.1038/nphoton.2010.284.

[22] Galan Moody and Steven T. Cundiff. "Advances in multi-dimensional coherent spectroscopy of semiconductor nanostructures". In: *Advances in Physics: X* 2.3 (2017). PMID: 28894306, pp. 641–674. DOI: 10.1080/23746149.2017.1346482.

[23] Torben L. Purz, Eric W. Martin, Pasqual Rivera, William G. Holtzmann, Xiaodong Xu, and Steven T. Cundiff. "Coherent exciton-exciton interactions and exciton dynamics in a $MoSe_2/WSe_2$ heterostructure". In: *Phys. Rev. B* 104 (24 Dec. 2021), p. L241302. DOI: 10.1103/PhysRevB.104.L241302.

[24] Veronica R. Policht, Mattia Russo, Fang Liu, Chiara Trovatello, Margherita Maiuri, Yusong Bai, Xiaoyang Zhu, Stefano Dal Conte, and Giulio Cerullo. "Dissecting Interlayer Hole and Electron Transfer in Transition Metal Dichalcogenide Heterostructures via Two-Dimensional Electronic Spectroscopy". In: *Nano Letters* 21.11 (2021). PMID: 34037406, pp. 4738–4743. DOI: 10.1021/acs.nanolett.1c01098.

[25] Kai-Chih Huang, Jeremy McCall, Pu Wang, Chien-Sheng Liao, Gregory Eakins, Ji-Xin Cheng, and Chen Yang. "High-Speed Spectroscopic Transient Absorption Imaging of Defects in Graphene". In: *Nano Letters* 18.2 (2018). PMID: 29342361, pp. 1489–1497. DOI: 10.1021/acs.nanolett.7b05283.

[26] Wei Min, Sijia Lu, Markus Rueckel, Gary R. Holtom, and X. Sunney Xie. "Near-Degenerate Four-Wave-Mixing Microscopy". In: *Nano Letters* 9.6 (2009). PMID: 19432483, pp. 2423–2426. DOI: 10.1021/nl901101g.

[27] Jianjun Wang, Xi Zhang, Junbo Deng, Xing Hu, Yun Hu, Jiao Mao, Ming Ma, Yuhao Gao, Yingchun Wei, Fan Li, Zhaohua Wang, Xiaoli Liu, Jinyou Xu, and Liqing Ren. "Simplified Near-Degenerate Four-Wave-Mixing Microscopy". In: *Molecules* 26.17 (2021). ISSN: 1420-3049. DOI: 10.3390/molecules26175178.

[28] Thomas Gottschall, Tobias Meyer, Cesar Jauregui, Florian Just, Tino Eidam, Michael Schmitt, Jürgen Popp, Jens Limpert, and Andreas Tünnermann. "All-fiber optical parametric oscillator for bio-medical imaging applications". In: *Fiber Lasers XIV: Technology and Systems*. Vol. 10083. International Society for Optics and Photonics. SPIE, 2017, pp. 252–255.

[29] P. Fimpel, C. Riek, L. Ebner, A. Leitenstorfer, D. Brida, and A. Zumbusch. "Boxcar detection for high-frequency modulation in stimulated Raman scattering microscopy". In: *Applied Physics Letters* 112.16 (2018), p. 161101. DOI: 10.1063/1.5022266.

[30] Yinpeng Zhong. "Ultrafast Dynamics in Polar and Magnetic Semiconductors: Optical and Free-Electron Laser Investigations". PhD thesis. Ruperto-Carola-University of Heidelberg, 2012. DOI: 10.11588/heidok.00014312.

[31] Lukas A. Jakob, William M. Deacon, Oliver Hicks, Ilya Manyakin, Oluwafemi S. Ojambati, Michael Traxler, and Jeremy J. Baumberg. "Single photon multiclock lock-in detection by picosecond timestamping". In: *Optica* 8.12 (Dec. 2021), pp. 1646–1653. DOI: 10.1364/OPTICA.441487.

[32] Gaël Nardin, Travis M. Autry, Kevin L. Silverman, and S. T. Cundiff. "Multidimensional coherent photocurrent spectroscopy of a semiconductor nanostructure". In: *Opt. Express* 21.23 (Nov. 2013), pp. 28617–28627. DOI: 10.1364/OE.21.028617.

[33] John H. Scofield. "Frequency-domain description of a lock-in amplifier". In: *American Journal of Physics* 62.2 (1994), pp. 129–133. DOI: 10.1119/1.17629.

[34] Paul K. Dixon and Lei Wu. "Broadband digital lock-in amplifier techniques". In: *Review of Scientific Instruments* 60.10 (1989), pp. 3329–3336. DOI: 10.1063/1.1140523.

[35] ZurichInstruments. *Principles of lock-in detection and the state of the art [White paper]*. 2016. URL: https://www.zhinst.com/sites/default/files/li_primer/zi_whitepaper_principles_of_lock-in_detection.pdf.

[36] Donald M. Monroe. *A Lock-In Amplifier Primer*. 1975. URL: https://wp.optics.arizona.edu/jpalmer/wp-content/uploads/sites/65/2018/11/LIA_Primer.pdf.

[37] Caroline Boule, Diana Vaclavkova, Miroslav Bartos, Karol Nogajewski, Lukas Zdražil, Takashi Taniguchi, Kenji Watanabe, Marek Potemski, and Jacek Kasprzak. "Coherent dynamics and mapping of excitons in single-layer $MoSe_2$ and WSe_2 at the homogeneous limit". In: *Phys. Rev. Materials* 4 (3 Mar. 2020), p. 034001. DOI: 10.1103/PhysRevMaterials.4.034001.

[38] Patrick F. Tekavec, Geoffrey A. Lott, and Andrew H. Marcus. "Fluorescence-detected two-dimensional electronic coherence spectroscopy by acousto-optic phase modulation". In: *The Journal of Chemical Physics* 127.21 (2007), p. 214307. DOI: 10.1063/1.2800560.

[39] Eric W. Martin and Steven T. Cundiff. "Inducing coherent quantum dot interactions". In: *Phys. Rev. B* (Feb. 2018), p. 081301. DOI: 10.1103/PhysRevB.97.081301.

[40] Jason Horng, Eric W. Martin, Yu-Hsun Chou, Emmanuel Courtade, Tsu-chi Chang, Chu-Yuan Hsu, Michael-Henr Wentzel, Hanna G. Ruth, Tien-chang Lu, Steven T. Cundiff, Feng Wang, and Hui Deng. "Perfect Absorption by an Atomically Thin Crystal". In: *Phys. Rev. Applied* 14 (2 Aug. 2020), p. 024009. DOI: 10.1103/PhysRevApplied.14.024009.

[41] Damon DePaoli, Émile Lemoine, Katherine Ember, Martin Parent, Michel Prud'homme, Léo Cantin, Kevin Petrecca, Frédéric Leblond, and Daniel C. Côté. "Rise of Raman spectroscopy in neurosurgery: a review". In: *Journal of Biomedical Optics* 25.5 (2020), pp. 1–36. DOI: 10.1117/1.JBO.25.5.050901.

CHAPTER VII

Imaging Dynamics of Exciton Interactions and Coupling in Transition Metal Dichalcogenides

Reproduced in part from:

Torben L. Purz, Eric W. Martin, William G. Holtzmann, Pasqual Rivera, Adam Alfrey, Kelsey M. Bates, Hui Deng, Xiaodong Xu, and Steven T. Cundiff "Imaging dynamic exciton interactions and coupling in transition metal dichalcogenides". *J. Chem. Phys.* **156**, 214704 (2022).

with permission of AIP Publishing.

7.1 Introduction

In previous chapters, we have motivated the study of TMDs, both for their interesting intrinsic physics and their potential for device applications. For most devices, reliable performance requires minimal device-to-device fluctuations in performance and homogeneous performance across the entire device area (e.g., when proposing to use TMDs for solar cells). Depending on the sample system, different physical parameters determine the feasibility of those applications.

In TMD monolayers, low inhomogeneity and long intralayer exciton dephasing times are crucial, especially for quantum information applications. Martin *et al.* [1]

demonstrated picosecond dephasing times for $MoSe_2$ monolayers by measuring the homogeneous linewidth, which is inversely proportional to the dephasing time. These dephasing times are well above previously reported values [2–5] due to the dominant contribution of inhomogeneous broadening in these samples. Meanwhile, Jakubczyk *et al.* [6, 7] and Boule *et al.* [8] have shown broader homogeneous linewidths, with the exciton optical response being in the homogeneous limit for certain areas. Identifying promising areas for quantum information applications thus requires finding uniquely suited sample areas with small inhomogeneity and large dephasing times. Unfortunately, there is a caveat to this condition: As previously established by Jakubczyk *et al.* [6, 7], anti-correlation between homogeneous and inhomogeneous linewidths is expected, favoring long dephasing times in areas of large inhomogeneity. Non-radiative broadening mechanisms can weaken this anti-correlation. However, a large inhomogeneity is detrimental to quantum information applications since it corresponds to several different emitters within the excitation volume.

For heterostructure systems, these considerations change based on the physical effects harnessed for quantum information applications. For example, ILEs have been proposed as potential candidates for qubits [9, 10]. Moreover, coherent coupling between excitons in the different layers of the heterostructures, as shown in Chap. V, is another pathway toward coherent control for quantum information applications. Lastly, the rapid charge transfer discussed in Chap. V is another property closely tied to applications such as photovoltaics.

Thus, for feasibility considerations, identifying areas with robustness of these properties - ILE lifetimes, coherent coupling strength, and charge transfer - is a requirement. Outside of quantum information applications, the rapid charge transfer is another property of interest for photovoltaic applications [11].

However, the intricate spatial and temporal variations of exciton interactions with their environment and amongst themselves in TMD monolayers and heterostructures

have remained mostly elusive due to limitations in the employed experimental techniques. With the MDCS technique introduced in Chaps. III and IV, the box lock-in amplifier introduced in the previous chapter, and the laser-scanning imaging setup described in Chap. IV, we have the pieces assembled to realize an imaging version of MDCS that we coin multidimensional coherent imaging spectroscopy, introduced in Sec. 4.5.

In the following, we use MDCIS to map the distribution of FWM strength, dephasing times, and inhomogeneity across a $MoSe_2$ monolayer, giving insight into strain and enabling the identification of promising and unfavorable areas for quantum information applications. We initially correlate findings from PL-detected and heterodyne-detected FWM, highlighting a spatially dependent distribution of bright and dark exciton states across the monolayer. Subsequently, we show maps of homogeneous and inhomogeneous linewidths and exciton resonance energies, establishing strain as the dominant source of sample inhomogeneity. In this context, we discuss the advantage of frequency over time-domain fitting by simulating the fit error for the two methods for varying noise levels. In the second part of this chapter, we use MDCIS to spatially map strain and conduction band changes across a $MoSe_2/WSe_2$ heterostructure. We achieve this by tracking the spatial exciton resonance energy changes for the two materials and correlating them with the ILE emission. Despite considerable, complex local strain and dielectric environment changes, we demonstrate the surprising robustness of key sample properties: The rapid electron and hole transfer, as well as coherent coupling between intralayer excitons in the $MoSe_2$ and WSe_2 monolayers and ILE lifetimes, are homogeneous across a majority of the heterostructure.

These results have larger implications for the commonly made claims for device applications: The dephasing times and inhomogeneity show significant variations across the sample, casting doubt on some quantum information claims with current sample

qualities. On the other hand, the robustness of coherent coupling, charge transfer, and ILE lifetimes strengthens the case for TMDs heterostructures as a promising choice for various applications, including quantum information and photovoltaics.

7.2 Four-Wave Mixing vs. Photoluminescence-Detected Four-Wave Mixing on a $MoSe_2$ Monolayer

Fig. 7.1(a) shows a white light microscope image of the $MoSe_2$ monolayer studied in this chapter. The monolayer (red lines) shows a region with cracks and bubbles towards the center but otherwise appears mostly pristine. The upper-left part of the monolayer region (shaded) is non-encapsulated, while the lower-right side of the monolayer (unshaded) is hBN encapsulated (brown lines). Given the reported instabilities and inconsistencies of non-encapsulated samples [1, 7, 12], we will focus our studies on the encapsulated area of the sample.

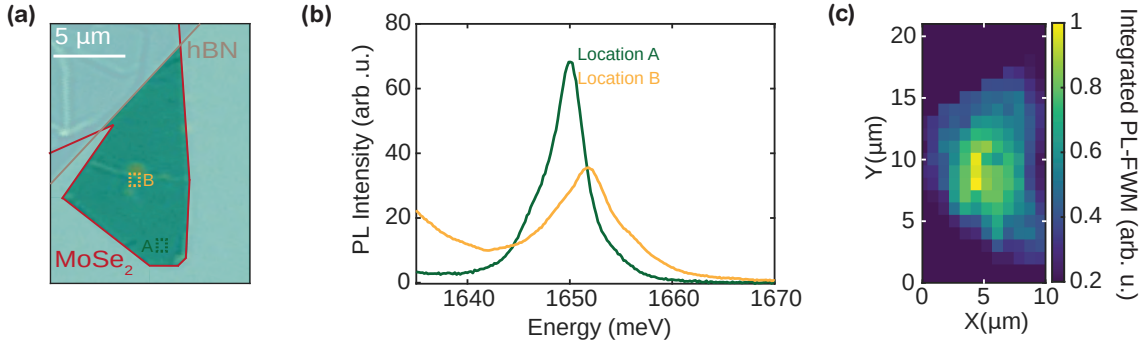

Figure 7.1: **(a)** White light microscopy image of the $MoSe_2$ monolayer. **(b)** PL-spectrum on the lower edge (Location A) and center area (Location B) of the $MoSe_2$ monolayer. For location B, the signal tail towards lower energies is associated with the trion. **(c)** PL-detected FWM image of the $MoSe_2$ monolayer.

A PL measurement of location A and location B, marked with a green and yellow rectangle in Fig. 7.1(a), is plotted in Fig. 7.1(b). The raw data of the PL measurement was provided to us by my collaborator Adam Alfrey. While the PL measurement shows changes in maximum PL intensity and linewidth, the integrated PL strength

(from 1630-1675 meV) for the two spots varies somewhat but is comparable with a ratio of 0.71. In Fig. 7.1(c), we plot a spatial map of the spectrally integrated PL-detected FWM with the raw data provided by my colleague Kelsey M. Bates. The spatial profile of the PL-detected FWM indicates dipole strength and density of stage changes since the integrated FWM will scale with dipole moment and density of states ($\propto N\mu^4$), with N being the density of states and μ the dipole moment. PL-detected FWM [13], compared to the heterodyne-detected FWM scheme presented otherwise in this work, uses the interaction of a fourth pulse with the sample to detect a modulation in PL intensity. Therefore, PL-detected FWM selects bright, luminescing states, while heterodyne-detected FWM(in the following simply referred to as FWM) is more sensitive to the ensemble as a whole, including non-luminescing states. The difference in sensitivity between the two techniques is similar to the difference between PL excitation spectroscopy and absorption in the linear regime. PL-detected FWM is thus better for comparison to FWM. We spectrally integrate the PL-detected FWM from 1630-1675 meV for both the absorption and emission axis. Fig. 7.1(c) then shows a clear maximum in integrated amplitude towards the center of the sample, with the signal decreasing towards the edge of the sample. However, a small area around Location B from Fig. 7.1(a) shows a decreased integrated amplitude.

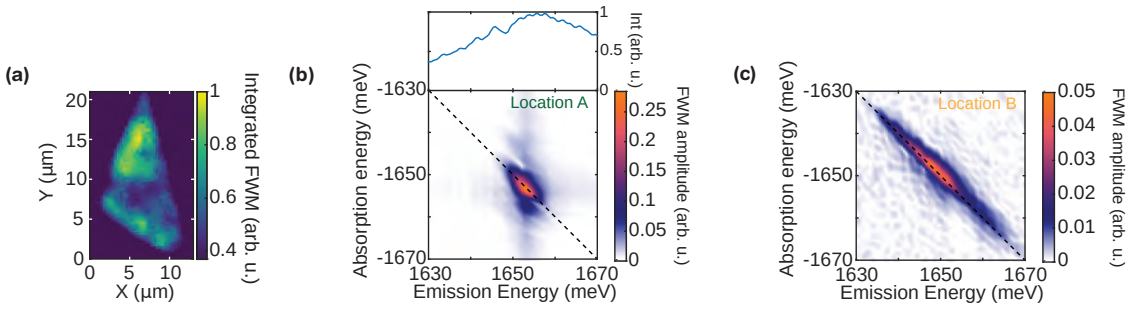

Figure 7.2: **(a)** Integrated FWM of the hBN-encapsulated $MoSe_2$ monolayer. **(b)** Low-power, low-temperature MDCS spectrum at location A. The excitation laser spectrum used for the experiments on the monolayer is shown atop. **(c)** Low-power, low-temperature MDCS spectrum for location B.

For comparison, a spectrally integrated heterodyne-detected FWM image of the

$MoSe_2$ monolayer is shown in Fig. 7.2(a). The spatial profile of the integrated FWM differs from the integrated PL-detected FWM. A large area on the top of the sample shows a strong and approximately homogeneous FWM amplitude. In contrast, a dark area towards the center of the samples coincides with cracks and bubbles visible in the white light microscope image in Fig. 7.1(a). The bottom area of the sample again shows a comparatively homogeneous strength. While the PL-detected and heterodyne-detected FWM have different spatial resolutions, mainly due to the 30° angle of the sample in the PL-detected FWM setup (for details, see Ref. 14), it is evident that the low FWM area in Fig. 7.2(a) shows the highest PL-detected FWM in Fig. 7.1(c). The reason behind the difference between PL-detected FWM and heterodyne-detected FWM (in the following, if not stated otherwise, simply FWM) can be understood from the difference in state-selectivity of the two techniques: PL and PL-detected FWM are only sensitive to bright, photoluminescing states, while heterodyne-detected FWM is sensitive to both bright and dark states, introduced in Sec. 2.5. As Smallwood et al. [13] discussed, the difference between PL-detected FWM strength and heterodyne-detected FWM strength thus suggests a highly spatially dependent distribution of bright and dark states, with a large number of dark states outside the center area of the monolayer.

Apart from the distinct behavior of PL-detected FWM and heterodyne-detected FWM toward the center (Location B) and edge (Location A) of the sample, the PL shows a noticeable linewidth change between the center and edge area of the monolayer. The exemplary MDCS spectra (not obtained from an MDCIS measurement) for Location A (Fig. 7.2(b)) and Location B (Fig. 7.2(c)) corroborate this linewidth observation. Location A shows some inhomogeneous broadening, but comparatively, Location B shows a more dominant inhomogeneous broadening, which manifests as an elongation along the diagonal of the MDCS spectrum (dashed line). The homogeneous linewidths for the two locations remain comparable. The broader linewidth

in the PL spectrum in Fig. 7.1(b) is thus caused by an increase in inhomogeneity and not related to homogeneous linewidth changes. Moreover, the inhomogeneously broadened spectrum of the center area shows more weight towards lower energies, suggesting the existence of notable resonance shifts on the order of several meV.

7.3 Spatial Dependence of Homogeneous and Inhomogeneous Linewidth Changes Across a $MoSe_2$ Monolayer

A more systematic study of resonance shifts and linewidths is required to understand the underlying physics and identify promising areas for quantum information and other applications. The linewidths are measures of spatial and temporal coherence, both of which are crucial for quantum information applications. However, there is a trade-off between spatial and temporal coherence: Spatial inhomogeneity, corresponding to local exciton energy changes due to a change in the environment, is associated with a lower spatial coherence because the energy shifts destroy the coherence between excitons. Hence, in the presence of a smaller inhomogeneity σ, the exciton coherence volume in real space, i.e., the spatial coherence, is larger. A larger real space volume corresponds to a smaller k-space volume. The smaller k-space volume increases the overlap of the exciton dispersion with the light cone, increasing the strength of the light-matter interaction (and hence dipole moment μ) and decreasing the radiative lifetime T_{rad}. A decreased radiative lifetime decreases the overall dephasing time T_2 via Eqs. 2.7 and 2.8 and yields an increased homogeneous linewidth γ. By this argument, one expects larger γ for smaller σ and hence an anti-correlation between the two linewidths. This relation was pointed out previously by Jakubczyk[6, 7] and Boule *et al.* [8]. In the following, we use the Pearson correlation coefficient, which measures the linear correlation between two sets of data, A, and B, to quantify the (anti-)correlation. The Pearson correlation coefficient is defined

as $\rho(A,B) = \mathrm{cov(A,B)}/(\sigma_A\sigma_B)$. Here, cov denotes the covariance of data sets A and B, and $\sigma_{A,B}$ is their respective standard deviation. In the idealized scenario of a radiatively limited homogeneous linewidth and no changes in the intrinsic linewidth (i.e., only changes in the radiative linewidth contribute to homogeneous linewidth changes), a perfect anti-correlation between γ and σ is expected. However, this anti-correlation might not be perfectly linear but display a strictly monotonous decrease of γ for increasing σ. Because ρ only captures the linear correlation, the coefficient would be close to but above -1. Furthermore, in the presence of non-radiative homogeneous broadening mechanisms such as non-radiative electron scattering, γ can be further increased [6, 7], weakening the anti-correlation. This weakened anti-correlation is reflected in the literature, where Ref. 7 measures correlations of $\rho = -0.06$ and $\rho = -0.425$ for two different MoS_2 monolayer samples.

For quantum information applications, linewidths in the homogeneous limit (i.e., $\sigma < \gamma$) and small homogeneous linewidths γ (i.e., long dephasing times) are desired. The definition of "long" dephasing times is somewhat arbitrary because the timescale has to be seen in relation to the time it takes to manipulate the qubit for quantum computing. A few years ago, the ratio of dephasing to manipulation time was approaching 10^4 [15], such that with single-cycle optical pulses (around 2.7 fs at 800 nm), dephasing times in the tens of ps range are desirable. Unfortunately, the smallest γ and σ are hard to achieve for a given materials platform because of the anti-correlation, which can only be weakened by an increase in γ due to non-radiative contributions, as explained above. However, based on the chosen materials platform, an overall low γ and σ can still be achieved.

Maps of γ and σ across the $MoSe_2$ monolayer are shown in Fig. 7.3(a) and (b), respectively. The linewidths are extracted by simultaneously fitting diagonal and cross-diagonal slices in the 2D frequency data with the analytical solutions for arbitrary amounts of γ and σ provided in Sec. 3.7. This is notably different from the

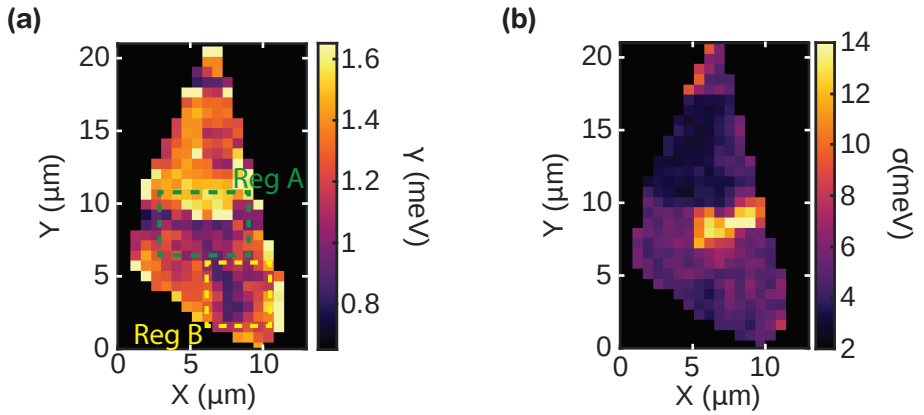

Figure 7.3: **(a)** Homogeneous (γ) linewidth map of the $MoSe_2$ monolayer. We average 2×2 pixels together for these maps, obtaining a pixel size close to the spatial resolution. **(b)** Inhomogeneous linewidth (σ) map of the $MoSe_2$ monolayer. For legibility, the color bar is capped at 14 meV.

procedure employed in [6–8] where linewidths are fitted in the temporal domain. As discussed in Sec. 7.4, the frequency domain fitting is less susceptible to measurement noise because the Fourier transform filters most of the high-frequency noise. After fitting, we further average 2×2 pixels together to reduce pixel-to-pixel noise. The averaging leaves us with a pixel size of 700 nm $\times$ 700 nm, close to the spatial resolution.

The areas of lower FWM show a significantly increased σ and a smaller γ. Overall, γ shows changes ranging between 0.75 meV and 1.7 meV, more than a factor of two difference. Depending on the sample spot, σ increases by up to a factor of 10, from below 3 meV to values up to 35 meV. As pointed out in Refs. 67816, these changes could be caused by strain, wrinkling, flake deformations, cracks, changes in the dielectric surrounding, doping, trapped charges, impurities, defects, and the free carrier concentration. In this chapter, we use the term "strain" to encompass all material deformations due to mechanical stress, including strain, wrinkling, and flake deformations. We can assign strain as the leading cause for the sample changes by considering the alternatives: As discussed by Ref. 1 and Ref. 17, the dielectric permittivity and doping variations are suppressed by hBN encapsulation and, therefore,

are unlikely to occur in this sample. A change in doping would cause a change in the exciton-trion ratio in the PL. The full energy-range PL for the $MoSe_2$ monolayer shown in Fig. 7.4 shows signatures of both the exciton (high energy) and trion (low energy). We quantify the ratio of the energy-integrated PL intensity (area under the curve) for the exciton and trion by isolating the exciton and trion peaks and fitting a Bi-Voigt profile to each of them, yielding a good agreement between PL Intensity and fit (dashed lines). We then integrate over the exciton and trion contribution isolated from the fits. The ratio between the PL for exciton and trion only modestly varies between locations A and B (ratio: 14.1 for Location A, 10.7 for Location B), suggesting no significant change in doping for the two locations.

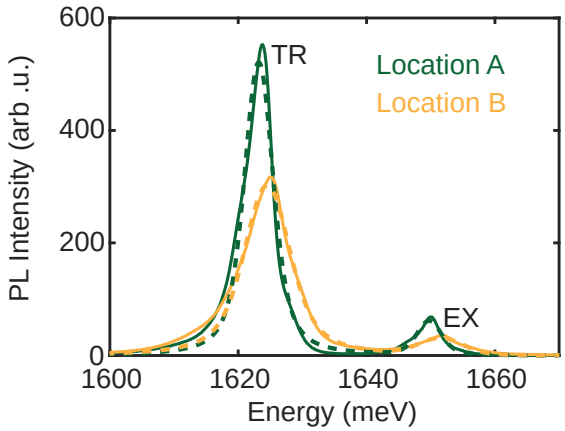

Figure 7.4: PL of the $MoSe_2$ monolayer for location A and location B (Fig. 7.1(a)), showing the exciton (high energy) and trion (low energy) emission.

In conclusion, similar to Ref. 6, we thus exclude changes in the dielectric environment of doping as the leading cause for the variations in the optical measurements. Similar to Ref. 67, we assign linewidth and dipole changes to strain. Strain is associated with larger exciton localization and larger σ, smaller γ, and smaller μ.

The (anti-)correlation between γ and σ across large areas of the sample can best be visualized by plotting σ against γ, as done in Fig. 7.5(a). Here, sample points falling within the green and yellow rectangle (Fig. 7.1(a)) are plotted in green and yellow, respectively, while all other sample points are plotted in black. A moderately

strong anti-correlation of $\rho = -0.47 \pm 0.1$ can be observed for the two linewidths across the sample.

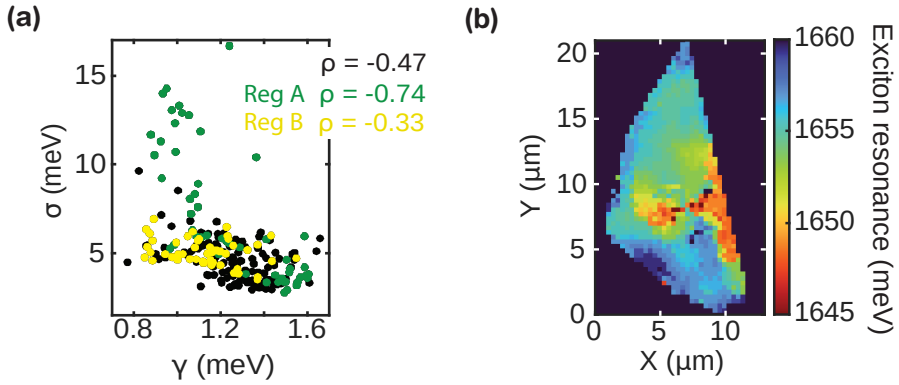

Figure 7.5: **(a)** σ vs. γ for all sample points. Sample points falling within the area of the green (yellow) rectangle in Fig. 7.3(a) are plotted in green (yellow). All other sample points are plotted in black. Correlation for the sample points within the colored rectangles and all data points together is calculated using the Pearson correlation coefficient. **(b)** Resonance energy map of the $MoSe_2$ monolayer.

A closer inspection of Fig. 7.5(a) together with Fig. 7.3(a,b) suggests that there are areas of stronger anti-correlation, while other areas show a weaker correlation between the linewidths. Indeed, the green sample points show a strong anti-correlation with a correlation coefficient $\rho = -0.74 \pm 0.13$. In contrast, the yellow points show a much weaker anti-correlation with a correlation coefficient $\rho = -0.33 \pm 0.26$. Most importantly, with regards to quantum information applications, the points within the yellow rectangle show values of γ around 0.9 meV with comparatively low σ between 4.5-7 meV, while for the green rectangle, similar values of γ can only be found with σ above 10 meV. Hence, the yellow rectangle area towards the bottom of the sample is a more favorable area than the green rectangle for quantum information applications that rely on low inhomogeneity and slow dephasing. However, another low-strain area towards the top of the sample (identified by its low σ), while showing an overall lower σ, also shows higher γ, illustrating that a low-strain area is not inherently a "good" area of the sample concerning the application potential. "Good" areas, with respect to quantum information applications, fulfill the abovementioned condition of small γ

and σ.

After assigning the linewidth and dipole changes to strain, we can further distinguish between tensile and compressive strain via the sign of resonance energy shifts across the sample [17]. We plot an image of the exciton resonance energy distribution across the sample in Fig. 7.5(b). This map shows significant shifts in the resonance energy between 1645 meV and up to 1660 meV across the 10 µm × 15 µm area of the sample. The areas of strongest resonance shifts also coincide with the areas of lower integrated FWM, further supporting the assignment to strain. The observation of both red and blue shifts across the sample points toward complex local strain dynamics involving both tensile (red-shifted energies) and compressive (blue-shifted energies) strain caused by the cracks and bubbles in the central area of the sample.

Before applying MDCIS to a more complicated material system, specifically a $MoSe_2/WSe_2$ heterostructure in Sec. 7.5, we will shortly discuss the advantage of frequency over time-domain linewidth fitting, which is a strength of the MDCIS technique.

7.4 Advantage of Frequency Over Time-Domain Linewidth Fitting

As pointed out in the previous section, we extract γ and σ through fits in the frequency domain. However, as discussed in Ref. 18, linewidths can be extracted in either the time or frequency domain. For complex systems, there are apparent advantages to the frequency domain fitting: In the case of more than one resonance, the time-domain trace will contain contributions from both resonances simultaneously, including interactions, and linewidths for the particular resonances cannot be reliably extracted in the time domain. In contrast, the resonances are separated in the frequency domain, and separate linewidth fits can be applied. Moreover, additional

sample dynamics, such as spectral diffusion, can be more easily accounted for in the frequency domain, as discussed in Sec. 3.7.

Time domain fitting has one major advantage over frequency-domain fitting: Diederich *et al.* show [18] that taking slices in the time domain is significantly faster than acquiring full MDCS spectra. Nonetheless, even in cases where extracting the linewidths in the temporal domain is theoretically possible (i.e., singular resonances, simple spectral response of the sample without noticeable spectral diffusion), the introduction of noise into the measurement can significantly alter the reliability and stability of the extracted fits.

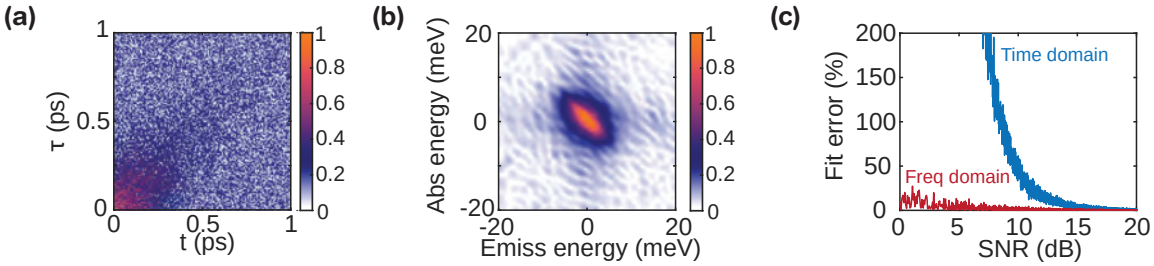

Figure 7.6: **(a)** Time trace for an MDCS measurement with an SNR of 7 dB. **(b)** Corresponding MDCS spectrum **(c)** Fit error as a function of SNR for both frequency domain and time domain slice fits.

Fig. 7.6(a) shows the simulated two-dimensional time trace for an MDCS measurement with an SNR of 7 dB. The simulation assumes a single resonance with $T_2 = 700\,\text{fs}$ ($\gamma = 1.34\,\text{meV}$) and $\xi = 250\,\text{fs}$ ($\sigma = 3.78\,\text{meV}$). Fig. 7.6(b) shows the corresponding MDCS spectrum obtained after Fourier transform. We extract γ (or equivalently T_2) with two different methods: either taking a slice in the time domain or a slice in the frequency domain, and subsequent fitting. The analytical form for the fits can be found in Sec. 3.7. We simulate the noise dependence of the fit error for the two cases and plot the results in Fig. 7.6(c). We use white Gaussian noise to model the experimental noise in the simulation, which is a valid assumption since our experiments are limited by the shot noise of the DC background.

While these two fitting procedures in the ideal, low-noise scenario (corresponding

to a large SNR) are equivalent, the advantage of the frequency domain fitting procedure becomes quickly apparent once noise becomes stronger. Both time and frequency domain show noticeable fit errors for low SNR, though the frequency-domain fit error never exceeds 25% for the noise levels displayed here. Meanwhile, the time domain error increases drastically below 15 dB and reaches unacceptable values around 10 dB. The secret behind the superiority of the frequency domain is Fellgett's advantage: In the case of signal-independent noise, as is the case here, the SNR improves by a factor of $\sqrt{m}$, with m being the number of sample points [19]. This advantage applies along both the t and τ axis. The improvement in SNR is evident from comparing Figs. 7.6(a,b). The considerations above are only true entirely for 2D-Fourier transform spectroscopy, where the data is fully acquired in the temporal domain. Mixed time-frequency domain spectroscopies as, e.g., employed by Refs. [12, 20] are more prone to noise since only one Fourier transform (either into the time domain or frequency domain) is performed. Additionally, the fitting procedures here assume a fit of the amplitude in both the time and frequency domains. The reasoning behind this assumption is that most setups that operate partially or fully in the time domain do not have the full phase information to extract real and imaginary parts [6]. The fit error can, however, be further reduced by fitting the real and imaginary parts in either the time or frequency domain.

In conclusion, the frequency-domain fitting allows for a much more robust retrieval of linewidths even for low SNR and reaches very reliable results at much lower SNR values than the time domain fitting.

7.5 Visualizing Strain and Exciton Coupling Strength Across a $MoSe_2/WSe_2$ Heterostructure

We extend our study to a $MoSe_2/WSe_2$ heterostructure encapsulated in hBN. Fig. 7.7(a) shows a white light microscopy image of the heterostructure, which is the same sample as in Chap. V. Three exemplary MDCS spectra (not obtained with the MDCIS technique, see App. C) taken at the three points marked in Fig. 7.7(a) are plotted in Fig. 7.7(b-d). For the $MoSe_2/WSe_2$ heterostructure, unless otherwise stated, data was taken at $T = 500\,\text{fs}$. Similar to Chap. V, we plot the absorptive spectrum obtained by adding the rephasing and non-rephasing spectra.

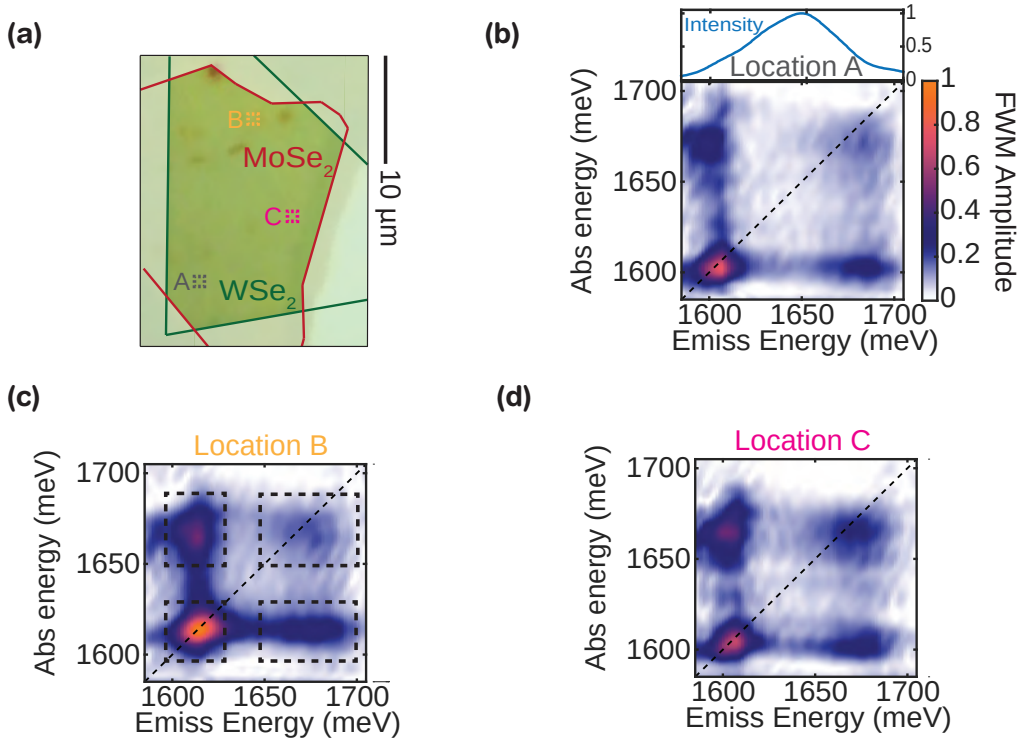

Figure 7.7: **(a)** White light microscopy image of the hBN-encapsulated $MoSe_2/WSe_2$ heterostructure. **(b-d)** Low-power, low-temperature MDCS spectra of $MoSe_2/WSe_2$ heterostructure at three different sample points marked by the three squares in (a). The laser spectrum used for all MDCIS experiments on the heterostructure is plotted atop.

The two on-diagonal (dashed line) peaks are associated with the $MoSe_2$ and WSe_2 intralayer A-excitons. As discussed in Chap. V, the two off-diagonal peaks indicate

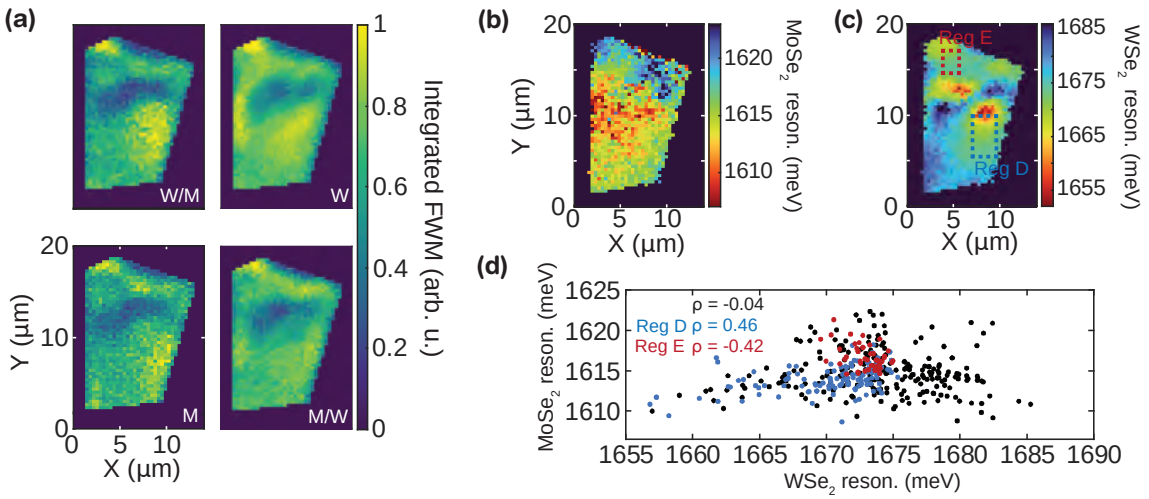

Figure 7.8: **(a)** Integrated FWM of the four peaks shown in Fig. 7.7(b-d). The integration area for the four peaks is shown for Location B in Fig. 7.7(c) and is kept fixed across the sample. The area of low intensity is a high-strain area with cracks and wrinkles. **(b)** $MoSe_2$ resonance energy map across the $MoSe_2/WSe_2$ heterostructure. **(c)** WSe_2 resonance energy map across the $MoSe_2/WSe_2$ heterostructure. **(d)** $MoSe_2$ resonance energy vs. WSe_2 resonance energy for all sample points. Sample points falling within the area of the red (blue) rectangle in (c) are plotted in red (blue). All other sample points are plotted in black. Correlation for the sample points within the colored rectangles and all data points together is calculated using the Pearson correlation coefficient.

both coherent coupling and incoherent electron and hole (charge) transfer. The spectra show significant energy shifts and varying peak strengths for the $MoSe_2$ and WSe_2 resonances across the sample. We spectrally integrate the four peaks to better visualize their strength variations across the sample. The integration area is highlighted in Fig. 7.7(c).

Maps of the integrated FWM for the four peaks (obtained from the rephasing MDCIS data) are shown in Fig. 7.8(a). The figures have the same order as the peaks - with the $MoSe_2$ (M) peak in the lower left, the WSe_2 (W) peak in the upper right, and the $MoSe_2/WSe_2$ (M/W) and $WSe_2/MoSe_2$ (W/M) peak in the lower right and upper left respectively. Similar to the $MoSe_2$ monolayer, there is a region of decreased FWM towards the upper center of the sample, which is associated with a high strain area due to wrinkles and bubbles formed during fabrication. Apart from this area,

the peak strength is mostly homogeneous across the sample for all four peaks, except for the $MoSe_2$ and $MoSe_2/WSe_2$ peaks having a lower strength towards the bottom left of the sample. The differences in peak strengths can partially be attributed to spatial variations of the dipole moment μ that differ for the two materials based on the local strain profile. Furthermore, the finite bandwidth of the employed laser and the reduced excitation density at sample points where the WSe_2 ($MoSe_2$) resonance shifts to higher (lower) energies can contribute to the spatial peak strength variations.

The resonance energy shifts for the two resonances are plotted in Fig. 7.9(b,c). A significant shift towards lower energies down to 1607 meV for the $MoSe_2$ resonance can be observed in the center-left of the sample. Meanwhile, the WSe_2 resonance shifts towards higher energies, up to 1680 meV in this area. Towards the bottom area of the sample, both resonances shift towards higher energies. Moreover, the $MoSe_2$ resonance shifts towards significantly higher energies up to 1622 meV in the upper part of the sample. To correlate the resonance shifts, we plot the $MoSe_2$ resonance vs. the WSe_2 resonance energy in Fig. 7.9(d). Sample points falling within the red (blue) rectangle are plotted in red (blue), and all other data points are plotted in black. While changes in the resonance energies seem correlated at first look, a Pearson coefficient of $\rho = -0.04 \pm 0.13$ suggests otherwise. A closer examination of Fig. 7.9(d) together with Fig. 7.9(b) and (c) shows both strong correlation and anti-correlation, whose simultaneous presence cannot be captured by the Pearson correlation coefficient. Instead, to visualize the substantial variation of correlation across the sample, we examine the select areas marked by a blue and red dashed rectangle in Fig. 7.9(c). For the area marked by the blue rectangle (Reg D), a moderately strong correlation with $\rho = 0.46 \pm 0.14$ can be observed. A correlation between the two resonances is what would be expected: It is well known that both encapsulation and heterostructure formation commonly redshift the excitons [1, 21]. At the same time, compressive (tensile) strain leads to red (blue) shifts [16]. Both monolayers should

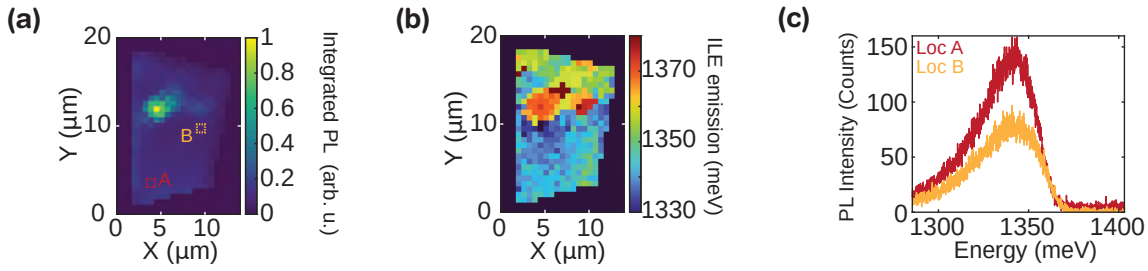

Figure 7.9: **(a)** Integrated ILE PL across the sample. **(b)** Map of ILE PL emission energy **(c)** PL-spectrum for two points on the center and bottom area of the heterostructure marked in (a).

be affected in the same way by these factors. Contrary to this expectation, the area marked by the red rectangle (Reg E) shows a moderately strong anti-correlation with $\rho = -0.42 \pm 0.23$. This points toward complex local strain dynamics, where the two monolayers experience different strain that leads to opposite resonance shifts. One possible scenario is the compression of one monolayer, which leads to a bubble in the other monolayer, inducing tensile strain and, thus, the opposite sign resonance shift. The attribution to strain is further supported by the fact that the largest resonance shifts can again be observed around an area of low FWM with physical imperfections (cracks, bubbles, wrinkles) visible in white light microscopy (see Fig. 7.7(a)).

The local strain profile also leads to large variations in the ILE PL. The integrated ILE PL plotted in Fig. 7.9(a) shows a strong maximum at the high-strain area of minimum FWM but appears otherwise relatively homogeneous in strength across the sample. These observations align with the observations on the $MoSe_2$ monolayer. The emission energy of the ILE is plotted in Fig. 7.9(b). The area of strong PL shows above average energy of ILE emission around 1370 meV. The upper area of the sample also shows a higher ILE emission energy of around 1355 meV, while the lower part shows lower emission energies down to 1330 meV. The substantial changes of the ILE PL, including emission strength and energy, even outside the high strain area, can be further emphasized when plotting two select spectra in what appears to be a relatively homogeneous region in the bottom half of the sample. These spectra

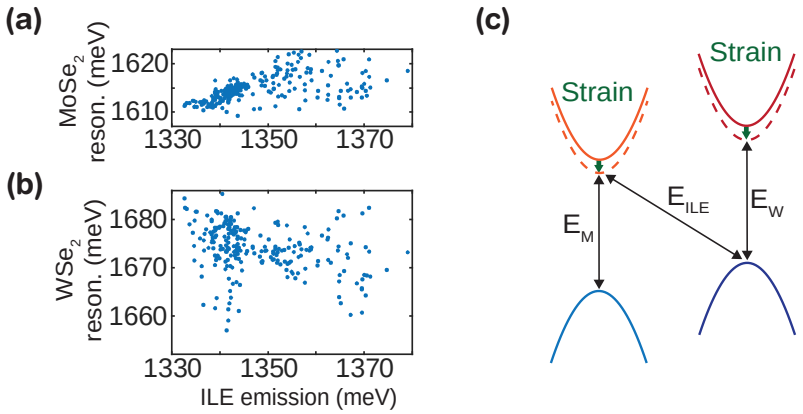

Figure 7.10: **(a)** Correlation between $MoSe_2$ resonance energy and ILE emission energy. **(b)** Correlation between WSe_2 resonance energy and ILE emission energy. **(c)** Schematic of conduction and valence band for $MoSe_2$ and WSe_2 under the influence of strain.

plotted in Fig. 7.9(c) demonstrate that even in the bottom part of the sample, ILE emission is highly spatially heterogeneous.

Another signature of strain-induced changes can be found by correlating the ILE PL emission energy with the $MoSe_2$ and WSe_2 resonance energy (measured with MDCS). In Fig. 7.10(a,b), we plot the $MoSe_2$ and WSe_2 resonance energy (measured with MDCS) against the ILE PL emission energy. Fig. 7.10(a) shows a moderately strong correlation and a correlation coefficient $\rho = 0.52 \pm 0.10$. The correlation with the WSe_2 resonance (Fig. 7.10(b)) is weaker ($\rho = -0.30 \pm 0.12$). This difference can be explained as follows: As Khatibi *et al.* [16] show, for TMD monolayers, along the K-point, strain mainly affects the conduction band, while effects on the valence band are negligible. Thus, as illustrated in Fig. 7.10(c), the strain-induced conduction band shift in the $MoSe_2$ immediately affects the ILE emission energy, while the strain-induced shift in the WSe_2 should have no effect. The residual anti-correlation between ILE emission energy and WSe_2 resonance energy stems from the local (anti-)correlation between $MoSe_2$ and WSe_2 resonances, established in the discussion of Fig. 7.8 above. Given these significant strain-induced changes to the heterostructure, if and how much these changes affect the coupling between excitons

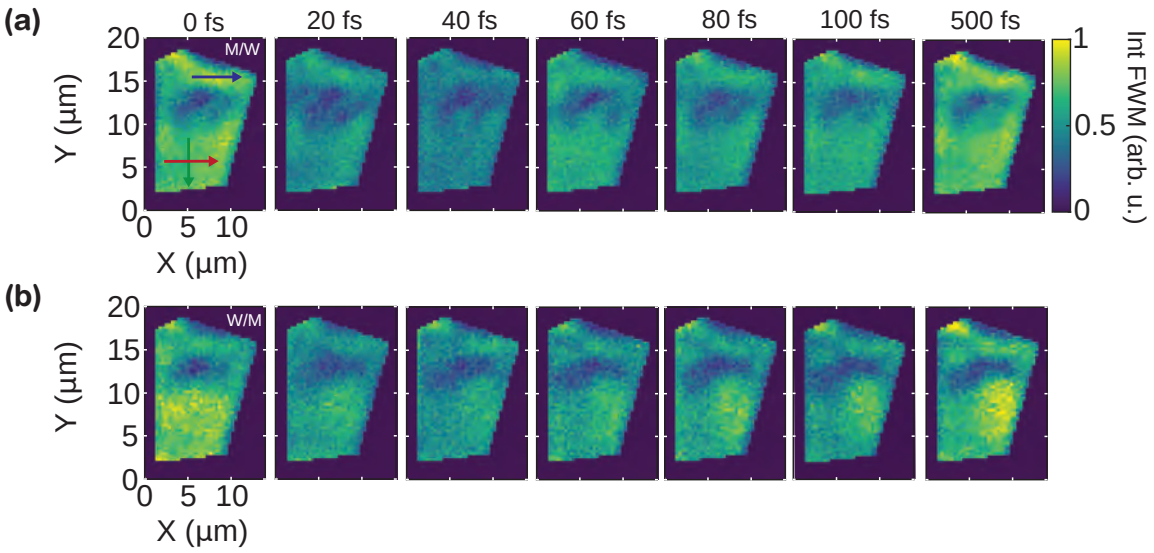

Figure 7.11: **(a)** Integrated FWM of the $MoSe_2/WSe_2$ coupling peak for varying T delays. **(b)** Integrated FWM of the $WSe_2/MoSe_2$ coupling peak for varying T delays. The strong amplitude signatures of the coherent coupling oscillations and charge transfer are evident.

in the two layers is a topic of interest.

Therefore, to shed some light on the coupling dynamics, we employ dynamic MD-CIS, where the pump-probe delay T varies to access coherent and incoherent coupling dynamics in the heterostructure. We plot the integrated FWM of the $MoSe_2/WSe_2$ (M/W) and $WSe_2/MoSe_2$ (W/M) coupling peaks for varying T delays in Fig. 7.11(a) and (b), respectively. All images for the two peaks are normalized by a single value so that the brightest pixel at $T = 0\,\text{fs}$ has a unity amplitude.

Initially, the signal decays from 0 to 40 fs for both coupling peaks but recovers again for 60 fs. A smaller variation of the integrated amplitudes can be observed between 60-100 fs. This behavior can be assigned to coherent coupling oscillations that we have shown to occur in $MoSe_2/WSe_2$ heterostructures in Chap. V. The coherent oscillation has an amplitude of approximately 50% (with respect to the peak amplitude) across the sample, the signature of strong coupling between excitons in the two layers. As Hao *et al.* [22] discussed, the amplitude is below unity due to interference between different coherent coupling contributions and exponentially decaying

phase-space filling nonlinearities. In between T=100 fs and T=500 fs, both coupling peaks show a rise that we assign to the charge transfer observed using MDCS in this specific heterostructure in Chap. V. The noticeable amplitude change between 100 fs and 500 fs suggests highly efficient electron and hole transfer in the heterostructure.

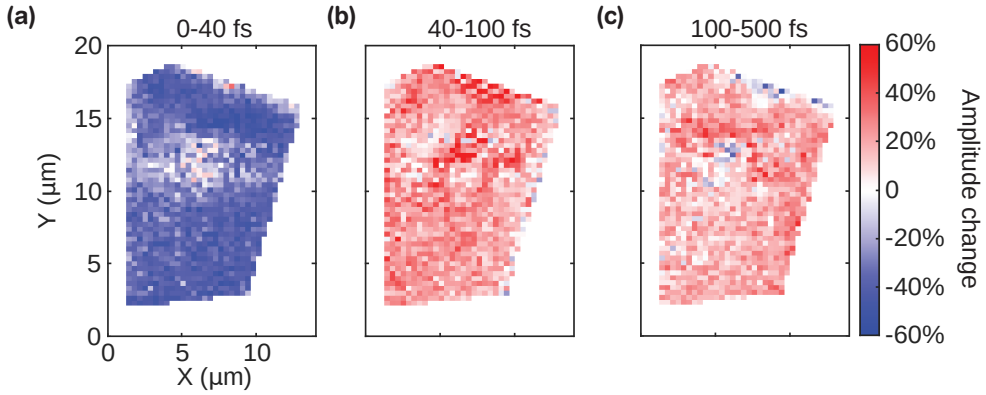

Figure 7.12: **(a)** Difference in integrated FWM amplitude for the $MoSe_2/WSe_2$ peak between various T delays, normalized by the $MoSe_2/WSe_2$ peak amplitude at T=0 fs. This visualization emphasizes the homogeneity of the coherent coupling and charge transfer.

Most strikingly, both coherent coupling and charge transfer appear mostly homogeneous across the sample. The homogeneity is evident from the fact that the relative peak strength across the sample remains mostly unchanged along T, while the absolute peak strength changes. The homogeneity can be visualized by comparing the relative strength profiles at T=0 fs, T=40 fs, T=100 fs, and T=500 fs, as done in Fig. 7.12. Here, we plot the difference between the integrated FWM maps for the M/W peak, normalized by the M/W map at T=0 fs. We plot the difference between T=0 fs and T=40 fs (Fig. 7.12(a)), T=40 fs and T=100 fs (Fig. 7.12(b)), and T=100 fs and T=500 fs (Fig. 7.12(c)). The initial decrease and increase of the FWM, part of the coherent coupling oscillations, show a homogeneous strength profile across the entire sample. Moreover, the charge transfer rise between 100 fs and 500 fs shows the same homogeneous strength profile apart from the low FWM area where no reliable FWM can be obtained.

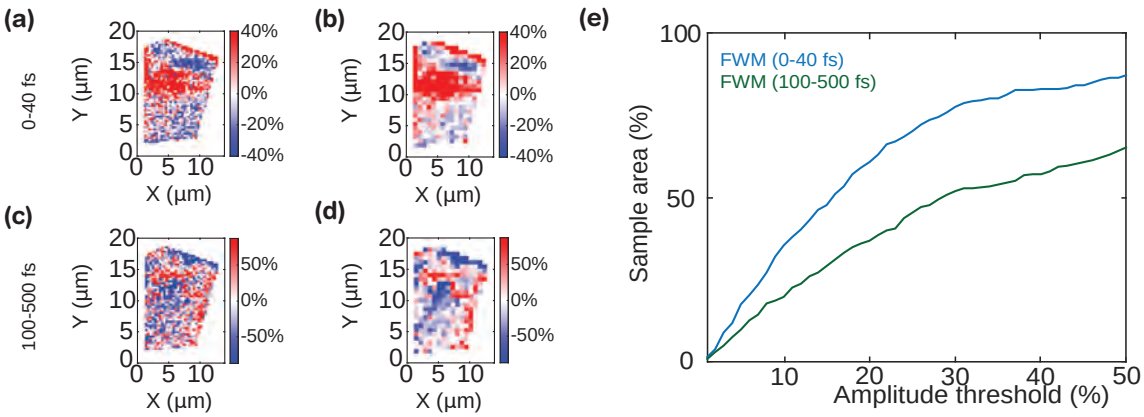

Figure 7.13: **(a)** Difference map for T=0-40 fs, offset by the average value. Figure **(b)** considers a 2x2 pixel average. **(c)** Difference map for T=100-500 fs, offset by the average value. Figure **(d)** considers a 2x2 pixel average. **(e)** Sample area falling within varying amplitude thresholds for the amplitude difference maps for T=0-40 fs and T=100-500 fs.

We propose two different methods to quantify the homogeneity of coherent coupling and charge transfer. The first characterization method involves determining how much of the sample falls within certain boundaries of the relative amplitude change for the amplitude change maps plotted in Fig. 7.12. We begin by normalizing the relative amplitude change maps for 0-40 fs and 100-500 fs by their respective average value. We exclude the low FWM signal area for determining the average because it would skew the average value. We then offset each of the normalized maps by 1, so pixels with the average value are 0.

These maps can be found in Fig. 7.13(a)-(d). Here, we show the difference maps for T=0-40 fs (a,b) and T=100-500 fs (c,d). Maps in (b) and (d) use a 2×2 pixel averaging to reduce noise. Subsequently, we determine for the collective sample points if they fall within the boundaries of a certain amplitude threshold, i.e., for an amplitude threshold of 30%, we only count sample points with a relative normalized amplitude change between -30% and 30%. We then determine which percentage of the sample area all sample points falling within those boundaries account for. This procedure leads to the two curves in Fig. 7.13(e). 84% of the sample falls within ±30% of the average relative amplitude change for T=0-40 fs. This method underestimates the

homogeneity of the coherent coupling because changes in oscillation frequency due to resonance shifts change the oscillation amplitude at the discrete sample points. Fig. 7.13(b) shows that the only areas of significant amplitude deviation are at the edge and the low FWM signal area towards the center, where no reliable oscillation can be measured. Similarly, 54% of the sample falls within ±30% of the average amplitude change for $T = 100 - 500$ fs for charge transfer. The lower percentage can be primarily attributed to increased noise because of the normalization procedure. Fig. 7.13(d) shows that areas of large deviations are again constrained towards the edge of the sample and the low-FWM signal area towards the center. We chose an amplitude threshold of 30% here because of the relatively large noise on the amplitude difference maps.

To overcome the noise limitations of this method, we propose another method to determine the homogeneity of coupling: Since the amplitudes of the two coupling peaks, in the case of coherent coupling, are proportional to the square of the $MoSe_2$ and WSe_2 dipole moments, $\propto {\mu_{0M}}^2 {\mu_{0W}}^2$, and the amplitudes of the two on-diagonal peaks are $\propto {\mu_{0M}}^4$ and $\propto {\mu_{0W}}^4$, respectively, normalizing the coupling peaks by the on-diagonal peaks removes the contribution of the dipole moment to the coupling peaks. Specifically, we can normalize the integrated FWM maps from Fig. 7.11 by the on-diagonal peak strength $\sqrt{M \cdot W}$, with M and W being the integrated FWM map of the $MoSe_2$ and WSe_2 peak at T=20 fs, respectively. We choose the $MoSe_2$ and WSe_2 peak map at T=20 fs for the normalization because finite pulse effects occur for small $T < 20$ fs [23], while population decay processes become important for $T >$20 fs. The normalization procedure is illustrated in Fig. 7.14(a). This normalization factors out changes in the spatial profile of the coupling peaks due to changing dipole moments which, as discussed above for Fig. 7.8, are a dominant effect. It also similarly eliminates contributions from finite bandwidth effects. Changes in the spatial profile should then be exclusively caused by a reduced coherent coupling strength

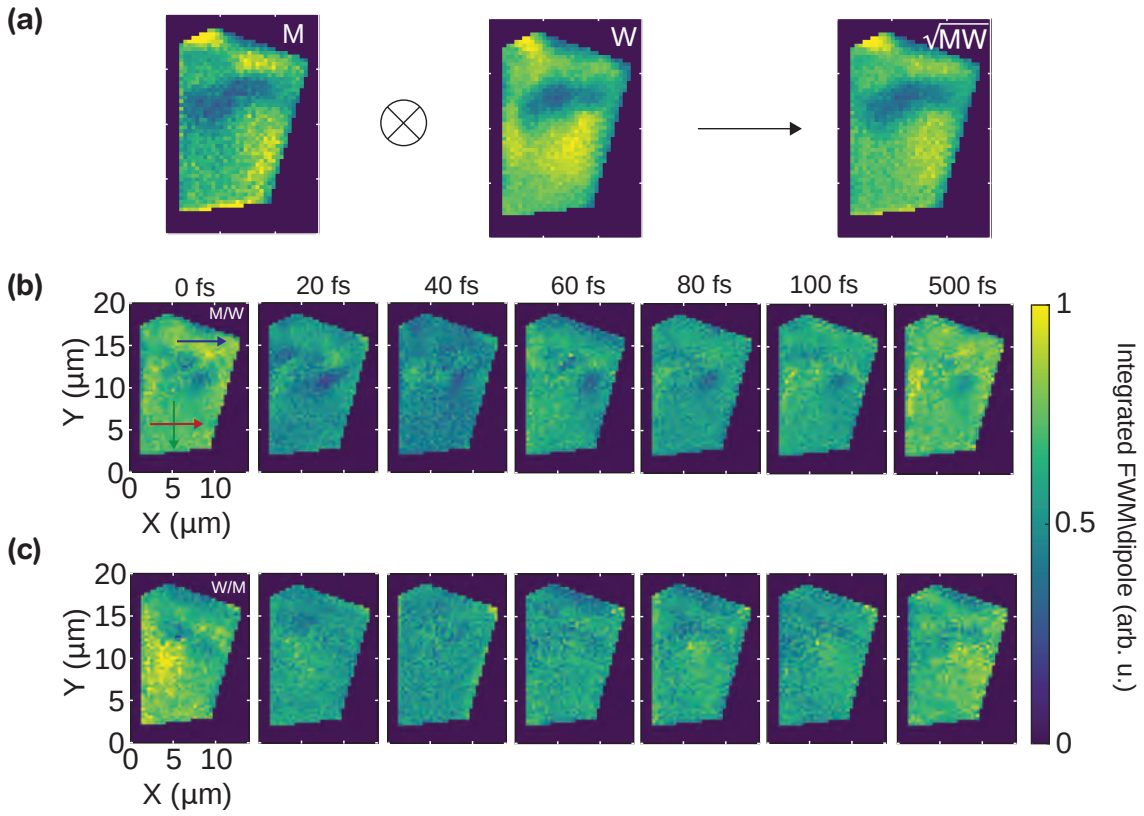

Figure 7.14: **(a)** In order to isolate coupling effects, we normalize the FWM maps by $\sqrt{M \cdot W}$, with M and W being the integrated FWM maps of the $MoSe_2$ and WSe_2 peaks, respectively. **(b)** Integrated FWM of the $MoSe_2/WSe_2$ coupling peak for varying T delays. **(c)** Integrated FWM of the $WSe_2/MoSe_2$ coupling peak for varying T delays. The strong amplitude signatures of the coherent coupling oscillations and charge transfer are evident.

or other incoherent transfer processes (e.g., charge transfer). The resulting dipole-normalized coupling peak maps for the $MoSe_2/WSe_2$ and $WSe_2/MoSe_2$ are plotted in Fig. 7.14(b,c), respectively.

To quantify the homogeneity of the coupling, we can then normalize the M/W coupling peak maps at T=40 fs and T=500 fs by their respective averages and determine how much of the sample area falls within certain amplitude boundaries of the average value. The resulting curves in Fig. 7.15 show that large areas of the sample show a very homogeneous coupling peak strength, both for T=40 fs and T=500 fs. As a matter of fact, 81% of the sample falls within ±20% of the average amplitude for T=40 fs. This T-step was chosen because finite pulse effects influence the signal at

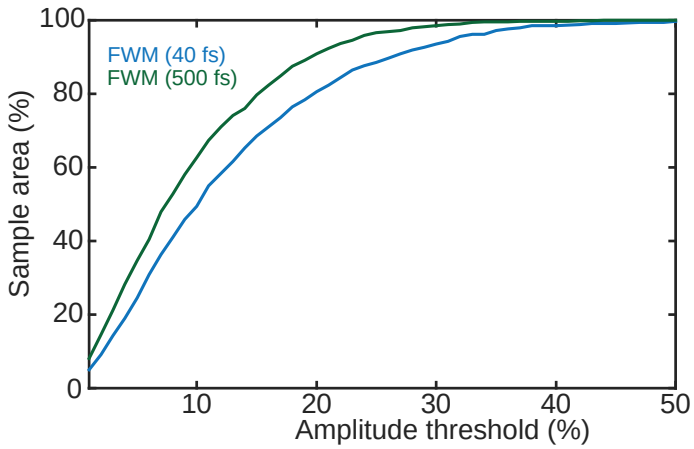

Figure 7.15: Sample area falling within varying amplitude threshold for the M/W coupling peak amplitude maps for T=40 fs and T=500 fs.

earlier T, while incoherent charge transfer dominates for later T, leading to a dominant coherent coupling contribution. Similarly, for T=500 fs, 91% of the sample falls within ±20% of the average amplitude.

The results from the two methods suggest that while some inhomogeneity of the coherent coupling and charge transfer remains, both are surprisingly robust toward the strain in this sample. Moderate resonance shifts due to strain on the order of 10-20 meV are not inherently expected to change the charge transfer dynamics significantly because the shift is comparatively small to the band offsets of hundreds of meVs [24, 25]. However, the sensitivity of charge transfer to sample parameters such as lattice separation [26] is well documented. With the resonance shifts being an indicator of complex local strain dynamics, this strain is expected to change the interlayer spacing, among other things. These previous findings render our observation of spatially homogeneous charge transfer somewhat surprising. It is worth mentioning that these results somewhat differ from the observations of Plankl *et al.* [27]. However, the spatial variations they observe are on the same spatial scale or below the spatial resolution of our experiment. Moreover, they perform their experiments on non-encapsulated samples, which are more sensitive to environmental changes and strain.

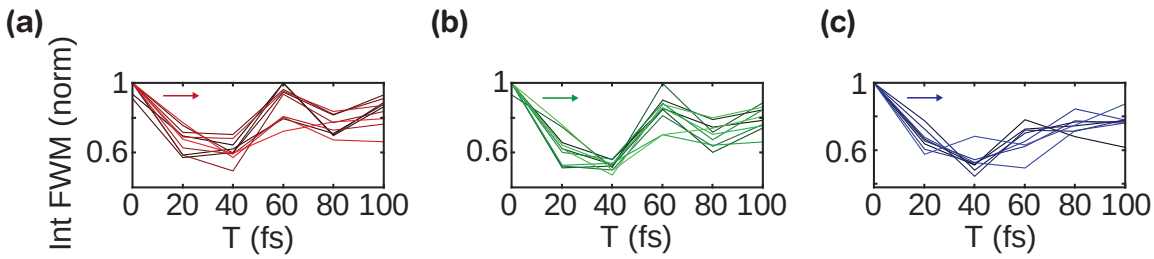

Figure 7.16: Integrated FWM of the $MoSe_2/WSe_2$ coupling peak for varying T delays along the arrows indicated in Fig. 7.11(a) and Fig. 7.14(b).

Furthermore, the coherent coupling between the resonances is also expected to depend on the intralayer separation. While there is overall robustness of the coupling properties, we would be remiss not to comment on a change of the coherent coupling that is observable for the top part of the sample, as illustrated in Fig. 7.16. Here, we plot the integrated FWM of the $MoSe_2/WSe_2$ coupling peak along the three arrows drawn in Fig. 7.11(a) and Fig. 7.14(b). Both the red and green arrows (Fig. 7.16(a,b)) on the lower part of the sample show a strong coherent coupling oscillation with only small, random changes when moving across the sample, consistent with the observations in Fig. 7.12. However, the data for the blue arrow (Fig. 7.16(c)) shows a reduced signature of the oscillation, which might be either caused by a reduced amplitude or a more rapid dephasing of the coherent coupling in the upper area of the sample. Because the peak-to-valley amplitude change in Fig. 7.16(c) is similar to those observed in Fig. 7.16(a,b), a more rapid dephasing seems more likely. The top area of the sample where this effect occurs also shows large resonance shifts for the $MoSe_2$ resonance in Fig. 7.8(b).

Another hint at the underlying physics can be found in the integrated linear reflectance map, plotted in Fig. 7.17(a), and spectra at select locations in Fig. 7.17(b). The lower area of the sample shows few changes in reflectance, as evident from both the integrated reflectance and the spectra at locations A and B in Fig. 7.17(b). The upper area of the sample, above the low FWM signal area, however, clearly shows a much stronger reflectance than the rest of the sample. Fig. 7.17(b) shows that

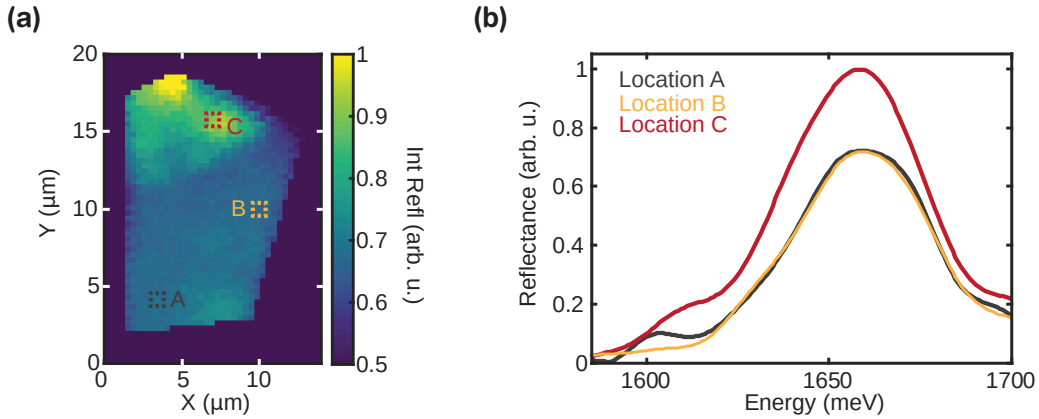

Figure 7.17: **(a)** Integrated reflectance for the $MoSe_2/WSe_2$ heterostructure. **(b)** Reflectance spectra for the three areas marked by colored squares in (a).

Location C has an increased reflectance across the entirety of the spectrum. Based on the combined observation of resonance shifts and reflectivity, we assume the top of the sample to be an area of increased interlayer spacing. This increased interlayer spacing can explain the reduced coherent coupling strength/more rapid dephasing.

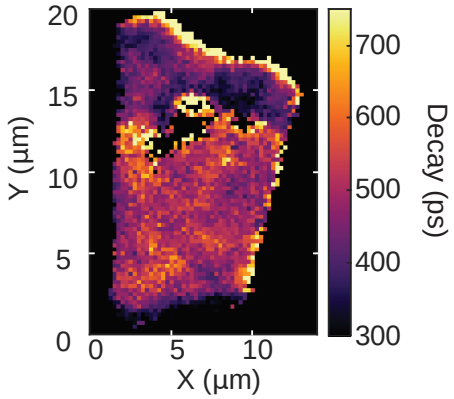

Figure 7.18: Decay time (T) map of the FWM signal taken at $t = \tau = 0$, indicative of the ILE lifetime.

This specific area also appears distinctly in the FWM decay time map plotted in Fig. 7.18. The decay time map is acquired at $t = \tau = 0$ while moving the T delay. We subsequently fit the data after 50 ps with a uni-exponential decay, similar to Sec. 5.6. The FWM decay in the heterostructure for $T > 50$ ps is dominated by ILE decay through ground-state bleaching contributions to the signal, as established in Chap. V. The decay time can thus be taken as an indirect probe of the ILE lifetime. The bottom

area of the sample again shows no notable spatial inhomogeneity in the lifetime, with values between 500-550 ps. Given the low twist angle of this sample, these values are in good agreement with the literature [28] and further match the values in Sec. 5.6. The top area of the sample has, on average, a 30-40% lower lifetime and larger inhomogeneity with values ranging from 300-550 ps. The combination of reduced ILE lifetime as well as reduced coherent coupling, together with the resonance shifts observed in this area, shows that the sample properties are not entirely immune to strain and defect-induced changes. Nonetheless, the relatively low sensitivity towards these changes remains surprising.

7.6 Conclusions and Outlook

In this chapter, we have examined an encapsulated $MoSe_2$ monolayer and an encapsulated $MoSe_2/WSe_2$ heterostructure using MDCIS. We visualize a spatially-dependent distribution of bright and dark exciton states using PL-detected FWM in conjunction with heterodyne-detected FWM. Furthermore, we visualize strain-dependent changes of resonance energy, dephasing, and inhomogeneity across the monolayer, showing a moderately strong anti-correlation between homogeneous and inhomogeneous linewidths that increases and decreases based on the area on the sample. Using MDCIS allows us to identify promising and unfavorable areas for quantum information applications unambiguously. Carrying this technique over to the heterostructure, we map the complex strain dynamics by correlating resonance energies. Our observations lead us to propose a phenomenological model for the band structure changes due to strain variations, using additional ILE PL measurements. Finally, by employing dynamic MDCIS, we visualize coherent coupling and electron and hole transfer across the sample. We employ two methods to determine the homogeneity of coherent coupling and charge transfer. While some regions of the sample show a reduced coherent coupling and decreased ILE lifetime, we demonstrate the overall

robustness of the coupling dynamics to strain and defects across the sample.

The future of these materials, especially in the realm of quantum information, is inherently coupled to the scalability and quality of fabricated devices. This work shows the reproducibility of crucial physical properties - charge transfer, coupling strength, and ILE lifetime - across large sample areas. The reproducibility lays the groundwork and strengthens the case for TMDs as a next-generation material. Conversely, certain material properties such as dephasing time and inhomogeneity show residual dependence on strain, showing that sample growth techniques need to improve for future large-scale applications of these materials.

We further demonstrate the usefulness of the MDCIS technique, which, on a smaller scale, has been realized by spatially-addressed MDCS [6–8, 29]. However, recent technological advances in lock-in detection [30] allow for a larger-scale realization of MDCIS and related techniques, advancing the forefront of materials and device characterization.

As this chapter clearly shows, standard material characterization techniques such as white light imaging, linear micro-reflectance spectroscopy, or PL imaging fall far short of accurately assessing sample quality. We present MDCIS as a powerful alternative, but scan durations currently remain too long for commercial applications. Motivated by this assertion, the future of nonlinear imaging requires simplified versions of FWM imaging that extract the principal quantities of interest for material characterization. The work in the following chapter shows how said future might look like, by introducing smart and rapid scanning schemes for FWM imaging in the temporal domain.

References

[1] Eric W. Martin, Jason Horng, Hanna G. Ruth, Eunice Paik, Michael-Henr Wentzel, Hui Deng, and Steven T. Cundiff. "Encapsulation Narrows and Preserves the Excitonic Homogeneous Linewidth of Exfoliated Monolayer $MoSe_2$".

In: *Phys. Rev. Applied* 14 (2 Aug. 2020), p. 021002. DOI: 10.1103/PhysRevApplied.14.021002.

[2] F. Cadiz, E. Courtade, C. Robert, G. Wang, Y. Shen, H. Cai, T. Taniguchi, K. Watanabe, H. Carrere, D. Lagarde, M. Manca, T. Amand, P. Renucci, S. Tongay, X. Marie, and B. Urbaszek. "Excitonic Linewidth Approaching the Homogeneous Limit in MoS_2-Based van der Waals Heterostructures". In: *Phys. Rev. X* 7 (2 May 2017), p. 021026. DOI: 10.1103/PhysRevX.7.021026.

[3] Obafunso A Ajayi, Jenny V Ardelean, Gabriella D Shepard, Jue Wang, Abhinandan Antony, Takeshi Taniguchi, Kenji Watanabe, Tony F Heinz, Stefan Strauf, X-Y Zhu, and James C Hone. "Approaching the intrinsic photoluminescence linewidth in transition metal dichalcogenide monolayers". In: *2D Materials* 4.3 (July 2017), p. 031011. DOI: 10.1088/2053-1583/aa6aa1.

[4] Jakob Wierzbowski, Julian Klein, Florian Sigger, Christian Straubinger, Malte Kremser, Takashi Taniguchi, Kenji Watanabe, Ursula Wurstbauer, Alexander W. Holleitner, Michael Kaniber, Kai Müller, and Jonathan J. Finley. "Direct exciton emission from atomically thin transition metal dichalcogenide heterostructures near the lifetime limit". In: *Scientific Reports* 7.1 (Sept. 2017), p. 12383. ISSN: 2045-2322. DOI: 10.1038/s41598-017-09739-4.

[5] Garima Gupta and Kausik Majumdar. "Fundamental exciton linewidth broadening in monolayer transition metal dichalcogenides". In: *Phys. Rev. B* 99 (8 Feb. 2019), p. 085412. DOI: 10.1103/PhysRevB.99.085412.

[6] Tomasz Jakubczyk, Karol Nogajewski, Maciej R Molas, Miroslav Bartos, Wolfgang Langbein, Marek Potemski, and Jacek Kasprzak. "Impact of environment on dynamics of exciton complexes in a WS_2 monolayer". In: *2D Materials* 5.3 (Apr. 2018), p. 031007. DOI: 10.1088/2053-1583/aabc1c.

[7] Tomasz Jakubczyk, Goutham Nayak, Lorenzo Scarpelli, Wei-Lai Liu, Sudipta Dubey, Nedjma Bendiab, Laëtitia Marty, Takashi Taniguchi, Kenji Watanabe, Francesco Masia, Gilles Nogues, Johann Coraux, Wolfgang Langbein, Julien Renard, Vincent Bouchiat, and Jacek Kasprzak. "Coherence and Density Dynamics of Excitons in a Single-Layer MoS_2 Reaching the Homogeneous Limit". In: *ACS Nano* 13.3 (2019). PMID: 30735350, pp. 3500–3511. DOI: 10.1021/acsnano.8b09732.

[8] Caroline Boule, Diana Vaclavkova, Miroslav Bartos, Karol Nogajewski, Lukas Zdražil, Takashi Taniguchi, Kenji Watanabe, Marek Potemski, and Jacek Kasprzak. "Coherent dynamics and mapping of excitons in single-layer $MoSe_2$ and WSe_2 at the homogeneous limit". In: *Phys. Rev. Materials* 4 (3 Mar. 2020), p. 034001. DOI: 10.1103/PhysRevMaterials.4.034001.

[9] Alberto Ciarrocchi, Dmitrii Unuchek, Ahmet Avsar, Kenji Watanabe, Takashi Taniguchi, and Andras Kis. "Polarization switching and electrical control of interlayer excitons in two-dimensional van der Waals heterostructures". In: *Nature Photonics* 13.2 (Feb. 2019), pp. 131–136. ISSN: 1749-4893. DOI: 10.1038/s41566-018-0325-y.

[10] Mauro Brotons-Gisbert, Hyeonjun Baek, Alejandro Molina-Sánchez, Aidan Campbell, Eleanor Scerri, Daniel White, Kenji Watanabe, Takashi Taniguchi, Cristian Bonato, and Brian D. Gerardot. "Spin-layer locking of interlayer excitons trapped in moiré potentials". In: *Nature Materials* 19.6 (June 2020), pp. 630–636. ISSN: 1476-4660. DOI: 10.1038/s41563-020-0687-7.

[11] A. Pospischil, M. Furchi, and T. Mueller. "Solar-energy conversion and light emission in an atomic monolayer p–n diode". In: *Nature Nanotechnology* 9.4 (Apr. 2014), pp. 257–261. DOI: 10.1038/nnano.2014.14.

[12] Tomasz Jakubczyk, Valentin Delmonte, Maciej Koperski, Karol Nogajewski, Clement Faugeras, Wolfgang Langbein, Marek Potemski, and Jacek Kasprzak. "Radiatively Limited Dephasing and Exciton Dynamics in $MoSe_2$ Monolayers Revealed with Four-Wave Mixing Microscopy". In: *Nano Letters* 16.9 (2016), pp. 5333–5339. DOI: 10.1021/acs.nanolett.6b01060.

[13] Christopher L. Smallwood, Ronald Ulbricht, Matthew W. Day, Tim Schröder, Kelsey M. Bates, Travis M. Autry, Geoffrey Diederich, Edward Bielejec, Mark E. Siemens, and Steven T. Cundiff. "Hidden Silicon-Vacancy Centers in Diamond". In: *Phys. Rev. Lett.* 126 (21 May 2021), p. 213601. DOI: 10.1103/PhysRevLett.126.213601.

[14] Kelsey M. Bates, Matthew W. Day, Christopher L. Smallwood, Rachel C. Owen, Tim Schröder, Edward Bielejec, Ronald Ulbricht, and Steven T. Cundiff. "Using silicon-vacancy centers in diamond to probe the full strain tensor". In: *Journal of Applied Physics* 130.2 (2021), p. 024301. DOI: 10.1063/5.0052613.

[15] Peter James Joyce O'Malley. "Superconducting Qubits: Dephasing and Quantum Chemistry". PhD thesis. University of California, Santa Barbara, 2016.

[16] Zahra Khatibi, Maja Feierabend, Malte Selig, Samnuel Brem, Christoper Linderälv, Paul Erhart, and Ermin Malic. "Impact of strain on the excitonic linewidth in transition metal dichalcogenides". In: *2D Materials* 6 (1 2018). DOI: 10.1088/2053-1583/aae953.

[17] Archana Raja, Lutz Waldecker, Jonas Zipfel, Yeongsu Cho, Samuel Brem, Jonas D. Ziegler, Marvin Kulig, Takashi Taniguchi, Kenji Watanabe, Ermin Malic, Tony F. Heinz, Timothy C. Berkelbach, and Alexey Chernikov. "Dielectric disorder in two-dimensional materials". In: *Nature Nanotechnology* 14.9 (Sept. 2019), pp. 832–837. ISSN: 1748-3395. DOI: 10.1038/s41565-019-0520-0.

[18] Geoffrey M. Diederich, Travis M. Autry, and Mark E. Siemens. "Diagonal slice four-wave mixing: natural separation of coherent broadening mechanisms". In: *Opt. Lett.* 43.24 (Dec. 2018), pp. 6061–6064. DOI: 10.1364/OL.43.006061.

[19] T. Hirschfeld. "Fellgett's Advantage in uv-VIS Multiplex Spectroscopy". In: *Appl. Spectrosc.* 30.1 (Jan. 1976), pp. 68–69. URL: http://opg.optica.org/as/abstract.cfm?URI=as-30-1-68.

[20] A. D. Bristow, D. Karaiskaj, X. Dai, T. Zhang, C. Carlsson, K. R. Hagen, R. Jimenez, and S. T. Cundiff. "A versatile ultrastable platform for optical multidimensional Fourier-transform spectroscopy". In: *Review of Scientific Instruments* 80.7 (2009), p. 073108. DOI: 10.1063/1.3184103.

[21] P. Rivera, J.R. Schaibley, A.M. Jones, J.S Ross, S. Wu, G. Aivazian, P. Klement, K. Seyler, G. Clark, N.J. Ghimire, J. Yan, D.G. Mandrus, W. Yao, and X. Xu. "Observation of long-lived interlayer excitons in monolayer $MoSe_2$-WSe_2 heterostructures". In: *Nat Commun* 6 (2015), p. 6242. DOI: 10.1038/ncomms7242.

[22] Kai Hao, Lixiang Xu, Philipp Nagler, Akshay Singh, Kha Tran, Chandriker Kavir Dass, Christian Schüller, Tobias Korn, Xiaoqin Li, and Galan Moody. "Coherent and Incoherent Coupling Dynamics between Neutral and Charged Excitons in Monolayer $MoSe_2$". In: *Nano Letters* 16.8 (2016). PMID: 27428509, pp. 5109–5113. DOI: 10.1021/acs.nanolett.6b02041.

[23] Christopher L. Smallwood, Travis M. Autry, and Steven T. Cundiff. "Analytical solutions to the finite-pulse Bloch model for multidimensional coherent spectroscopy". In: *J. Opt. Soc. Am. B* 34.2 (Feb. 2017), pp. 419–429. DOI: 10.1364/JOSAB.34.000419.

[24] Ming-Hui Chiu, Chendong Zhang, Hung-Wei Shiu, Chih-Piao Chuu, Chang-Hsiao Chen, Chih-Yuan S. Chang, Chia-Hao Chen, Mei-Yin Chou, Chih-Kang Shih, and Lain-Jong Li. "Determination of band alignment in the single-layer MoS_2/WSe_2 heterojunction". In: *Nature Communications* 6.1 (July 2015), p. 7666. ISSN: 2041-1723. DOI: 10.1038/ncomms8666.

[25] Neil R. Wilson, Paul V. Nguyen, Kyle Seyler, Pasqual Rivera, Alexander J. Marsden, Zachary P. L. Laker, Gabriel C. Constantinescu, Viktor Kandyba, Alexei Barinov, Nicholas D. M. Hine, Xiaodong Xu, and David H. Cobden. "Determination of band offsets, hybridization, and exciton binding in 2D semiconductor heterostructures". In: *Science Advances* 3.2 (2017). DOI: 10.1126/sciadv.1601832.

[26] Hongzhi Zhou, Yida Zhao, Weijian Tao, Yujie Li, Qiaohui Zhou, and Haiming Zhu. "Controlling Exciton and Valley Dynamics in Two-Dimensional Heterostructures with Atomically Precise Interlayer Proximity". In: *ACS Nano* 14.4 (2020). PMID: 32181635, pp. 4618–4625. DOI: 10.1021/acsnano.0c00218.

[27] M. Plankl, P. E. Faria Junior, F. Mooshammer, T. Siday, M. Zizlsperger, F. Sandner, F. Schiegl, S. Maier, M. A. Huber, M. Gmitra, J. Fabian, J. L. Boland, T. L. Cocker, and R. Huber. "Subcycle contact-free nanoscopy of ultrafast interlayer transport in atomically thin heterostructures". In: *Nature Photonics* 15.8 (Aug. 2021), pp. 594–600. ISSN: 1749-4893. DOI: 10.1038/s41566-021-00813-y.

[28] Junho Choi, Matthias Florian, Alexander Steinhoff, Daniel Erben, Kha Tran, Dong Seob Kim, Liuyang Sun, Jiamin Quan, Robert Claassen, Somak Majumder, Jennifer A. Hollingsworth, Takashi Taniguchi, Kenji Watanabe, Keiji Ueno, Akshay Singh, Galan Moody, Frank Jahnke, and Xiaoqin Li. "Twist Angle-Dependent Interlayer Exciton Lifetimes in van der Waals Heterostructures". In: *Phys. Rev. Lett.* 126 (4 Jan. 2021), p. 047401. DOI: 10.1103/PhysRevLett.126.047401.

[29] Vivek Tiwari, Yassel Acosta Matutes, Alastair. T. Gardiner, Thomas L.C. Jansen, Richard J. Cogdell, and Jennifer P. Ogilvie. "Spatially-resolved fluorescence-detected two-dimensional electronic spectroscopy probes varying excitonic structure in photosynthetic bacteria". In: *Nat. Comm.* 16 (2018), p. 4219. DOI: 10.1038/s41467-018-06619-x.

[30] Torben L. Purz, Steven T. Cundiff, and Eric W. Martin. "Lock-in detector for accelerated nonlinear imaging". In: *Opt. Lett.* 46.19 (Oct. 2021), pp. 4813–4816. DOI: 10.1364/OL.432353.

CHAPTER VIII

Rapid Multiplex Ultrafast Nonlinear Microscopy for Material Characterization

8.1 Introduction

Since the invention of the microscope over 400 years ago, the need to improve imaging techniques and modalities for obtaining previously inaccessible information, as well as obtaining it faster, has been a common theme surrounding microscopy. As new groups of advanced materials shift into focus, the need to image these materials for fundamental science and characterization in a manufacturing/fabrication setting has spurred numerous experimental innovations. These materials include two-dimensional quantum materials such as TMDs (extensively studied in this thesis) and graphene [1–9], III-V semiconductors such as GaAs and GaN in both science [10–12] and industry [13] (e.g., for high-power, high-frequency applications), and silicon carbide (SiC) for electric vehicles [14]. Material characterization of advanced materials, and TMDs in particular, has seen a plethora of techniques, from white-light optical microscopy to PL imaging [15], micro-reflectance and transmission [16], scanning tunneling microscopy [17], ARPES [17], Raman spectroscopy [18–20], atomic force microscopy imaging [21], tip-enhanced spectroscopy [22], ultrafast nanoscopy [23], and FWM imaging [24–28]. Specifically using ultrafast lasers, Huang *et al.* [8] have

shown the practicality of two-color transient absorption decay times for defect sensing in graphene, while we (in Chap. VII and Ref. 28) and Jacubczyk *et al.* [26] and have shown the potential of dephasing times as an indicator of material quality for TMDs.

In the previous chapter, we introduced our approach to FWM imaging, featuring three-dimensional (two frequency, one time dimension) spectro-temporal information on top of the two-dimensional spatial information. While useful in a research setting, different experimental schemes are necessary to make FWM imaging a commodity in the microscopy space.

With many advanced measurement techniques, there is a tradeoff between the amount of useful information acquired and acquisition speed. To overcome the limitations of previous techniques concerning their lack of information or acquisition speed, we here introduce rapid multiplex nonlinear imaging to characterize advanced materials. Specifically, we demonstrate the technique's feasibility on WSe_2 monolayers grown by CVD, which serve as a canonical example. The presented technique employs degenerate FWM, which has a high sensitivity to defects and interfaces due to its scaling with material oscillator strength. We acquire resonant linear reflectance and nonlinear FWM images that provide rich information about the materials' quality in real-time while acquiring full exciton dephasing and lifetime maps within a minute. We correlate the results from the dephasing maps with MDCIS data to corroborate our findings while also highlighting areas with strong many-body effects. Subsequently, we present exciton population decay maps that display a bi-exponential decay indicative of a spatially dependent dark exciton state distribution. We also show that the dephasing times are radiatively limited by correlating dephasing and lifetime maps. Areas of the monolayer flakes that can be distinguished by their FWM strength also show up distinctly in the dephasing and decay maps. In the context of acquiring rapid dephasing and population decay maps, we discuss how to treat finite pulse effects in multi-pulse FWM experiments. Lastly, we demonstrate how the techniques modali-

ties can be further accelerated in the future by modeling the robustness of decay time fits across an extensive range of decay times for different sampling point spacing.

These results constitute an important step toward real-time material characterization of advanced materials on an industrial scale, a necessity for devices to make it out of the lab and into the marketplace.

8.2 Rapid Imaging

The MDCIS technique helps us unravel the changes of dephasing time, coherent coupling, and charge transfer in the presence of strain across TMD samples, as shown in chapter VII. However, for material characterization, the need for speed often outweighs the need for full spectroscopic or temporal detail. Therefore, more rudimentary temporal or spectral data is often sufficient to assess the sample quality. Quantities that can be used to assess the quality of a sample include the FWM strength, the exciton dephasing time, and the exciton population decay time across the sample. All of these modalities can be extracted from complete MDCIS measurements with data acquisition times of at least 30 minutes. However, specific parameter images can be acquired within a minute or less.

In our rapid imaging technique, we still use the four pulse (3+1) scheme detailed in Chap. III in the same setup used to acquire the MDCIS data in Chap. VII. FWM strength can be assessed by setting all time delays to zero and recording a single image by scanning the laser beam across the sample. Similarly, decay maps of the sample can be obtained by setting the τ- and t-delay to zero while scanning the T-delay. Obtaining dephasing time maps involves scanning the τ and t-delay simultaneously across the photon-echo while leaving the T-delay stationary. As established from Eq. 3.52 in Sec. 3.7, the dephasing time can then be extracted by fitting a uni-exponential decay to the data. The authors in Refs. [26, 27] fit slices along the diagonal and cross-diagonal in the time domain to extract dephasing times and in-

homogeneous linewidths but still acquire a complete, two-dimensional time domain signal. To clarify, here, instead of scanning the full range of τ- and t-delays, we scan along the diagonal in the scheme detailed above and initially perceived by Diederich *et al.* [29]. This measurement can be obtained in less than a minute and thus yields rapid information about the dephasing time across the sample.

8.3 Comparison of Techniques

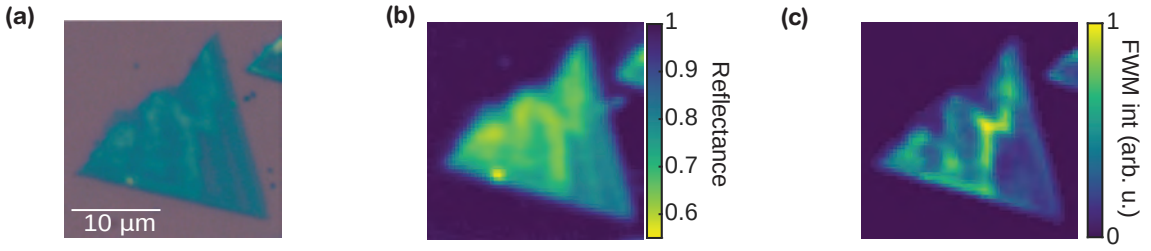

Figure 8.1: **(a)** White-light microscopy image (false color) of a CVD-grown WSe_2 monolayer. **(b)** Resonant integrated reflectance from 1600 meV to 1700 meV of the WSe_2 monolayer. Here, we set the substrate to have a reflectance of one. **(c)** FWM intensity image of the WSe_2 monolayer.

An image of the sample acquired with a conventional white-light microscope is shown in Fig. 8.1(a). The sample is a commercially available CVD-grown flake of WSe_2 (6Carbon Technologies), grown on a separate substrate and transferred onto a new substrate of SiO_2/Si. In contrast to the samples discussed in previous chapters, this sample is not hBN encapsulated. The monolayer shows an uneven structure due to residue remaining from the transfer process, a common problem in CVD-grown materials [30]. A resonant (with the exciton) integrated reflectance image is shown in Fig. 8.1(b). Here, we use a sample point on the substrate to reference a reflectance of one and integrate over the laser spectrum spanning a range from 1600 meV to 1700 meV. The sample reflectance is influenced by both reflections from the sample and the back-reflected signal from the substrate absorbed by the sample. The spatial structure of the integrated reflectance coincides with the spatial structure in the

white light microscopy image in Fig. 8.1(a). Nonetheless, differences (e.g., at the bottom of the sample) remain. A FWM intensity image of the sample is shown in Fig. 8.1(c). It indicates a strong spatial dependence of the FWM strength, attributed to local strain profiles, changes in the dielectric environment, doping, trapped charges, impurities, defect densities, and distribution of dark states [25–28, 31]. Some regions of stronger FWM correlate with areas of weaker reflectance (e.g., the bright center structure). In contrast, some areas of weaker reflectance (e.g., towards the center-left of the sample) show an overall weaker FWM signal. Moreover, some areas of higher reflectance, such as the bottom of the sample, show a stronger FWM signal. These observations highlight one of the benefits of nonlinear FWM imaging: while white light microscopy and even resonant linear micro-reflectance spectroscopy can be helpful for sample characterization, the sensitivity of FWM to material changes, including doping, defects, strain, dielectric environment, and dark state distribution changes [24, 28, 31, 32], yields more detailed information about the quality of a sample.

8.4 Dephasing Maps

Next, we acquire dephasing time maps of the sample. By the procedure described in the experimental methods section, we extract dephasing times for every image pixel and plot the resulting dephasing time maps in Fig. 8.2(a). Before fitting a uni-exponential decay, we subtract a background determined from an image acquired after the FWM response of the sample has fully decayed. The measured sample response is commonly modeled by convolving an exponential decay fit function with the instrument response function [26, 27] to account for the finite pulse duration. However, finite pulse effects in nonlinear multi-pulse experiments are more complicated [33]. Therefore, here we only fit the exponential decay for sample points with $t' \geq 40\,\mathrm{fs}$, such that $t = \tau \geq 20\,\mathrm{fs}$ while also convolving the fit function with the Gaussian

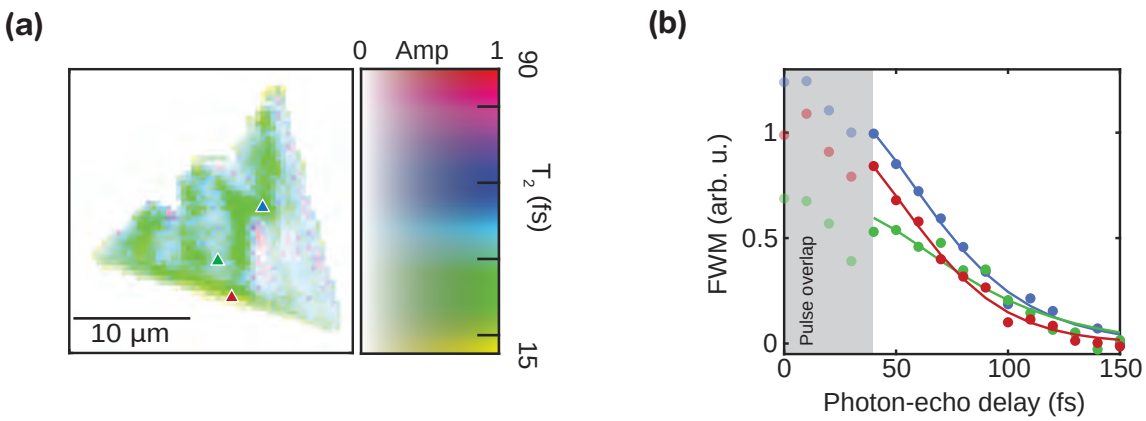

Figure 8.2: **(a)** Dephasing time T_2 map of the sample obtained by fitting a uni-exponential decay in the time domain. The hue level signifies the dephasing time, while the saturation signifies the FWM strength. **(b)** FWM amplitude dephasing curves at select sample spots marked with colored triangles in (a). Uni-exponential fits are plotted as solid lines. Only sample points with photon echo times $t+\tau = t' \geq 40\,\text{fs}$ are fitted to exclude finite pulse effects present for early t'.

instrument response function. Fig. 8.2(a) shows a joint representation of FWM intensity and dephasing times. Here, the hue level signifies the dephasing times, while the saturation signifies the FWM intensity. The high FWM intensity area of the sample shows approximately homogeneous dephasing times across the sample, except for the bottom part, which shows faster dephasing. However, several low FWM areas on the sample show a significantly increased dephasing time. To understand the physical reasoning behind such behavior, Fig. 8.2(b) shows three exemplary dephasing curves for the sample points marked with blue, red, and green triangles in Fig. 8.2(a). The red curve clearly shows a faster decay than the blue curve, establishing that the decreased dephasing time for the bottom of the sample is not an artifact of the fits but is reflected in the data. In contrast, the green curve initially rises before peaking at 70 fs and decaying for larger photon echo time values. For the red and blue curves, the fits agree well with the data in the range of 40 fs-150 fs for the photon-echo times, while early times show a deviating behavior due to both finite pulse and time-ordering effects during pulse overlap [34]. The map in Fig. 8.2(a) shows increased speckle noise compared to the linear and FWM images in Fig. 8.1(b,c), which can be traced back

to fit errors, especially in areas of lower FWM intensity and areas that show a behavior deviating from a simple exponential decay (see green curve). However, the noise level is still sufficient for material characterization because regions of interest remain unobscured by the noise.

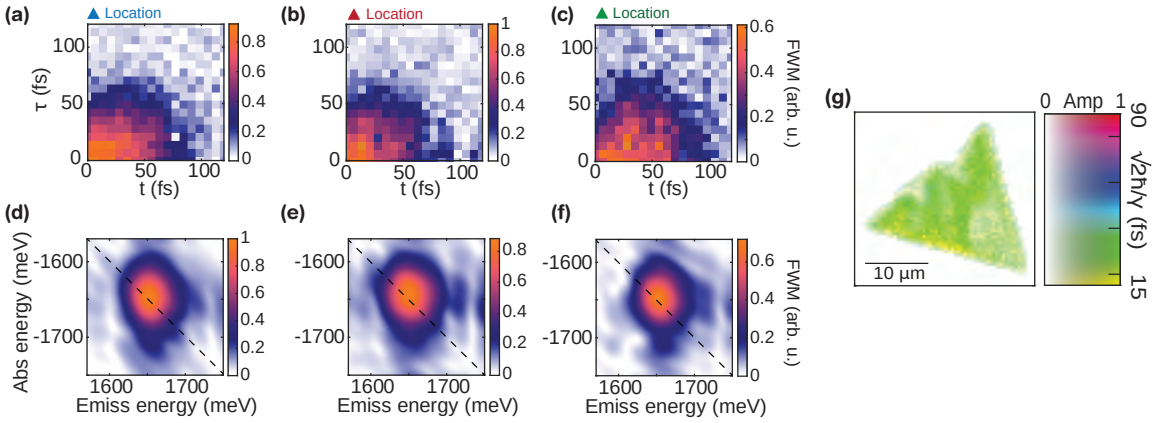

Figure 8.3: **(a-c)** Two-dimensional time domain signal for the three locations marked in Fig. 8.2(c), obtained by scanning the τ- and t-delay. **(d-f)** MDCS spectra for the three locations marked in Fig. 8.2(a), obtained by Fourier transforming the time domain signals displayed in (a-c). **(g)** Joint map of dephasing time T_2 map of the sample obtained by fitting the linewidths of the MDCIS spectrum with the procedure outlined in [35] and FWM strength.

A better understanding of the physical behavior that causes the non-trivial temporal behavior for the sample region marked by the green triangle in Fig. 8.3(a) can be gained by taking a full MDCIS scan at T=25 fs. Exemplary two-dimensional time domain signals and MDCS spectra at the three sample spots marked in Fig. 8.2(a) are plotted in Fig. 8.3(a-c) and (d-f), respectively. The time domain photon echo signal and corresponding spectra for Fig. 8.3(a,b) and (d,e) show similar behavior, with the echo in Fig. 8.3(b) showing a slightly faster decay, and hence a slightly increased homogeneous linewidth in the spectrum presented in Fig. 8.3(e). In contrast to these two sample spots, the sample spot marked with a green rectangle whose MDCIS data is plotted in Fig. 8.3(c,f) shows a photon-echo that is delayed along t. The delayed sample response along t has been observed previously [36–38] and can be explained by increased many-body effects in this sample area. The shift in the time domain

explains the dephasing curves' shape in Fig. 8.2(b). While the extracted dephasing times T_2 at those sample spots are unreliable, our rapid technique still unequivocally identifies these areas, and, using MDCIS, these areas can be studied further.

To prove that the dephasing times extracted for the higher FWM signal sample areas can be reliably determined by scanning along the diagonal of the photon echo, we fit the linewidths of the MDCIS measurements using the procedure outlined in [35]. We plot the T_2 times determined via $T_2 = \sqrt{2}\hbar/\gamma$ from the MDCIS measurements in Fig. 8.3(g). Firstly, the qualitative changes of the linewidths across the sample extracted from the two methods agree well for the high FWM signal areas. The good qualitative agreement is especially evident for the sample's bottom area, which shows reduced dephasing times in both measurements. Furthermore, a reasonable quantitative agreement between the dephasing times extracted from the rapid dephasing curves and the MDCIS linewidths can be observed. Over large areas of the sample, the dephasing times lie within 15 fs of each other. The systematically lower dephasing time for the MDCIS measurement can be explained by finite pulse and time-ordering effects that play a significant role in this measurement because $T_2 \approx T_{\text{pulse}}$. While early delay times where those effects dominate can be filtered out efficiently in the time domain fits, the same treatment is not as straightforward in the frequency domain. An in-depth discussion of these effects can be found in the literature [33, 34] and section 8.6. For $T_2 > T_{\text{pulse}}$, these effects become negligible.

8.5 Decay Maps

An additional modality of our nonlinear microscope is the ability to take rapid FWM decay images, characterizing the exciton population lifetime by varying the T delay. We apply a bi-exponential fit to the data to capture the full temporal decay dynamics of the WSe_2 flake, which displays rapid, sub-50 fs decay, followed by a slower decay on the order of a few picoseconds. Similar to the dephasing time

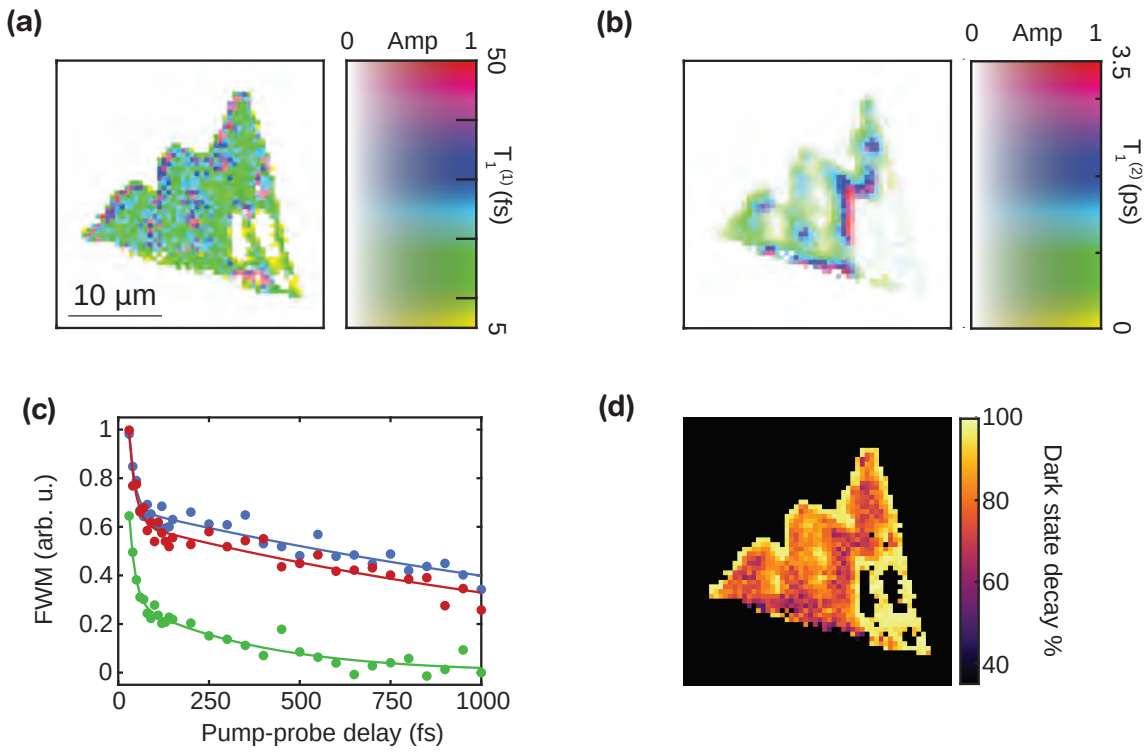

Figure 8.4: **(a)** FWM amplitude decay curves at select sample spots marked with colored rectangles in Fig. 8.2(a). Bi-exponential fits are plotted as solid lines. **(b)** Joint representation of fast fit amplitude and decay time $T_1{}^{(1)}$, obtained from the bi-exponential fit to the decay curves. **(c)** Joint representation of slow fit amplitude and decay time $T_1{}^{(2)}$, obtained from the bi-exponential fit to the decay curves. **(d)** Spatial map of the percentage of the exciton population that decays into dark states, obtained by normalizing the fit amplitude of the fast decay by the sum of slow and fast fit amplitudes.

maps, we exclude sample points with $T \leq 20$ fs to avoid the influence of finite pulse effects and consider the finite pulse duration by convolving the fit function with the instrument response function. The fast decay components' fitted amplitude and decay time are plotted in the joint representation introduced earlier in Fig. 8.4(a). Across the sample, the intensity of the first decay component is relatively homogeneous, while the decay time fluctuates mainly between 10-25 fs, approximately twice as fast as the dephasing time. These observations suggest a radiatively limited dephasing time via the relation $T_2 = 2T_1$. Although we observe a factor between 1.5-2 in our measurements, this deviation can be explained by the dephasing and decay times

approaching the temporal resolution of the experimental setup. The second decay component plotted in Fig. 8.4(b) shows a more distinct spatial profile, matching the spatial intensity profile of the FWM plotted in Fig. 8.1(c). The bottom and center of the sample display a longer decay time on the order of 2-3 ps, while the rest of the sample shows decay times of around 1 ps. The exemplary decay curves for the three sample spots marked in Fig. 8.2(a), plotted in Fig. 8.4(c), further corroborate this behavior. The rapid sub-50 fs decay component shows comparable amplitudes (the FWM dropping by approximately 0.4 during the first 100 fs) for all three sample points. However, the green curve has a remaining amplitude of 0.2, while both the blue and green curves have a remaining amplitude of 0.6, showing the stark contrast in amplitude for the slow decay.

Bi-exponential decays for monolayer TMDs have been observed in the past, with the fast component being attributed to the population relaxation of bright excitons and the second decay component attributed to additional states such as dark states or localized states (in the following: dark states) beyond a simple two-level system [6], with the dark state constituting the ground state of the exciton in WSe_2 [39]. In this case, the fast decay is caused by decay into the dark states. After exciton populations of bright and dark states equilibrate, excitons tunnel back from dark into bright states, and subsequent radiative decay of the bright excitons causes the slow decay of the signal [40]. Hence, by dividing the amplitude of the fast decay by the sum of the two fit amplitudes, we can further extract which percentage of the exciton population decays into dark states and observe the spatial variation of this quantity across the sample. A spatial map of this quantity is plotted in Fig. 8.4(d). On average, the stronger FWM signal regions of the sample show a lower percentage of exciton population decaying into dark states. Among these regions, the bottom of the sample stands out, with only 40% of excitons decaying into dark states, while the center area shows approximately 60-70% of excitons decaying into dark states. Low

signal areas of the FWM show more than 90% of excitons decaying into dark states. This observation corroborates earlier findings from FWM strength and dephasing maps: Low FWM signal areas of the sample, which have been identified by both their FWM strength as well as dephasing and population maps to be distinct in their physical properties from other regions of the sample also have more available dark states. Given that the exciton ground state in WSe_2 is dark, the higher number of dark states can explain the lowered measured FWM signal.

The ability to observe these physical changes across the sample is an important distinction in capabilities between ultrafast FWM imaging and other techniques presented here - resonant micro-reflectance, white light microscopy, and even the static FWM image (taken at fixed $\tau-, T-$, and t-delays): While static FWM imaging at least provides an identification of areas with stronger and weaker FWM (which is a measure of underlying changes in material parameters that FWM is more sensitive to than linear imaging techniques), dephasing and decay imaging show which physical properties of the sample are altered and where. These insights into the sample changes can be incorporated into the manufacturing process: either for sample repair (e.g., through chemical processing) or within a feedback loop used to adjust the fabrication process.

8.6 Treating Finite Pulse Effects in Multi-Pulse Four-Wave Mixing Experiments

Despite efficient pulse compression, when the pulse duration T_{pulse} approaches the time scales of the sample dynamics, such as dephasing time T_2 or population decay time T_1, finite pulse effects influence the retrieved dynamics of the sample. The influence of finite pulse effects is evident from Fig. 8.5(a), where we plot the simulated sample response for 20 fs pulses to a dephasing process with a dephasing time $T_2 =$

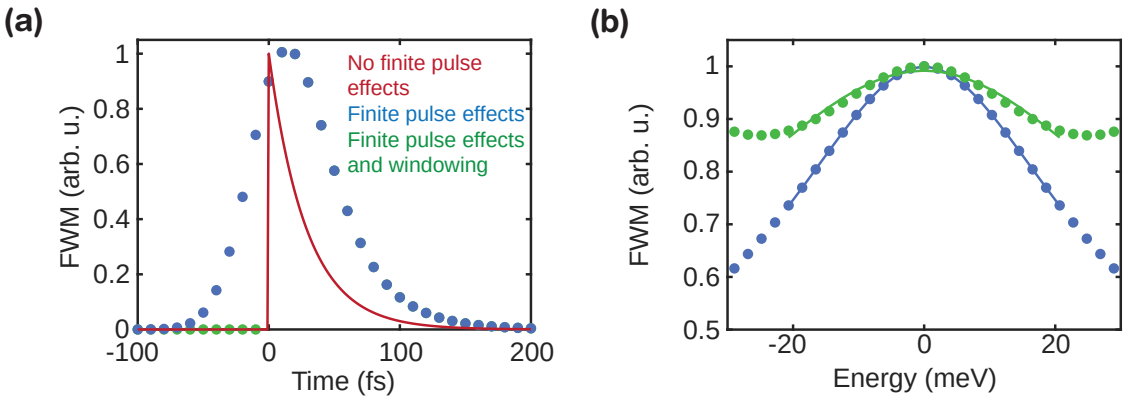

Figure 8.5: **(a)** Dephasing curve with $T_2 = 30\,\text{fs}$ without finite pulse effects (red) and with finite pulse effects for a 20 fs pulse (blue curve). **(b)** Lineshape retrieved from the blue curve in (a) (blue) and retrieved from the green curve in (a) where all signal at negative times is set to zero. Both lineshapes have been spectrally normalized with the procedure outlined below.

30 fs. The pure sample response (red) does not consider finite pulse effects, while the actual response (blue) takes them into account. The effects of finite pulse effects on the sample response differ for the different modalities (dephasing vs. population decay) presented above. For population scans, the sample response is modeled by convolving an exponential decay with the cross-correlation of the intensities of the pump and probe pulses [41]. The same procedure as for MDCS needs to be employed for dephasing maps. As inferred from Ref. 33, when also considering heterodyne detection with a fourth pulse, finite pulse effects in the frequency domain correspond to finite bandwidth effects. In order to determine the bandwidth-independent sample response, all finite-bandwidth effects can be treated by dividing the MDCS spectrum by the intensity spectrum of the laser pulse along the two frequency axes. Given the Gaussian shape of the spectrum, this corresponds to convolving the time domain response along the diagonal with $E^{1/4}(t')$. Here, $E(t')$ is the Gaussian pulse profile in the temporal domain. Considering the finite pulse effects in the frequency domain is identical to considering them in the time domain for the idealized scenario presented here. In Fig. 8.5(a), the real sample response extends to negative times, Fourier transforming this response and doing a Lorentzian linewidth fit in the frequency

domain after employing the spectral normalization procedure introduced above yields the same results for the dephasing time T_2 as the time domain fit. The resulting lineshape and fit after considering the finite pulse effects in the frequency domain are shown in blue in Fig. 8.5(b). As discussed by Ref. 34, interaction ordering of the various pulses plays a vital role in multi-pulse experiments. In this scenario, negative time delays are often excluded because they contain contributions from additional signal pathways that interfere with the sample response of interest. However, this also removes the real negative time signal in Fig. 8.5(a). Setting the signal to zero for negative times (green dots) yields a significantly altered lineshape in Fig. 8.5(b). The corresponding fit deviates from the data points and shows a significantly broadened linewidth compared to the blue fit. The retrieved dephasing time in this scenario is T_2=18 fs, significantly below the true value of 30 fs. We avoid underestimating the dephasing time in our time domain experiments and fits by considering finite pulse effects in our fit function and only fitting data points for sufficiently large delay times at which interaction-ordering effects are negligible. Excluding these effects is non-trivial in the frequency domain and elucidated further in Ref. 34. The time-ordering effects are the reason why our MDCIS measurements underestimate the retrieved dephasing times by a few femtoseconds. In practice, it is often common to plot the MDCS spectrum with the local oscillator bandwidth normalized out. This can lead to the underestimation of linewidths, depending on the laser bandwidth and linewidths.

8.7 Accelerating Ultrafast Nonlinear Imaging Through Smart Scanning Schemes

Lastly, we discuss how to further accelerate and improve the presented material characterization techniques. In an ideal, noise-free scenario, two sample points are sufficient to determine the fit parameters for a uni-exponential decay. However, as

experimental noise increases, a higher number of points increases the reliability of the extracted fit parameters. The increased noise is evident in Fig. 8.6, where we plot the dephasing time maps for a different selection of data points: Fig. 8.6(a) shows the dephasing time map obtained by considering all 12 time data points (per pixel) between 40 fs and 150 fs, equidistantly spaced by 10 fs, Fig. 8.6(b) shows the dephasing time map obtained by omitting the last three data points, Fig. 8.6(c) shows the dephasing time map obtained by omitting the last six data points. As more data points get omitted, the noise for the dephasing time map visibly increases while also showing a systematic shift towards higher dephasing times. However, while using the same number of data points as in Fig. 8.6(c), Fig. 8.6(d) uses every second data point between 40 fs and 150 fs. This sampling scheme shows a significantly improved noise, effectively comparable to the dephasing time map in Fig. 8.6(a), which takes twice as long to acquire. The absolute values for the dephasing times in Fig. 8.6(a) and (d) also agree.

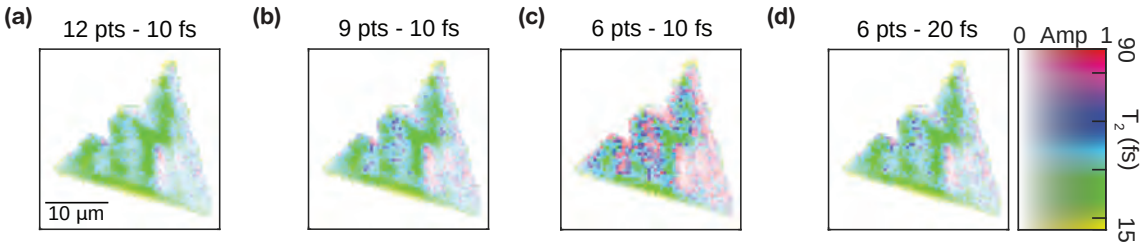

Figure 8.6: **(a)** Dephasing time map obtained by considering all 12 time-data points per pixel between 40 fs and 150 fs, spaced by 10 fs. **(b)** Dephasing time map obtained by disregarding the last three data points. **(c)** Dephasing time map obtained by disregarding the last six data points. **(d)** Dephasing time maps obtained by considering 6 data points between 40 fs and 150 fs, spaced by 20 fs.

These observations spark the question of which distribution of sample points yields the highest robustness to inevitable noise sources in the FWM measurement. The possibility of gaining an SNR advantage with non-equidistant sample point spacing is well known and exponential sampling has been known to the nuclear magnetic resonance community since the 1960s [42]. To answer the question of which distribution

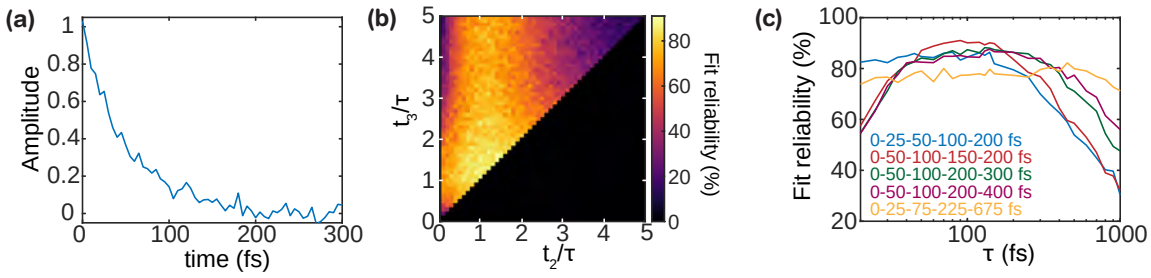

Figure 8.7: **(a)** Uni-exponential amplitude decay with a decay time $\tau = 50\,\text{fs}$. We add average white Gaussian noise with an SNR of 10 for the amplitude, corresponding to -20 dB. **(b)** Simulated fit reliability, defined as a fitted decay constant within $\pm 10\%$ of the true value, for 200 iterations with randomized noise as a function of sampling point spacing for the second (t_2) and third (t_3) sample points. The first sampling point is fixed to time zero. **(c)** Simulated fit reliability as a function of time constant for five sampling points with varying spacing.

of sample points is best in our scenario, we simulate a uni-exponential amplitude decay curve with added average white Gaussian noise with an SNR of 10 for the amplitude (-20 dB), exemplarily plotted in Fig. 8.7(a). The dominant noise source is the DC shot noise from the four beams impinging on the detector, which does not scale with the FWM intensity and remains constant as the time delay is changed, therefore following a Gaussian distribution. Comparing this curve to Fig. 8.2(f) and Fig. 8.4(a), we determine that this constitutes a reasonable approximation for the measurement noise level. We first simulate the scenario of three sampling points. While this is one more sampling point than necessary, this allows us to see if/how increasing the number of sampling points helps the reliability of the extracted decay times in the presence of noise. We fix the first sampling point to time-zero and simulate a grid of sample points $t_{2,3}$ between zero and five times the decay time τ in steps of $\tau/10$. Due to symmetry conditions, we also enforce $t_3 > t_2$. For each grid point, we run 200 iterations with randomized average white Gaussian noise, all with a -20 dB noise floor. We fit each curve and consider the fit reliable if it reconstructs the decay time $\tau = 50\,\text{fs}$ within $\pm 10\%$. The result of the simulation is plotted in Fig. 8.7(b). The vertical stripe structure indicates that a reliable decay constant can almost always be extracted as long as the second sampling point is close to the decay time τ. To cor-

roborate this observation, for low values of t_2, a higher fit reliability can be observed for values of t_3 close to 1. Despite the vertical stripe structure, choosing t_3 in areas of meaningful signal within 2-3 τ yields a higher reliability of the fit. In this case, the third data point contributes meaningful information to the fit instead of being close to zero, a value all exponential fits eventually approach.

However, this model considers a priori knowledge of the decay times, which is not always given. Moreover, decay times will inherently vary across the sample. Another area of interest is hence which range of decay constants can be reliably retrieved with a particular spacing of points. The answer is relatively straightforward in the three sample point case: Setting the second sampling point to the lowest expected decay time while setting the third sample point to the largest expected decay time will yield the largest range of possible decay times. However, there is a potential decrease in reliability for intermediate values, depending on the range of decay times explored. In this case, acquiring more sample points, compromising speed for reliability to a certain extent, can be advantageous. We simulate the reliability of fits for a range of decay times from 20 fs to 1000 fs with five sampling points and plot the results in Fig. 8.7(c). Here, we choose five different spacings: A non-equidistant spacing of sampling points where the distance between each sampling points doubles, once with an initial 25 fs spacing (blue curve) and an initial 50 fs spacing (purple curve), a non-equidistant spacing of sampling points where the distance is tripled, with an initial spacing of 25 fs (yellow curve). We also simulate a scenario with an equidistant spacing of 50 fs (red curve) and a curve with mixed spacing (green curve). We simulate a thousand fits with the same -20 dB average white Gaussian noise for each decay time.

From Fig. 8.7(c), we observe that non-equidistant spacing is preferable in most scenarios. While the non-equidistant curves show a lower peak fit reliability (80% for the blue/green/purple curve, 75% for the yellow curve, instead of 90% for the equidistant red curve), the range of decay times they span is significantly higher.

The blue curve shows fit reliabilities above 80% down to the shortest decay times simulated. In comparison, the purple curve shows fit reliabilities above 50% for decay times up to 1000 fs and down to 20 fs. Non-equidistant spacing is also not limited to doubling the distance between the sampling points, i.e., exponential spacing with base 2. From the yellow curve, which uses a tripled spacing (exponential spacing with base 3) between sampling points, we observe that the range of reliably extracted decay times can be further extended, with fit reliabilities over 70% for the entire 20-1000 fs range. However, the peak fit reliability is further decreased in this case. A decreased sample point spacing at early times and an increased sample point spacing at later times is thus a powerful tool that can be adjusted as needed for fit reliability and extracted decay time range changes.

8.8 Conclusions and Outlook

This chapter presents an approach to rapid multiplex ultrafast nonlinear imaging of advanced materials based on FWM generated by three pulses. An evolution from our MDCS spectroscopy setup, which constitutes a sophisticated but slow technique, using three pulses to generate the FWM allows us to track FWM intensity, dephasing times, and exciton lifetimes across a CVD-grown monolayer of WSe_2 rapidly when employing smart scanning schemes in the temporal domain. We show that a single FWM image alone allows us to distinguish areas that show distinct exciton dephasing, population decay times, and distribution of dark states. The access to the variation of these parameters across the sample gives the ultrafast FWM modality presented in this work a selectivity that can be employed as a feedback mechanism in a manufacturing setting where material throughput is important. FWM strength, dephasing, and decay times are material parameters that reveal more about the sample's quality than current techniques such as white light microscopy, micro-reflectance/transmission, or even PL [28].

Furthermore, we demonstrate how to extract these parameters without compromising acquisition speed by performing all measurements in the time domain using few sampling points. We further show via simulations that non-equidistant spacing of the time domain sampling points allows for the retrieval of a more extensive range of decay times at only a small cost of reduced fit reliability.

Given the broad usability of FWM-based ultrafast imaging from two-dimensional quantum materials (see Chap. VII) and defects in graphene [43] to distinguishing benign from malignant melanoma [44], these method advancements constitute an essential step toward material inspection in both research and industrial settings and potentially life-science and medical imaging. Moreover, the acceleration of the MDCIS technique allows for in-situ, real-time imaging of sample parameters during sample alteration processes such as annealing or chemical reactions.

References

[1] A. K. Geim and I. V. Grigorieva. "Van der Waals heterostructures". In: *Nature* 499.7459 (July 2013), pp. 419–425. ISSN: 1476-4687. DOI: 10.1038/nature12385.

[2] A. Pospischil, M. Furchi, and T. Mueller. "Solar-energy conversion and light emission in an atomic monolayer p–n diode". In: *Nature Nanotechnology* 9.4 (Apr. 2014), pp. 257–261. DOI: 10.1038/nnano.2014.14.

[3] Nikolaus Flöry, Achint Jain, Palash Bharadwaj, Markus Parzefall, Takashi Taniguchi, Kenji Watanabe, and Lukas Novotny. "A $WSe_2/MoSe_2$ heterostructure photovoltaic device". In: *Applied Physics Letters* 107.12 (2015), p. 123106. DOI: 10.1063/1.4931621.

[4] Yu Ye, Zi Jing Wong, Xiufang Lu, Xingjie Ni, Hanyu Zhu, Xianhui Chen, Yuan Wang, and Xiang Zhang. "Monolayer excitonic laser". In: *Nature Photonics* 9.11 (Nov. 2015), pp. 733–737. ISSN: 1749-4893. DOI: 10.1038/nphoton.2015.197.

[5] Carmen Palacios-Berraquero, Matteo Barbone, Dhiren M. Kara, Xiaolong Chen, Ilya Goykhman, Duhee Yoon, Anna K. Ott, Jan Beitner, Kenji Watanabe, Takashi Taniguchi, Andrea C. Ferrari, and Mete Atatüre. "Atomically thin quantum light-emitting diodes". In: *Nature Communications* 7.12978 (2016). DOI: 10.1038/ncomms12978.

[6] Galan Moody, Chandriker Kavir Dass, Kai Hao, Chang-Hsiao Chen, Lain-Jong Li, Akshay Singh, Kha Tran, Genevieve Clark, Xiaodong Xu, Gunnar Berghäuser, Ermin Malic, Andreas Knorr, and Xiaoqin Li. "Intrinsic homogeneous linewidth and broadening mechanisms of excitons in monolayer transition metal dichalcogenides". In: *Nat Commun* 6 (2015), p. 8315. DOI: 10.1038/ncomms9315.

[7] Torben L. Purz, Eric W. Martin, Pasqual Rivera, William G. Holtzmann, Xiaodong Xu, and Steven T. Cundiff. "Coherent exciton-exciton interactions and exciton dynamics in a $MoSe_2/WSe_2$ heterostructure". In: *Phys. Rev. B* 104 (24 Dec. 2021), p. L241302. DOI: 10.1103/PhysRevB.104.L241302.

[8] Kai-Chih Huang, Jeremy McCall, Pu Wang, Chien-Sheng Liao, Gregory Eakins, Ji-Xin Cheng, and Chen Yang. "High-Speed Spectroscopic Transient Absorption Imaging of Defects in Graphene". In: *Nano Letters* 18.2 (2018). PMID: 29342361, pp. 1489–1497. DOI: 10.1021/acs.nanolett.7b05283.

[9] Xin Jiat Lee, Billie Yan Zhang Hiew, Kar Chiew Lai, Lai Yee Lee, Suyin Gan, Suchithra Thangalazhy-Gopakumar, and Sean Rigby. "Review on graphene and its derivatives: Synthesis methods and potential industrial implementation". In: *Journal of the Taiwan Institute of Chemical Engineers* 98 (2019). Microreactor: Fundamentals and Applications in Chemical Engineering, pp. 163–180. ISSN: 1876-1070. DOI: https://doi.org/10.1016/j.jtice.2018.10.028.

[10] Yan Liang, Chandrasekar Perumal Veeramalai, Guochen Lin, Xiangbin Su, Xiaoming Zhang, Shuai Feng, Yingqiang Xu, and Chuanbo Li. "A review on III-V compound semiconductor short wave infrared avalanche photodiodes". In: *Nanotechnology* 33.22 (Mar. 2022), p. 222003. DOI: 10.1088/1361-6528/ac5442.

[11] Ziyuan Li, Jeffery Allen, Monica Allen, Hark Hoe Tan, Chennupati Jagadish, and Lan Fu. "Review on III-V Semiconductor Single Nanowire-Based Room Temperature Infrared Photodetectors". In: *Materials* 13.6 (2020). ISSN: 1996-1944. DOI: 10.3390/ma13061400.

[12] Julie Tournet, Yonghwan Lee, Siva K. Karuturi, Hark H. Tan, and Chennupati Jagadish. "III–V Semiconductor Materials for Solar Hydrogen Production: Status and Prospects". In: *ACS Energy Letters* 5.2 (2020), pp. 611–622. DOI: 10.1021/acsenergylett.9b02582.

[13] Desire Athow. "How GaN is changing the future of semiconductors". In: *Techradar* (Mar. 2021). URL: https://www.techradar.com/news/how-gan-is-changing-the-future-of-semiconductors.

[14] Hana Askren and Mark Andress. "New Semiconductor Technologies Driving Down Cost Of Electric Vehicle Batteries". In: *Forbes* (Jan. 2020). URL: https://www.forbes.com/sites/mergermarket/2020/01/08/new-semiconductor-technologies-driving-down-cost-of-electric-vehicle-batteries/?sh=57ac00de2f0a.

[15] Evgeny M. Alexeev, Alessandro Catanzaro, Oleksandr V. Skrypka, Pramoda K. Nayak, Seongjoon Ahn, Sangyeon Pak, Juwon Lee, Jung Inn Sohn, Kostya S. Novoselov, Hyeon Suk Shin, and Alexander I. Tartakovskii. "Imaging of Interlayer Coupling in van der Waals Heterostructures Using a Bright-Field Optical Microscope". In: *Nano Letters* 17.9 (2017). PMID: 28753319, pp. 5342–5349. DOI: 10.1021/acs.nanolett.7b01763.

[16] Riccardo Frisenda, Yue Niu, Patricia Gant, Aday J Molina-Mendoza, Robert Schmidt, Rudolf Bratschitsch, Jinxin Liu, Lei Fu, Dumitru Dumcenco, Andras Kis, David Perez De Lara, and Andres Castellanos-Gomez. "Micro-reflectance and transmittance spectroscopy: a versatile and powerful tool to characterize 2D materials". In: *Journal of Physics D: Applied Physics* 50.7 (Jan. 2017), p. 074002. DOI: 10.1088/1361-6463/aa5256.

[17] Kinga Lasek, Jingfeng Li, Sadhu Kolekar, Paula Mariel Coelho, Lu'an Guo, Min Zhang, Zhiming Wang, and Matthias Batzill. "Synthesis and characterization of 2D transition metal dichalcogenides: Recent progress from a vacuum surface science perspective". In: *Surface Science Reports* 76.2 (2021), p. 100523. ISSN: 0167-5729. DOI: https://doi.org/10.1016/j.surfrep.2021.100523.

[18] R Saito, Y Tatsumi, S Huang, X Ling, and M S Dresselhaus. "Raman spectroscopy of transition metal dichalcogenides". In: *Journal of Physics: Condensed Matter* 28.35 (July 2016), p. 353002. DOI: 10.1088/0953-8984/28/35/353002.

[19] Xin Zhang, Xiao-Fen Qiao, Wei Shi, Jiang-Bin Wu, De-Sheng Jiang, and Ping-Heng Tan. "Phonon and Raman scattering of two-dimensional transition metal dichalcogenides from monolayer, multilayer to bulk material". In: *Chem. Soc. Rev.* 44 (9 2015), pp. 2757–2785. DOI: 10.1039/C4CS00282B.

[20] Maria O'Brien, Niall McEvoy, Damien Hanlon, Toby Hallam, Jonathan N. Coleman, and Georg S. Duesberg. "Mapping of Low-Frequency Raman Modes in CVD-Grown Transition Metal Dichalcogenides: Layer Number, Stacking Orientation and Resonant Effects". In: *Scientific Reports* 6.1 (Jan. 2016), p. 19476. ISSN: 2045-2322. DOI: 10.1038/srep19476.

[21] Hang Zhang, Junxiang Huang, Yongwei Wang, Rui Liu, Xiulan Huai, Jingjing Jiang, and Chantelle Anfuso. "Atomic force microscopy for two-dimensional materials: A tutorial review". In: *Optics Communications* 406 (2018). Optoelectronics and Photonics Based on Two-dimensional Materials, pp. 3–17. ISSN: 0030-4018. DOI: https://doi.org/10.1016/j.optcom.2017.05.015.

[22] Hyeongwoo Lee, Inki Kim, Chulho Park, Mingu Kang, Jinseong Choi, Kwang-Yong Jeong, Jungho Mun, Yeseul Kim, Jeonghoon Park, Markus B. Raschke, Hong-Gyu Park, Mun Seok Jeong, Junsuk Rho, and Kyoung-Duck Park. "Inducing and Probing Localized Excitons in Atomically Thin Semiconductors via Tip-Enhanced Cavity-Spectroscopy". In: *Advanced Functional Materials* 31.33 (2021), p. 2102893. DOI: https://doi.org/10.1002/adfm.202102893.

[23] M. Plankl, P. E. Faria Junior, F. Mooshammer, T. Siday, M. Zizlsperger, F. Sandner, F. Schiegl, S. Maier, M. A. Huber, M. Gmitra, J. Fabian, J. L. Boland, T. L. Cocker, and R. Huber. "Subcycle contact-free nanoscopy of ultrafast interlayer transport in atomically thin heterostructures". In: *Nature Photonics* 15.8 (Aug. 2021), pp. 594–600. ISSN: 1749-4893. DOI: 10.1038/s41566-021-00813-y.

[24] Tomasz Jakubczyk, Valentin Delmonte, Maciej Koperski, Karol Nogajewski, Clement Faugeras, Wolfgang Langbein, Marek Potemski, and Jacek Kasprzak. "Radiatively Limited Dephasing and Exciton Dynamics in $MoSe_2$ Monolayers Revealed with Four-Wave Mixing Microscopy". In: *Nano Letters* 16.9 (2016), pp. 5333–5339. DOI: 10.1021/acs.nanolett.6b01060.

[25] Caroline Boule, Diana Vaclavkova, Miroslav Bartos, Karol Nogajewski, Lukas Zdražil, Takashi Taniguchi, Kenji Watanabe, Marek Potemski, and Jacek Kasprzak. "Coherent dynamics and mapping of excitons in single-layer $MoSe_2$ and WSe_2 at the homogeneous limit". In: *Phys. Rev. Materials* 4 (3 Mar. 2020), p. 034001. DOI: 10.1103/PhysRevMaterials.4.034001.

[26] Tomasz Jakubczyk, Karol Nogajewski, Maciej R Molas, Miroslav Bartos, Wolfgang Langbein, Marek Potemski, and Jacek Kasprzak. "Impact of environment on dynamics of exciton complexes in a WS_2 monolayer". In: *2D Materials* 5.3 (Apr. 2018), p. 031007. DOI: 10.1088/2053-1583/aabc1c.

[27] Tomasz Jakubczyk, Goutham Nayak, Lorenzo Scarpelli, Wei-Lai Liu, Sudipta Dubey, Nedjma Bendiab, Laëtitia Marty, Takashi Taniguchi, Kenji Watanabe, Francesco Masia, Gilles Nogues, Johann Coraux, Wolfgang Langbein, Julien Renard, Vincent Bouchiat, and Jacek Kasprzak. "Coherence and Density Dynamics of Excitons in a Single-Layer MoS_2 Reaching the Homogeneous Limit". In: *ACS Nano* 13.3 (2019). PMID: 30735350, pp. 3500–3511. DOI: 10.1021/acsnano.8b09732.

[28] Torben L. Purz, Eric W. Martin, William G. Holtzmann, Pasqual Rivera, Adam Alfrey, Kelsey M. Bates, Hui Deng, Xiaodong Xu, and Steven T. Cundiff. "Imaging dynamic exciton interactions and coupling in transition metal dichalcogenides". In: *The Journal of Chemical Physics* 156.21 (2022), p. 214704. DOI: 10.1063/5.0087544.

[29] Geoffrey M. Diederich, Travis M. Autry, and Mark E. Siemens. "Diagonal slice four-wave mixing: natural separation of coherent broadening mechanisms". In: *Opt. Lett.* 43.24 (Dec. 2018), pp. 6061–6064. DOI: 10.1364/OL.43.006061.

[30] Adam J Watson, Wenbo Lu, Marcos H D Guimarães, and Meike Stöhr. "Transfer of large-scale two-dimensional semiconductors: challenges and developments". In: *2D Materials* 8.3 (May 2021), p. 032001. DOI: 10.1088/2053-1583/abf234.

[31] Archana Raja, Lutz Waldecker, Jonas Zipfel, Yeongsu Cho, Samuel Brem, Jonas D. Ziegler, Marvin Kulig, Takashi Taniguchi, Kenji Watanabe, Ermin Malic, Tony F. Heinz, Timothy C. Berkelbach, and Alexey Chernikov. "Dielectric disorder in two-dimensional materials". In: *Nature Nanotechnology* 14.9 (Sept. 2019), pp. 832–837. ISSN: 1748-3395. DOI: 10.1038/s41565-019-0520-0.

[32] Eric W. Martin, Jason Horng, Hanna G. Ruth, Eunice Paik, Michael-Henr Wentzel, Hui Deng, and Steven T. Cundiff. "Encapsulation Narrows and Preserves the Excitonic Homogeneous Linewidth of Exfoliated Monolayer $MoSe_2$". In: *Phys. Rev. Applied* 14 (2 Aug. 2020), p. 021002. DOI: 10.1103/PhysRevApplied.14.021002.

[33] Christopher L. Smallwood, Travis M. Autry, and Steven T. Cundiff. "Analytical solutions to the finite-pulse Bloch model for multidimensional coherent spectroscopy". In: *J. Opt. Soc. Am. B* 34.2 (Feb. 2017), pp. 419–429. DOI: 10.1364/JOSAB.34.000419.

[34] Sarah M. Gallagher Faeder and David M. Jonas. "Two-Dimensional Electronic Correlation and Relaxation Spectra: Theory and Model Calculations". In: *The Journal of Physical Chemistry A* 103.49 (1999), pp. 10489–10505. DOI: 10.1021/jp9925738.

[35] Mark E. Siemens, Galan Moody, Hebin Li, Alan D. Bristow, and Steven T. Cundiff. "Resonance lineshapes in two-dimensional Fourier transform spectroscopy". In: *Opt. Express* 18.17 (Aug. 2010), pp. 17699–17708. DOI: 10.1364/OE.18.017699.

[36] M. Wegener, D. S. Chemla, S. Schmitt-Rink, and W. Schäfer. "Line shape of time-resolved four-wave mixing". In: *Phys. Rev. A* 42 (9 Nov. 1990), pp. 5675–5683. DOI: 10.1103/PhysRevA.42.5675.

[37] H. Wang, K. B. Ferrio, D. G. Steel, P. R. Berman, Y. Z. Hu, R. Binder, and S. W. Koch. "Transient four-wave-mixing line shapes: Effects of excitation-induced dephasing". In: *Phys. Rev. A* 49 (3 Mar. 1994), R1551–R1554. DOI: 10.1103/PhysRevA.49.R1551.

[38] J. M. Shacklette and S. T. Cundiff. "Nonperturbative transient four-wave-mixing line shapes due to excitation-induced shift and excitation-induced dephasing". In: *J. Opt. Soc. Am. B* 20.4 (Apr. 2003), pp. 764–769. DOI: 10.1364/JOSAB.20.000764.

[39] Malte Selig, Gunnar Berghäuser, Archana Raja, Philipp Nagler, Christian Schüller, Tony F. Heinz, Tobias Korn, Alexey Chernikov, Ermin Malic, and Andreas Knorr. "Excitonic linewidth and coherence lifetime in monolayer transition metal dichalcogenides". In: *Nature Communications* 7.1 (Nov. 2016), p. 13279. ISSN: 2041-1723. DOI: 10.1038/ncomms13279.

[40] G. Moody, M. E. Siemens, A. D. Bristow, X. Dai, A. S. Bracker, D. Gammon, and S. T. Cundiff. "Exciton relaxation and coupling dynamics in a GaAs/Al_xGa_xAs quantum well and quantum dot ensemble". In: *Phys. Rev. B* 83 (24 June 2011), p. 245316. DOI: 10.1103/PhysRevB.83.245316.

[41] D. Polli, D. Brida, S. Mukamel, G. Lanzani, and G. Cerullo. "Effective temporal resolution in pump-probe spectroscopy with strongly chirped pulses". In: *Phys. Rev. A* 82 (5 Nov. 2010), p. 053809. DOI: 10.1103/PhysRevA.82.053809.

[42] J.C.J Barna, E.D Laue, M.R Mayger, J Skilling, and S.J.P Worrall. "Exponential sampling, an alternative method for sampling in two-dimensional NMR experiments". In: *Journal of Magnetic Resonance (1969)* 73.1 (1987), pp. 69–77. ISSN: 0022-2364. DOI: https://doi.org/10.1016/0022-2364(87)90225-3.

[43] Pedro Miguel M.C. de Melo, Pedro Miguel, Zeila Zanolli, and Matthieu J. Verstraete. "Optical Signatures of Defect Centers in Transition Metal Dichalcogenide Monolayers". In: *Advanced Quantum Technologies* 4.3 (2021), p. 2000118. DOI: https://doi.org/10.1002/qute.202000118.

[44] Kuk-Youn Ju, Simone Degan, Martin C. Fischer, Kevin C. Zhou, Xiaomeng Jia, Jin Yu, and Warren S. Warren. "Unraveling the molecular nature of melanin changes in metastatic cancer". In: *Journal of Biomedical Optics* 24.5 (2019), pp. 1–13. DOI: 10.1117/1.JBO.24.5.051414.

CHAPTER IX

Summary and Outlook

In this thesis, we have provided crucial insights into the exciton physics of TMDs alongside the advancement of nonlinear (spectroscopic) imaging techniques. All chapters in this thesis contain an outlook specific to those projects. In this last chapter, we want to provide a more all-encompassing perspective. As the thesis is two-fold, covering both technique development and insights into materials physics, so is the outlook presented below.

9.1 The Future of Transition Metal Dichalcogenides

While charge transfer had been observed previously in TMD heterostructures [1–4], our MDCS experiments in Chap. V, quantifying both electron and hole transfer to occur on a sub-150 fs time scale, provide a unique perspective on the simultaneous electron and hole transfer. The electron charge transfer times were also not previously reported for this specific heterostructure. Furthermore, we observe coherent coupling between intralayer excitons in the $MoSe_2$ and WSe_2 monolayers. Coherent coupling had only been previously observed between excitons and trions in TMD monolayers [5, 6], but not between excitons in different layers of a TMD heterostructure. Lastly, our measurement of the ILE binding energy as 254 meV adds to the compelling case of ILE applications at room temperature and beyond.

These findings manifest an essential step toward the applicability of TMDs: For applications relying on charge transfer, such as photovoltaic applications, gaining a better understanding of the charge transfer scales in a "natural" setting where electrons and holes transfer simultaneously is vital. Our approach is in contrast to the more common approach in the literature of isolating either electron or hole transfer [1–4]. In addition, coherent coupling opens the avenue for quantum coherent control. Given that TMD heterostructures are highly tunable material systems that can interface photons, charges, and spin states, the prospect of tunable quantum coherent control is certainly enticing.

In addition to the findings from simple MDCS, no spatial study of either coherent coupling or charge transfer homogeneity had been performed previously. Bearing in mind that current TMD devices have only been demonstrated on tens of microns scales and less [7–10], the reproducibility of key properties across large areas of these devices is inevitable for scalable, translatable devices. Our MDCIS scheme reveals a surprising robustness of charge transfer and coherent coupling in the presence of complex strain in Chap. VII, with 81% of the sample showing strong coherent coupling of intralayer excitons and 91% of the sample showing strong charge transfer. Our results are encouraging for the possible translation of these technologies from the lab to the marketplace and warrant further investment into growth techniques that yield large-scale TMD layers. In addition to studying heterostructures in MDCIS, we expand on the work from Kasprzak and Boule *et al.* [11–13] in studying the distribution of dephasing and inhomogeneity across TMD monolayers in Chap. VII. While our MDCIS experiments affirm some of the promises of TMDs, they also reveal shortcomings regarding the homogeneity of linewidths across the sample for TMD monolayers. We observe large changes of an order of magnitude for the inhomogeneous linewidth and a factor of two for the homogeneous linewidth.

Despite the progress of the field and the progress presented in this thesis, much

work remains to be done. For example, even though we have demonstrated coherent coupling between intralayer excitons, the underlying mechanism is unknown for TMDs. Kasprzak *et al.* [5] show how different types of coherent coupling mechanisms can be distinguished by studying the real part of MDCS spectra. Utilizing the phase information provided by the real part of the signal in MDCIS would further allow us to study whether the coupling mechanism changes across the sample or is sample-dependent. Furthermore, demonstrating quantum coherent control, similar to the experiments of Day *et al.* on silicon vacancy centers [14], represents a large step toward quantum information applications of TMDs.

Further insight into TMDs could be gained by polarization-dependent MDCS. Many applications harness the strong spin-valley coupling of the excitons, and a better understanding of the nature and homogeneity of this coupling could be obtained through polarization-dependent MDCIS. Moreover, studying the spatial dependence of many-body effects such as EID and EIS could shed further light on the complex many-body dynamics in these samples. Either the acquisition of power-dependent MDCIS or two-quantum MDCS or MDCIS can reveal signatures of these effects that have not been sufficiently studied in TMDs. We briefly discuss the spatial dependence of these dynamics in Chap. VIII, in which we observe enhanced many-body effects in some regions of the sample. Further studies into the cause of these changes are vital for a more thorough understanding of TMDs.

Moreover, the heterostructure samples studied in this thesis are small - only a few micrometers in size. Hence, much work in high-quality, large-scale material growth remains to be done. CVD growth still appears promising for this direction [15], but its resulting sample quality currently remains well below exfoliated samples' quality.

Lastly, the future of TMDs rests on which application is deemed most attractive. In recent years, the field of TMDs has seen an ever-growing production of research, with strain-engineering for single-photon emission [16] or diffusion [17] and Moiré

engineering [18], to only name a few. However, many previous "TMD crazes" have cooled down after a few years of intense research, and which application emerges as the "killer" application remains to be seen.

9.2 The Future of Nonlinear (Spectroscopic) Imaging

Pushing nonlinear imaging further toward industrial applicability requires additional work, especially on the electrical engineering side, covering everything from detector development to detection electronics. However, for most scientific purposes, the current technique is sufficient and far exceeds most current experimental capabilities. The key development behind the acceleration of nonlinear imaging during this thesis work was introduced in Chap. VI, where we show that an FIR box lock-in reduces the blurring of images and increases the suppression of extraneous modulations, which improves SNR and reduces data acquisition times. Smart scanning themes introduced in Chap. VIII further reduce data acquisition times for useful material properties such as dephasing times and lifetimes.

At the accelerated data acquisition rate of the current technique, acquiring complex-valued linear and FWM images with pixel dwell times of 240 µs and less, new bottlenecks are being reached. For one, as lock-in time constants are further reduced, detector noise becomes a more important source of noise. The noise-equivalent-power of the currently-used detector could be improved, for example, by adding a cooling capability, which would benefit any imaging/MDCIS applications. Other possible improvements include synchronization of the FPGA with the laser repetition rate and accelerating data transfer between the FPGA and the computer.

These engineering improvements aside, an immense scientific benefit could be gained by expanding the current "multifunctional spectrometer" setup to other techniques such as SRS. Raman microscopy is used in a variety of contexts, from biomedical imaging [19] and clinical medicine [20] to semiconductors (including TMDs [21,

22]). SRS, offering a signal improvement for dense samples because of its coherent nature, can be easily added to our current CINeMaS setup with few modifications. It could serve as an added modality that is helpful for material characterization but also allows the technique to enter different application spaces, such as biomedical imaging.

Even with conventional MDCIS, different sample systems, such as the photosynthetic bacteria explored in spatially-addressed MDCS by Tiwari *et al.* [23], would benefit from the technique. Hence, expanding this technique beyond TMDs or similar semiconductor nanostructures can be another avenue for impact.

Furthermore, access to the nanometer scale has been crucial to unravel some of the more intricate sample dynamics for TMDs [24, 25]. Integrating full MDCS with near-field techniques would allow for a better understanding of the fundamental physics behind coherent coupling and many-body effects, giving access to spatial variations on the tens of nanometers scale.

Finally, it is important to continue seeking benefits and applications of rapid FWM imaging outside of pure academia. On this point, we explored some of the potential applications in Chap. VIII. While beyond the scope of this thesis, defect inspection using FWM intensity or population decay maps, similar to Ref. 26, is undoubtedly an exciting avenue for exploration in the private sector.

To summarize, the results presented in this thesis are only a small piece of the puzzle that is understanding TMDs. I believe that the combined might of spectroscopy and imaging with ultrafast temporal resolution and bandwidth tunability can provide revolutionary insights in many fields, including, but not limited to, TMDs. Progress is a combination of many small steps forward, and as such, I hope that this work is a small step in the right direction.

References

[1] Xiaoping Hong, Jonghwan Kim, Su-Fei Shi, Yu Zhang, Chenhao Jin, Yinghui Sun, Sefaattin Tongay, Junqiao Wu, Yanfeng Zhang, and Feng Wang. "Ul-

trafast charge transfer in atomically thin MoS_2/WS_2 heterostructures". In: *Nature Nanotechnology* 9.9 (Sept. 2014), pp. 682–686. ISSN: 1748-3395. DOI: 10.1038/nnano.2014.167.

[2] Daichi Kozawa, Alexandra Carvalho, Ivan Verzhbitskiy, Francesco Giustiniano, Yuhei Miyauchi, Shinichiro Mouri, A. H. Castro Neto, Kazunari Matsuda, and Goki Eda. "Evidence for Fast Interlayer Energy Transfer in $MoSe_2/WS_2$ Heterostructures". In: *Nano Letters* 16.7 (2016), pp. 4087–4093. DOI: 10.1021/acs.nanolett.6b00801.

[3] Hailong Chen, Xiewen Wen, Jing Zhang, Tianmin Wu, Yongji Gong, Xiang Zhang, Jiangtan Yuan, Chongyue Yi, Jun Lou, Pulickel M. Ajayan, Wei Zhuang, Guangyu Zhang, and Junrong Zheng. "Ultrafast formation of interlayer hot excitons in atomically thin MoS_2/WS_2 heterostructures". In: *Nat Commun* 7 (2016), p. 12512. DOI: 10.1038/ncomms12512.

[4] Jonas E. Zimmermann, Young Duck Kim, James C. Hone, Ulrich Höfer, and Gerson Mette. "Directional ultrafast charge transfer in a $WSe_2/MoSe_2$ heterostructure selectively probed by time-resolved SHG imaging microscopy". In: *Nanoscale Horiz.* 5 (12 2020), pp. 1603–1609. DOI: 10.1039/D0NH00396D.

[5] B. Kasprzak J.and Patton, V. Savona, and W. Langbein. "Coherent coupling between distant excitons revealed by two-dimensional nonlinear hyperspectral imaging". In: *Nature Photonics* 5.1 (Jan. 2011), pp. 57–63. DOI: 10.1038/nphoton.2010.284.

[6] Kai Hao, Lixiang Xu, Philipp Nagler, Akshay Singh, Kha Tran, Chandriker Kavir Dass, Christian Schüller, Tobias Korn, Xiaoqin Li, and Galan Moody. "Coherent and Incoherent Coupling Dynamics between Neutral and Charged Excitons in Monolayer $MoSe_2$". In: *Nano Letters* 16.8 (2016). PMID: 27428509, pp. 5109–5113. DOI: 10.1021/acs.nanolett.6b02041.

[7] A. Pospischil, M. Furchi, and T. Mueller. "Solar-energy conversion and light emission in an atomic monolayer p–n diode". In: *Nature Nanotechnology* 9.4 (Apr. 2014), pp. 257–261. DOI: 10.1038/nnano.2014.14.

[8] Yu Ye, Zi Jing Wong, Xiufang Lu, Xingjie Ni, Hanyu Zhu, Xianhui Chen, Yuan Wang, and Xiang Zhang. "Monolayer excitonic laser". In: *Nature Photonics* 9.11 (Nov. 2015), pp. 733–737. ISSN: 1749-4893. DOI: 10.1038/nphoton.2015.197.

[9] Nikolaus Flöry, Achint Jain, Palash Bharadwaj, Markus Parzefall, Takashi Taniguchi, Kenji Watanabe, and Lukas Novotny. "A $WSe_2/MoSe_2$ heterostructure photovoltaic device". In: *Applied Physics Letters* 107.12 (2015), p. 123106. DOI: 10.1063/1.4931621.

[10] Carmen Palacios-Berraquero, Matteo Barbone, Dhiren M. Kara, Xiaolong Chen, Ilya Goykhman, Duhee Yoon, Anna K. Ott, Jan Beitner, Kenji Watanabe, Takashi Taniguchi, Andrea C. Ferrari, and Mete Atatüre. "Atomically thin quantum light-emitting diodes". In: *Nature Communications* 7.12978 (2016). DOI: 10.1038/ncomms12978.

[11] Tomasz Jakubczyk, Karol Nogajewski, Maciej R Molas, Miroslav Bartos, Wolfgang Langbein, Marek Potemski, and Jacek Kasprzak. "Impact of environment on dynamics of exciton complexes in a WS_2 monolayer". In: *2D Materials* 5.3 (Apr. 2018), p. 031007. DOI: 10.1088/2053-1583/aabc1c.

[12] Tomasz Jakubczyk, Goutham Nayak, Lorenzo Scarpelli, Wei-Lai Liu, Sudipta Dubey, Nedjma Bendiab, Laëtitia Marty, Takashi Taniguchi, Kenji Watanabe, Francesco Masia, Gilles Nogues, Johann Coraux, Wolfgang Langbein, Julien Renard, Vincent Bouchiat, and Jacek Kasprzak. "Coherence and Density Dynamics of Excitons in a Single-Layer MoS_2 Reaching the Homogeneous Limit". In: *ACS Nano* 13.3 (2019). PMID: 30735350, pp. 3500–3511. DOI: 10.1021/acsnano.8b09732.

[13] Caroline Boule, Diana Vaclavkova, Miroslav Bartos, Karol Nogajewski, Lukas Zdražil, Takashi Taniguchi, Kenji Watanabe, Marek Potemski, and Jacek Kasprzak. "Coherent dynamics and mapping of excitons in single-layer $MoSe_2$ and WSe_2 at the homogeneous limit". In: *Phys. Rev. Materials* 4 (3 Mar. 2020), p. 034001. DOI: 10.1103/PhysRevMaterials.4.034001.

[14] Matthew W. Day, Kelsey M. Bates, Christopher L. Smallwood, Rachel C. Owen, Tim Schröder, Edward Bielejec, Ronald Ulbricht, and Steven T. Cundiff. "Coherent Interactions between Silicon-Vacancy Centers in Diamond". In: *Phys. Rev. Lett.* 128 (20 May 2022), p. 203603. DOI: 10.1103/PhysRevLett.128.203603.

[15] Jiawen You, Md Delowar Hossain, and Zhengtang Luo. "Synthesis of 2D transition metal dichalcogenides by chemical vapor deposition with controlled layer number and morphology". In: *Nano Convergence* 5.1 (Sept. 2018), p. 26. ISSN: 2196-5404. DOI: 10.1186/s40580-018-0158-x.

[16] Kamyar Parto, Shaimaa I. Azzam, Kaustav Banerjee, and Galan Moody. "Defect and strain engineering of monolayer WSe_2 enables site-controlled single-photon emission up to 150 K". In: *Nature Communications* 12.3585 (2021). DOI: 10.1038/s41467-021-23709-5.

[17] Kanak Datta, Zhengyang Lyu, Zidong Li, Takashi Taniguchi, Kenji Watanabe, and Parag B. Deotare. "Spatiotemporally controlled room-temperature exciton transport under dynamic strain". In: *Nature Photonics* 16.3 (Mar. 2022), pp. 242–247. ISSN: 1749-4893. DOI: 10.1038/s41566-021-00951-3.

[18] Di Huang, Junho Choi, Chih-Kang Shih, and Xiaoqin Li. "Excitons in semiconductor moiré superlattices". In: *Nature Nanotechnology* 17.3 (Mar. 2022), pp. 227–238. ISSN: 1748-3395. DOI: 10.1038/s41565-021-01068-y.

[19] Christian W. Freudiger, Wei Min, Brian G. Saar, Sijia Lu, Gary R. Holtom, Chengwei He, Jason C. Tsai, Jing X. Kang, and X. Sunney Xie. "Label-Free Biomedical Imaging with High Sensitivity by Stimulated Raman Scattering Microscopy". In: *Science* 322.5909 (2008), pp. 1857–1861. ISSN: 0036-8075. DOI: 10.1126/science.1165758.

[20] Daniel G. Eichberg, Ashish H. Shah, Long Di, Alexa M. Semonche, George Jimsheleishvili, Evan M. Luther, Christopher A. Sarkiss, Allan D. Levi, Sakir H. Gultekin, Ricardo J. Komotar, and Michael E. Ivan. "Stimulated Raman histology for rapid and accurate intraoperative diagnosis of CNS tumors: prospective blinded study". In: *Journal of Neurosurgery JNS* 134.1 (2021), pp. 137–143. DOI: 10.3171/2019.9.JNS192075.

[21] R Saito, Y Tatsumi, S Huang, X Ling, and M S Dresselhaus. "Raman spectroscopy of transition metal dichalcogenides". In: *Journal of Physics: Condensed Matter* 28.35 (July 2016), p. 353002. DOI: 10.1088/0953-8984/28/35/353002.

[22] Maria O'Brien, Niall McEvoy, Damien Hanlon, Toby Hallam, Jonathan N. Coleman, and Georg S. Duesberg. "Mapping of Low-Frequency Raman Modes in CVD-Grown Transition Metal Dichalcogenides: Layer Number, Stacking Orientation and Resonant Effects". In: *Scientific Reports* 6.1 (Jan. 2016), p. 19476. ISSN: 2045-2322. DOI: 10.1038/srep19476.

[23] Vivek Tiwari, Yassel Acosta Matutes, Alastair. T. Gardiner, Thomas L.C. Jansen, Richard J. Cogdell, and Jennifer P. Ogilvie. "Spatially-resolved fluorescence-detected two-dimensional electronic spectroscopy probes varying excitonic structure in photosynthetic bacteria". In: *Nat. Comm.* 16 (2018), p. 4219. DOI: 10.1038/s41467-018-06619-x.

[24] M. Plankl, P. E. Faria Junior, F. Mooshammer, T. Siday, M. Zizlsperger, F. Sandner, F. Schiegl, S. Maier, M. A. Huber, M. Gmitra, J. Fabian, J. L. Boland, T. L. Cocker, and R. Huber. "Subcycle contact-free nanoscopy of ultrafast interlayer transport in atomically thin heterostructures". In: *Nature Photonics* 15.8 (Aug. 2021), pp. 594–600. ISSN: 1749-4893. DOI: 10.1038/s41566-021-00813-y.

[25] Hyeongwoo Lee, Inki Kim, Chulho Park, Mingu Kang, Jinseong Choi, Kwang-Yong Jeong, Jungho Mun, Yeseul Kim, Jeonghoon Park, Markus B. Raschke, Hong-Gyu Park, Mun Seok Jeong, Junsuk Rho, and Kyoung-Duck Park. "Inducing and Probing Localized Excitons in Atomically Thin Semiconductors via Tip-Enhanced Cavity-Spectroscopy". In: *Advanced Functional Materials* 31.33 (2021), p. 2102893. DOI: https://doi.org/10.1002/adfm.202102893.

[26] Kai-Chih Huang, Jeremy McCall, Pu Wang, Chien-Sheng Liao, Gregory Eakins, Ji-Xin Cheng, and Chen Yang. "High-Speed Spectroscopic Transient Absorption Imaging of Defects in Graphene". In: *Nano Letters* 18.2 (2018). PMID: 29342361, pp. 1489–1497. DOI: 10.1021/acs.nanolett.7b05283.

APPENDICES

APPENDIX A

Additional Details on Pulse Compression

The collinear MDCS setup employed for the work in this thesis leads to significant dispersion of the pulses traveling through the setup, as the AOMs consist of highly dispersive material. To obtain transform-limited pulses at the sample, the pulses need to be chirp-precompensated for GDD and TOD. We used a Grism compressor for the results presented in Chap. V. Because of residual dispersion and low tunability, we upgraded to an SLM-based pulse compressor for the results presented in Chaps. VII and VIII.

Grism Compressor

We initially chose a Grism compressor because prism pairs compensate only small amounts of material dispersion [1], well below the values needed for our experiment. Grating-based compressors do not compress but worsen the TOD when compensating for GDD [1]. It has been shown that with a grism (a prism on top of a grating)-based compressor, both GDD and TOD can be compensated [2, 3].

Here, we use a grism compressor design based on the calculations provided by Dou *et al.* [3]. The design of the grism compressor is shown in Fig. A.1(a), while a photograph of the actual setup in the lab is shown in A.1(b). The initial grating distances,

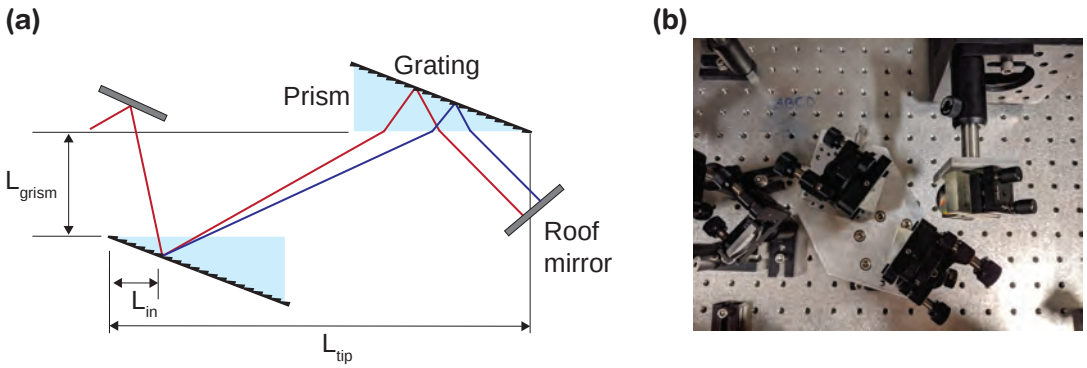

Figure A.1: **(a)** Schematic of a grism compressor consisting of two grisms (prisms glued onto gratings). Different colors (i.e., the red and blue beam) experience a different path length in the compressor, allowing for efficient pulse compression. **(b)** Photograph of the Grism compressor used in the CINeMaS setup.

insertion distances, and angles were designed based on an initial characterization of the laser pulses at the sample plane.

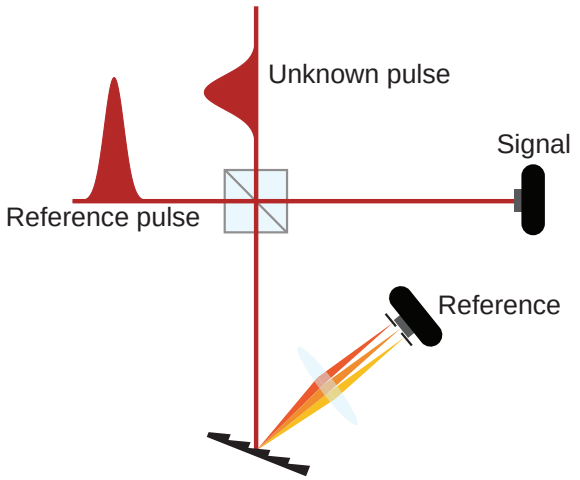

Figure A.2: Cross-correlation pulse characterization scheme with self-referencing.

To characterize our pulses, we employ phase-resolved cross-correlation with a known reference pulse, shown in Fig. A.2. We interfere the reference pulse with the unknown pulse which has passed through the CINeMaS experimental setup and generate a reference for the phase-resolved measurement as follows: After combining the two pulses, we take one of the beamsplitter outputs and spectrally narrow it using a grating and thin slit before sending the beams onto a detector. A focusing lens

is placed a distance f (focal length) away from the grating and the detector/slit. The spectral narrowing ensures that the reference is temporally longer lived than the signal. This scheme is similar to the procedure employed in [4] for generating a reference signal. The reference signal is subsequently electronically processed with the procedure outlined in [5]. The signal can be efficiently filtered out by exploiting the beat note between the amplitude modulation that the laser repetition rate imparts on the reference pulse and the amplitude modulation imparted on the unknown pulse by the AOM. The other beamsplitter output is sent directly onto a detector and used as the lock-in input. By scanning the delay between the reference and unknown pulse, we obtain full amplitude and phase information in the temporal domain and, via Fourier transform, can obtain spectral amplitude and phase information of our laser pulse. The reference pulse is characterized using second harmonic generation (SHG)-frequency-resolved optical gating (FROG). Figs. A.3(a,b) show the measured and reconstructed FROG traces. The corresponding spectrum and spectral phase of the reference pulse are shown in Fig. A.3(c).

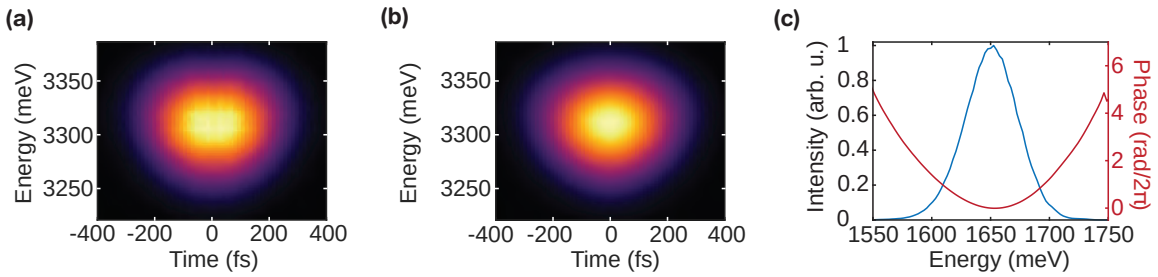

Figure A.3: **(a)** Measured FROG trace of the reference pulse. **(b)** Reconstructed FROG trace of the reference pulse. **(c)** Reconstructed spectrum and spectral phase of the reference pulse.

Optimizing the grism compressor, we obtain sub-100 fs pulses, with estimates for the effective temporal resolution of our technique derived from the method outlined in Ref. [6]. This work notes that absorption profiles narrower than the pulse bandwidth have an effectively higher temporal resolution than what the chirp-limited pulse duration might initially suggest. In Fig. A.4(a), we plot the pulse profile at the sample

characterized via cross-correlation. In Fig. A.4(b), we plot the assumed absorption profile for the $MoSe_2$ and WSe_2 resonance on the heterostructure sample discussed in Chap. V, estimated from the MDCS spectra. Since we are only interested in a rough estimate of our temporal resolution, this is sufficient. In Fig. A.4 (c), we plot the corresponding temporal response function for the on-diagonal $MoSe_2$ and WSe_2 peaks and the two coupling peaks. We generalize the procedure of Ref. [6] by using the sample absorption (which also corresponds to the emission) of the two resonances in both the preparation and observation window. Using the $MoSe_2$ absorption for both the preparation and observation window, we obtain the temporal profile for the $MoSe_2$ peak in Fig. A.4. Similarly, we obtain the temporal profile for the WSe_2 peak. We obtain the profile for the coupling peak by assuming absorption from one resonance for the preparation and emission from the other resonance in the observation window. The symmetry of Eq. (12) in Ref. [6] automatically leads to the same temporal resolution for both coupling peaks. We then estimate the temporal resolution from the full-width-half-maximum (FWHM) of the displayed temporal intensity profiles, which read 83 fs for the $MoSe_2$ peak, 100 fs for the WSe_2 peak, and 92 fs for the coupling peaks.

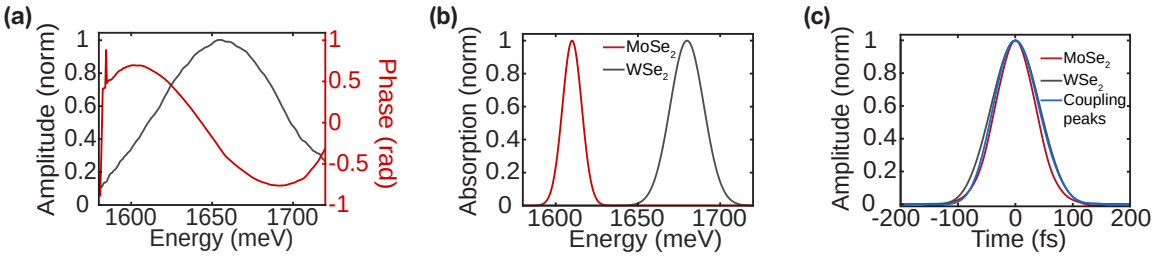

Figure A.4: **(a)** Temporal profile (amplitude and phase) of the pulse at the sample, characterized via cross-correlation. **(b)** Approximated absorption profile on the heterostructure for $MoSe_2$ and WSe_2. **(c)** Temporal intensity profile of the on-diagonal and coupling peak response assuming an instantaneous sample response and the absorption profile shown in (b).

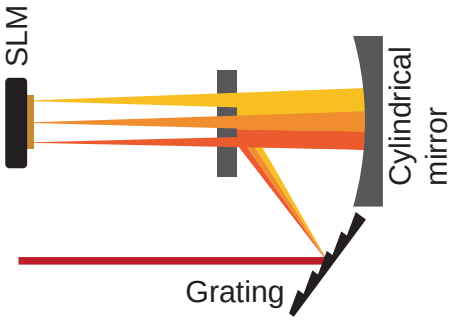

Figure A.5: Schematic drawing of SLM-based pulse shaper used to compress pulses for the experiments presented in Chaps. VII and VIII.

Spatial Light Modulator Compressor

Because of the complex and large chirp imparted onto the pulses by the CINeMaS setup and the desire to maintain the center wavelength and bandwidth adjustability of the laser pulses, we moved from a grism compressor-based setup to an SLM-based pulse shaper for pulse compression. Our design is inspired by the apparatus presented in Ref. [7]. This compressor was built by Blake Hipsley.

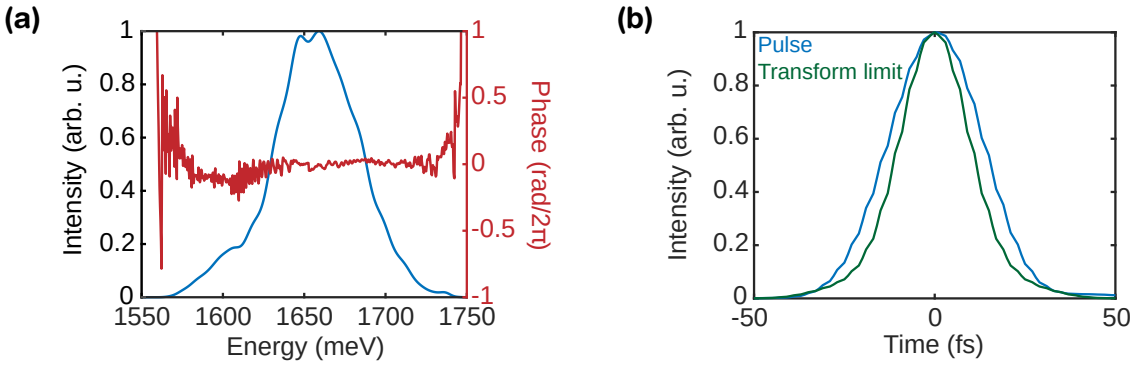

Figure A.6: **(a)** Laser pulse spectrum and corresponding phase and **(b)** time-domain trace and transform-limited pulse of the laser spectrum.

The SLM-based pulse shaper employed in our setup is shown in Fig. A.5. The laser pulses are spatially dispersed using a 1200 grooves/mm grating and focused onto the SLM using a 10 cm focal length concave cylindrical mirror. These optics have been chosen to spread the laser spectrum across many pixels on the SLM, mitigating the detrimental effects of pixelation and cross-talk between adjacent pixels on the

compressed pulses. The SLM (Meadowlark Optics 1x12K Linear SLM) then acts as a variable phase mask and is used to alter the phase of individual wavelengths of the laser spectrum. We generate a phase mask on the SLM to specifically pre-compensate for the dispersion acquired from the optical elements in the experimental setup.

We present spectral amplitude and phase information of our laser pulses measured at the sample position in Fig. A.6(a). Within the bandwidth of our laser, the complex phase is mostly flat. This observation suggests that the pulse compression system has corrected much of the dispersion. In Fig. A.6(b), we show the compressed pulse and its transform limit in the temporal domain. Fitting the time domain traces to Gaussian pulses, we determine the FWHM of the laser pulse to be 30 fs as compared to the FWHM of 24 fs for the transform limit, suggesting near-transform-limited pulses.

References

[1] R. L. Fork, O. E. Martinez, and J. P. Gordon. "Negative dispersion using pairs of prisms". In: *Opt. Lett.* 9.5 (May 1984), pp. 150–152. DOI: 10.1364/OL.9.000150.

[2] S. Kane and J. Squier. "Grism-pair stretcher-compressor system for simultaneous second- and third-order dispersion compensation in chirped-pulse amplification". In: *J. Opt. Soc. Am. B* 14.3 (Mar. 1997), pp. 661–665. DOI: 10.1364/JOSAB.14.000661.

[3] Tai H. Dou, Raphael Tautz, Xun Gu, Gilad Marcus, Thomas Feurer, Ferenc Krausz, and Laszlo Veisz. "Dispersion control with reflection grisms of an ultra-broadband spectrum approaching a full octave". In: *Opt. Express* 18.26 (Dec. 2010), pp. 27900–27909. DOI: 10.1364/OE.18.027900.

[4] Patrick F. Tekavec, Geoffrey A. Lott, and Andrew H. Marcus. "Fluorescence-detected two-dimensional electronic coherence spectroscopy by acousto-optic phase modulation". In: *The Journal of Chemical Physics* 127.21 (2007), p. 214307. DOI: 10.1063/1.2800560.

[5] Eric W. Martin, Christopher L. Smallwood, Torben L. Purz, Hanna G. Ruth, and Steven T. Cundiff. "Real-Time Reference for Frequency-Shifted Fourier-Transform Spectrometers Using an Arbitrary-Wavelength CW Reference Laser". In: *2019 Conference on Lasers and Electro-Optics (CLEO)*. 2019, pp. 1–2. DOI: 10.1364/CLEO_SI.2019.SM4F.4.

[6] D. Polli, D. Brida, S. Mukamel, G. Lanzani, and G. Cerullo. "Effective temporal resolution in pump-probe spectroscopy with strongly chirped pulses". In: *Phys. Rev. A* 82 (5 Nov. 2010), p. 053809. DOI: 10.1103/PhysRevA.82.053809.

[7] J. Pupeikis, N. Bigler, S. Hrisafov, C. R. Phillips, and U. Keller. "Programmable pulse shaping for time-gated amplifiers". In: *Opt. Express* 27.1 (Jan. 2019), pp. 175–184. DOI: 10.1364/OE.27.000175.

APPENDIX B

Transfer Matrix Method for Linear Reflectance Spectra of Transition Metal Dichalcogenide Samples

To understand the reflection spectra of TMDs such as the ones presented in App. C, the contributions from numerous backreflections caused by the typical encapsulation in hBN and backreflections from the substrate that interfere with other reflections must be considered. For a complete understanding of the experiments, a thorough treatment using the transfer matrix method is thus inevitable.

The transfer matrix method relates the incoming and outgoing fields on one side of the interface to the incoming and outgoing fields on the other side of the interface [1],

$$\begin{bmatrix} {E_j}^+ \\ {E_j}^- \end{bmatrix} = M \begin{bmatrix} {E_i}^+ \\ {E_i}^- \end{bmatrix} , \tag{B.1}$$

with i,j signifying the side of the respective interface. This form is convenient when several interfaces are considered, as is the case for conventional encapsulated TMD samples. As an example, we present the case of an encapsulated $MoSe_2$ monolayer treated experimentally in Chap. VII.

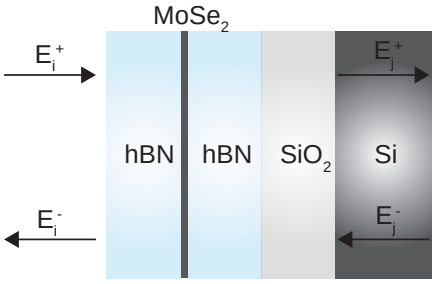

Figure B.1: Illustration of the sample geometry. The $MoSe_2$ monolayer is surrounded by two layers of hBN and mounted onto a SiO_2/Si substrate.

The general structure of such a sample is shown in Fig. B.1. The $MoSe_2$ monolayer is encapsulated with layers of hBN on both sides, which weaken both dielectric effects from the substrate and surface effects [2, 3]. A typical substrate for TMD samples is a thin layer of SiO_2 on a hundreds of micron-thick layer of Si, which can be effectively treated as a bulk material. As derived in Ref. [4], the general structure of the transfer matrix then reads

$$T_{\text{tot}} = T_{\text{SiO}_2\to\text{Si}} T_{\text{SiO}_2} T_{\text{SiO}_2\to\text{Si}} T_{\text{hBN}\to\text{SiO}_2} T'_{\text{hBN}} T_{\text{air}\to\text{hBN}} T_{\text{MoSe}_2} T^{-1}_{\text{air}\to\text{hBN}} T_{\text{hBN}} T_{\text{air}\to\text{hBN}} \,, \tag{B.2}$$

with the matrix $T_{\text{air}\to\text{hBN}}$ and its inverse matrix being incorporated because the transfer matrix for the $MoSe_2$ monolayer, T_{MoSe_2}, assumes a monolayer in vacuum. The three-matrix expression $T_{\text{air}\to\text{hBN}} T_{\text{MoSe}_2} T^{-1}_{\text{air}\to\text{hBN}}$ can be shortened to T_{MoSe_2} with

$$\frac{1}{t}\begin{pmatrix} t^2 - r^2 & r \\ -r & 1 \end{pmatrix} \,, \tag{B.3}$$

with the reflection coefficient

$$r = \frac{i{\Gamma_0}^{hBN}}{\omega_0 - \omega - i({\Gamma_0}^{hBN} + \Gamma)} \,, \tag{B.4}$$

where ${\Gamma_0}^{\text{hBN}} = {\Gamma_0}^{\text{vac}}/n_{\text{hBN}}$ considers the change of the radiative linewidth Γ_0^{vac} due

to the dielectric environment of the hBN. Using the relation $t = 1 + r$, the transfer for the hBN-embedded $MoSe_2$ can be determined. The transfer matrix between two interfaces, marked by the $\rightarrow$ in the subscript

$$T_{n_1 \rightarrow n_2} = \frac{1}{2n_1} \begin{pmatrix} n_1 + n_2 & n_2 – n_1 \\ n_2 – n_1 & n_2 + n_1 \end{pmatrix}, \tag{B.5}$$

can be determined by using the refractive indices $n_{1,2}$ for the two materials.

Similarly, the transfer matrix for the propagation in a material can be determined by

$$T_{ML} = \begin{pmatrix} \exp(ikL) & 0 \\ 0 & \exp(-ikL) \end{pmatrix}, \tag{B.6}$$

with $k = 2\pi n/\lambda$ and L the thickness of the material. We use the Sellmeier equation for the refractive indices given the broad excitation bandwidth of the laser used in our spectroscopy experiments.

Once the transfer matrix T_{tot} is obtained from Eq. B.2, the relation

$$T_{tot} \begin{pmatrix} 1 \\ r_{tot} \end{pmatrix} = \begin{pmatrix} t_{tot} \\ 0 \end{pmatrix}, \tag{B.7}$$

can be used to obtain the reflection coefficient of the entire sample structure, r_{tot}. The ultimate form of the reflection strongly depends on numerous parameters, most of which are expected to remain approximately constant across the sample, such as substrate and encapsulation thickness. However, as shown by Refs. 56 and in Chap. VII, the radiative linewidth and scattering contributions can strongly vary across the sample, affecting the linear reflectance. The change in reflectance is important to consider in spectroscopy setups where the heterodyne reference reflects off the sample, which is the case for Chaps. VII and VIII.

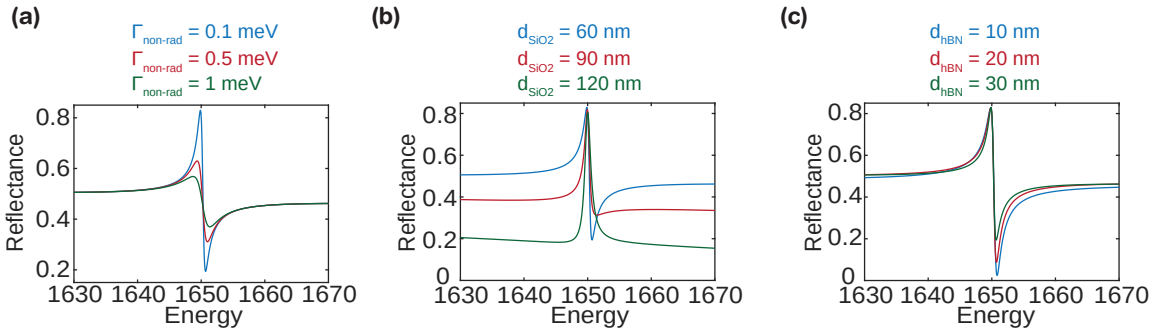

Figure B.2: Simulated reflectivity of the sample geometry shown in Fig. B.1 for **(a)** varying scattering decay rate, **(b)** varying Si_2 thickness, and **(c)** varying top hBN thickness.

We have plotted exemplary spectra obtained for the sample geometry in Fig. B.1 in Fig. B.2. In Fig. B.2(a), we vary the contribution of the non-radiative decay from 0.1 meV to 1 meV. The fixed parameters are $\Gamma_{\mathrm{rad}} = 1\,\mathrm{meV}$, $E_R = 1650\,\mathrm{meV}$, $d_{\mathrm{hBN},1} = 30\,\mathrm{nm}$, $d_{\mathrm{hBN},2} = 30\,\mathrm{nm}$, and $d_{\mathrm{SiO_2}} = 200\,\mathrm{nm}$. As the non-radiative contribution increases, the general reflectivity curve shape is preserved. However, the maximum visibly decreases, and the minimum increases. In Fig. B.2(b,) we keep the non-radiative contribution to the linewidth fixed at $\Gamma_{\mathrm{non-rad}} = 0.1\,\mathrm{meV}$ but vary the thickness of the SiO_2 layer between 60 nm and 120 nm. As the thickness of the SiO_2 layer increases, the overall reflectivity outside the exciton resonance decreases. Furthermore, the dispersive lineshape features increasingly narrow. Lastly, in Fig. B.2(c), we vary the top hBN thickness between 10 nm and 30 nm. In this case, the maximum of the reflectance remains approximately constant, while the minimum decreases for decreasing hBN thickness. As further discussed in App. C, the interplay between these parameters guarantees a reflectivity that will vary from sample to sample and, most importantly, across the sample.

References

[1] Max Born, Emil Wolf, A. B. Bhatia, P. C. Clemmow, D. Gabor, A. R. Stokes, A. M. Taylor, P. A. Wayman, and W. L. Wilcock. *Principles of Optics: Electromagnetic Theory of Propagation, Interference and Diffraction of Light*. 7th ed. Cambridge University Press, 1999. DOI: 10.1017/CBO9781139644181.

[2] Archana Raja, Lutz Waldecker, Jonas Zipfel, Yeongsu Cho, Samuel Brem, Jonas D. Ziegler, Marvin Kulig, Takashi Taniguchi, Kenji Watanabe, Ermin Malic, Tony F. Heinz, Timothy C. Berkelbach, and Alexey Chernikov. "Dielectric disorder in two-dimensional materials". In: *Nature Nanotechnology* 14.9 (Sept. 2019), pp. 832–837. ISSN: 1748-3395. DOI: 10.1038/s41565-019-0520-0.

[3] Eric W. Martin, Jason Horng, Hanna G. Ruth, Eunice Paik, Michael-Henr Wentzel, Hui Deng, and Steven T. Cundiff. "Encapsulation Narrows and Preserves the Excitonic Homogeneous Linewidth of Exfoliated Monolayer $MoSe_2$". In: *Phys. Rev. Applied* 14 (2 Aug. 2020), p. 021002. DOI: 10.1103/PhysRevApplied.14.021002.

[4] C. Robert, M. A. Semina, F. Cadiz, M. Manca, E. Courtade, T. Taniguchi, K. Watanabe, H. Cai, S. Tongay, B. Lassagne, P. Renucci, T. Amand, X. Marie, M. M. Glazov, and B. Urbaszek. "Optical spectroscopy of excited exciton states in MoS_2 monolayers in van der Waals heterostructures". In: *Phys. Rev. Materials* 2 (1 Jan. 2018), p. 011001. DOI: 10.1103/PhysRevMaterials.2.011001.

[5] Tomasz Jakubczyk, Karol Nogajewski, Maciej R Molas, Miroslav Bartos, Wolfgang Langbein, Marek Potemski, and Jacek Kasprzak. "Impact of environment on dynamics of exciton complexes in a WS_2 monolayer". In: *2D Materials* 5.3 (Apr. 2018), p. 031007. DOI: 10.1088/2053-1583/aabc1c.

[6] Tomasz Jakubczyk, Goutham Nayak, Lorenzo Scarpelli, Wei-Lai Liu, Sudipta Dubey, Nedjma Bendiab, Laëtitia Marty, Takashi Taniguchi, Kenji Watanabe, Francesco Masia, Gilles Nogues, Johann Coraux, Wolfgang Langbein, Julien Renard, Vincent Bouchiat, and Jacek Kasprzak. "Coherence and Density Dynamics of Excitons in a Single-Layer MoS_2 Reaching the Homogeneous Limit". In: *ACS Nano* 13.3 (2019). PMID: 30735350, pp. 3500–3511. DOI: 10.1021/acsnano.8b09732.

APPENDIX C

Additional Data on Chapter VII

Linewidth Fitting and Absorption Correction

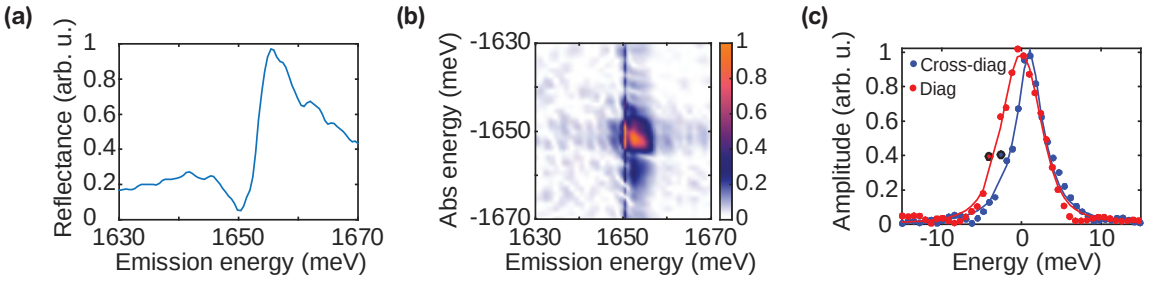

Figure C.1: **(a)** Reflectance spectrum for the $MoSe_2$ monolayer, showing a noticeable dip around 1650 meV. **(b)** Using the reflectance spectrum from (a) in the correction scheme leads to a singular line at fixed emission energy dominated by noise. In contrast, the rest of the MDCS spectrum is reconstructed reliably. **(c)** Fit of diagonal and cross-diagonal slices when excluding specific emission energies with low reflectance. Data points that are excluded in the fits have a black edge.

Since the fourth pulse used for heterodyne detection is also sent onto the sample, the absorption has to be considered to retrieve the accurate spectral weight along the emission energy axis. Rapid imaging and the desire for phase stability make this option more viable than routing the fourth beam across the sample as down for the experiments in Chap. V.

However, TMD monolayers at cryogenic temperatures have strong absorption. Due to multiple reflections stemming from the substrate and hBN encapsulation, reflectance spectra with strong absorption dips, as plotted in Fig. C.1(a) and discussed in App. B can result. In this case, FWM signals around the reflectance dip will be noise dominated, and the absorption correction procedure fails for small parts of the spectrum, as illustrated in Fig. C.1(b). As evident from the spectrum, data points towards the left and the right of the sharp, bright line at 1650 meV are unaffected. Hence, excluding the erroneous data point(s) can yield robust fits that reliably extract the homogeneous and inhomogeneous linewidths. The fit robustness is illustrated in Fig. C.1(c), which shows the diagonal and cross-diagonal slices of the spectrum in Fig. C.1(b), with all data points where the reflection amplitude falls below 7.5% of the maximum excluded (marked with a black edge). The fits (solid lines) match the data points well, and the extracted linewidths can be trusted. We employ the described cutoff procedure for data points where the reflected spectrum has an amplitude below 7.5% for all linewidth fit maps in Chap. VII.

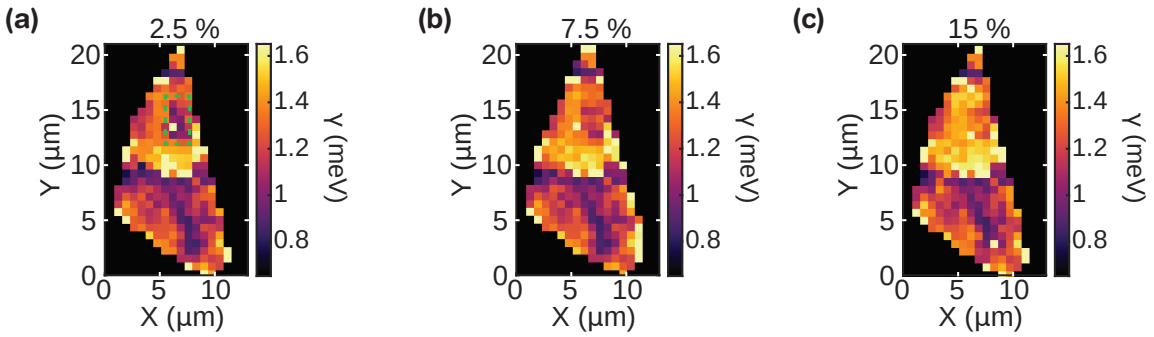

Figure C.2: Homogeneous linewidth (γ) map of the $MoSe_2$ monolayer with an amplitude cutoff of (a) 2.5%, (b) 7.5%, (c) 15%.

The value 7.5% has been determined as a reasonable cutoff by observing fit errors and reliability of extracted linewidths for cutoffs between 2.5% and 15%. The extracted linewidths were only sensitive for a few sample points, as shown in Fig. C.2, where we plot the extracted homogeneous linewidth for three different amplitude cutoffs. The area marked with a green rectangle in Fig. C.2(a) is the only area of

the sample showing noticeable linewidth changes when changing the cutoff to 7.5% (Fig. C.2(b)) and 15% (Fig. C.2(c)).

Linear Reflectance of $MoSe_2$ Monolayer

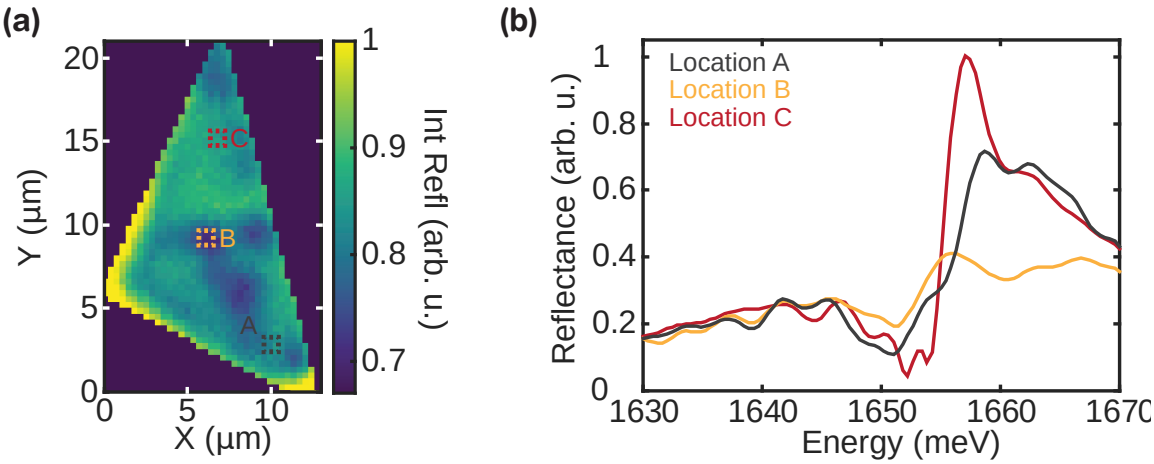

Figure C.3: **(a)** Integrated reflectance for the $MoSe_2$ monolayer. **(b)** Reflectance spectra for the three areas marked by colored squares in (a).

The cutoff procedure described in the previous section is only crucial for a few select data points on the sample, as the reflectance spectrum varies strongly across the sample. The integrated reflectance map of the $MoSe_2$ monolayer sample is shown in Fig. C.3(a). The high strain area of the sample identified in Chap. VII shows a lower integrated reflectance. The lower reflectance of this area (yellow square) is due to an overall lower reflection, especially towards higher energies, as evident from Fig. C.3(b). For the two other sample areas selected here, the difference between the depth of the reflectance dip around 1652 meV and the height of the reflectance peak around 1657 meV is smaller. The stark differences can be explained by linewidth changes, which strongly influence the reflection coefficient for an encapsulated monolayer with numerous backreflections, as further discussed in App. B and the literature [1].

Multidimensional Coherent Imaging Spectroscopy Data on $MoSe_2$/ WSe_2 heterostructure

Fig. C.4 shows three exemplary MDCIS spectra corresponding to the locations from Fig. 7.7 in the main text.

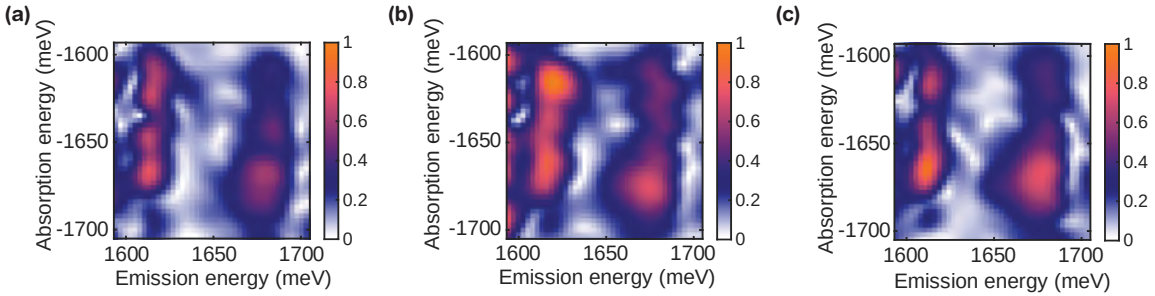

Figure C.4: MDCIS data on Location A **(a)**, Location B **(b)**, and Location C **(c)** from Fig. 7.7.

The rephasing data shows broader linewidth than the absorptive spectrum and shifts in energy along the absorption energy axis can be observed due to the high sensitivity towards phase-shifts in the τ stage (see discussion of phase stability in Sec. 4.2.2). This is exacerbated in the MDCIS data in Fig. C.4 due to the long acquisition time of 30-60 minutes, but can even be observed in Fig. C.5, where we plot the rephasing part of the spectra from Fig. 7.7.

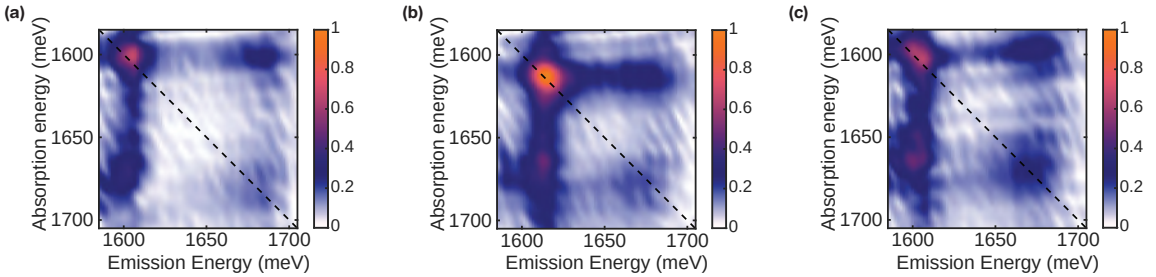

Figure C.5: Rephasing one-quantum MDCS data (T=500 fs) on Location A **(a)**, Location B **(b)**, and Location C **(c)** from Fig. 7.7

The difference between the MDCIS and MDCS data can be attributed to phase-shifts along τ and t, which also affects the normalization spectrum and can explain the difference in strength distribution of the two peaks at $MoSe_2$ and WSe_2 emission. The

quality of the MDCIS data can further be improved by averaging, which has not been done for this T-dependent data set due to data acquisition time constraints. Further increasing the phase-stability of the setup through an improved enclosure (which has been built after the acquisition and publication of this data) and parallel-oriented Michelson interferometers can also improve the quality of the MDCIS spectra. The effect of improved phase-stability can be seen in Ref. 2.

However, the spectrally integrated data in Chap. VII alleviates many of these issues (including reduction of noise), allowing for a consistent extraction of resonance energies as well as temporal dynamics of the four peaks.

References

[1] C. Robert, M. A. Semina, F. Cadiz, M. Manca, E. Courtade, T. Taniguchi, K. Watanabe, H. Cai, S. Tongay, B. Lassagne, P. Renucci, T. Amand, X. Marie, M. M. Glazov, and B. Urbaszek. "Optical spectroscopy of excited exciton states in MoS_2 monolayers in van der Waals heterostructures". In: *Phys. Rev. Materials* 2 (1 Jan. 2018), p. 011001. DOI: 10.1103/PhysRevMaterials.2.011001.

[2] Torben L. Purz, Blake T. Hipsley, Eric W. Martin, Ronald Ulbricht, and Steven T. Cundiff. "Rapid multiplex ultrafast nonlinear microscopy for material characterization". In: *Opt. Express* 30.25 (Dec. 2022), pp. 45008–45019. DOI: 10.1364/OE.472054.

APPENDIX D

Additional Data on Chapter VIII

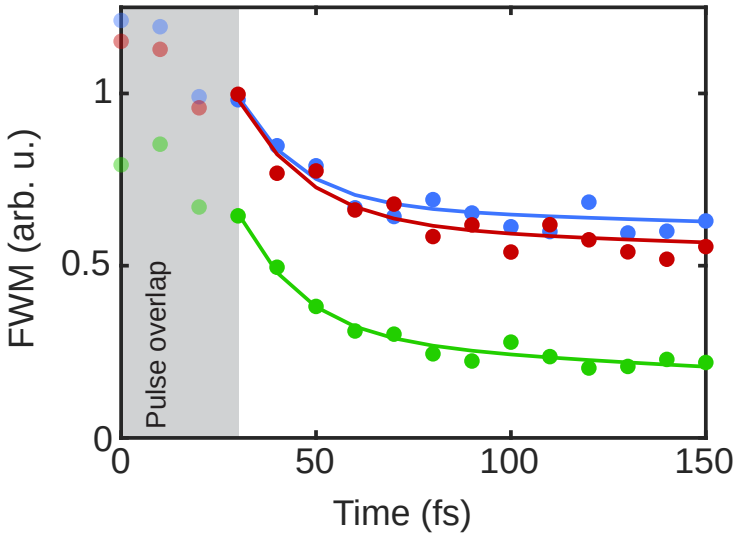

Figure D.1: Decay curves for T delays between 0-150 fs, highlighting the rapid decay and finite pulse effects at early times.

Fig. D.1 shows the decay curves from Fig. 8.4 in the range of 0-150 fs for the time delay T. Again, finite pulse effects are observable during early delay times, followed by a rapid decay. The excellent agreement between fit and data for early times yields reliable retrieval of exciton population decay times.